Universitat Internacional de Catalunya
Facultat de Medicina i Ciències de la Salut
Departament de Ciències Bàsiques

uιC
barcelona

Tesi doctoral

DEVELOPMENT OF C75-CoA LOADED POLYMERIC MICELLES TARGETING BRAIN CPT1A: A NOVEL NANOMEDICINE-BASED APPROACH TO FIGHT OBESITY AND CANCER

Jesús García Chica

UNIVERSITAT INTERNACIONAL DE CATALUNYA

MEDICINE AND HEALTH SCIENCE FACULTY

BASIC SCIENCE DEPARTMENT

DEVELOPMENT OF C75-CoA LOADED POLYMERIC MICELLES TARGETING BRAIN CPT1A: A NOVEL NANOMEDICINE-BASED APPROACH TO FIGHT OBESITY AND CANCER

Jesús García Chica

2023

uic barcelona

DEVELOPMENT OF C75-CoA LOADED POLYMERIC MICELLES TARGETING BRAIN CPT1A: A NOVEL NANOMEDICINE-BASED APPROACH TO FIGHT OBESITY AND CANCER

Doctoral thesis manuscript presented by Jesús García Chica to opt for the degree of Doctor of Philosophy (PhD) awarded by the Universitat Internacional de Catalunya.

This thesis has been conducted in the Basic Science Department from the Medicine and Health Science Faculty of the Universitat Internacional de Catalunya, under the co-direction of Dr. Rosalía Rodríguez Rodríguez, from Universitat Internacional de Catalunya, and Dr. Xavier Ariza Piquer, from Universitat de Barcelona,

Sant Cugat del Vallés, 2023

Dr. Rosalía Rodríguez	**Dr. Xavier Ariza**	**Jesús García**
Director	Director	PhD student

Abstract

Brain lipid metabolism has a key role in many physiological processes, and its malfunction is associated with a plethora of diseases, such as obesity and glioblastoma multiforme (GBM). Carnitine palmitoyl transferase 1A (CPT1A), an important protein in the fatty acid oxidation (FAO) pathway, has a prominent role in this association. In the brain, activation of CPT1A in hypothalamic neurons increases food intake and body weight in mice, while its inhibition causes the opposite effect, indicating its antiobesity potential. In GBM cells, overexpression of CPT1A and other lipid metabolism proteins has been described as a crucial pathway for GBM cell survival. Then, pharmacological inhibition of CPT1A and therefore fatty acid oxidation, could constitute a promising treatment for these diseases. However, targeting CPT1A in brain cells is difficult to reach with the current formulations in vivo. The racemic drug Compound 75 (C75) is a well-known CPT1A inhibitor when conjugated with Coenzyme A, but with important constraints such as polarity and low cell-permeability that limit the cellular uptake.

In this Thesis, we have developed an advanced core crosslinked poly-ion complex (PIC) micelle type nanomedicine that can stably encapsulate the CPT1A inhibitor C75-CoA and its enantiomers to improve CPT1A targeting in brain cells. These polymeric nanomedicines have been validated in vitro in cellular models of GBM and hypothalamic neurons, and also in vivo in mice, compared to the free drug.

We synthesized PEG-PAsp(DET) PIC micelles encapsulating (±)-, (+)- and (–)-C75-CoA. After physico-chemical characterization, the micelles showed the ability to strongly inhibit ATP synthesis and FAO compared to the free drug in GT1-7, a hypothalamic neuronal cell line, and U87MG, a GBM cell line. We also developed micelles encapsulating Fluorescein-CoA to use as a fluorescent model particle. Treatment of cells (2D and 3D spheroids) with these

crosslinked based-nanomedicines showed that Fluorescein-CoA was more easily internalized by these cell lines compared to free fluorescein-CoA and non-crosslinked micelles, indicating a higher uptake of the cargo when using the proposed nanomedicine in vitro.

For *in vivo* studies, we synthesized a new crosslinked PIC micelle composed of PEG-PAsp(Aldehyde)-Plys and PEG-PAsp(Hydrazide) polymers. These polymers are able to covalently conjugate, forming a much more stable micelle for in vivo applications. Intracerebroventricular administration of these crosslinked PIC micelles encapsulating C75-CoA, led to a reduction in food intake and body weight in lean mice already appreciated after 3h, significantly higher compared to the free drug. This satiating effect was in line with a modulation in the expression of hunger-related hypothalamic neuropeptides and an induction of neuronal activation in specific hypothalamic nuclei after central administration of the C75-CoA micelle, that was not appreciated with the free drug. These changes induced by the micelle in the hypothalamus were also associated with an alteration in the metabolic profile of peripheral tissues such as the liver and brown fat.

These results demonstrate that crosslinked PIC micelles encapsulating the CPT1A inhibitor are able to modulate lipid metabolism *in vitro* and can regulate food intake and body weight through modulation of hypothalamic neuropeptide expression and neuronal activation *in vivo*, thereby driving a central and peripheral response. This research lays the foundation for the application of PIC micelles as drug delivery systems for the development of treatments against pathologies related to alterations in lipid metabolism.

Resumen

El metabolismo lipídico del cerebro tiene un rol principal en muchos procesos fisiológicos, y su mal funcionamiento está asociado a una plétora de enfermedades, como la obesidad y el glioblastoma multiforme (GBM). La carnitina palmitoil transferasa 1 (CPT1A), una proteína importante en la vía de oxidación de ácidos grasos (FAO), tiene un rol prominente en esta asociación. En el cerebro, la activación de CPT1A en el hipotálamo incrementa la ingesta y el peso corporal, mientras que su inhibición causa el efecto opuesto, indicando su potencial antiobesidad. En células de GBM, se ha descrito la sobreexpresión de CPT1A y otras proteínas del metabolismo lipídico como una vía metabólica crucial para la supervivencia de las células de GBM. De esta forma, la inhibición farmacológica de CPT1A y por tanto de la oxidación de ácidos grasos podría constituir un tratamiento prometedor para estas enfermedades. Sin embargo, es difícil tratar CPT1A en las células cerebrales *in vivo* con las formulaciones actuales. El fármaco racémico Compuesto 75 (C75) es un inhibidor conocido de CPT1A cuando está en su forma conjugada con Coenzima A, pero con importantes limitaciones como una alta polaridad y baja permeabilidad celular, que limitan la entrada en las células.

En esta tesis, hemos desarrollado una nanomedicina basada en avanzadas micelas de tipo "poly-ion complex" (PIC) con núcleo entrelazado, capaces de encapsular de forma estable el inhibidor de CPT1A C75-CoA y sus enantiómeros para mejorar el tratamiento de CPT1A en células cerebrales.

Hemos sintetizado micelas PIC compuestas de PEG-PAsp(DET) que encapsulan (±)-, (+)- y (−)-C75-CoA. Tras la caracterización físico-química, estas micelas mostraron la capacidad de inhibir fuertemente la síntesis de ATP y la FAO comparadas al fármaco libre en GT1-7, una línea celular de neuronas hipotalámicas, y U87MG, una línea celular de GBM. También hemos desarrollado micelas que encapsulan Fluoresceína-CoA para usarlas como

partículas modelo. El tratamiento de células (2D y esferoides 3D) tratadas con estas micelas mostró que las micelas cargadas con Fluoresceína-CoA eran más fácilmente internalizadas por las células que la Fluoresceína-CoA libre y las micelas no entrelazadas, indicando una mayor internalización de la carga al usar las nanomedicinas propuestas *in vitro*.

Para los estudios *in vivo*, sintetizamos una nueva micela PIC covalente compuesta delos polímeros PEG-PAsp(Aldehído)-PLys y PEG-PAsp(Hidrazida). Estos polímeros son capaces de unirse entre ellos de forma covalente, formando una micela mucho más estable para aplicaciones *in vivo*. La administración intracerebroventricular de estas micelas PIC entrelazadas encapsulando C75-CoA llevó a una reducción en el peso y la ingesta de ratones delgados tras 3 h, significativamente más alto comparado con el fármaco libre. Este efecto saciante fue concurrente a la modulación en la expresión de neuropéptidos hipotalámicos relacionados con la ingesta, y a la activación neuronal en núcleos hipotalámicos tras la administración central de la micela C75-CoA, que no se apreció con el fármaco libre. Los cambios inducidos por la micela en el hipotálamo también estuvieron asociados a una alteración en el perfil metabólico de tejidos como el hígado y el tejido adiposo marrón

Estos resultados demuestran que las micelas PIC encapsulando inhibidores de CPT1A son capaces de modular el metabolismo lipídico *in vitro* y que pueden regular la ingesta y el peso corporal a través de la modulación de la expresión de péptidos hipotalámicos y activación neuronal *in vivo*, causando de este modo una respuesta central y periférica. Esta investigación pone los cimientos para la aplicación de micelas PIC como sistemas de entrega de fármacos para el desarrollo de tratamientos contra patologías relacionadas con alteraciones en el metabolismo lipídico.

TABLE OF CONTENTS

INTRODUCTION

1. Brain lipid metabolism and related disorders

Lipids are essential macromolecules for the normal function of the organism. They can perform structural or physiological functions. Based on their structure, they can be broadly divided into six categories: fatty acids, triglycerides, phospholipids, sterol lipids, terpenes and sphingolipids (Tracey et al. 2018). The main peripheral functions of lipids are making up cell membranes (mainly phospholipids), regulatory and signaling functions (isoprenoids and lipid hormones),as well as being stored as an energy source (triglycerides) (R. Guo et al. 2020).

Their importance is exacerbated in the brain, where the lipid content amounts to more than 50% of the dry weight, only surpassed by the adipose tissue (Hamilton et al. 2007). Acylated phospholipids are used as structural components for neuronal cell membranes, and it is known that several fatty acids (FAs) are necessary for the structure and function of the brain. Furthermore, sensing of FAs by different cells in the brain is paramount for several key functions such as energy homeostasis or cognitive processes (Bruce et al. 2017; Lam et al. 2005). Some of these FAs can be synthesized locally, but most of them are transported from the liver (Rapoport 2001). At the beginning of the century, brain lipid metabolism, and particularly the metabolism of FA in different brain areas, was described as having a prominent role in the regulation of the energy homeostasis of the organism (Schwartz et al. 2000; Spiegelman et al. 2001).

FAs can be synthesized and oxidized in the brain. FA synthesis starts with the carboxylation of acetyl-CoA (originating from the glucose metabolism) into malonyl-CoA via acetyl-CoA carboxylase (ACC)(Wakil et al. 1983). Malonyl-CoA constitutes the first substrate in fatty acid synthesis and at the same time is the inhibitor of the first step of the fatty acid oxidation (FAO) pathway. Next,

unreacted acetyl-CoA and malonyl-CoA undergo transacylation to an acyl-carrier protein (ACP) to form acetyl-ACP and malonyl-ACP. After this, fatty acid synthase (FAS), is in charge of performing a cycle of four sequential reactions: condensation, reduction, dehydration, and second reduction. The result of these reactions is the addition of 2 carbons to the malonyl-ACP backbone, and the product of this reaction will undergo these four reactions again for the elongation of the FA chain, and then a thioesterase will catalyze the formation of the FA by removing ACP (**Figure 1A**).

FAO is primarily performed in order to meet the energy requirements of tissues, including the brain. It is carried out in the mitochondrial matrix. FAs transported into the cell are converted to fatty acyl-CoA by acyl-CoA synthases, and then the carnitine shuttle system comes into play to translocate fatty acyl-CoA molecules to the mitochondrial matrix. The first step of the carnitine shuttle system involves the translocation into the mitochondrial outer compartment by the production of acylcarnitines from fatty acyl-CoAs. This reaction is performed by carnitine acyltransferase proteins. There are several of these proteins to accommodate for the diversity in chain length and site preference of fatty acids. Carnitine palmitoyl transferase 1 and 2 (CPT1 and CPT2) are in charge of medium-long chain FAs (12 to 18 carbons). In the mitochondrial outer membrane, CPT1 produces acyl carnitines, which are translocated into the mitochondrial matrix in exchange for free carnitine by carnitine acylcarnitine transferase (CACT). In the mitochondrial inner matrix, CPT2 transfers acyl groups back to CoA (Mcgarry et al. 1997; Schlaepfer et al. 2020). Once inside the mitochondrial matrix, acyl-CoAs will produce energy through beta-oxidation, a sequential four reaction cycle that yields one $FADH_2$, one NADH, one acetyl-CoA and a two carbon shorter acyl-CoA (**Figure 1B**). This cycle can be repeated until the entire carbon backbone has been broken down, producing a significant amount of ATP (Balaban 1990). However, the high consumption of oxygen from this process
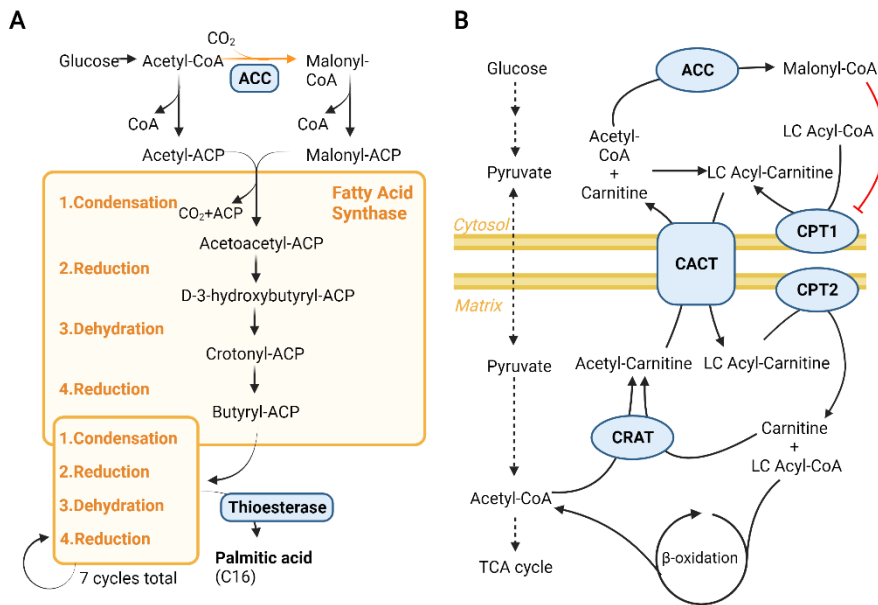
Figure 1. Schematic representation of a) Fatty acid synthesis pathway, and b) Fatty acid oxidation pathway. Adapted from a) Tracey et al 2018, and b) Stark et al 2015.

produces a significant amount of reactive oxygen species (Murphy 2009; Perevoshchikova et al. 2013).

Metabolism of lipids in the brain, as previously mentioned, is involved in many important processes in the organism (Picard et al. 2014). Specifically, FAs are the key players, and their synthesis, sensing and oxidation in brain cells leads to necessary outcomes for the correct function of the body. It is known that despite most of FA oxidation in the brain is performed by astrocytes (Escartin et al. 2007), some neuronal populations are able to take up FAs and express FAO genes, for functions beyond energy production. Indeed, neurons of the hypothalamus are responsive to the presence of FAs, and this sensing is necessary for the regulation of food intake, insulin secretion, glucose production and lipogenesis (Obici et al. 2002; Ross et al. 2010).

Since lipid metabolism in the brain plays a role in critical processes for the correct functioning of the organism, it is not surprising that defects in its regulation have been linked to several pathologies (Yang et al. 2022). In fact, alterations in brain lipid metabolism take place in neurodegenerative diseases, such as Alzheimer's disease (Liu et al. 2014), Parkinson's disease (Cole et al. 2002) and other disorders, but they can also be involved in metabolic pathologies, such as non-alcoholic fatty liver disease (NAFLD)(Ren et al. 2022), diabetes (Yue et al. 2012), and obesity (Wolfgang et al. 2006; Sarma et al. 2021) and glioblastoma (Balaban et al. 2015; Sperry et al. 2020). Furthermore, a relationship between cancer and alterations in lipid metabolism, both at central and peripheral level, has been elucidated (Currie et al. 2013). In the last few years, targeting proteins involved in FA metabolism in the brain has been proposed as a promising strategy to treat these diseases. Among them, key enzymes in FAO such as CPT1A, has been a matter of interest against brain lipid metabolism-related disorders such as obesity and glioblastoma.

1.1 Glioblastoma Multiforme

Glioblastoma Multiforme (GBM) is the most common primary malignant brain tumor in adults, and has a very short patient survival rate, with a mean survival of less than 15 months and less than 5% of the patients surviving for more than 5 years (Lah Turnšek et al. 2021; Gupta et al. 2020). It is still incurable, and the current treatment, which consists on maximal surgical resection followed by radiotherapy and concomitant treatment with temozolomide, has only increased the mean survival time by 3 months compared to the previous standard of care, suggesting that there is room for improvement in this regard (Quader et al. 2017; Khosla 2016).

GBM is thought to originate from oligodendrocyte-type 2-astrocyte progenitors of the astroglial lineage, in the brain (Gupta et al. 2020). Around 90% of GBM cases occur as primary tumors, while the remaining 10% are secondary tumors originating from lower grade gliomas. It is characterized by rapid proliferation of small cells infiltrating surrounding tissues, rendering total resection of the tumor impossible (Schröder et al. 1991). The tumor presents high vascularization and necrotic foci in the central area (Urbanska et al. 2014). Molecularly, GBM is defined as a diffuse astrocytic glioma with no mutations in IDH genes nor histone H3 genes (Weller et al. 2021), but it may present other molecular features, such as *TERT* promoter mutation or *EGFR* amplification (Lah Turnšek et al. 2021).

Cancer is essentially a cell growth and proliferation alteration. Therefore, cancer cells need metabolic flexibility in order to shift cellular metabolic pathways to produce the necessary energy and building blocks for cell growth (Currie et al. 2013). Glioma cells use FAO through overexpression of CPT1A in low glucose environments, such as those from rapidly proliferating tumors (Petővári et al. 2020; Sperry et al. 2020). This dependence on FAO increases with tumor malignancy, being most prominent in GBM (Cirillo et al. 2014).

However, despite the increasing understanding of GBM metabolic pathways and the discovery of potential targets, no improved standard treatments have been developed since the introduction of temozolomide in 2005. The difficulty of developing new treatments lies in the blood-brain barrier (BBB), a cellular barrier present in the brain capillaries that regulates ionic composition and protects the brain from cells, macromolecules and toxins (Van Tellingen et al. 2015). The BBB will be addressed in depth in the following sections. Then, it is imperative to develop new treatments that can extend the patient's survival time and improve the quality of life.
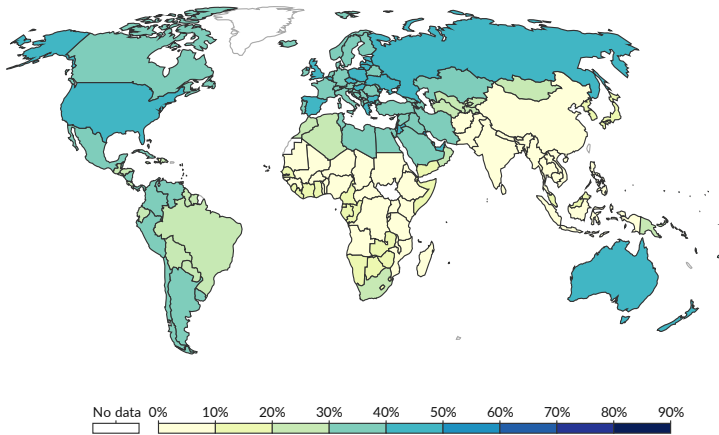
1.2 Obesity

Obesity is classically defined as the excessive accumulation of fat that may impair health (Anon 2021), but that concept is much more complex than this. Regarded as a symbol of wealth and well-being for centuries, it was the Greek physician Hippocrates who identified obesity as having negative effects for health. However, it was not until the 18th century that obesity and its consequences started to be noted in the medical literature (Eknoyan 2006), and only in the 20th century it was associated with higher risk of mortality.

Excess of adiposity, once an issue associated specifically to high-income countries, has increased alarmingly in middle- and low-income countries, especially in urban settings (Anon 2021). As of 2016, 39% of adults were overweight and 13% were obese, more than triple the rate from the year 1975 (**Figure 2**), and these numbers are expected to go up (Müller et al. 2022). Presently, the most widely used indicator for the classification of excess weight is the Body Mass Index (BMI), which uses body weight and height to classify overweight and obesity. According to BMI, values between 18.5-24.9 are considered normal weight, while values between 25-29.9 are considered overweight and values over 30 are considered obesity (Sarma et al. 2021; Balke et al. 2013). However, BMI alone does not identify high levels of body fat, as well as distribution of body fat, so direct measurement of body fat is recommended. In addition, BMI does not assess the chance of comorbidities, or other important factors such as biological, genetic, environmental and behavioral factors (Fosch et al. 2023; Garvey 2022). Indeed, excessive body weight is frequently related to increased risk of comorbidities such as cardiovascular disease (CVD), type-2 diabetes, NAFLD, dyslipidemia and other disorders (Garvey 2022; Sarma et al. 2021).

Share of adults that are overweight or obese, 1975

A person is defined as overweight if they have a body-mass index (BMI) equal to or greater than 25. BMI is a person's weight in kilograms divided by his height in metres squared.

No data 0% 10% 20% 30% 40% 50% 60% 70% 80% 90%

Source: WHO, Global Health Observatory   OurWorldInData.org/obesity • CC BY

Share of adults that are overweight or obese, 2016

A person is defined as overweight if they have a body-mass index (BMI) equal to or greater than 25. BMI is a person's weight in kilograms divided by his height in metres squared.
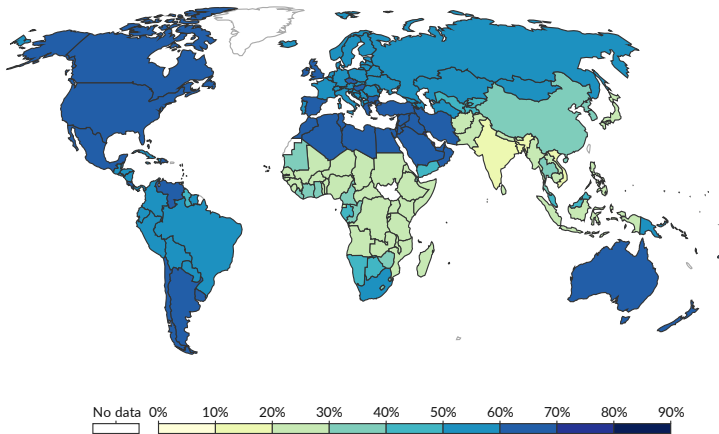

No data 0% 10% 20% 30% 40% 50% 60% 70% 80% 90%

Source: WHO, Global Health Observatory   OurWorldInData.org/obesity • CC BY

Figure 2. Percentage of overweight and obese individuals per country in 1975 (top) and 2016 (bottom). Overweight and obesity defined as having a BMI > 25. Source: IHME, Global Burden of Disease (2019).

Weight gain is caused by a sustained positive energy balance, that is, the ingestion of more calories than are spent over a long period of time (Hill et al. 2012). The energy uptake term of the energy balance equation is all energy

ingested through food and beverage consumption, while the energy expenditure term is more complex. Total daily energy expenditure (TDEE) can be divided into different categories: Basal metabolic rate (BMR), which is the energy expended by the organism to maintain vital functions, activity thermogenesis (AT), which is the energy spent by doing physical activity, whether it is voluntary exercise or other physical tasks, and the thermic effect of food (TEF), which is the energy spent by digesting, absorbing and metabolizing food (Levine 2002; Careau et al. 2021). BMR is highly predicted by lean mass and usually accounts for about 60% of the TDEE (Dériaz O, Fournier G, Tremblay A, Després JP 1992). AT is the most variable term between individuals and the easiest to modify in order to increase TDEE (D'Alessio et al. 1988).

Traditionally, the tendency of some individuals to gain weight and maintain a positive energy balance by overeating or not exercising enough has been regarded as laziness, a lack of character or willpower, and therefore people suffering from obesity have usually been stigmatized, adding a severe mental health component to the disease (Brewis et al. 2018). Social stigmatization also increases emotional eating and binge-eating episodes (Rubino et al. 2020). However, studies involving monozygotic twins have shown that the response to weight loss through a calorie deficit is highly similar in twin pairs, highlighting the significant role of genetic factors in body weight changes (Bouchard et al. 1990; Hainer et al. 2000). Furthermore, the genetic background interacts with biological factors and lifestyle patterns, accounting for variations in obesity prevalence across different communities. Specifically, societal bias in perceiving obesity as a lifestyle choice, especially when evidence suggests that weight loss alone can reduce the prevalence of comorbidities such as CVD (Wing et al. 2011) results in reduced access to healthcare (Kaplan et al. 2018). Finally, and of great significance in our increasingly unequal societies, obesity prevalence is also associated with low

socioeconomic status and limited health literacy (Garvey 2022). It is evident that obesity is a complex condition influenced by a myriad of factors and disorders that can lead to a positive energy balance (**Figure 3**).

The energy homeostasis of the organism is a tightly controlled process. This is clear because, after a long fasting in mice, there is an overfeeding that lasts until lost weight has been regained (Harris et al. 1986). In humans, it has been seen that, even though short-term energy balance shows a lot of variability, over longer time frames the energy balance is finely tuned (Hill 2009; Levitsky et al. 2012). These observations, along with the discovery of leptin and its anorectic effects in the central nervous system (CNS), gave way to the postulation of the set point theory, which states that energy homeostasis is finely regulated and that the body "defends" certain levels of adiposity against external changes such as caloric restriction or caloric surplus, and does so by increasing or reducing energy expenditure to match energy intake (Farias et
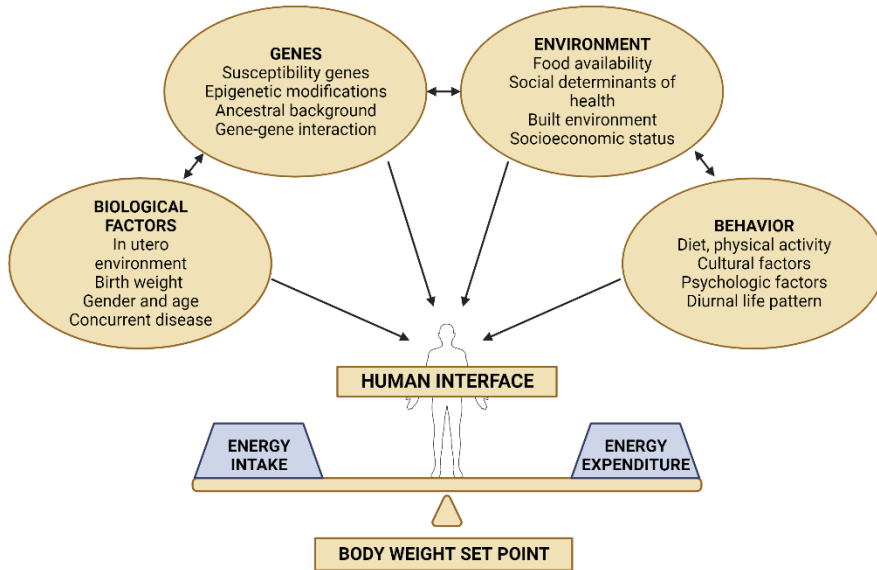

Figure 3. The seemingly simple energy balance regulation is affected by biological, genetic, environmental and behavioral factors that interact differently in each individual to create an altered body weight set point. Adapted from Garvey et al. 2022.

al. 2011; Speakman et al. 2011). More modern theories, such as the "settling points" theory, allow the integration of non-physiological signals and leave room for the defended body weight set point to increase or decrease due to external changes (Farias et al. 2011; Speakman et al. 2011), but keeping in mind that, probably due to evolutionary reasons, decreasing the set point is more difficult than increasing it (Waterson et al. 2015) . According to this, metabolic obesity could be defined as a disorder in which the set point (i.e., the adiposity level at which energy expenditure matches energy intake) is found in the obesity range. There have also been reports defining "hedonic obesity", in which metabolic control of energy intake works correctly, but a hedonic drive to consume food for pleasure is strong enough to sustain weight gain (Yu et al. 2015).

Therapeutic interventions for overweight or obesity frequently involve lifestyle changes to reduce energy intake or increase energy expenditure, in conjunction with pharmacological treatments and bariatric surgery, especially in cases of morbid obesity. Pharmacological interventions are commonly prescribed, and there are several long-term anti-obesity drugs on the market. However, most of these drugs results in less than 10% weight loss, which is typically regained after discontinuing treatment (Tak et al. 2020). Recently, the promising drug semaglutide, a glucagon-like peptide receptor (GLP1R) analog previously used for diabetes treatment, has been approved for obesity treatment after producing a 14.9% reduction in body weight after 68 weeks of treatment in a phase III clinical trial (Tak et al. 2020). Nevertheless, there remains a need to develop new pharmacological strategies to address this unmet medical issue.

The physiological components responsible for maintaining energy homeostasis are populations of neurons within the different nuclei of the hypothalamus. These neurons integrate hormonal and neuronal signals from

peripheral organs to modulate the feeding behavior of the organism. In the following section, we will explore the functions of these different components.

2. Role of the hypothalamus in brain lipid metabolism

The hypothalamus has been recognized as a pivotal brain region in the regulation of food intake since 1942 when Hetherington and Ranson (Hetherington et al. 1940) reported that lesions in the ventromedial hypothalamus (VMH) led to obesity. In a parallel finding, Anand and Brobeck reported that bilateral ablation of the lateral hypothalamus (LH) caused loss of interest in food and eventually led to death by starvation (Anand et al. 1951). Subsequent research in this field has further elucidated the intricate network of hypothalamic and extrahypothalamic neuronal connections and their effect in energy homeostasis and peripheral metabolism, as well as a plethora of other physiological functions (Dietrich et al. 2012).

Alterations in nutrient and hormonal signaling can impair the hypothalamic regulation of energy homeostasis. Particularly, abnormal levels of fatty acids, leptin and insulin negatively impact the ability of the organism to control energy intake, leading up to obesity, hyperphagia and hyperleptinemia (Moullé et al. 2014; Thon et al. 2016).

In this section we will review the different hypothalamic nuclei and their role in energy homeostasis, as well as the neuronal populations that are most important in the regulation of food intake and body weight (**Figure 4**).

2.1 Hypothalamic nuclei and function

The most anterior and rostral hypothalamic nucleus is the paraventricular hypothalamus (PVH). The PVH plays a crucial role in the hypothalamic signaling for energy homeostasis. It is the main hypothalamic receiver of
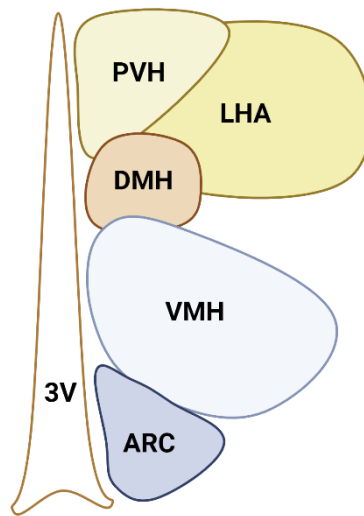
Figure 4. Distribution of the neuronal nuclei of the hypothalamus in respect to the third ventricle.

signals coming from the arcuate (ARC) nucleus, and it is also the primary site of neuronal projections to extrahypothalamic nuclei involved in satiety signaling, such as the parabrachial nucleus (PBN) and the nucleus of the solitary tract (NTS). Lesions in PVH result in hyperphagic obesity, and activation of cells in the PVH increases energy expenditure and reduces food intake (Hetherington et al. 1940; Sutton et al. 2016).

The dorsomedial nucleus of the hypothalamus (DMH) is located dorsal and ventral to the PVH. It has been related to energy expenditure control through regulation of brown adipose tissue (BAT) thermogenesis. DMH also takes part in the control of body temperature and food intake (Fosch et al. 2023; Bi et al. 2012; DiMicco et al. 2007).

Ventrally but in a more lateral position is located the lateral hypothalamic area (LHA). One of the first findings connecting hypothalamic function to energy metabolism was that ablation of the LHA produced aphasia and weight loss (Hetherington et al. 1940; Anand et al. 1951). LHA neurons produce

neuropeptides such as orexin, melanin-concentrating hormone (MCH) and cocaine and amphetamine-regulated transcript (CART) to induce food intake (Gao et al. 2016).

Continuing in a dorsal-ventral order we find the ventromedial hypothalamus (VMH) Its ablation produces hyperphagia and obesity, and it is thought to regulate energy balance through leptin sensing and proopiomelanocortin (POMC) (Khodai et al. 2021), in addition to glucose homeostasis through regulation of the autonomic nervous system (Fosch et al. 2023).

Lastly, located just below the VMH in the most rostral position and adjacent to the third ventricle and the median eminence (ME), we find the ARC. The ARC is a crucial site for feeding regulation, expressing both orexigenic and anorexigenic peptides, and sending neuronal projections to various hypothalamic nuclei, including LH, PVH and VMH (Gao et al. 2016). Its proximity to the ME offers privileged access for nutrient and hormone sensing. Indeed, it is well-documented that the ME and the ARC present a more permissive BBB that allows for enhanced hormone sensing and secretion, as well as improved nutrient sensing (Miyata 2015; Rodríguez et al. 2010). Within the ARC, two functionally opposed neuronal populations play a central role in the regulation of food intake: the melanocortin system (Jais et al. 2022).

These two populations are the orexigenic neurons expressing neuropeptide Y and Agouti related protein (NPY/AgRP) and the anorexigenic neurons expressing POMC/CART.

2.2 The melanocortin system: NPY/AgRP and POMC/CART neurons

The melanocortin system is primarily composed of two neuronal populations that innervate the same intrahypothalamic areas, including the LH and PVH (Wang et al. 2015). These neuronal populations interact with each other through the effect of several neuropeptides. For instance, POMC/CART neurons, whose activation has an anorexigenic effect, express POMC peptide, which is cleaved into alpha melanocyte-stimulating hormone (α-MSH)(Mountjoy 2015; Quarta et al. 2021). α-MSH is a potent agonist of melanocortin receptors 3 and 4 (MC3R and MC4R), and the activation of these receptors induces an anorexigenic response.

In contrast, the activation of NPY/AgRP neurons has an orexigenic effect. AgRP acts as an endogenous melanocortin antagonist, blocking the binding of α-MSH and thus inhibiting the MC4R-mediated anorexigenic effects (Zagmutt et al. 2018). Concomitantly, NPY and GABA release inhibit POMC activity, along with downstream second-order neuronal activity, mainly in the PVH. In fact, the inhibition of downstream PVH neurons is necessary for NPY/AgRP orexigenic effect (Atasoy et al. 2012). The NPY effect is mediated by NPY receptors, of which NPY1R, NPY2R and NPY5R are most important in feeding regulation (Brothers et al. 2010).

The neurons in the melanocortin system respond to hormones and nutrients present in the blood in order to exert their function. The most important regulatory hormones in this system are leptin, ghrelin and insulin. Leptin is produced by the adipose tissue in a manner proportional to fat mass, and acts on leptin receptors (LEPR), found in various cell groups in the brain (Scott et al. 2009). Leptin activates POMC neurons and inhibits AgRP neurons (Cowley et al. 2001), but this effect occurs in a timescale of hours (Beutler et al. 2017). Leptin is, therefore, secreted as a signal of energy abundance. Oppositely,

ghrelin, a hormone secreted by the empty stomach, is secreted in energy deficit situations. Its levels decrease post-prandially and increase pre-prandially, which suggests a role in meal initiation and termination (Cummings et al. 2001; Müller et al. 2015) . Ghrelin induces activation of AgRP neurons and orexigenic behavior through activation of its receptor, GHS-R (Sun et al. 2004). Insulin secretion has been demonstrated to increase in proportion to body fat and to lower food intake and body weight by inhibition of AgRP neurons (Woods et al. 1979; Könner et al. 2007).

Although it is clear that leptin, ghrelin and insulin have an effect on food intake, body weight and energy consumption, it is thought that their role is to control long-term changes in energy balance. Recently, a plethora of short-term modulators of food intake have been described and are being studied from a therapeutic perspective (Müller et al. 2022). Currently the most studied are cholecystokinin (CCK), peptide tyrosine tyrosine (PYY), glucagon-like peptide 1 (GLP-1). CCK is secreted from intestinal L cells especially upon fat ingestion, and can inhibit neurons in the NTS and area postrema (AP), that can relay satiety signals to the hypothalamus, apart from NPY/AgRP neurons (Müller et al. 2022; Beutler et al. 2017). PYY is co-secreted with GLP-1 from L cells in the distal bowel. Its major circulating form, PYY3-36, promotes satiety by inhibiting NPY/AgRP through Y2 receptor activation, therefore activating POMC/CART neurons (Batterham et al. 2002). GLP-1 decreases food intake via activation of POMC/CART and activation of the neurons in the NTS and AP (Müller et al. 2019).

Clearly, the interplay between activation and inactivation of NPY/AgRP and POMC/CART neurons and other neurons in the VMH, PVH and LH, mediated by food cues, hormonal and nutrient signals, is tightly regulated and holds profound importance for the regulation of the energy homeostasis in both

normal and pathological conditions (**Figure 5**). Now we will focus on a key element in the energy homeostasis by the hypothalamus; the CPT1A protein.
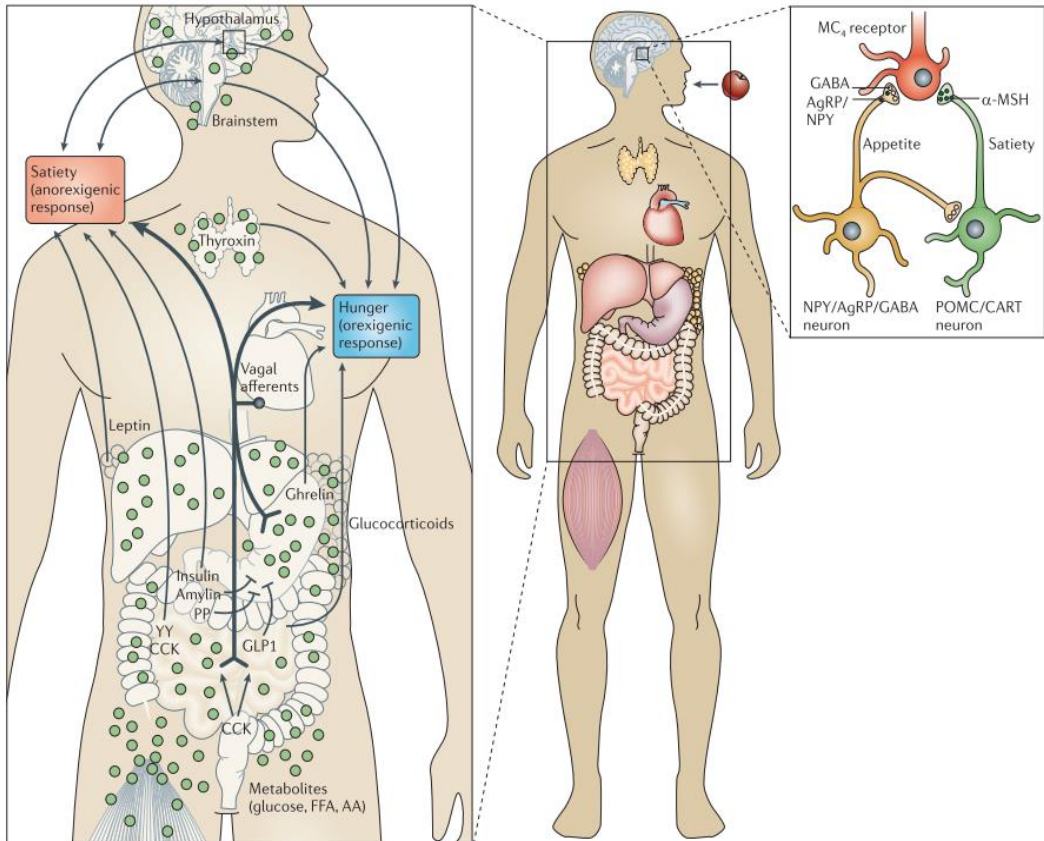

Figure 5. Schematics of action of different peripheral hormones on satiety and hunger. Peripheral hormones convey information about energy availability to neurons in the hypothalamus and the brainstem. In the hypothalamus, two populations of neurons (NPY/AgRP) and POMC/CART) integrate this information and promote hunger or satiety. PP, pancreatic polypeptide; CCK, cholecystokinin; YY, peptide YY; FFA, free fatty acids; AA, aminoacids; GLP-1, glucagon-like peptide 1; MC4, melanocortin receptor 4; α-MSH, α-melanocyte stimulating hormone. From Dietrich et al. 2012.

3. Hypothalamic carnitine palmitoyltransferase 1 A (CPT1A) and control of energy balance

CPT1A is a key player in lipid metabolism. Particularly, in hypothalamic neurons, CPT1A controls neuronal tone and therefore energy homeostasis (Stark et al. 2015). A main pathway related to CPT1A in the nutrient sensing in the hypothalamus and control of energy balance is the AMPK/ACC/Malonyl-CoA/CPT1 axis (Fadó et al. 2021; López et al. 2016). In the hypothalamus, AMP-activated protein kinase (AMPK) a central nutrient sensor protein, is phosphorylated and thus activated by signals of low energy (i.e., hypoglycemia, ghrelin) and inactivated by signals of high energy (i.e., hyperglycemia, leptin, insulin). Activated AMPK can phosphorylate and inhibit acetyl-CoA carboxylase (ACC), the enzyme responsible for the synthesis of malonyl-CoA, which is the substrate of FAS, the first step in fatty acid anabolism, and the endogenous inhibitor of CPT1A, the first step of the FAO pathway.

Hypothalamic malonyl-CoA, is an important mediator of feeding behavior. It is known that malonyl-CoA levels fluctuate greatly in response to hormones and nutrients in different tissues. However, these fluctuations are crucial in the hypothalamus, where they mediate the response to metabolic challenges such as fasting or feeding (**Figure 6**) (Fadó et al. 2021). Systemic or central administration of FAS inhibitors (such as cerulenin and C75) produced a satiating effect and body weight loss, probably due to an accumulation of malonyl-CoA (Thomas M. Loftus et al. 2000). The decrease of hypothalamic malonyl-CoA levels was seen to be enough to cause an increase in appetite and body weight by overexpressing malonyl-CoA decarboxylase (MCD), the
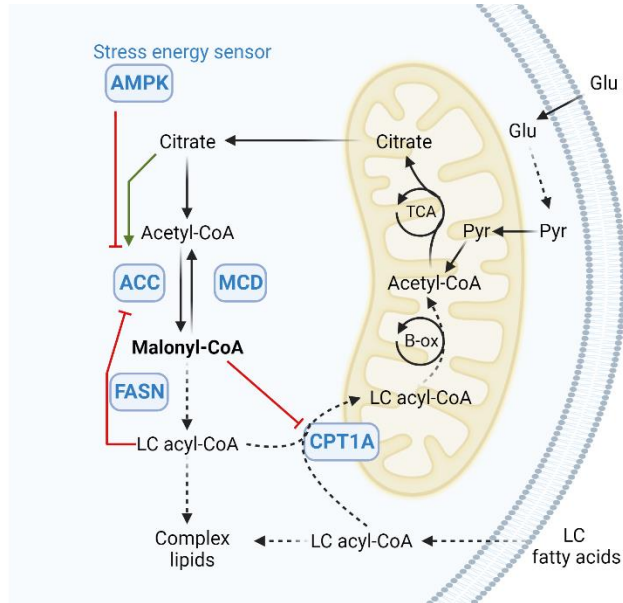
Figure 6. Malonyl-CoA plays a central role in lipid metabolism, as it is the precursor for fatty acid synthesis and the negative regulator of CPT1A. In this manner, fluctuations of malonyl-CoA coordinate the switch from fatty acid synthesis to fatty acid oxidation. Adapted from Fadó et al. 2021.

enzyme responsible for degrading malonyl-CoA, in the hypothalamus of rodents (Hu et al. 2005). Furthermore, in conditions of high glucose, increased malonyl-CoA inhibits CPT1A and stops FAO in favor of fatty acid synthesis (Stark et al. 2015). However, it is known that the functions of hypothalamic malonyl-CoA do not stop at feeding regulation, but it also produces peripheral effects. Increased hypothalamic malonyl-CoA levels increased FAO and energy expenditure in skeletal muscle through the sympathetic nervous system (Cha, Hu, Chohnan & Daniel Lane 2005), and activated brown adipose tissue (BAT) thermogenesis (López et al. 2010). In this manner, FAS and CPT1A work as a "metabolic crossroad" between FAO and fatty acid synthesis (Ronnett et al. 2006). Thus, it is clear that carnitine metabolism is an important regulatory element in energy homeostasis. We will look more closely into FAO, carnitine metabolism, the CPT1 proteins and their role in NPY/AgRP neuronal activity.

CPT1s are a family of proteins involved in lipid metabolism. They catalyze the conversion of acyl-CoAs into acylcarnitines. There are three isoforms of human CPT1: CPT1A, which is expressed ubiquitously, CPT1B, which is expressed mainly in muscle, and CPT1C, which is expressed in neurons (**Figure 7**) (Casals et al. 2016).The canonical isoforms CPT1A and CPT1B have a similar function, but vary in their localization, while CPT1C has a lower catalytic activity compared to CPT1A and B (Sierra et al. 2008). CPT1A and B catalyze the first and limiting step in the FAO pathway. They are both endogenously inhibited by malonyl-CoA, but sensitivity of CPT1B to inhibition by malonyl-CoA is at least 30 times higher than CPT1A (Zhu et al. 1997). In the brain, CPT1A is expressed mostly in astrocytes. However, it has been demonstrated that hypothalamic neurons need the expression of CPT1A in order to regulate feeding (Jernberg et al. 2017; Zagmutt et al. 2023).

CPT1A and FAO activation states have a multifaceted role in peripheral and central tissues. Peripherally, it has been demonstrated that FAO and CPT1A genes are downregulated in obese and diabetic patients. In line with this,
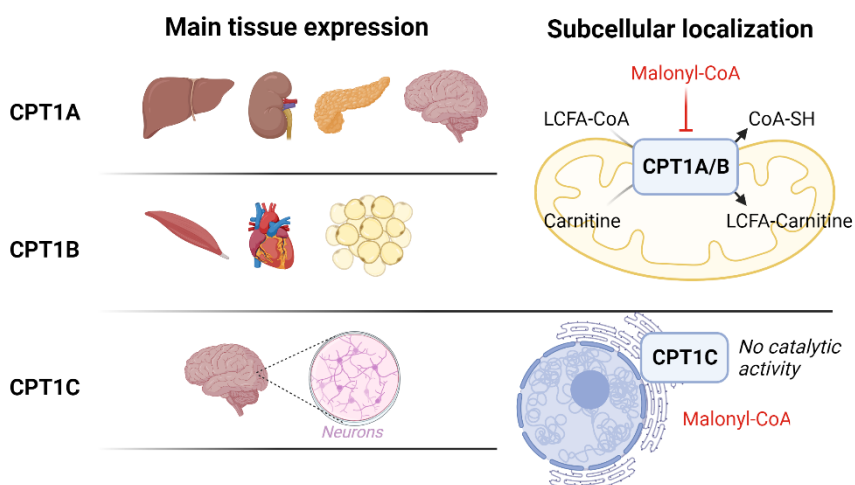

Figure 7. Schematics of tissue expression and subcellular localization of the different CPT1 isoforms. Adapted from Rodríguez-Rodríguez et al. 2023.

activation of CPT1A and FAO in the liver decreases insulin resistance and protects against body weight gain (Orellana-Gavaldá et al. 2011; Weber et al. 2020). CPT1A also plays a crucial role in the hypothalamic regulation of food intake. Inhibition of hypothalamic CPT1A by intracerebroventricular (ICV) infusion of a riboprobe reduced food intake and body weight, besides a decrease in AgRP and NPY mRNA levels, as well as liver gluconeogenesis (Obici et al. 2003). This inhibition is followed by an accumulation of long-chain FAs, which mimics the effects on food intake caused by ICV injection of oleic acid (Obici et al. 2002). Conversely, overexpression of CPT1A in the VMH induced hyperphagia and body weight gain in mice (Gao et al. 2013). Furthermore, the expression in the VMH of a mutant CPT1A insensitive to malonyl-CoA inhibition also increased food intake and body weight, while also producing changes in lipid profile and expression levels of glutamate and GABA transporters (Mera et al. 2014). More recently, genetic deletion of CPT1A in AgRP neurons of the ARC in male and female mice led to a reduction in appetite, body weight and activation of BAT thermogenesis (the later only in female mice) (Zagmutt et al. 2023). Overall, these finding indicate a prominent role of VMH and ARC CPT1A activity in the regulation of satiety signaling and energy balance, possibly mediated by the fluctuating levels of long-chain FAs in the brain.

The anti-obesity potential of CPT1A is then based on two different approaches depending on central or peripheral tissue targeting. In peripheral tissues (i.e liver and adipose tissue) it selective activation of CPT1A produces beneficial outcomes, such as decreased insulin resistance and weight control (Weber et al. 2020). Oppositely, it is the inhibition of hypothalamic CPT1A which has been identified as a promising intervention for body weight, energy expenditure and feeding management (Mera et al. 2014; Zagmutt et al. 2023). Therefore, in order to reduce off-target peripheral effects, pharmacological inhibitors of CPT1A need to be specifically delivered to the hypothalamus.

Besides its importance in the pathology of metabolic diseases it has been shown that CPT1A levels of activity and expression are critical for the development of several tumors (Liang 2023). As previously stated, in GBM, CPT1A inhibition can result in increased macrophage phagocytosis of tumor cells (Jiang et al. 2022). CPT1A inhibition has also been proven to be essential for tumor growth and survival in hormone receptor positive breast cancer (Jariwala et al. 2021) and prostate cancer (Guth et al. 2020).

From these results, it is clear that CPT1A plays a key role in the modulation of FA levels in the ARC and VMH. We believe pharmacological inhibition of CPT1A in specific brain cells could be of great therapeutic value for the treatment of metabolic disorders, as well as some types of cancer. This inhibition should be tissue selective (central but not peripheral tissues), cell selective (to neurons that express certain receptors) and specific. In the next section we will review the current pharmacological inhibitors of CPT1A and focus on one of them, compound 75 (C75).

4. Pharmacological inhibitors of CPT1A: C75

Pharmacological inhibition of fatty acid metabolism has been used for decades, mainly to characterize its molecular mechanism (Declercq et al. 1987). The interest in the matter grew once the importance of fatty acid metabolism for metabolic disorders was stated. Cerulenin, a natural compound extracted from the fungus *Cephalosporium caerulens*, was one of the first known inhibitors of FAS enzyme, thus inhibiting fatty acid synthesis (D'agnony et al. 1973). However, cerulenin is chemically unstable and presents several side effects, which is the reason behind the research and development of new derivatives (Pandey et al. 2012). Two of the most important cerulenin derivatives are etomoxir and Compound 75 (C75).

Etomoxir was developed as an antidiabetic drug, but later it was seen that it effectively inhibited CPT1 (Brady et al. 1986). Later it was repurposed as a cardiovascular disease drug, as it was shown that inhibition of FAO could reduce permanent damage in ischemic hearts (Lopaschuk et al. 1988). Etomoxir still retains in its structure a strongly reactive epoxy-group, which causes instability and undesired reactivity. Etomoxir successfully cleared phase I trials, but was discontinued in phase II trials due to hepatotoxicity issues (Holubarsch et al. 2007). Interestingly, orally administered etomoxir did not reduce food intake but appeared to stimulate it in the study environment (Kahler et al. 1999).

C75 was patented by Kuhajda et al. in 1997. Initially, it was developed and described as a FAS inhibitor for antitumoral treatment. The antitumoral effects were observed in both *in vitro* MCF-7 breast cancer cell line and *in vivo* with nude mice (Kuhajda 2000; Pizer et al. 2000). Concomitantly, a decrease

in food intake was also described as a side effect of treatment with C75. This discovery opened a line of work on C75 as a potential antiobesity drug. Indeed, intraperitoneal treatment with C75 reduced food intake, body weight and adiposity in mice in a dose-dependent manner. This body weight loss observed was dependent on the reduction of food intake (Thomas M. Loftus et al. 2000). C75 was also shown to to increase levels of hypothalamic POMC/CART mRNA and reduce levels of AgRP/NPY mRNA compared to fasted levels (Shimokawa et al. 2002). Furthermore, C75 treatment was found to influence neuronal activation in the ARC, LH, NTS and AP. It appeared to do so by carrying out a dual-onset effect; a short-term effect through activation of NTS and AP neurons that inhibit PVH, and a long-term effect primarily elicited by the hypothalamus (Gao et al. 2003).

It was suggested that C75 acts in the CNS, because both intraperitoneal and intracerebroventricular administration of C75 cause the described effects. Additionally, central C75 treatment can induce short-term peripheral changes in expression of thermogenesis markers in skeletal muscle (Cha, Hu, Chohnan & Lane 2005) and decrease the secretion of ghrelin in the hypothalamus and stomach (Hu et al. 2005).Altogether, these results were supportive of the hypothesis that increase in malonyl-CoA levels in the hypothalamus through inhibition of FAS inhibits FAO, therefore eliciting the anorexigenic response. In this context, C75 was thought to have a mildly stimulatory effect in CPT1A (Nicot et al. 2004).

In the direction of solving this discrepancy, it was discovered that, regardless of its possible CPT1-stimulatory behavior, C75 could form a coenzyme A ester. This derivative, C75-CoA, is formed *in vitro* and irreversibly inhibits CPT1A activity and FAO (Bentebibel et al. 2006). C75-CoA is also formed in the hypothalamus when C75 is administered centrally in rats. This result supported the notion that the anorectic effect of C75 was mediated by C75-

CoA inhibition of CPT1A, possibly with concomitant inhibition of FAS, which would reinforce CPT1A inhibition by increasing malonyl-CoA concentration (Mera et al. 2009).

It is essential to note that C75 is a racemic compound, an equimolar mixture of two enantiomers: (+)-C75 and (−)-C75. Consequently, each enantiomer within C75 may exhibit distinct biological and pharmacological properties, as it was confirmed with subsequent work where differential effect of (+)- and (−)-C75 enantiomers in CPT1 and FAS. Interestingly, (−)-C75 was able to inhibit FAS activity but (+)-C75 had little to no effect when incubated with mitochondrial protein extracts. Neither (+) nor (−)-C75-CoA adducts had an effect on FAS activity. Regarding CPT1, both (+)-C75-CoA and the racemic mixture (±)-C75-CoA exerted a potent inhibitory effect on CPT1 activity, while (−)-C75-CoA showed a weak inhibitory effect. None of the non-CoA forms had any effect in CPT1 (Makowski et al. 2013) From these results, it is concluded that (−)-C75 inhibits FAS and (+)-C75-CoA inhibits CPT1 (**Figure 8**).

As discussed previously, a solution is required to achieve tissue-selective, cell-selective, and specific CPT1A inhibition mediated by C75-CoA. C75 has traditionally been administered via intravenous administration or via ICV. Intravenous administration of C75 leads to distribution through the whole organism, readily crossing the BBB and reaching targets in the CNS, but also in peripheral tissues. This pathway of administration leads to the desired therapeutic effects but is also prone to side effects and off-target activity. On the other hand, ICV administration is more direct and reduces effective dose, but is not feasible for recurrent administration. In order to avoid off-target effects and effectively deliver C75-CoA to the hypothalamus, we need to look for new administration and targeting strategies. One of such strategies are drug delivery systems based on nanotechnology. These drug delivery systems offer several possibilities for customization and tuning of the drug
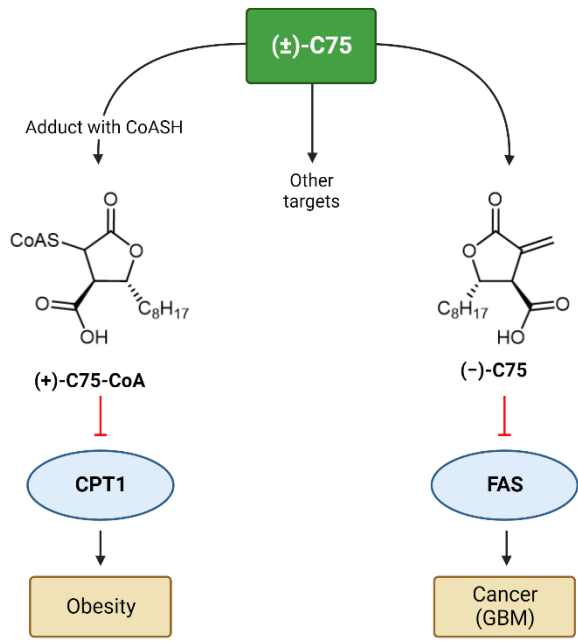
Figure 8. Mode of action of C75 enantiomers. (-)-C75 inhibits FAS, while (+)-C75-CoA inhibits CPT1A. Adapted from Makowski et al. 2013.

characteristics. Among the different types of drug delivery systems, to address these specific issues, we have chosen to encapsulate C75 in polymeric micelle nanomedicines (PM).

5. Targeting brain cells by using nanotechnology

Nanotechnology is defined as "intentional design, characterization, production, and applications of materials, structures, devices, and systems by controlling their size and shape in the nanoscale range (1 to 100 nm)" (British Standards Institute, 2007). Since their discovery, nano-engineered materials have been researched for use in a wide variety of different applications, such as chemical synthesis or information technologies, with medical applications being some of the most expected. Indeed, the possibility to engineer the shape, size and surface of nanomaterials, and the fact that they find themselves in the same size-scale as most biological constituents, makes them suitable for applications depending on interaction with such biological entities.

5.1 Nanotechnology, overview and advances.

The use of nanotechnological solutions is set to revolutionize the pharmacology field. As we have reached a time in which methods have been developed for high throughput development of bioactive molecules, the challenge is shifting from the discovery of new molecules to solving the issues presented by poor physicochemical characteristics of said molecules for *in vivo* administration. Compounds with low water solubility or short circulating half-life are not useful even if their biological activity is high. Encapsulation or conjugation of these molecules to nanoengineered materials can greatly change these physicochemical characteristics so that they become suitable for pharmaceutical applications. Indeed, many nanotechnology-based products recycle and improve previously approved drugs (Shi et al. 2017).

Due to this ability to improve physicochemical characteristics of drugs, nanotechnology-based approaches could prove very useful for CNS-related diseases. Currently, CNS-related diseases impose a heavy-burden on human health, due to the impossibility to deliver therapeutically relevant doses across the BBB, paired with side effects and toxicity caused by the exposure of non-target cells to the drugs (Zhang et al. 2016). There is a lot of research effort into several nanotechnology-based strategies to overcome these challenges and successfully treat these diseases (Garcia-Chica et al. 2020). There is still a wide gap between laboratory research and bedside treatment, but the positive results achieved ignite hope in the future of this promising field.

5.2 Types of Nanomedicines. Polymeric Nanomedicines.

The different nanotechnological formulations that have been tested for improving drug delivery are commonly referred to as nanocarriers. These formulations can be classified into lipid-based nanocarriers, polymeric nanocarriers, inorganic nanocarriers, and cell-derived nanocarriers (**Table 1**). Nanocarriers need to have certain properties in order to function properly. Perhaps the most important quality to consider would be the ability to easily attach or encapsulate drugs. These drugs can be covalently attached to the structure of the nanocarrier, adsorbed to the surface or encapsulated in the core (Wilczewska et al. 2012). The toxicity of the nanocarrier needs to be considered. It is important that nanocarriers have good biocompatibility, low toxicity and low immunogenicity (Chamundeeswari et al. 2019). It is usually advantageous that the nanocarriers exhibit long-term blood circulation. Being stable in blood circulation for longer times allows distribution towards the tissues where the therapeutic effect is needed. Lastly, it can be very useful

that the nanocarrier is directed towards the target tissue or that it can be modified to do so. An example of the former would be nanocarriers directed for tumors due to the enhanced permeability and retention (EPR) phenomenon. These nanocarriers make use of the differential characteristics present in tumoral capillaries. Specifically, tumoral capillaries present a deficient structure that makes them highly permeable to macromolecules, and an impaired lymphatic drainage. Altogether, this causes accumulation and retention of macromolecules over 40kDa and nanocarriers between 100 and 200 nanometers (Wu 2021). However, some nanocarriers can also be physically or chemically modified to target specific tissues or cells. One such family of nanocarriers are polymeric micelles.

Polymeric micelles consist of spherical supramolecular assemblies formed by amphiphilic block-copolymers that self-assemble forming a hydrophobic core and a hydrophilic shell. The hydrophobic core can function as a pocket for hydrophobic drugs while the hydrophilic shell can improve drug solubility (Bae et al. 2003). Poly (ethylene glycol)-poly (amino acids) (PEG-PAAs) are the easiest and most commonly used block copolymers, due to their biocompatibility, lack of toxicity and versatility (Lavasanifar et al. 2002). Drugs can be loaded into the micelle core by physical means or it can be covalently attached to the micelle components. Micelles with covalently attached drugs display increased stability and reduced drug leakage, but can also have problems releasing the drug in the target cells. For this reason, a method has been developed to conjugate drugs to block copolymers using *in vivo* stimuli-responsive linkers, such as pH-sensitive linkers. With this strategy, nanoparticles can carry the drug into the cell, and then release the drug when the pH drops in the lysosomal compartment (Bae et al. 2003).
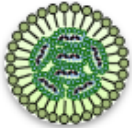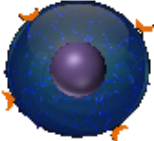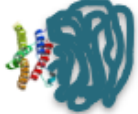
Type of nanomedicine		Physicochemical properties relevant for neuron targeting
Lipid-based nanomedicines	Liposome	• Liposomes are prepared from phospholipids, for example dioleoyl or distearoyl phosphatidylcholine. • Liposomes with single lipid layers are generally 25-100 nm.
	Lipoplex	• Lipoplexes are prepared from cationic lipids having a cationic head and hydrophobic tail, for example, Dioleoyl-3-trimethylammonium propane (DOTAP). • The size of lipoplexes varies widely, from couple of 100 nm to couple of μM.
Polymeric nanomedicines	Polymer micelle	• Polymeric micelle has characteristic core-shell structure with optimal size range of 10-100 nm. • While, drug or gene can be loaded inside the core for CNS therapy, the surface can be modified with neuron targeting ligand.
	Polymer-protein conjugate	• Polymer-protein conjugates are composite macromolecules derived from covalently combining protein and synthetic polymers. • PEGylated interferon beta-1a, PLEGRIDY®, is an FDA approved drug for multiple sclerosis (MS).
Inorganic nanomedicines	Quantum rods	• Semiconductor nanocrystals are made of CdSe/CdS. • Rod-shaped nanocrystals, the quantum rods induce neuronal stimulation through its local electric field associated with permanent dipole moment. • Surface modifications with different functional groups can produce quantum rods with adaptable surface charge.
Cell-derived nanomedicines	Exosomes with AuNP	• Exosomes are lipid-bound membrane vesicles with 50 to 100 nm in diameter. • Structural flexibility of exosomes allows encapsulating AuNPs. • With adaptable size and shape AuNPs can act as a support for various bio-macromolecules. • Neuron-targeted exosomes were used to cover AuNPs for efficient BBB penetration.

Table 1. Main type of platforms used for brain delivery of therapeutics are shown, highlighting a few physicochemical characteristics relevant to neuron-targeting. Adapted from García-Chica et al. 2020.

5.3 Brain targeting

The polymeric micelle technologies we have seen so far allow only for passive targeting. However, polymeric micelles can be chemically modified to perform active targeting. For this, a molecule can be attached to the surface of the polymeric micelle that increases its affinity for a receptor. This strategy works better with small molecules or oligopeptides, although larger molecules can be used (Bae et al. 2009). Nonetheless, it is imperative that the chosen molecule has a high affinity and specificity for the receptor, as well as that the expression of the candidate receptor is specific to the target cells.

As we have discussed before, one of the main issues concerning drug delivery to the brain is the BBB. The BBB is a physical barrier that impedes the free diffusion of molecules to the CNS and controls the concentration of ions and other metabolites (Pandit et al. 2020; Garcia-Chica et al. 2020). It is mainly composed of endothelial cells, basement membrane, pericytes and astrocytes. The endothelial cells of the brain capillaries form continuous capillaries through the expression of tight junction proteins, limiting paracellular transport. Moreover, vesicular traffic is diminished in these cells, effectively reducing transcellular transport (De Bock et al. 2016). The endothelial cells of the BBB present a very polarized expression of several transport receptors. The main role of these receptors is the transport of nutrients, hormones and vitamins (Pandit et al. 2020). The endothelial cells are mechanically supported by the basement membrane, a specialized layer of extracellular matrix mainly composed of type IV collagen, laminins, fibronectin, heparin sulfate and other proteoglycans (Thomsen et al. 2017). The pericytes are perivascular cells embedded in the basement membrane. They are in charge of producing the proteins that form the basement membrane, as well as producing contractile proteins that regulate capillary diameter and therefore cerebral blood flow (Brown et al. 2019). Finally,

astrocytes produce protrusions that completely envelop the BBB endothelium and have a role in the water, ion and neurotransmitter homeostasis, as well as modulating the integrity of the BBB (Sweeney et al. 2019). Moreover, protrusions in astrocytes engulf neuronal synapses, providing a link between neurons and vasculature (Abbott et al. 2006). Among other nanocarriers, polymeric nanoparticles have been modified to actively target the receptors expressed in the luminal side. Indeed, intravenously administered polymeric micelles decorated with surface glucose have been successfully used for BBB crossing and brain targeting via the GLUT1 receptor, highly expressed in the BBB (Anraku et al. 2017). Other approaches make use of different BBB-expressed receptors, such as transferrin (Liu et al. 2013), or they have increased delivery to the brain exclusively due to their pathway of administration or improved physicochemical characteristics of nanoencapsulated drugs (Musumeci et al. 2018; Pahuja et al. 2015). However, these strategies increase the concentration of drugs in the CNS, but they do not specifically target any type of cells (i.e., neurons, astrocytes or microglia) or any subset of those cells (i.e., neurons expressing NPY2R).

In order to optimize the administered dose and therefore reduce the possibility of side effects, a cell-specific delivery strategy is needed. In the case of neuron-related diseases, few examples use peptides to direct polymeric micelles to neurons, but not specific subsets of neurons (Q. Guo et al. 2020; Wang et al. 2018; Hu et al. 2011).

CONTEXT, HYPOTHESIS AND OBJECTIVES

Brain lipid metabolism, particularly CPT1A activity in brain cells, has emerged as a crucial player in the pathophysiology of devastating diseases such as GBM or obesity. The prevalence of these specific pathologies is on the rise, and innovation in therapeutic strategies enhancing efficacy and reducing off-target actions is an urgent need.

In this context, the CPT Obesity Cancer Drug Delivery (CONCORD) project was born. This Thesis has been carried out in the context of this project. The CONCORD project is a Spain-Japan collaboration proposal led by Dr. Rosalia Rodríguez from Universitat Internacional de Catalunya (UIC) and Dr. Sabina Quader, from the Innovation Center of Nanomedicine (iCONM) (AEI/MINECO and AEMPS; 2019-2022). The general objective of the CONCORD project is to develop drug-loaded polymeric nanomedicines for selective targeting of neurons or tumoral cells in order to treat diseases originating in the CNS such as obesity and GBM. CPT1A was the main protein target aimed in the project to fight against both diseases: CPT1A in hypothalamic nucleus for obesity and CPT1A in tumoral glial cells for GBM. In the context of CONCORD project, different type of polymeric micelles and strategies of encapsulation of C75 were proposed, as well as different approaches for surface decoration of the nanomedicines for selective targeting of i) hypothalamic nucleus in the treatment of obesity or ii) tumoral glial cells in the treatment of GBM. The present Thesis is focused in the part of the project for the design and development of the drug, the micelles, selection of the most adequate type of micelle, and finally the validation of the undecorated micelles *in vitro* and *in vivo*.

Then, the main **hypothesis** of the present Thesis is that encapsulation of the CPT1A inhibitor drug C75 could serve as a targeted drug-delivery system, inhibiting CPT1A and altering the lipid and energy metabolism *in vitro* models of neurons and GBM and *in vivo* animal models of neuronal targeting, while

reducing the dose, improving the efficacy and causing less side effects compared to the free drug.

To validate this hypothesis, we have established the following **objectives**:

1. To synthesize C75 and C75-CoA as racemic mixtures and enantiopure compounds, along with the required C75 derivatives (Publication 1 and Annex).

2. To synthesize, characterize and optimize C75-CoA loaded micelles, as well as Fluorescein-CoA loaded micelles (Publications 1 and 2).

3. To characterize the ability of the developed micelles to enter brain cells (glioblastoma and hypothalamic neurons) and to modify CPT1A-lipid metabolism *in vitro*, while evaluating their cytotoxicity in brain cells (Publication 1 and Annex).

4. To characterize the potential of the developed micelles to alter the hypothalamic neuronal circuits and the regulation of feeding and peripheral metabolism *in vivo* in lean mice via CPT1A/FAO regulation (Publication 2).

CHAPTER 1

Poly-ion complex micelles effectively deliver CoA-conjugated CPT1A inhibitors to modulate lipid metabolism in brain cells

Objectives 1, 2 and 3.

Article summary

Fatty acid metabolism plays several important roles in the function of the organism. In the hypothalamus, it has been revealed as a key player in the regulation of hunger and satiety, and pharmacological targeting of this system could be useful for the control of metabolic diseases originated in the brain, such as obesity. The objective of this research was the development and characterization of nanoparticles encapsulating C75-CoA, an inhibitor of CPT1A, which is a key enzyme in the lipid metabolism and is also overexpressed in GBM cells. Pharmacological inhibition of hypothalamic CPT1A constitutes a promising strategy against obesity and GBM.

C75-CoA and other related molecules were synthesized as previously described. From an array of polymers, PEG-PAsp(DET) was chosen for its characteristic hydrophobic and hydrophilic parts, and for the positive charges of DET that allowed interaction with negative charges in CoA to form the PIC micelle. Micelles encapsulating racemic C75-CoA, as well as its enantiopure forms, were synthesized.

The capability of the micelles to modulate fatty acid metabolism was assessed. Hypothalamic neuronal cells, GT1-7, and glioblastoma cell line, U87MG, were used as *in vitro* models. Cells were treated with the different C75-CoA micelles and subjected to ATP inhibition assays and FAO inhibition assays, as major indicators of CPT1A function, compared to cells exposed to free drug and vehicles. The cytotoxicity of the micelles was also evaluated *in vitro* in GT1-7 and U87MG cells, as well as their capacity to enter the cells both in 2D cellular models and 3D cellular models, analyzed by flow cytometry and confocal microscopy.

The synthesis of the drug and the encapsulation was successful. Then, C75-CoA micelles revealed a substantial inhibition of ATP synthesis and FAO, higher than free C75-CoA. These effects were similar in GT1-7 and U87MG. They also produced an elevated cytotoxicity compared to free C75-CoA. These results are in accordance with cell internalization assays, in which it was seen that C75-CoA micelles could enter the cells more easily than free C75-CoA, and they could diffuse deeper in 3D spheroid models. Cell internalization of the micelles reached saturation in GT1-7 sooner than in U87MG, and the fluorescence intensity in U87MG was much higher than in GT1-7.

In summary, it was demonstrated that the developed C75-CoA micelles had the ability to enter GT1-7 and U87MG cells *in vitro* and modulate ATP synthesis and FAO, as indicators of lipid and energy metabolism.
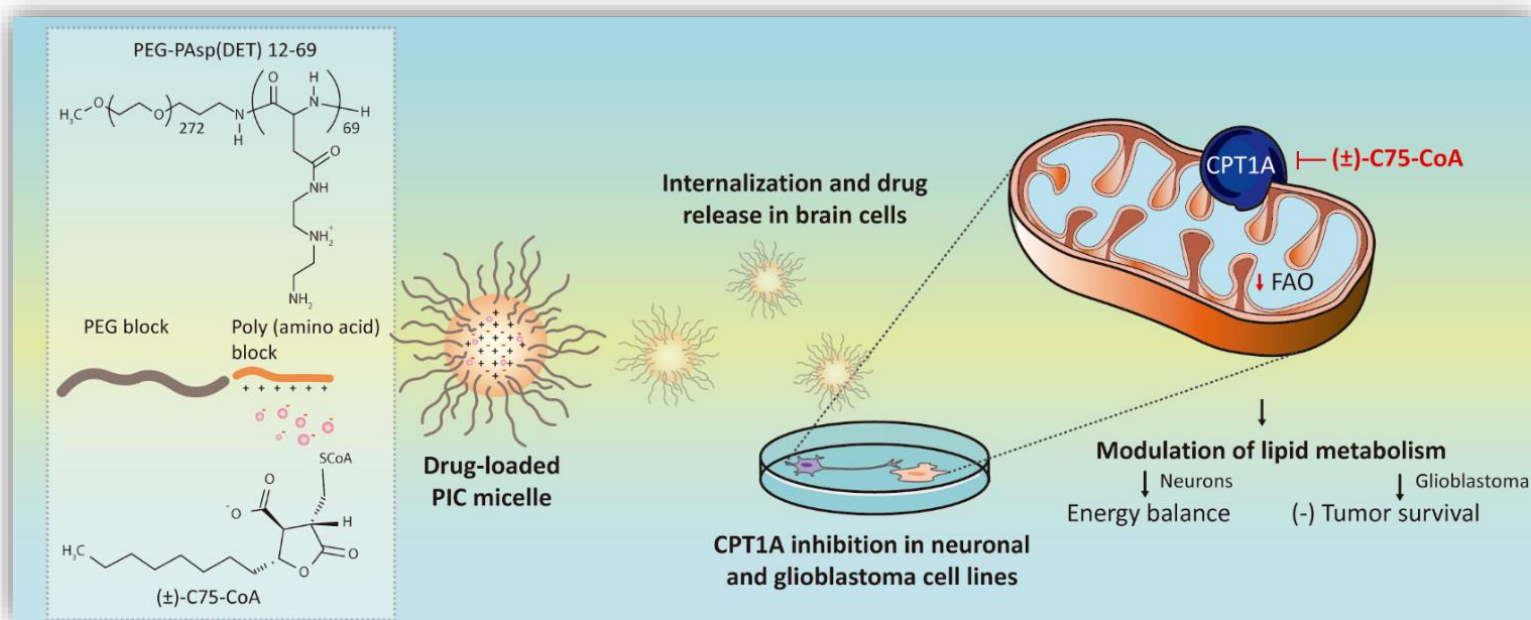
Graphical abstract

Figure 9. Graphical abstract of chapter 1. Amphipatic polymers were used to encapsulate C75-CoA and Fluorescein-CoA to evaluate cytotoxicity, internalization and modulation of lipid metabolism in GBM and hypothalamic neuron cell models.

Poly-ion complex micelle effectively delivers CoA-conjugated CPT1A inhibitors to modulate lipid metabolism in brain cells

West Kristian D. Paraiso[1], Jesús Garcia-Chica[2,3,4], Xavier Ariza[3,5], Sebastián Zagmutt[2], Shigeto Fukushima[1], Jordi Garcia[3,5], Yuki Mochida[1], Dolors Serra[4,5], Laura Herrero[4,5], Hiroaki Kinoh[1], Núria Casals[2,5], Kazunori Kataoka[1,6], Rosalía Rodríguez-Rodríguez[2,*], and Sabina Quader[1,*]

[1]Innovation Center of Nanomedicine, Kawasaki Institute of Industrial Promotion, Kawasaki, Kanagawa 210-0821 Japan

[2]Basic Sciences Department, Faculty of Medicine and Health Sciences, Universitat Internacional de Catalunya, Sant Cugat del Vallès, E-08195 Spain.

[3]Department of Inorganic and Organic Chemistry, Faculty of Chemistry, Institut de Biomedicina de la Universitat de Barcelona (IBUB), Universitat de Barcelona, Barcelona, E-08028 Spain.

[4]Department of Biochemistry and Physiology, School of Pharmacy and Food Sciences, Institut de Biomedicina de la Universitat de Barcelona (IBUB), Universitat de Barcelona, Barcelona, E-08028 Spain.

[5]Centro de Investigación Biomédica en Red de Fisiopatología de la Obesidad y la Nutrición (CIBEROBN), Instituto de Salud Carlos III, Madrid, E-28029 Spain.

[6]Institute for Future Initiatives, The University of Tokyo, Tokyo 113-0033 Japan.

Corresponding authors: Rosalía Rodríguez-Rodríguez (rrodriguez@uic.es) (Tel. +34-935-042-002) and Sabina Quader (sabina-q@kawasaki-net.ne.jp) (Tel. +81-44-589-5920)

ABSTRACT

Carnitine palmitoyltransferase 1A (CPT1A) is a central player in lipid metabolism, catalyzing the first committed step to fatty acid oxidation (FAO). Inhibiting CPT1A, especially in the brain, can have several pharmacological benefits, such as in obesity and brain cancer. C75-CoA is a strong competitive inhibitor to CPT1A. However, due to its negatively-charged nature, it has low cellular permeability. Herein, we report the use of poly-ion complex (PIC) micelles to deliver the specific CPT1A inhibitors, (±)-, (+)-, and (−)-C75-CoA into U87MG glioma cells and GT1-7 neurons. PIC micelles were formed through charge-neutralization of the cargo with the cationic side chain of PEG-poly{*N*-[*N'*-(2-aminoethyl)-2-aminoethyl]aspartamide} (PEG-PAsp(DET)), forming particles with 55 to 65-nm diameter. Upon short-term incubation with cells, the micelle-encapsulated CPT1A inhibitors resulted up to 5-fold reduction of ATP synthesis, compared to the free drug, without an apparent decline in cell viability. Micelle treatment showed a discernible decrease in ^{14}C-palmitate oxidation into CO_2 and acid-soluble metabolites, confirming that the substantial lowering of ATP production was related to FAO inhibition. Micelle treatment also diminished IC_{50} by 2 to 4-fold over the free drug-treated U87MG after long-term incubation. To measure cellular uptake of these CoA-adduct loaded PIC micelles, we synthesized a fluorescent CoA derivative and prepared Fluor-CoA micelle which showed efficient internalization in both cell types and both in 2D and 3D culture models, especially in neurons where uptake reached up to 3-fold over the free dye. Our results starkly demonstrate that the PIC micelle is a promising delivery platform for anionic inhibitors of CPT1A in glioma cells and neurons, laying the groundwork for future research or clinical applications.

1. INTRODUCTION

Lipids, which include triglycerides, phospholipids, steroids, and other fat-soluble biological molecules, are important elements of the brain's structure and function, where they constitute 50% of its dry weight [1,2]. Among these, fatty acids (FAs) function as energy source, lipid membrane component, as well as starting material for signaling molecules [3]. Carnitine palmitoyltransferase 1 (CPT1) is an enzyme that catalyzes the rate-limiting step in fatty acid oxidation (FAO) – transesterification of long-chain fatty acid-coenzyme A (LCFA-CoA) and carnitine to form CoA and LCFA-carnitine esters. The resulting LCFA-carnitine can then be transported across membranes for further metabolism [4]. In mammals, there are three different CPT1 isoforms: CPT1A, which is the most ubiquitous isoform and highly expressed in liver, and kidney, pancreas, but also astrocytes and neurons, CPT1B, which is expressed mainly in muscle and brown adipose tissue, and CPT1C, which is found exclusively in neurons and has residual CPT1 activity [5].

The CPT1 system is pivotal for the regulation of FA metabolism in most of the tissues. In the brain, particularly in hypothalamic neurons, CPT1A has been revealed as a potential target against obesity [4,6]. Accordingly, knockdown and pharmacological inhibition of CPT1A in the hypothalamus contributes to reduced food intake in rodents because of the accumulation of LCFA-CoA in the neurons [7,8]. This is thought to be a satiety signal as it precedes reduced expression of orexigenic (feeding-promoting) proteins, leading to reduced food intake [9,10], making it an appealing target for obesity. In addition to hypothalamic neurons for the regulation of energy homeostasis, CPT1A is crucial to the survival of certain cancer types, including brain cancer. Particularly, glioblastoma (GBM) has been related to increased CPT1A expression and FA metabolism alterations. Importantly, this elevated

expression of CPT1A is a very common event (90-95% cases) among human diffuse gliomas [11–13]. CPT1A-expressing tumor cells show increased FAO, promoting survival in conditions of metabolic stress like glucose deprivation and hypoxia [14]. While tumor molecular heterogeneity is an emerging critical concern in oncology, homogeneous elevated expression of CPT1A in GBM is indeed an attractive molecular target for GBM therapy.

Several pharmacological inhibitors of CPT1A, which act by competing with the natural inhibitor malonyl-CoA, have been investigated [15]. An example is etomoxir (ETO) and (±)-C75, which are converted to their CoA derivatives and act on CPT1A[16,17], leading to decreased body weight and food intake in rodents [16,17]. However, it was deemed too toxic for clinical use, exemplified by causing severe hepatotoxicity as a side effect [18,19].

A more promising compound is (±)-C75 (4-methylene-2-octyl-5-oxotetrahydrofuran-3-carboxylic acid). It is converted intracellularly by endogenous acyl-CoA synthetase to its CoA adduct, (±)-C75-CoA, a strong competitive inhibitor to CPT1A [16]. Its systemic administration in rats led to food intake decline, and body weight decrease, as the drug was shown to cross the BBB and get converted to (±)-C75-CoA in the ARC hypothalamic nucleus [17,20]. Makowski *et al* [8] performed the stereoselective synthesis of (+)-C75 [(2*R*,3*S*) isomer] and (–)-C75 [(2*S*,3*R*) isomer] to explain their differential pharmacological activities. (+)-C75 was found to be an anorectic by inhibiting CPT1 activity after conversion to (+)-C75-CoA. On the other hand, the effect of (–)-C75 in CPT1A activity is indirect, acting via FAS inhibition driving an increase in malonyl-CoA levels, which is the physiological inhibitor of CPT1. In addition, the effects of (–)-C75 without CoA adduct on food intake were negligible, but show antitumoral effects in several cell lines [8]. The presence of the CoA adduct in C75 is then crucial to exert selective inhibitory effect on

CPT1 while limiting off-target effect on FAS , but it considerably reduces the uptake of the drug into the target cell. Therefore, strategies to deliver C75 derivatives with intact CoA adduct into the target cells is needed. Additionally, since brain CPT1 is implicated in both cancer and obesity, the administration of (±)-C75-CoA and its enantio-separated CoA forms into specific brain cells presents a novel therapeutic strategy to treat both diseases.

The chemical structure of (±)-C75-CoA presents challenges to cellular entry. It is a small, polar, and charged metabolite, having low permeability across the cell membrane [21] and consequently needing a delivery system for intracellular transport. With its phosphate groups ionized at physiological pH, its anionic state, together with its long aliphatic side-chain enables CoA to interact with cation-conjugated polymers through a combination of electrostatic and hydrophobic interactions [22]. Therefore, forming a poly-ion complex (PIC) micelle with (±)-C75-CoA is a sound approach in designing a delivery system since it neutralizes the overall negative charge that would hinder its cellular entry. Although PIC micelles are well used for various nucleic acid-based macromolecular cargoes such as plasmid DNA, mRNA, siRNA, and anti-sense oligonucleotides (ASOs) [23–25], applications for small, ionic molecule delivery [26] are relatively scarce.

The cationic polymer used is PEG-poly{N-[N'-(2-aminoethyl)-2-aminoethyl]aspartamide} (PEG-PAsp(DET)), which has a monoprotonated side chain at pH 7.4, at which point it only causes minimal membrane destabilization. At pH 5.5, the side chain becomes diprotonated, selectively destabilizing the endosomal membrane once inside the cell, enabling less toxic gene transfer into cells [27,28]. This system has been used for mRNA transfection into neurons [29] as well as astrocytes and oligodendrocytes [30], making it an excellent candidate for (±)-C75-CoA delivery. We have successfully prepared

PIC micelles from PEG-PAsp(DET) that encapsulated (±)-C75-CoA and its enantio-separated forms, potentiating the opportunity to study their biological activity on LCFA metabolism defying the cellular entry limitation. Accordingly, the micelles were tested on two brain-derived cell lines, U87MG human glioma cells and GT1-7 murine hypothalamic neurons, which revealed that FAO and ATP synthesis were successfully inhibited in both. Using a model particle encapsulating a fluorescent CoA derivative, we were also able to demonstrate that the PIC micelle is efficiently taken up by both cell lines and both in 2D and 3D culture models. This paper is the first report to describe the delivery of CoA-conjugated CPT1A inhibitors using PIC micelles to target CPT1A and modulate lipid metabolism in glioma cells and neurons.
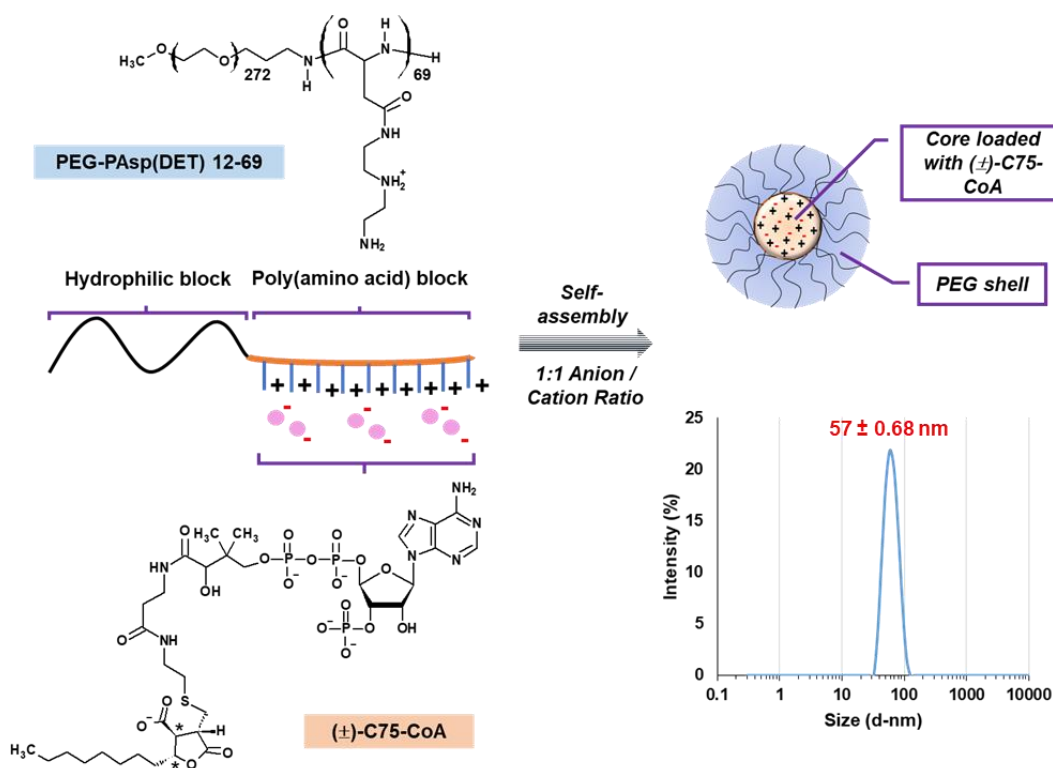

Figure 1. Schematic of a poly-ion complex (PIC) micelle formation of (±)-C75-CoA with PEG-PAsp(DET), including its size distribution profile (hydrodynamic size *versus* intensity %).

2. RESULTS AND DISCUSSION

2.1 Preparation of C75-CoA micelles

The preparation of (±)-C75-CoA was carried out as previously described [17] (see detailed information in ESI†). Enantioselective syntheses of (+)-C75 [(2R,3S) isomer] and (−)-C75 [(2S,3R) isomer] were performed by using enantiomeric chiral auxiliaries also as previously reported [8] (**Figure S1, ESI†**). (±)-C75-CoA were formed by nucleophilic addition to the α,β-unsaturation of (±)-C75 by the –SH group of CoA. We confirmed the synthesis by comparing the ^{1}H NMR and HPLC profiles of the starting materials and product (**Figure S2, ESI†**). PEG-PAsp(DET) was prepared by anionic ring-opening polymerization of benzyl-L-aspartate N-carboxyanhydride (BLA-NCA) initiated from the terminal –NH$_2$ group of CH$_3$O-PEG-NH$_2$ (MW 12,000) to form CH$_3$O-PEG-b-poly(β-benzyl-L-aspartate) (PEG-PBLA), and then subsequent aminolysis with diethylenetriamine (DET) (**Figure S3, ESI†**). The degrees of polymerization (DP) and substitution (DS) were measured from the ^{1}H NMR spectra. Using the proton peak intensity ratio of the PEG methylene protons (δ = 3.4-3.6 ppm) to the aromatic ring protons (δ = 7.1-7.5 ppm) in the polypeptide side chain of PBLA, DP was calculated to be 69. After aminolysis, the same PEG methylene protons were then compared with all the methylene protons in the DET side chains (δ = 2.7-3.6 ppm), and the DS was found to be 63.

The aqueous solutions of (±)-C75-CoA and PEG-PAsp(DET) were mixed in a 1:1 anion/cation (A/C) ratio, defined as the ratio between the overall anionic charge imparted by the phosphate and carboxylate groups in (±)-C75-CoA and the overall cationic charge given by the protonated secondary amines in PEG-PAsp(DET). We diluted the solutions using 10 mM phosphate buffer (PB) pH 7.4 to give 57-nm PIC micelles with a unimodal size profile and narrow polydispersity (PdI). The 1:1 A/C ratio was selected based on the optimal physicochemical properties obtained with this micelle, mainly the smallest

micellar size and lowest PdI value (Figure S4, ESI†). The zeta potential (ZP) was also close to neutral (**Figure 1, Table 1**). At pH 7.4, around 51% of the aminoethylene units in the PEG-PAsp(DET) side chain are protonated [27], this imparts a cationic charge to the block co-polymer for neutralizing the negative charge of the anionic cargo, forming PIC micelles. The PEG chain of the polymer (MW 12,000) was also crucial in imparting these measured physicochemical properties, decreasing aggregation tendency and maintaining a neutral surface charge [23]. Transmission electron microscopy (TEM) revealed that (±)-C75-CoA micelles are spherical in shape and possess a core size of 31 nm with a unimodal size distribution **(Figure S5, ESI†)**. The core size of the micelle does not include the PEG outer shell, hence it is smaller than the hydrodynamic diameter obtained using DLS. Size and PEGylation are important considerations for brain-targeted nanoparticles (NPs). NP diffusion in the brain is affected by the finite width of the brain extracellular space (ECS) and pores in the extracellular matrix (ECM) [31]. When surface PEG density is sufficiently high, 114-nm NPs can diffuse effectively in human and rodent brains [32]. This was corroborated in subsequent literature, and now ECS widths are estimated to be 80-220 nm in diameter while pores are around 100 nm [33-35]. Increased PEG surface density is also shown to restrain non-specific cellular uptake of NPs [36]. which removes another impediment for diffusion. The size of (±)-C75-CoA micelle is therefore ideal for moving through the brain parenchyma.

(+)- and (–)-C75-CoA were synthesized from the same procedure as (±)-C75-CoA and their corresponding micelles were also successfully prepared, with near-similar physicochemical properties (**Table 1**). Additionally, micelles loaded with other CoA derivatives were prepared in order to confirm the applicability of the delivery system to molecules with similar structures. First, we used commercially available palmitoyl-CoA since its hydrophobic tail

resembled that of (±)-C75 and their molecular weights were also numerically close. Indeed, micelle formation was observed based on DLS measurements. However, when we used CoA (767.5 g/mol) only or malonyl-CoA (853.6 g/mol), micelle formation was not detected. The probable reasons are that their MWs were much smaller from (±)-C75-CoA and that they did not possess the characteristic hydrophobic moieties, despite having the phosphate groups necessary for PIC formation. This indicates that hydrophobicity was to some degree a part of the driving force for micelle formation. To determine the percentage of (±)-C75-CoA loaded inside the micelle, ultracentrifugation was used to remove the unencapsulated free drug. The ratio of the drug concentration in the upper fraction of the filter and the total drug added in the micelle preparation was calculated. From this, we ascertained that (±)-, (+)-, and (−)-C75-CoA micelles all have high drug encapsulation rates (above 80%). The ionic interaction between the drug and polymer was further confirmed by the statistically significant decrease in scattering light intensity and % encapsulation when (±)-C75-CoA micelle was mixed with concentrated salt solutions (0.5 or 1 M NaCl) (**Figure S6**, **ESI†**). Formation of PIC is driven primarily by the liberation of counterions [23] which is prompted when the cationic DET side chain and anionic drug paired up, leading to a large entropic gain. The increased NaCl concentration apparently reduced this entropic gain, which resulted in the destabilization of the PIC structure.

Cargo		Micelle			
Molecule	**MW (g/mol)**	**Size (d-nm)**	**Polydispersity**	**Zeta potential (mV)**	**Encapsulation (%)**
(±)-C75-CoA	1004	56.7 ± 0.68	0.055 ± 0.0037	-0.29 ± 1.98	84.2 ± 0.52

(+)-C75-CoA	1004	63.5 ± 1.45	0.054 ± 0.0082	-0.68 ± 2.25	82.2 ± 0.01
(−)-C75-CoA	1004	55.0 ± 0.38	0.024 ± 0.0232	0.17 ± 2.62	87.3 ± 0.03
Palmitoyl-CoA	1005.9	59.5 ± 0.69	0.022 ± 0.0017	2.37 ± 0.85	66. 8 ± 0.05
Fluorescein-CoA	1175.8	56.9 ± 0.16	0.037 ± 0.0070	0.38 ± 1.46	94.3 ± 0.18

Table 1. Physicochemical characteristics of (±)-C75-CoA, Palmitoyl-CoA and Fluorescein-CoA micelles. Experiments were performed in triplicate, with values expressed as mean ± SD.

Next, to evaluate its long-term stability in cold storage, the change in micelle characteristics was monitored every 7 days for a total of 28 days during storage at 4 °C (**Figure 2**). The purpose of this experiment was to ensure that micelles prepared in advance can still be used in biological assays after a few days of storage enabling easy and efficient reproducibility of experimental results. One-way analysis of variance (ANOVA) revealed apparent linear relationships between each physicochemical parameter and incubation time. We observed micelle size to increase slightly with time (R^2 = 0.9609) (**Figure 2 a**). This increase in size was accompanied by a steady increase in scattering light intensity (R^2 = 0.9984) (**Figure 2 b**) as expected, indicating that no apparent decrease in particle concentration occurred. There
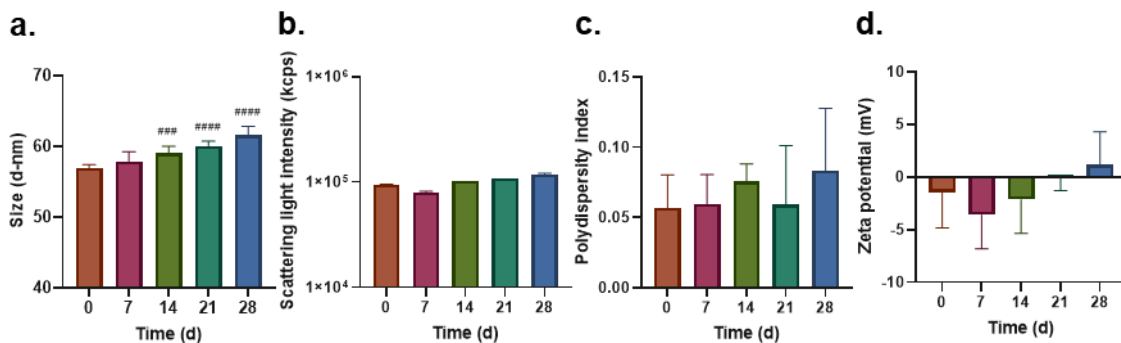
Figure 2. Long term stability studies of (±)-C75-CoA micelle, including measuring changes in physicochemical properties over 28 days in storage at 4 °C: size (a), scattering light intensity (b), polydispersity (c), and zeta potential (d). Experiments were performed in triplicate (values expressed in mean ± SD) and linear relationships were established using ANOVA. Comparison of means among treatment groups were done using ANOVA (with Tukey's test as post-hoc analysis; [###]$P<0.001$, [####]$P<0.0001$ *versus* day 0 of measuremen

was also no apparent change in PdI throughout the observation period (**Figure 2 c**). The size profile remained monodisperse, as the PdI remained well below 0.1, which was narrow. ZP stayed close to neutral all throughout the observation period, despite a weak increase associated with time ($R^2 = 0.7432$) (**Figure 2 d**). However, there was no significant change between the initial and final values. Overall, despite the tendency to gradually change over time, it is reasonable to conclude that micelle integrity was maintained for 28 days in storage at 4 °C.

PIC micelles from charged block copolymers exhibit critical association behavior [24], which predicts the stability of a drug delivery system in an environment where it is highly diluted. Using static light scattering (SLS), we measured the scattered light intensity of diluted PIC micelle solutions as expressed by the following equation:

$$\frac{Kc}{\Delta R(\theta)} = \frac{1}{M_{w,app}} + 2A_2 c$$

where $M_{w,app}$ is the apparent molecular weight of the micelle, A_2 is the second virial coefficient, c is the concentration of the micelle solution, $\Delta R(\theta)$ is the difference between the Rayleigh ratio of the micelle solution and the solvent (10 mM phosphate buffer), and K, the Debye constant, is calculated using $4\pi^2 n^2 (\frac{dn}{dc})^2 / \lambda^4 N_A$ (where N_A is Avogadro's number).

Abrupt changes in the $Kc/\Delta R(\theta)$ values in a Debye plot reveal changes in molecular weight of micelles. When these measurements are near-constant at a certain concentration range, micelle integrity is maintained. At lower ($\pm$)-C75-CoA micelle concentrations (0.005 to 0.1 mg/mL), a sharp decrease in $Kc/\Delta R(\theta)$ was apparent (**Figure 3**). However, at higher concentrations (0.15 to 1.0 mg/mL), $Kc/\Delta R(\theta)$ values became nearly constant. The point of intersection of two straight lines drawn from the lower and higher concentration range give the critical association concentration (CAC) of the micelle, which is 0.09 mg/mL. Thus, given its low CAC value, the micelle formed from PEG-PAsp(DET) is expected to have excellent stability in dilute systems. The equivalent drug concentration at CAC is 0.03 mM ($\pm$)-C75-CoA. Concentrations much higher than this were employed in subsequent biological experiments.
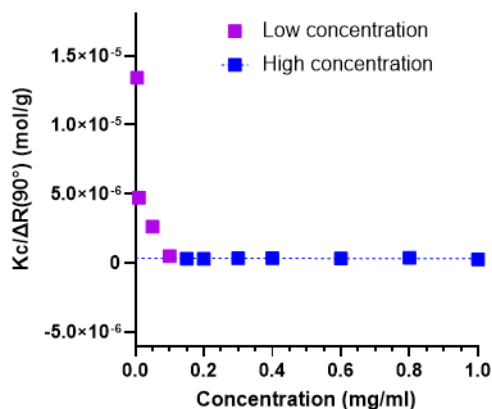
Figure 3. Critical association behavior of (±)-C75-CoA micelle. Gray squares indicate lower micelle concentrations while black squares indicate higher micelle concentrations. The known Rayleigh ratio of toluene used as calibration standard and the detection angle θ = 90° was used. Measurements were carried out at 25 °C.

2.2 Inhibition of fatty acid metabolism

2.2.1 ATP synthesis

LCFAs need to enter the mitochondria to undergo β-oxidation. They are first esterified into the LCFA-CoA form, which is shuttled into the mitochondria by CPT1A (**Figure 4 a**). Upon entry, the LCFA-CoA undergoes β-oxidation to form several acetyl-CoA molecules, which then enters the Krebs cycle. Acetyl-CoA is eventually degraded into CO_2, and in the process produces NADH, which enters the electron transport chain (ETC) to finally yield ATP [37,38]. By this pathway, FAO inhibition is known to impair ATP production. We examined whether C75-CoA will show this effect by measuring ATP concentration in cells after incubation with free and micellar C75-CoA (**Figure 4 b-c**) for 45 minutes. In general, the micelle effect is well-pronounced as the ATP concentrations from micelle-treated cells are significantly lower than those from free drug-treated groups. This suggests that the effective delivery of C75-CoA inside the cells led to a higher concentration of the compound reaching the

mitochondria, further steering into a substantial inhibition of FAO by the nano-encapsulated drugs.

U87MG is the most widely used cell line for human glioma research [39].It was also reported to express CPT1A [12],making it an appropriate model for our subsequent experiments. For U87MG, neither ETO nor the free drugs with CoA adduct, were able to effectively reduce ATP levels (**Figure 4 b**). Nevertheless, cells treated with (±)-, (–)- and (+)-C75-CoA micelles showed significant reduction in ATP levels compared to their corresponding non-encapsulated drugs. This ATP lowering effect is particularly appreciated with (–)-C75-CoA micelle, which was the most effective compared to all other groups. Although the lack of effect of ETO in ATP levels did not correlate with previous publications [40,41], we observed a reduction in FAO assay with ETO in U87MG (Figure 5 c), confirming the inhibitory effect of this drug on mitochondrial metabolism, although the dosage-dependent off-target effects attributed to ETO could explain the result in ATP levels [42].

GT1-7 is an immortalized murine hypothalamic neuronal cell line which is used in endocrinology and metabolism studies [43]. It was also reported to express CPT1A [44] and since it is in our interest to measure its inhibition in the hypothalamus, this cell line is an appropriate *in vitro* model. ATP levels in GT1-7 were discernibly reduced in response to ETO and by the free (±)- and (–)-C75-CoA derivatives, but no changes were observed in the (+)-C75-CoA-treated group (**Figure 4 c**). Drug encapsulation led to a statistical enhancement in ATP reduction induced by both (+)- and (–)-C75-CoA forms. As shown in U87MG, (–)-C75-CoA micelle was still most effective in reducing ATP among all treatment groups including ETO.

A concurrent cell viability assay confirmed that the treatments in both U87MG and GT1-7 cells did not cause any apparent cell death, compared to the non-treated group (**Figure 4 d-e**). This highlights one of the advantages of the delivery system that we used, since PEG-PAsp(DET) causes only minimal toxicity [27]. Although other cationic polymers like poly-(L-lysine) and poly(ethylenimine) (PEI) are well-used to deliver anionic molecules, their toxicity upon micellar disassembly limits their biological applications [45]. Overall, our results verify that for both cell types, the micelles were more successful in reducing ATP synthesis as compared to the free drug without causing excessive cell death.

2.2.2   FAO assay

Palmitate oxidation in both U87MG and GT1-7 cells was evaluated in terms of: oxidation to CO_2 (**Figure 5 a & d**), conversion to acid-soluble products (ASPs) (**Figure 5 b & e**) and total FAO rate calculated as the sum of ASP plus CO_2 oxidation (**Figure 5 c & f**). The final fate of palmitate oxidation in both cell types was significantly different. In particular, most of palmitate oxidation levels measured in U87MG cells come from ASPs (ranging 7.5 nmol/mg prot/h), with minimal contribution of oxidation to CO_2 (ranging 0.1 nmol/mg prot/h), whereas GT1-7 cell lines showed more equitable contribution of palmitate oxidation to ASPs and CO_2 total FAO. The differences in palmitate oxidation fate between GBM or neuronal cell lines agree with previous publications indicating the different metabolic profile of both cell types [12,40,46,47].
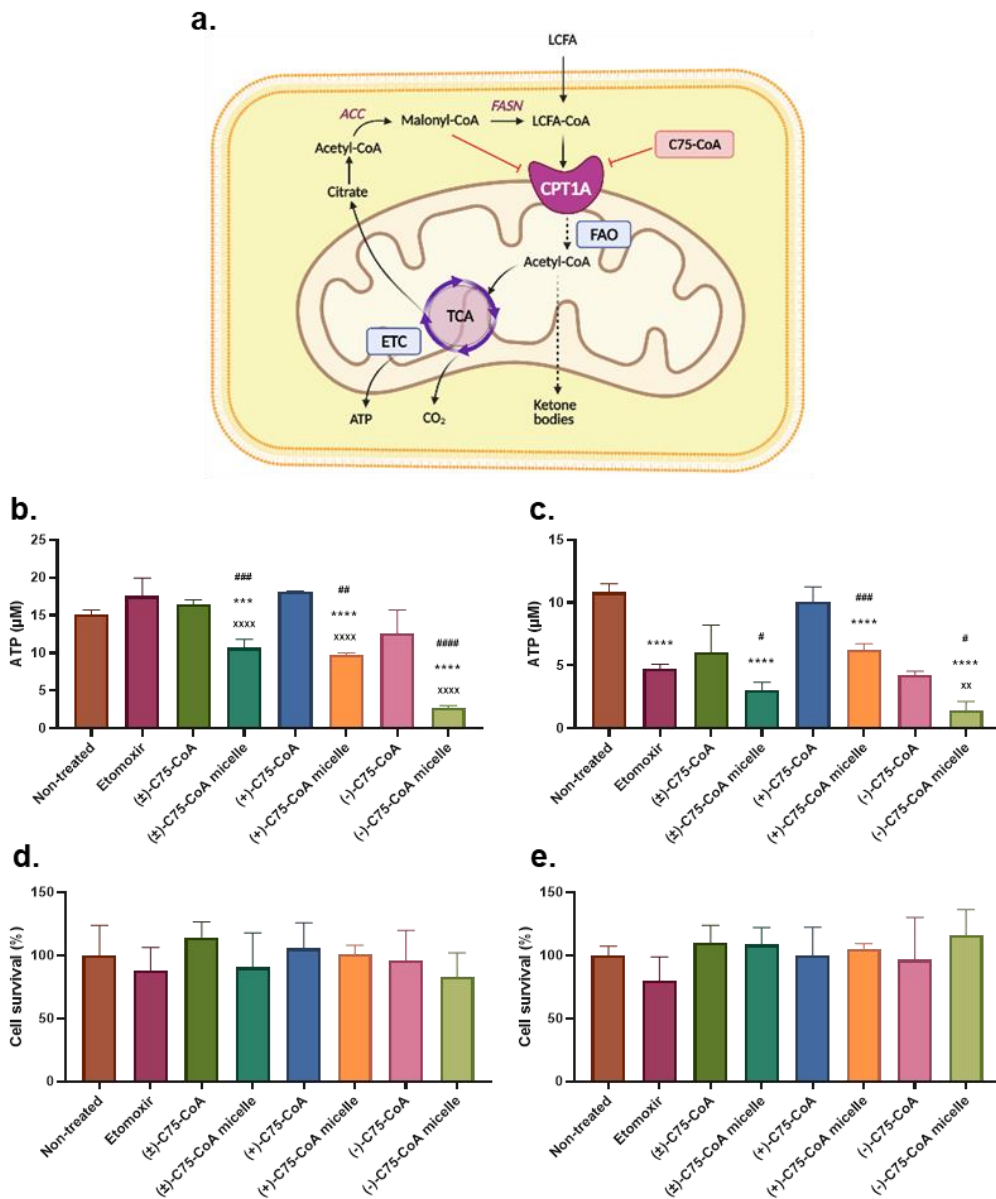
Figure 4. Illustration of ATP generation from LCFA metabolism (a). Levels of ATP produced by U87MG (b) and GT1-7 (c) after treatment with FAO inhibitors. Simultaneous Calcein AM cell viability assay for U87MG (d) and GT1-7 (e) using the same conditions and treatments as ATP assay. Experiments were performed in quadruplicates (values expressed in mean ± SD) and comparison of means among treatment groups were done using ANOVA (with Tukey's test as post-hoc analysis;

Figure 4 (continued). ***P<0.001, ****P<0.0001 *versus* non-treated cells; ^{xx}P<0.01, ^{xxxx}P<0.0001 *versus* ETO; [#]P<0.05, ^{##}P<0.01, ^{###}P<0.001, ^{####}P<0.0001 *versus* the corresponding free form of C75-CoA). Concentrations of all inhibitors used = 0.5 mM.

In U87MG cells, ETO effectively reduced FAO in terms of both CO_2 and ASP (**Figure 5 a-c**), since ASP oxidation was the main pathway contributing to total reduction of FAO. In contrast, the free forms of C75-CoA were unable to modify these oxidation parameters compared to non-treated cells. Micelles of the three forms of C75-CoA, led to a substantial attenuation of total FA oxidation (**Figure 5 c**), reaching similar levels to ETO-treated cells, and these changes were due to palmitate oxidation to ASP (**Figure 5 b**), probably reducing the generation of TCA intermediary metabolites and ketone bodies crucial for GBM cell proliferation [12,40]. Similar levels of FAO attenuation were reached in (±)-, (+)- and (−)-C75-CoA micelles-treated U87MG cells (**Figure 5 c**).

In GT1-7, ETO was also able to reduce FAO, whereas it remained unchanged after treatment with the free C75-CoA forms, in line with previous results (**Figure 5 d-f**). The micelle forms of C75-CoA derivatives induced a statistically significant attenuation in total FAO, being the contribution of both palmitate fates, to CO_2 and ASP, similar to total oxidation of FA (**Figure 5 d-f**). Cells treated with (±)-C75-CoA micelle showed the highest reduction in FAO compared to non-treated conditions, reaching similar levels to those induced by ETO (**Figure 5 c**).

Altogether, our results indicate that the delivery of C75-CoA derivatives using a PIC micelle resulted in a substantial improvement in FAO inhibition by these drugs in both U87MG and GT1-7 cell lines. We have also evidenced the differential contribution of either CO_2 or ASPs to FA oxidation in both cell lines,

in agreement with the literature. Considering the recently identified role of FAO as a metabolic node in the aggressive phenotype of glioma cell lines [40,41], and the significant role of FA oxidation and CPT1 in neuronal metabolism and survival [44,47] the improved FAO inhibition showed by these micelles indicate the potential of these nanoparticles to modify brain metabolism in associated diseases such as cancer.
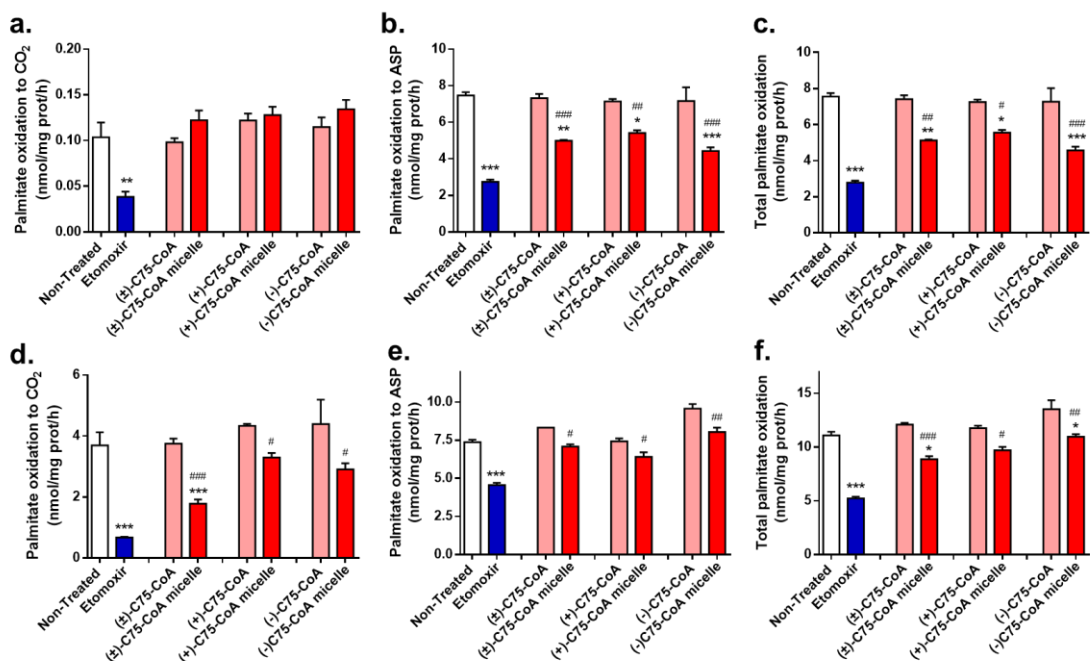

Figure 5. FAO oxidation in U87MG (a-c) and GT1-7 (d-f) cells after treatment with C75-CoA derivatives in free form or nano-encapsulated in micelles. ETO was used as positive control of FAO inhibition. FAO is represented as palmitate oxidation to CO_2 (a, d), ASP (b, e), and total palmitate oxidation (CO_2 + ASP; c, f). Results are the mean ± SD of two independent experiments performed by biological triplicates (n=5-6 samples per condition). Comparison of means were done using ANOVA followed by Tukey's comparison test; *P<0.05, **P<0.01, ***P<0.001 *versus* non-treated cells; #P<0.05, ##P<0.01, ###P<0.001 *versus* the corresponding form of C75-CoA. Concentrations of all inhibitors used = 1 mM.

2.3   Cytotoxicity of C75-CoA micelles

Since GBM cells overexpress CPT1A [11] to increase their chances of survival, inhibiting this enzyme would negatively affect their proliferation. We incubated free and micellar C75-CoA with U87MG for 72 h, with ETO as a comparison drug. The drug and micelle-produced responses generally followed a sigmoidal shape (Figure 6 a-d). C75-CoA (racemic and enantio-separated forms) is overall significantly more cytotoxic to the respective free drug (Figure 6 e). Notably, the mean IC50 of free (±)-C75-CoA was decreased 4-fold when delivered in micelle form. After 72 h, the difference between the mean IC50 of (±)- and (−)-C75-CoA micelles are not statistically significant, however, (+)-C75-CoA micelle is discernibly less cytotoxic than (±)-C75-CoA micelle. Free (+)-C75-CoA is less cytotoxic than ETO. On the other hand, ETO shows comparable toxicity to (±)- and (−)-C75-CoA micelles despite being a free drug, owing to other mechanisms outside of CPT1 inhibition such as production of reactive oxygen species [38,48].

Two-way ANOVA revealed that the mean IC_{50} values of all FAO inhibitors were all found to decrease with time in a linear fashion ($R^2 > 0.9$). The cytotoxicity of (±)-C75-CoA micelle was demonstrated to be more pronounced at longer incubation periods, approaching comparable values as ETO after 72 h (**Figure 6 f**). Note that decrease in cell viability is achieved only upon lengthier exposure, since the 45-min incubation in the ATP assay (**Figure 4 c**) was not enough to kill the cells. Cellular morphologies were also retained after short-term incubation with both free and micellar (±)-C75-CoA in the FAO assay (**Figure S7, ESI†**), including the neuronal and astrocytic processes for GT1-7 and U87MG, respectively. These results provide the initial evidence to support the further development of these PIC micelles as a therapeutic platform against GBM. It also shows that the delivery of (±)-C75-CoA inside the cell is

important in amplifying its growth inhibitory properties. Given its anionic state, it is assumed to have limited permeability across the cell membrane [21], with the micelle state neutralizing this negative charge and promoting its transport into the cell through endocytosis.
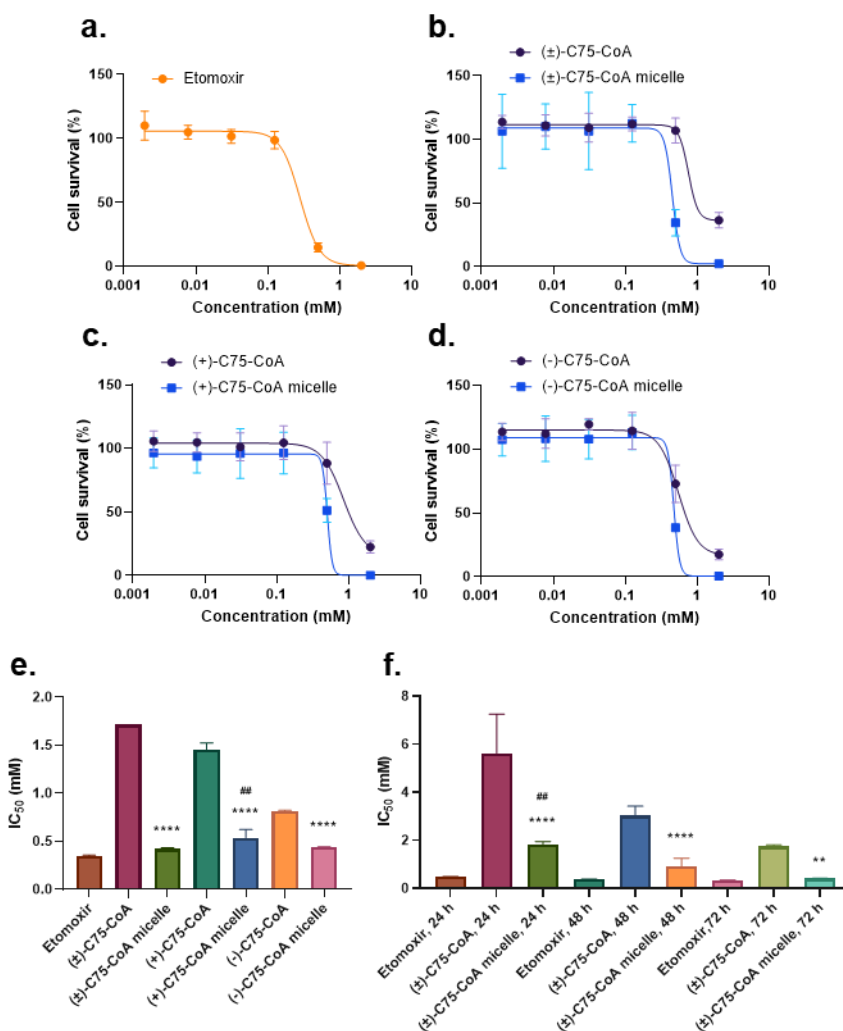

Figure 6. Cytotoxicity of FAO inhibitors on U87MG at 72 h incubation, including the dose-response curves of ETO (a) and the free *versus* micelle forms of (±)-C75-CoA (b), (+)-C75-CoA (c), and (−)-C75-CoA (d). IC_{50} of ETO, free. and micelle forms of (±)-, (+)-, and (−)-C75-CoA at 72 h incubation (e) and only for (±)-C75-CoA at 24-, 48-, and 72-h incubation periods.

Figure 6 (continued). (f). Experiments were performed in triplicates (n=4 samples per condition; values expressed in mean ± SD) and comparison of means among treatment groups were done using one-way ANOVA (with Tukey's test as post-hoc analysis; **P<0.01, ****P<0.001 *versus* the corresponding form of C75-CoA; [##]P<0.01 *versus* ETO).

2.4   Quantification of cellular uptake using Fluorescein-CoA encapsulated PIC micelle in 2D and 3D culture models

To confirm that PIC micelle type system facilitated cellular uptake of CoA-conjugated (±)-C75 by neutralizing the negative charges, we synthesized a fluorescein analogue of CoA (**Figure 7**; Fluorescein-CoA; herein Fluor-CoA) and encapsulated it inside the PIC micelle. Fluor-CoA was prepared by simple maleimide chemistry starting from fluorescein-5-maleimide. The resulting compound had a MW (1175.8 g/mol) close to (±)-C75-CoA (1004 g/mol), including the same number of carboxylate and phosphate groups, which therefore imparted analogous physicochemical properties. The fluorescein moiety also imparted sufficient hydrophobic character to CoA, which is necessary for PIC micelle formation. The addition of fluorescence emission ($\lambda_{excitation}$ = 475-490 nm, $\lambda_{emission}$ = 510-520 nm) made cellular uptake studies using confocal microscopy or flow cytometry possible. The –SH group of CoA added to the maleimide ring of fluorescein-5-maleimide to give the desired product (**Figure S8 a, ESI†**), which we confirmed by comparing the ^{1}H NMR and HPLC profiles of the starting materials and product (**Figure S8 b-c, ESI†**). In the chromatogram, the Fluor-CoA peak is revealed by both the fluorescence and UV absorbance (λ_{max} of CoA) detectors. In a similar fashion to (±)-C75-CoA, the aqueous solution of Fluor-CoA was combined with PEG-
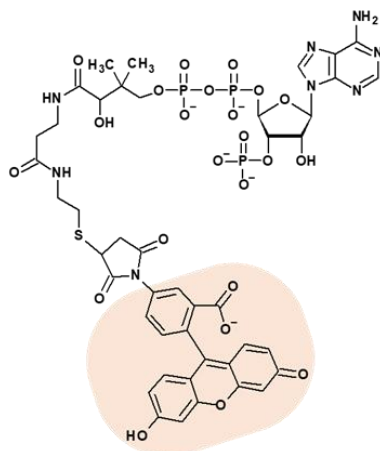
Figure 7. Structure of Fluor-CoA. The fluorescein moiety (highlighted) enables uptake evaluation using flow cytometry or confocal microscopy. PAsp(DET) in a 1:1 anion/cation ratio in 10 mM phosphate buffer (PB) pH 7.4 to give 50-nm micelles with a narrow polydispersity (**Table 1**).

Cellular uptake in both U87MG and GT1-7 was visualized using confocal laser scanning microscopy (CLSM) and quantified using flow cytometry (**Figure 8**). We incubated the micelles with the cells at different time points (1, 3, or 6 h) and at a fixed concentration of Fluor-CoA micelle (0.25 mg/mL), which contained 0.1 mg/mL free dye. The equivalent Fluor-CoA concentration was therefore used in the free dye-treated groups. In flow cytometry, only DAPI-stained dead cells were excluded in order to measure only live cells. The data we obtained included mean fluorescence intensity (MFI), to indicate extent of micelle internalization, and percentage of Fluor-CoA+ cells after gating, to quantify the % of cell population in which the free or micellar Fluor-CoA have entered. Internalization of both free dye and micelle increased with time in both cell types (**Figure 8**). Mutually, micellar uptake in terms of MFI was statistically higher than free dye uptake, at all measured time points (**Figure 8 b & e**). In addition, the values for %Fluor-CoA+ cells were discernibly greater for the micelle compared to the free dye, for both cell lines (**Figure 8 c & f**). Even after 1 h of incubation, the micelles have entered more than 95% of the
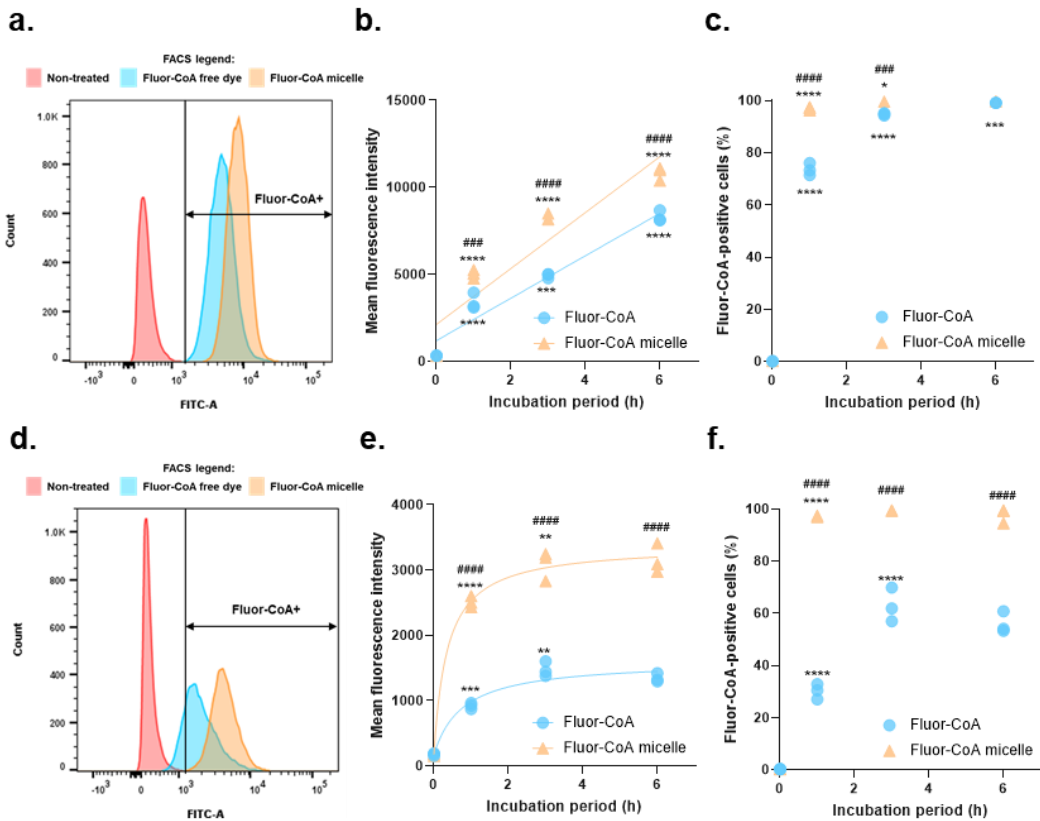
Figure 8. Analysis of cellular uptake of Fluor-CoA micelles *versus* free dye in 2D cultures using flow cytometry and confocal microscopy. U87MG data (a-c) are presented as sample histogram (a), mean fluorescence intensity (b), and percentage of Fluor-CoA-positive cells.

cells. Specifically, for U87MG, MFI corresponding to micelle uptake was 1.5-fold elevated, on average, compared to that of the free dye (**Figure 8 b**). We found that cellular uptake displayed a strong linear increased over time for both micelle ($R^2 = 0.8708$) and free dye ($R^2 = 0.9394$). This meant that the cells were expected to continue internalization beyond the 6-h observation period. In terms of %Fluor-CoA+ cells, free dye uptake started at only 70% (1 h) but gradually increased and eventually matched the corresponding value for the micelle at 6 h (**Figure 8 c**). However, the micelle-treated cells still produced a higher fluorescence signal, signifying that the overall amount of Fluor-CoA
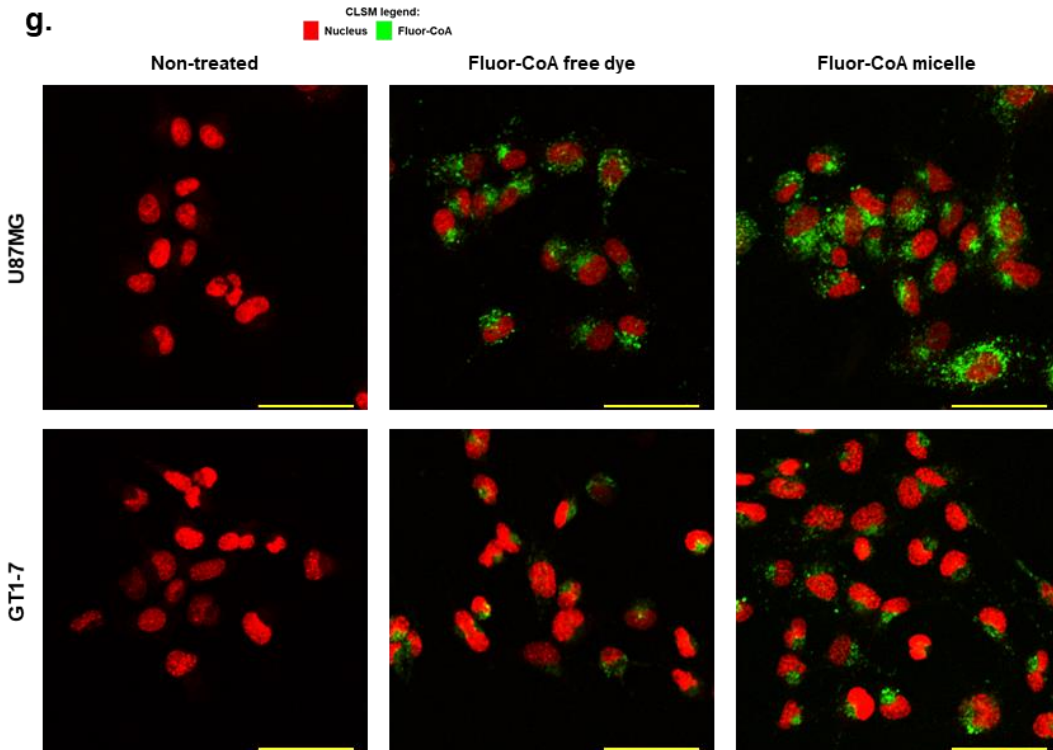
g.

Figure 8 (continued) (c). GT1-7 data (d-f) are presented as sample histogram (d), mean fluorescence intensity (e), and percentage of Fluor-CoA-positive cells (f). Experiments were performed in triplicate (values expressed in mean ± SD) and comparison of means among treatment groups were done using ANOVA (with Tukey's test as post-hoc analysis; *$P<0.05$, **$P<0.01$, ***$P<0.001$, ****$P<0.0001$ *versus* measurement at preceding time point; ###$P<0.001$, ####$P<0.0001$ *versus* corresponding free Fluor-CoA). Representative confocal microscopy images (g) of U87MG and GT1-7 after 1 h incubation with Fluor-CoA free dye and micelle. Scale bar = 50 μm, magnification 5×.

delivered to the cells was higher. Mo et al. [49] has previously described the tendency of U87MG to internalize polymeric NPs at a steady linear rate up to 6 h, which supports our findings.

The difference between micellar and free Fluor-CoA uptake was more amplified in GT1-7. MFI of micelle uptake was around 2 to 3 times higher than free dye uptake through all the time points that we measured, which clearly indicated the penetration-enhancing effects of the micelle (**Figure 8 e**). In

terms of %Fluor-CoA+ cells, the uptake started from 30% at 1 h, doubled at 3 h, and then plateaued (**Figure 8 f**). Unlike in U87MG, the rates of internalization did not increase in a linear fashion but fit a non-linear model called the Padé (1,1) approximant (Fluor-CoA R^2 = 0.9493; Fluor-CoA micelle R^2 = 0.9870). In addition, the free drug entered only around 60% of the cell population even at a 6-h incubation period, never quite reaching the 98% uptake that the micelle has attained after only 1 h of incubation. The saturable uptake of PEGylated polymeric micelles has previously been demonstrated for neurons by Rabanel *et al.* [50] who attributed it to their limited capacity to accommodate NPs.

Multi-cellular spheroids were generated by seeding cells in low-adhesion plates and allowing them to form clusters by secreting their own ECM [51], which provides additional penetration barriers for the NPs [52], therefore more accurately modeling the *in vivo* environment as compared to the monolayer culture. We found that micellar internalization was also 1.4- and 2-folds higher compared to the free dye in U87MG and GT1-7 spheroids, respectively (**Figure 9 a & c**). In GT1-7 spheroids, 30% of the cells have internalized the free dye, compared to the 80% which internalized the micelles (**Figure 9 d**). For U87MG, the difference of %Fluor-CoA+ cells between the free dye- and micelle-treated groups remain small but still statistically significant, similar to the 2D culture model (**Figure 9 b**).

Confocal images from the periphery to the core of the spheroids show the contrasting penetration abilities between Fluor-CoA free dye and micelle (**Figure 9 e-h, Figure S9, ESI†**). For both cell lines, the peak presence of Fluor-CoA is found between 0-20 µm from the periphery. The signal steadily decreased towards the core. Generally, fluorescence intensity coming from micelle-treated spheroids are consistently higher in micelle-treated spheroids,
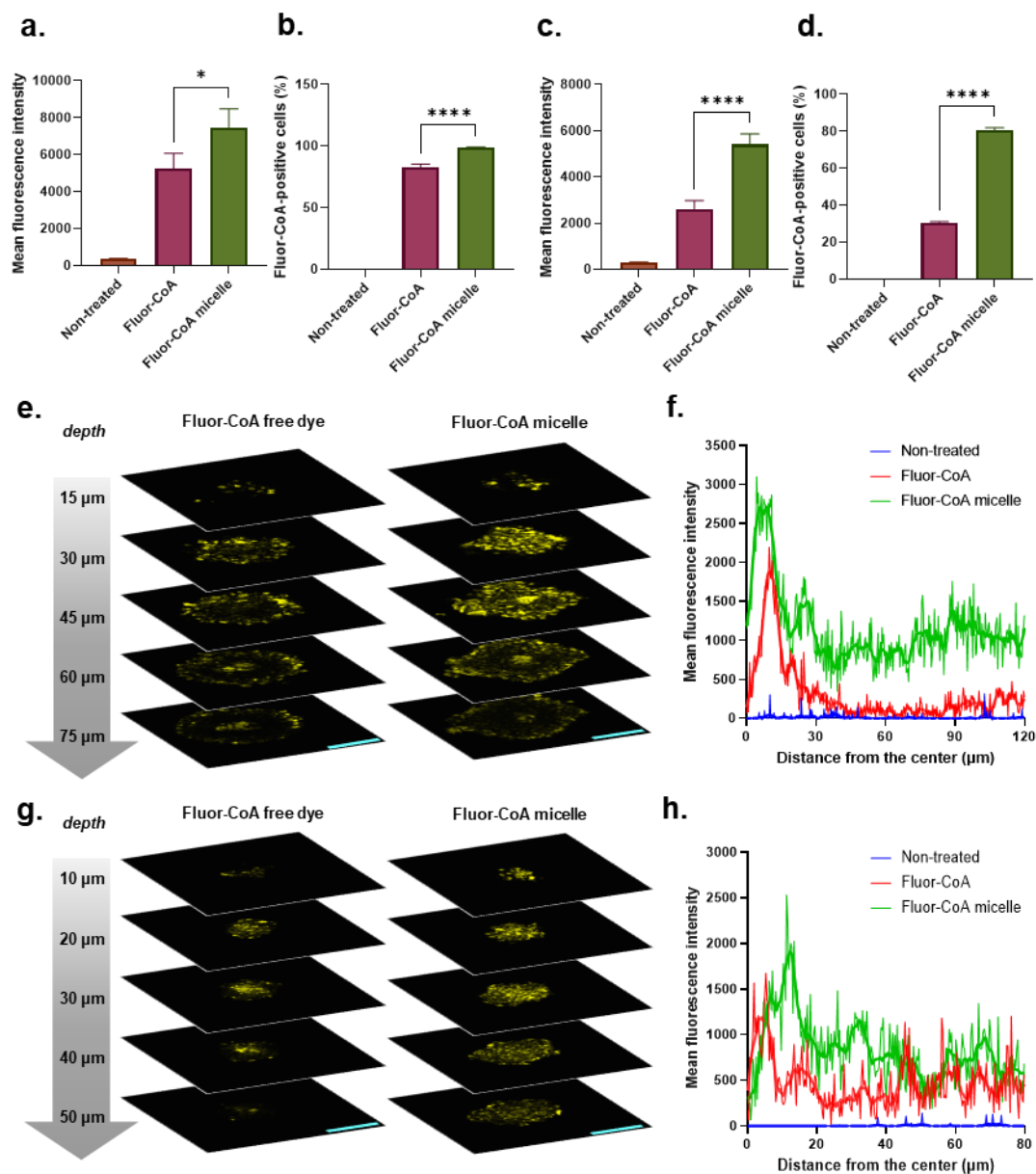
Figure 9. Analysis of cellular uptake of Fluor-CoA micelles *versus* free dye in 3D cultures using flow cytometry and confocal microscopy. FACS analysis for U87MG presented as mean fluorescence intensity (a), and percentage of Fluor-CoA+ cells (b) and for GT1-7 presented as mean fluorescence intensity (c), and percentage of Fluor-CoA+ cells (d). Experiments were performed in triplicate (values expressed in mean ± SD) and comparison of means among treatment groups were done using ANOVA (with Tukey's test as post-hoc analysis) (*p<0.05, ****p<0.0001). Representative confocal microscopy images of U87MG (e) and GT1-7 (g) spheroids taken at Z-positions. Yellow signals represent fluorescence from the FITC channel. Scale bar = 100 μm, magnification 1.2×.

Figure 9 (continued). Radial profile of fluorescence from Fluor-CoA micelles *versus* free dye in U87MG (f) and GT1-7 (h) spheroids. Actual fluorescence intensity as well as 10-point moving average as represented by a smoothing curve are shown. All data were taken after 3 h incubation with Fluor-CoA micelle or free dye.

confirming what was already shown in flow cytometry measurements: that internalization of Fluor-CoA micelles is higher than the free dye. Through the confocal images, we also demonstrated that Fluor-CoA micelles have higher penetrating ability than the free Flour-CoA. The results suggest that even in a 3D model with additional barriers, our above findings in the monolayer hold true. Additionally, this implies that the PIC micelles that we prepared are equipped to navigate through the pores of the ECM.

3. CONCLUSION

We have successfully prepared PIC micelles loaded with the CPT1A inhibitors (±)-, (+)-, and (−)-C75-CoA. The cationic block-copolymer PEG-PAsp(DET) provided a platform by neutralizing the negative charge of the cargo molecules, generating micelles with optimal physicochemical properties (55-65 nm size range and neutral surface charge) that are stable in long term storage. Through targeting CPT1A, FAO was effectively impeded, which led to overall decreased metabolism of ^{14}C-palmitate into CO_2 and acid-soluble products. We found that these results were consistent with the ATP inhibition experiments, where ATP production in both U87MG and GT1-7 was diminished up to 5-folds by the micelles, in comparison with the free drug counterparts. During these short-term incubation experiments, no apparent decrease in viability was induced by the micelles. When we assayed the cytotoxicity in glioma cells after longer incubation periods, C75-CoA micelles

inhibited cell growth more discernibly compared to the free drug forms, where IC_{50} was reduced 2 to 4-folds. (±)- and (−)-C75-CoA micelles even showed comparable efficacy to the known FAO inhibitor ETO. The fluorescent dye-loaded model particle, Fluor-CoA micelle, showed a statistically increased internalization in both cell lines as well, in comparison with the free dye, reaching a 2 to 3-fold increase especially in GT1-7 neurons. Higher cellular internalization corroborated the cytotoxicity and FAO inhibition results, that delivery through PIC micelle resulted in increased cellular concentration of the cargo, which further led to increased biological activity. Although internalization was generally time-dependent, we showed that the micellar uptake kinetics differed between the cell lines. Effective cellular entry of Fluor-CoA micelle was further confirmed in 3D spheroids derived from both cell lines, inferring the superior activity of CoA-adducts when loaded in micelles in a biological model that is transitional in complexity between standard 2D *in vitro* and diseased tissue *in vivo*. The size range and neutral surface charge of these PIC micelles, combined with their efficient penetration in 3D spheroids, imply that this platform is ideal in navigating through the brain parenchyma. This justifies further exploration of its *in vivo* properties in subsequent works. This PIC micelle has previously been reported to be effective in gene delivery to the brain including in glial cells like astrocytes and oligodendrocytes [30] as well as neurons [29]. From our data, we can compellingly conclude that uptake in neuronal and glioma cells of small anionic cargoes like Fluor-CoA and by extension, C75-CoA, is thoroughly improved by using a PIC micelle. Additionally, the advantage of using a micelle-type delivery system was more pronounced for the neurons. Drug delivery into neurons is generally more challenging compared to other cells and this is reflected in the fact that there is a lack of neuron-targeted delivery systems present in the clinic [53]. Our results contribute to the growing pool of knowledge on glioma- and neuron-targeted delivery, therefore warranting further development into effective brain

therapeutics, especially those that involve the delivery of CPT1A inhibitors and other negatively-charged molecules for management of diseases where modulating lipid metabolism is a key emerging strategy.

4. MATERIALS AND METHODS

4.1 Synthesis of (±)-C75-CoA, (+)-C75-CoA and (−)-C75-CoA

The preparation of (±)-C75-CoA was carried out as previously described [17] (see detailed information in **ESI†**). Enantioselective synthesis of (+)-C75 and (−)-C75 was performed by using enantiomeric chiral auxiliaries (**Figure S1, ESI†**).

4.2 Synthesis of PEG-PAsp(DET)

The preparation of PEG-PBLA through NCA ring-opening polymerization of BLA-NCA (Chuo Kaseihin Co., Inc.) using CH_3O-PEG-NH_2 (MW 12,000; NOF Corp.) was carried out as previously reported [54]. Subsequent aminolysis of the polymer with freshly distilled DET (TCI, cat. # D0493) was carried out also as described earlier [27,28]. See detailed information in **ESI†**.

4.3 Preparation and characterization of PIC micelles

PEG-PAsp(DET) was dissolved in 10 mM phosphate buffer pH 7.4 at 10 mg/mL concentration by overnight stirring at 4 °C. After which, the solution was passed through using 0.22-µM filter. The polymer and (±)-C75-CoA solutions were mixed in a 1:1 anion-to-cation ratio, vortexed, and then again filtered (0.22-µM) under sterile conditions prior to succeeding experiments. For DLS

measurements (Zetasizer Ultra, Malvern Panalytical, Spectris plc, UK), micelle suspensions were diluted to 1 mg/mL and placed inside a ZEN2112 quartz cuvette. Light scattering data was measured using a 50-mW 532 nm DPSS laser incident beam at a detection angle of 173° with a He-Ne laser 633 nm (temperature = 25 °C). The autocorrelation function produced was analyzed through the cumulant approach. Size is expressed as the hydrodynamic diameter, which was calculated with the Stokes−Einstein equation. Attenuator selection was automated. For zeta potential measurements, micelle suspensions were introduced in a ZEN1010 HC cell, using the Smoluchowski approach. During stability studies, micelles were kept at 4 °C and measurements were repeated every 7 d for 28 d in total.

For static light scattering (SLS) measurements, Dynamic Light Scattering Photometer DLS-8000 (Otsuka Electronics, Osaka, Japan) was used. Measurements were performed using a detection angle of 90° with a He-Ne laser 633 nm at 25 °C on micelle solutions with a concentration range of 0.005 to 1 mg/mL. To measure background light scattering, the solvent phosphate buffer pH 7.4 (10 mM) was used. Calibration was performed using toluene.

Micelle morphology was observed on a Transmission Electron Microscope (JEM-2100, JEOL, Japan) operated with 120 kv acceleration voltages and approximately 60 μA beam current. The diluted micelle (1 mg/mL) was stained by mixing with uranyl acetate solution (2%, w/v) and placed on 400-mesh copper grids before drying and observation. Micelle diameter (n = 105) was measured using IC Measure version 2.0.0.245.

4.4   Quantification of drug inside PIC micelles

Micelle solutions were pipetted into Amicon Ultra-0.5 mL centrifugal filters (MWCO 10,000, Merck Millipore, cat. # UFC501096) and spun (14,000 g, 15 min, 4 °C). The filtrate was then collected, weighed, and then transferred into UV-transparent 96-well plates. Its absorption at λ_{max} CoA = 259 nm was measured using a microplate reader (Infinite® M1000 Pro, Tecan Trading AG, Switzerland). Drug encapsulation was calculated by getting the ratio of the filtrate absorbance to that of the original (±)-C75-CoA solution added to form the micelle.

4.5   Cell cultures and treatments

Glioblastoma U87MG cell line (Merk Millipore, Sigma, Madrid, Spain) was cultured in DMEM (4.5 g/L glucose) supplemented with 10% FBS and murine hypothalamic neuronal cells GT1-7 (Merk Millipore, Sigma, Madrid, Spain) were cultured in DMEM (4.5 g/L glucose) supplemented with 10% FBS, 4 mM L-glutamine, 1% penicillin-streptomycin, and 1 mM sodium pyruvate at 37 °C in a humidified atmosphere of 95% air and 5% CO_2.

4.6   Cytotoxicity assays

In vitro cytotoxicity of etomoxir (ETO, Cayman, cat. # 11969) and free and micellar C75-CoA derivatives (racemic and enantiopures with CoA adduct) were evaluated against U87MG. The cells (3×10^4 cells / well) were seeded in a 96-well plate using DMEM (Sigma-Aldrich, cat. # D6429) containing 10% FBS in 96-well-plates 24 h prior to the assay. The cells were then incubated with the test solutions. Cell viability was measured after 24, 48, and 72 h of exposure, by using cell-counting kit-8 (CCK8) (Dojindo, cat. # CK04) by

measuring the product absorbance at λ_{max} = 450 nm using a microplate reader (Infinite® M1000 Pro, Tecan Trading AG, Switzerland).

4.7   Synthesis of Fluor-CoA and preparation of Fluor-CoA micelles

Synthesis of Fluor-CoA has been adopted from a previous protocol (New England Biolabs Inc. n.d.). Briefly, 11.1 mg CoA sodium salt hydrate was dissolved in 100 µL 10 mM phosphate buffer pH 7.4. To this, 4.8 mg fluorescein-5-maleimide (TCI, cat. # F0810) in 900 µL DMF was added. The reaction mixture was stirred overnight at 30 °C. After which, benzene was added the resulting mixture, flash-frozen using liquid N_2 and then dried *in vacuo*. To confirm product formation, the same HPLC procedure was performed as in (±)-C75-CoA, but in addition to UV absorption at λ_{max} CoA = 259 nm and λ_{max} fluorescein = 460 nm, fluorescence detection ($\lambda_{excitation}$ = 494 nm, $\lambda_{emission}$ = 521 nm) was added. The HPLC peak passing all the detection criteria corresponds to the compound with both CoA and fluorescein moieties. ^{1}H NMR was recorded on a JEOL ECS 400 (400 MHz) spectrometer (JOEL Ltd., Tokyo Japan) and chemical shift was calculated as parts per million (ppm). Data was processed using MestReNova version 14.2.1-27684.

PEG-PAsp(DET) and Fluor-CoA solutions in 10 mM phosphate buffer pH 7.4 were then mixed in a 1:1 anion-to-cation ratio, vortexed, and then again filtered (0.22-µM) under sterile conditions.

4.8   Measurement of ATP levels

Measurement of ATP levels in parallel to cell viability assays were performed according to a previously reported procedure [38]. Produced ATP was quantified

using a luminescence assay. Cells (2×10^5 cells/well) were seeded in a white, flat-bottom 96-well tissue culture plate 24 h prior to the assay. The cells were then incubated with ETO, C75-CoA, and C75-CoA micelle (0.5 mM) in bicarbonate-free DMEM (Sigma-Aldrich, cat. # D5030) supplemented with 2.5 mM glucose (Gibco, cat. # A2494001) and 275 nM oleate-BSA (Sigma-Aldrich, cat. # O3008) for 45 minutes in a separate incubator with 0% CO_2. The assay was then performed according to manufacturer protocol (CellTiter-Glo® Luminescent Cell Viability Assay, Promega, cat. # G9241). A calibration curve for ATP (TCI, cat. # A0157) was prepared. Luminescence signal for 10s were measured in each well using GloMax® Multi Detection System (Promega Corp, Madison, Wisconsin).

For the relative cell viability Calcein AM cell staining was performed. The relative viability was determined using the Calcein AM assay. In parallel to the ATP assay, cells (2×10^4 cells/well) were seeded in a white 96-well tissue culture plate 24 h prior to the assay. The cells were then incubated with ETO, C75-CoA, and C75-CoA micelle (1 mM) in bicarbonate-free DMEM (with 25 mM glucose and 6 mM glutamine) for 45 minutes in a separate incubator with 0% CO_2. The assay was then performed according to manufacturer protocol (Calcein AM; Invitrogen). Calcein AM was added to each well 30 min before measuring fluorescence intensity ($\lambda_{excitation}$ = 495 nm, $\lambda_{emission}$ = 515 nm) using a microplate reader (Infinite® M1000 Pro, Tecan Trading AG, Switzerland). Viability was normalized against non-treated cells.

4.9   Measurement of FAO

Palmitate oxidation to CO_2 and acid-soluble products (ASPs), essentially acyl-carnitine, Krebs cycle intermediates, and acetyl-CoA, were measured in U87 and GT1-7 cell lines grown in 12-well plates. Cells were treated with ETO, C75-

CoA (racemic and enantiomers), and C75-CoA micelle (racemic and enantiomers) (1 mM) in DMEM (4.5 g/L glucose) for 45 minutes. The day of the assay, cells were washed in KRBH-0.1% BSA, preincubated for 30 min at 37°C in KRBH-1% BSA. Cells were then incubated for 3 h at 37°C with fresh KRBH containing 2.5 mM glucose and 80 nM of labeled palmitate per well. Oxidation was measured as described [56]. The scintillation values were normalized to the protein content of each well and the result for CO_2 and ASPs are expressed as previously described [56].

4.10 Confocal laser scanning microscopy (CLSM)

Confocal images were taken using an LSM880 confocal microscope (Carl Zeiss, Oberkochen, Germany) at a magnification of 5× using white light, 488- and 633-nm lasers for $\lambda_{excitation}$ of Fluor-CoA and NucSpot® 650, respectively. U87MG and GT1-7 cells (6×10^4 cells / well) were seeded in μ-slide 8-well chambered coverslip (ibidi, cat. # 80826) 24 h prior to observation. Cells were then incubated with 100.0 μL nanoparticle suspension in medium (0.25 mg Fluor-CoA micelle/mL containing 0.1 mg Fluor-CoA/mL) as well as NucSpot® 650 (Biotium, cat. # 40082) as nuclear stain (1 μL/mL suspension) and Verapamil HCl as efflux pump inhibitor (1 μL/mL suspension) for 1 h. Cells were then washed 2 × with PBS (–) before replacing medium with DMEM containing Trypan Blue (0.5 μL/mL) to quench fluorescent dyes attached on the cell surface.

4.11 Quantification of cellular uptake using FACS

U87MG and GT1-7 cells (3×10^5 cells / well) were seeded in 6-well plates 24 h prior to the assay. Cells were then incubated with nanoparticle suspension in medium (0.25 mg Fluor-CoA micelle/mL containing 0.1 mg Fluor-CoA/mL) with

varying incubation times (1, 3, and 6 h). Nanoparticle suspension was washed twice with 1 mL PBS (−) and then incubated with 300 μL Accutase® Cell Detachment Solution (Innovative Cell Technologies, San Diego, California) for 3 minutes at 37 °C. The cells were then collected by adding 1 mL PBS (−) and transferring to a 25-mL plastic tube. The cell suspension was then centrifuged at 300 g for 5 mins at 4 °C. The cells were further washed twice with PBS (−) and twice with 2% FBS in PBS (−). After final washing, the cells were resuspended in 500 μL of 1 μg/mL DAPI in 2% FBS in PBS (−) to stain live cells, then passed through a cell strainer and kept on ice. Mean fluorescence intensity and percentage of Fluor-CoA+ cells in FITC channel were measured by flow cytometry (BD LSRFortessa™ Flow Cytometer, BD Biosciences, San Jose, California) using FSC and SSC detection to gate out debris, and the UV (355 nm) and blue lasers (488 nm) for the detection of DAPI and Fluor-CoA, respectively. Data analysis was performed using FlowJo software (BD Biosciences, San Jose, California).

4.12   Spheroid culture and uptake measurement

For spheroid culture, cell suspensions (50 μL) were seeded into each well (1000 cells/well) of a low-adhesion Prime Surface™ 96-well U-bottom plate (Sumitomo Bakelite Co., Japan) and incubated for 3 d. Cells were then incubated with Fluor-CoA free dye or micelle suspension (50 μL) in medium (final concentration: 0.25 mg Fluor-CoA micelle/mL containing 0.1 mg Fluor-CoA/mL) for 3 h. Cells were then harvested using a pipette and collected into a 25-mL plastic tube. Washing and analysis were performed as above.

For confocal imaging, spheroids were also incubated with NucSpot® 650 (Biotium, cat. # 40082) as nuclear stain (1 μL/mL suspension) and Verapamil HCl as efflux pump inhibitor (1 μL/mL suspension) in addition to Fluor-CoA free

dye or micelle suspension. After 3 h, cells were then harvested using a pipette and collected into a 25-mL plastic tube. The spheroids were collected by centrifugation at 700 rpm for 3 mins at 4 °C and washed twice with PBS (−) before fixing with 4% paraformaldehyde for 30 mins. After fixing, the spheroids were further washed with PBS (−) before mounting with 90% glycerol in a μ-slide 8-well chambered coverslip (ibidi, cat. # 80826). Images were taken with LSM880 confocal microscope (Carl Zeiss, Oberkochen, Germany) at a magnification of 1.2× using white light, 488- and 633-nm lasers for $\lambda_{excitation}$ of Fluor-CoA and NucSpot® 650, respectively. Z-stack images were taken at 15-μm intervals for U87MG and at 10-μm images for GT1-7. Images were analyzed using Zeiss Zen software, including measurement of spheroid diameters and radial fluorescence profile.

4.13   Statistical analysis

Data are expressed as means ± SD of assays performed at least triplicates. Several statistical analyses were performed using GraphPad version 9: (1) statistical significances were determined Student's t-test (column analysis), one-way ANOVA with Tukey's post-hoc (grouped analysis), or two-way ANOVA and (2) relationships between variables were analyzed using linear and non-linear regression using the same software.

AUTHOR CONTRIBUTIONS

CONFLICTS OF INTEREST

There are no conflicts to declare.

ACKNOWLEDGEMENTS

REFERENCES

1	K. D. Bruce, A. Zsombok and R. H. Eckel, Front. Endocrinol. (Lausanne)., 2017, 8, 1–11.
2	J. A. Hamilton, C. J. Hillard, A. A. Spector and P. A. Watkins, in Journal of Molecular Neuroscience, Springer, 2007, vol. 33, pp. 2–11.
3	E. Currie, A. Schulze, R. Zechner, T. C. Walther and R. V. Farese, Cell Metab., 2013, 18, 153–161.
4	N. Casals, V. Zammit, L. Herrero, R. Fadó, R. Rodríguez-Rodríguez and D. Serra, Prog. Lipid Res., 2016, 61, 134–148.
5	R. Fadó, R. Rodríguez-Rodríguez and N. Casals, Prog. Lipid Res., 2021, 81.
6	I. R. Schlaepfer and M. Joshi, Endocrinol. (United States), 2020, 161.
7	A. Pocai, T. K. T. Lam, S. Obici, R. Gutierrez-Juarez, E. D. Muse, A. Arduini and L. Rossetti, J. Clin. Invest., 2006, 116, 1081–1091.
8	K. Makowski, P. Mera, D. Paredes, L. Herrero, X. Ariza, G. Asins, F. G. Hegardt, J. García and D. Serra, Chirality, 2013, 25, 281–287.
9	S. Obici, Z. Feng, A. Arduini, R. Conti and L. Rossetti, Nat. Med., 2003, 9, 756–761.
10	R. Lage, M. J. Vázquez, L. Varela, A. K. Saha, A. Vidal-Puig, R. Nogueiras, C. Diéguez and M. López, FASEB J., 2010, 24, 2670–2679.

11   A. Cirillo, A. Di Salle, O. Petillo, M. A. B. Melone, G. Grimaldi, A. Bellotti, G. Torelli, M. S. De' Santi, G. Cantatore, A. Marinelli, U. Galderisi and G. Peluso, Cancer Biol. Ther., 2014, 15, 735–41.

12   J. Sperry, M. C. Condro, L. Guo, D. Braas, N. Vanderveer-Harris, K. K. O. Kim, W. B. Pope, A. S. Divakaruni, A. Lai, H. Christofk, M. G. Castro, P. R. Lowenstein, J. E. Le Belle and H. I. Kornblum, iScience, 2020, 23, 101453.

13   G. Petővári, T. Dankó, I. Krencz, Z. Hujber, H. Rajnai, E. Vetlényi, R. Raffay, J. Pápay, A. Jeney and A. Sebestyén, Pathol. Oncol. Res., 2020, 26, 23–33.

14   K. Zaugg, Y. Yao, P. T. Reilly, K. Kannan, R. Kiarash, J. Mason, P. Huang, S. K. Sawyer, B. Fuerth, B. Faubert, T. Kalliomäki, A. Elia, X. Luo, V. Nadeem, D. Bungard, S. Yalavarthi, J. D. Growney, A. Wakeham, Y. Moolani, J. Silvester, A. Y. Ten, W. Bakker, K. Tsuchihara, S. L. Berger, R. P. Hill, R. G. Jones, M. Tsao, M. O. Robinson, C. B. Thompson, G. Pan and T. W. Mak, Genes Dev., 2011, 25, 1041–51.

15   S. M. Ceccarelli, O. Chomienne, M. Gubler and A. Arduini, J. Med. Chem., 2011, 54, 3109–3152.

16   A. Bentebibel, D. Sebastián, L. Herrero, E. López-Viñas, D. Serra, G. Asins, A. Paulino Gómez-Puertas, Fausto G. Hegardt, P. Gómez-Puertas and F. G. Hegardt, Biochemistry, 2006, 45, 4339–4350.

17   P. Mera, A. Bentebibel, E. López-Viñas, A. G. Cordente, C. Gurunathan, D. Sebastián, I. Vázquez, L. Herrero, X. Ariza, P. Gómez-Puertas, G. Asins, D. Serra, J. García and F. G. Hegardt, Biochem. Pharmacol., 2009, 77, 1084–1095.

18   R. Conti, E. Mannucci, P. Pessotto, E. Tassoni, P. Carminati, F. Giannessi and A. Arduini, Diabetes, 2011, 60, 644–651.

19   R. S. O'Connor, L. Guo, S. Ghassemi, N. W. Snyder, A. J. Worth, L. Weng, Y. Kam, B. Philipson, S. Trefely, S. Nunez-Cruz, I. A. Blair, C. H. June and M. C. Milone, Sci. Rep., 2018, 8, 1–9.

20   K. Makowski, P. Mera, J. Ariza, D. Serra, J. Garcia, L. Herrero, M. López and A. Venegas, Rev. Bionatura, 2019, 4, 1–5.

21   A. Gautier and M. J. Hinner, Site-Specific Protein Labeling Methods Protoc., 2015, 1–267.

22   M. C. Cheng, X. H. Qiang and C. M. Du, Chinese Sci. Bull., 2013, 58, 1256–1261.

23   H. Cabral, K. Miyata, K. Osada and K. Kataoka, Chem. Rev., 2018, 118, 6844–6892.

24   A. Harada and K. Kataoka, Polym. J., 2018, 50, 95–100.

25   S. Quader and K. Kataoka, Mol. Ther., 2017, 25, 1501–1513.

26   C. Wang, Q. Chen, Z. Wang and X. Zhang, Angew. Chemie - Int. Ed., 2010, 49, 8612–8615.

27   H. Uchida, K. Miyata, M. Oba, T. Ishii, T. Suma, K. Itaka, N. Nishiyama and K. Kataoka, J. Am. Chem. Soc., 2011, 133, 15524–15532.

28   H. Uchida, K. Itaka, T. Nomoto, T. Ishii, T. Suma, M. Ikegami, K. Miyata, M. Oba, N. Nishiyama and K. Kataoka, J. Am. Chem. Soc., 2014, 136, 12396–12405.

29   C. Y. Lin, F. Perche, M. Ikegami, S. Uchida, K. Kataoka and K. Itaka, J. Control. Release, 2016, 235, 268–275.

30   S. T. Crowley, Y. Fukushima, S. Uchida, K. Kataoka and K. Itaka, Mol. Ther. - Nucleic Acids, 2019, 17, 465–476.

31   H. Helmbrecht, A. Joseph, M. McKenna, M. Zhang and E. Nance, Curr. Opin. Chem. Eng., 2020, 30, 112–119.

32   E. A. Nance, G. F. Woodworth, K. A. Sailor, T.-Y. Shih, Q. Xu, G. Swaminathan, D. Xiang, C. Eberhart and J. Hanes, Sci. Transl. Med., 2012, 4, 149ra119-149ra119.

33   E. Nance, K. Timbie, G. W. Miller, J. Song, C. Louttit, A. L. Klibanov, T. Y. Shih, G. Swaminathan, R. J. Tamargo, G. F. Woodworth, J. Hanes and R. J. Price, J. Control. Release, 2014, 189, 123–132.

34   A. G. Godin, J. A. Varela, Z. Gao, N. Danné, J. P. Dupuis, B. Lounis, L. Groc and L. Cognet, Nat. Nanotechnol., 2017, 12, 238–243.

35   C. Paviolo, F. N. Soria, J. S. Ferreira, A. Lee, L. Groc, E. Bezard and L. Cognet, Methods, 2020, 174, 91–99.

36   C. Curtis, M. McKenna, H. Pontes, D. Toghani, A. Choe and E. Nance, Nanoscale, 2019, 11, 22515–22530.

37   Y. Ma, S. M. Temkin, A. M. Hawkridge, C. Guo, W. Wang, X. Y. Wang and X. Fang, Fatty acid oxidation: An emerging facet of metabolic transformation in cancer, Elsevier B.V., 2018, vol. 435.

38   L. S. Pike, A. L. Smift, N. J. Croteau, D. A. Ferrick and M. Wu, Biochim. Biophys. Acta - Bioenerg., 2011, 1807, 726–734.

39   M. Allen, M. Bjerke, H. Edlund, S. Nelander and B. Westermark, Sci. Transl. Med., 2016, 8, 354re3-354re3.

40   S. Kant, P. Kesarwani, A. Prabhu, S. F. Graham, K. L. Buelow, I. Nakano and P. Chinnaiyan, Cell Death Dis., 2020, 11, 1–13.

41   B. Juraszek, J. Czarnecka-Herok and K. A. Nałęcz, J. Neurochem., 2020, jnc.15124.

42   A. S. Divakaruni, W. Y. Hsieh, L. Minarrieta, T. N. Duong, K. K. O. Kim, B. R. Desousa, A. Y. Andreyev, C. E. Bowman, K. Caradonna, B. P. Dranka, D. A. Ferrick, M. Liesa, L. Stiles, G. W. Rogers, D. Braas, T. P. Ciaraldi, M. J. Wolfgang, T. Sparwasser, L. Berod, S. J. Bensinger and A. N. Murphy, Cell Metab., 2018, 28, 490-503.e7.

43   Y. Arai, H. Ishii, M. Kobayashi and H. Ozawa, J. Physiol. Sci., 2017, 67, 313–323.

44   B. Taïb, K. Bouyakdan, C. Hryhorczuk, D. Rodaros, S. Fulton and T. Alquier, J. Biol. Chem., 2013, 288, 37216–37229.

45   A. C. Hunter, Adv. Drug Deliv. Rev., 2006, 58, 1523–1531.

46   S. J. Choi, F. Kim, M. W. Schwartz and B. E. Wisse, Am. J. Physiol. Metab., 2010, 298, E1122–E1130.

47   J. F. Mir, S. Zagmutt, M. P. Lichtenstein, J. García-Villoria, M. Weber, A. Gracia, G. Fabriàs, J. Casas, M. López, N. Casals, A. Ribes, C. Suñol, L. Herrero and D. Serra, Mol. Neurobiol., 2018, 55, 7216–7228.

48   H. Lin, S. Patel, V. S. Affeck, I. Wilson, D. M. Turnbull, A. R. Joshi, R. Maxwell, E. A. Stoll, V. S. Affleck, I. Wilson, D. M. Turnbull, A. R. Joshi, R. Maxwell and E. A. Stoll, Neuro. Oncol., 2017, 19, 43–54.

49   L. Mo, L. Hou, D. Guo, X. Xiao, P. Mao and X. Yang, Int. J. Pharm., 2012, 436, 815–824.

50   J. M. Rabanel, P. A. Piec, S. Landri, S. A. Patten and C. Ramassamy, J. Control. Release, 2020, 328, 679–695.

51   R. Vadivelu, H. Kamble, M. Shiddiky and N.-T. Nguyen, Micromachines, 2017, 8, 94.

52   A. Tchoryk, V. Taresco, R. H. Argent, M. Ashford, P. R. Gellert, S. Stolnik, A. Grabowska and M. C. Garnett, Bioconjug. Chem., 2019, 30, 1371–1384.

53   J. Garcia-Chica, W. K. D. Paraiso, S. Tanabe, D. Serra, L. Herrero, N. Casals, J. Garcia, X. Ariza, S. Quader and R. Rodriguez-Rodriguez, Nanomedicine (Lond)., 2020, 15, 1617–1636.

54   S. Quader, H. Cabral, Y. Mochida, T. Ishii, X. Liu, K. Toh, H. Kinoh, Y. Miura, N. Nishiyama and K. Kataoka, J. Control. Release, 2014, 188, 67–77.

55   New England Biolabs Inc., Reaction Conditions for Chemical Coupling with CoA-SH (S9352S), https://international.neb.com/protocols/2012/08/09/reaction-conditions-for-chemical-coupling-with-coa-sh-s9352s, (accessed 11 May 2020).

56   M. I. Malandrino, R. Fucho, M. Weber, M. Calderon-Dominguez, J. F. Mir, L. Valcarcel, X. Escoté, M. Gómez-Serrano, B. Peral, L. Salvadó, S. Fernández-Veledo,

SUPPLEMENTARY INFORMATION

OUTLINE

Synthesis Procedure

1.   Synthesis of C75

4-Benzyl-3-(trans-2-octyl-5-oxotetrahydrofuran-3-carbonyl)oxazolidin-2-one
[**4** and **5**]. Compound (±)-**3** (1.000 g, 4 mmol) was added to a round-bottom flask. Anhydrous THF (45.6 mL) was added under N_2 atmosphere. The solution

was cooled to -78 °C. Triethylamine (0.59 mL, 4.23 mmol) and pivaloyl chloride (0.52 mL, 4.22 mmol) were added. The solution was stirred for 1 h at 0 °C and then cooled down to -78 °C. In parallel, (*S*)-4-benzyl-2-oxazolidinone (700 mg, 4 mmol) was added to a round-bottom flask, anhydrous THF (9.4 mL) was added under N_2 atmosphere, and the solution was cooled to -78 °C. 2M BuLi in hexane (2.0 mL, 4 mmol) was slowly added to the (*S*)-4-benzyl-2-oxazolidinone solution. The (*S*)-4-benzyl-2-oxazolidinone solution was transferred to the compound (±)-**3** solution by using a cannula. The mixture was stirred for 15 minutes at -78 °C and then 30 minutes at 0 °C. The reaction was quenched with a saturated aqueous NH_4Cl solution (35 mL). The organic phase was washed with brine, and dried over $MgSO_4$, filtered and evaporated under reduced pressure. After a column chromatography with silica gel using CH_2Cl_2 as eluent, compounds **4** (0.703 g, 1.75 mmol, 44%) and **5** (0.778 g, 1.93 mmol, 48%) were obtained.

Compound [**4**]: white solid; $[\alpha]_D$ = +82.3 (*c* 1.0, $CHCl_3$); ^{1}H-NMR (400 MHz, $CDCl_3$): δ 7.39 – 7.27 (m, 3H), 7.18 (m, 2H), 4.80 (m, 1H), 4.71 (m, 1H), 4.34 – 4.21 (m, 2H), 4.21 – 4.08 (m, 1H), 3.26 (dd, *J* = 13.4, 3.4 Hz, 1H), 3.00 (dd, *J* = 17.6, 9.4 Hz, 1H), 2.83 (dd, *J* = 13.4, 9.3 Hz, 1H), 2.71 (dd, *J* = 17.6, 7.0 Hz, 1H), 1.69 (m, 2H), 1.60 – 1.16 (m, 12H), 0.88 (t, *J* = 6.9 Hz, 3H). ^{13}C-NMR (101 MHz, $CDCl_3$): δ 174.3, 171.1, 153.0, 134.6, 129.3, 129.1, 127.6, 81.5, 66.7, 55.2, 45.0, 37.7, 35.1, 32.5, 31.8, 29.3, 29.2, 29.1, 25.3, 22.6, 14.1.

Compound [**5**]: white solid; $[\alpha]_D$ = +24.8 (*c* 1.0, $CHCl_3$); ^{1}H-NMR (400 MHz, $CDCl_3$): δ 7.47 – 7.09 (m, 5H), 4.71 (m, 2H), 4.37 – 4.23 (m, 2H), 4.24 – 4.14 (m, 1H), 3.26 (dd, *J* = 13.5, 3.3 Hz, 1H), 2.96 – 2.71 (m, 3H), 1.87 – 1.62 (m, 2H), 1.63 – 1.12 (m, 12H), 0.88 (t, *J* = 6.8 Hz, 3H). ^{13}C-NMR (101 MHz, $CDCl_3$): δ 174.5, 171.2, 153.1, 134.5, 129.4, 129.0, 127.6, 82.1, 66.7, 55.2, 44.9, 37.8, 35.1, 31.9, 31.8, 29.4, 29.2, 29.1, 25.3, 22.6, 14.1.

(+)-Trans-2-octyl-5-oxotetrahydrofuran-3-carboxylic acid [(+)-**3**]. Compound **4** (1.918 g, 4.76 mmol) was added to a round-bottom flask with a THF/H_2O 1:1

solution (175 mL) and the solution was cooled to 0 °C. H_2O_2 30% w/w (4.3 mL, 41.8 mmol) and LiOH (0.238 g, 9.93 mmol) were added. The solution was stirred for 3 h at 0 °C and then 30 minutes at RT. Aqueous Na_2SO_3 15% w/w (25.2 mL) was added, and then the mixture was basified with NaOH 1N. Solvent was evaporated under reduced pressure. The aqueous solution was washed with CH_2Cl_2 (5×80 mL) and acidified to pH=1 with concentrated HCl. The solution was stirred overnight at RT. The aqueous solution was extracted with CH_2Cl_2 (4×80 mL). The combined organic layer was washed with brine, dried over $MgSO_4$, filtered and evaporated under reduced pressure. Compound (+)-**3** (1.070 g, 4.34 mmol, 91%) was obtained.

Compound [(+)-**3**]: white solid; $[\alpha]_D$ = +33.4 (*c* 1.0, MeOH); ^{1}H-NMR (400 MHz, $CDCl_3$) δ 4.62 (td, *J* = 7.5, 4.8 Hz, 1H), 3.18 – 3.04 (m, 1H), 2.94 (dd, *J* = 17.8, 8.5 Hz, 1H), 2.82 (dd, *J* = 17.8, 9.6 Hz, 1H), 1.90 – 1.62 (m, 2H), 1.62 – 1.15 (m, 12H), 0.88 (t, *J* = 6.9 Hz, 3H).

(−)-Trans-2-octyl-5-oxotetrahydrofuran-3-carboxylic acid [(−)-**3**]. Compound **5** (2.078 g, 5.17 mmol) was added to a round-bottom flask with a THF/H_2O 1:1 solution (250 mL) and the solution was cooled to 0 °C. H_2O_2 30% w/w (5.3 mL, 51.9 mmol) and LiOH (0.28 g, 11.69 mmol) were added. The solution was stirred for 3 h at 0 °C and then 30 minutes at RT. Aqueous Na_2SO_3 15% w/w (31 mL) was added, and then the mixture was basified with NaOH 1N. Solvent was evaporated under reduced pressure. The aqueous solution was washed with CH_2Cl_2 (5×100 mL) and acidified to pH=1 with concentrated HCl. The solution was stirred overnight at RT. The aqueous solution was extracted with CH_2Cl_2 (4×100 mL). The combined organic layer was washed with brine, dried over $MgSO_4$, filtered and evaporated under reduced pressure. Compound (−)-**3** (1.22 g, 4.95 mmol, 95%) was obtained.

Compound [(−)-**3**]: white solid; $[\alpha]_D$ = −40.0 (*c* 1.0, MeOH); ^{1}H-NMR (400 MHz, $CDCl_3$): δ 4.62 (td, *J* = 7.5, 4.7 Hz, 1H), 3.16 – 3.04 (m, 1H), 2.94 (dd, *J* = 17.9,

8.5 Hz, 1H), 2.82 (dd, *J* = 17.9, 9.6 Hz, 1H), 1.90 – 1.62 (m, 2H), 1.58 – 1.15 (m, 12H), 0.88 (t, *J* = 6.9 Hz, 2H).

(2R,3S)-4-Methylene-2-octyl-5-oxotetrahydrofuran-3-carboxylic acid   [(+)-C75]. Compound (**+**)-**3** (0.300 g, 1.21 mmol) was added to a round-bottom flask. Under N_2 atmosphere, 2.0 M MMC in DMF (20 mL, 0.04 mmol) was added. The mixture was stirred for 48 h at 135 °C. The mixture was cooled to RT. HCl 6M (30 ml) cooled to 0 °C was added slowly while stirring. A dark solid was formed, and it dissolved slowly upon addition of the HCl 6M solution. CH_2Cl_2 (30 mL) was added, and the aqueous phase was extracted with CH_2Cl_2 (2×15 mL). The combined organic layer was dried over $MgSO_4$, filtered and evaporated under reduced pressure at RT. A fresh solution of acetic acid (3 mL), formol (2.25 mL), *N*-methylaniline (0.78 mL) and AcONa (90 mg) was prepared, and this solution (4.4 mL) was added to the reaction mixture. The mixture was stirred for 1 h 45 minutes at RT. A 10:1 solution of brine/concentrated HCl (15 mL) was added. CH_2Cl_2 (20 mL) was added, and the mixture was extracted with CH_2Cl_2 (3×10 mL). The combined organic layer was washed with LiCl 5% (2×12.5 mL), 0.02N HCl (2×12.5 mL), and H_2O (3×15 mL). The organic phase was then stirred for 5 min at RT with a saturated solution of $NaHCO_3$ (20 mL). The aqueous phase was acidified to pH=1 with concentrated HCl. The aqueous solution was extracted with CH_2Cl_2 (4×15 mL). The combined organic layer was dried over $MgSO_4$, filtered and evaporated under reduced pressure. (+)-C75 (0.237 g, 0.93 mmol, 76%) was obtained.

Compound [(+)-**C75**]: white solid [α]$_D$ = +11.4 (*c* 1.0, CHCl₃); ^{1}H NMR (CDCl₃, 400 MHz): δ 6.46 (d, *J* = 3.0 Hz, 1H), 6.02 (d, *J* = 2.7 Hz, 1H), 4.81 (td, *J* = 7.2, 5.6 Hz, 1H), 3.63 (dt, *J* = 5.6, 2.8 Hz, 1H), 1.79 – 1.67 (m, 2H) , 1.53 – 1.20 (m, 12H), 0.88 (t, *J* = 6.9 Hz, 3H).

(2S,3R)-4-Methylene-2-octyl-5-oxotetrahydrofuran-3-carboxylic acid   [(−)-C75]. Compound (**−**)-**3** (0.600 g, 2.43 mmol) was added to a round-bottom flask. Under N_2 atmosphere, 2.0 M MMC in DMF (40 mL, 0.08 mmol) was

added. The mixture was stirred for 48 h at 135 °C. The mixture was cooled to RT. HCl 6M 60 mL) cooled to 0 °C was added slowly while stirring. A dark solid was formed, and it dissolved slowly upon addition of the HCl 6M solution. CH_2Cl_2 (50 mL) was added, and the aqueous phase was extracted with CH_2Cl_2 (2×30 mL). The combined organic layer was dried over $MgSO_4$, filtered and evaporated under reduced pressure at RT. A fresh solution of acetic acid (6.25 mL), formol (4.68 mL), N-methylaniline (1.63 mL) and AcONa (187.5 mg) was prepared, and this solution (8.75 mL) was added to the reaction mixture. The mixture was stirred for 1 h 45 minutes at RT. A 10:1 solution of brine/concentrated HCl (30 mL) was added. CH_2Cl_2 (37.5 mL) was added, and the mixture was extracted with CH_2Cl_2 (3×20 mL). The combined organic layer was washed with LiCl 5% (2×25 mL), 0.02N HCl (2×25 mL), and H_2O (3×30 mL). The organic phase was then stirred for 5 min at RT with a saturated solution of $NaHCO_3$ (35 mL). The aqueous phase was acidified to pH=1 with concentrated HCl. The aqueous solution was extracted with CH_2Cl_2 (4×20 mL). The combined organic layer was dried over $MgSO_4$, filtered and evaporated under reduced pressure. (±)-C75 (0.455 g, 1.78 mmol, 73%) was obtained.

Compound [(–)-**C75**]: white solid; $[\alpha]_D$ = –11.4 (c 1.0, $CHCl_3$); ^{1}H NMR ($CDCl_3$, 400 MHz): δ 6.46 (d, J = 3.0 Hz, 1H), 6.02 (d, J = 2.7 Hz, 1H), 4.81 (dt, J = 7.2, 5.6 Hz, 1H), 3.63 (dt, J = 5.6, 2.8 Hz, 1H), 1.79 – 1.67 (m, 2H), 1.53 – 1.20 (m, 12H), 0.88 (t, J = 6.9 Hz, 3H).
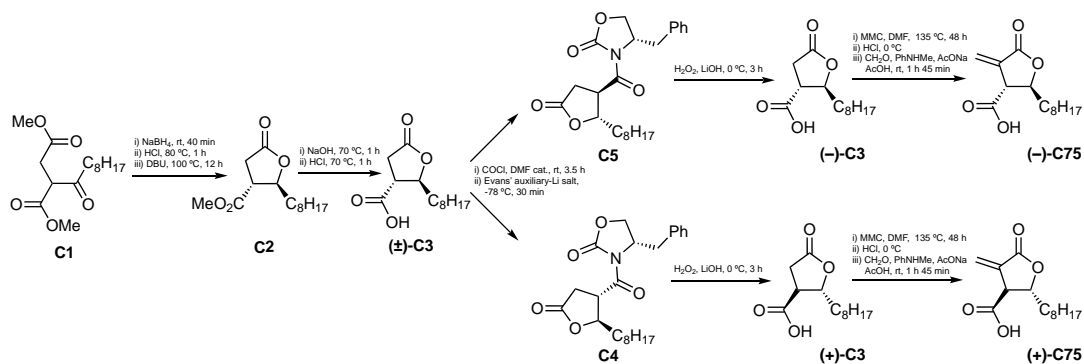

Figure S1. The enantioselective synthesis of the two enantiomers of C75.

Synthesis of (±)-C75-CoA: For ^{1}H NMR confirmation: Coenzyme A (HSCoA) sodium salt hydrate (8.6mg), and $Na_3PO_4 \cdot 12H_2O$ (7.6mg) were added to a solution of (±)-C75 (2.5mg) in D_2O (0.8ml) in an NMR tube as previously reported[1]. ^{1}H NMR was recorded on a JEOL ECS 400 (400 MHz) spectrometer (JOEL Ltd., Tokyo Japan) and chemical shift was calculated as parts per million (ppm). Data was processed using MestReNova version 14.2.1-27684. For micelle preparation and biological assays, the reaction was carried out in 90 mM Na_3PO_4 and left at RT overnight. The same procedure was performed to synthesize (+)-C75-CoA and (−)-C75-CoA. HPLC analysis (LC-2000 series, JASCO, Tokyo, Japan) was performed to confirm whether all (±)-C75 was consumed in the reaction. Conditions include: C-18 RP-column (TSKgel ODS-100V 5μm particle size, 4.6 mm I.D. × 15 cm, TOSOH Bioscience, cat. # 21455), mobile phase 7:3 100 mM phosphate buffer pH 3/acetonitrile, flow rate 1.2 mL/minute, 259-nm detection.

2. Synthesis of PEG-PAsp(DET)

The diblock co-polymer was prepared by aminolysis of CH_3O-PEG-*b*-poly(β-benzyl-L-aspartate) (PEG-PBLA). PEG-PBLA was synthesized by anionic ring-opening polymerization of BLA-NCA initiated from the terminal –NH_2 group of CH_3O-PEG-NH_2 [2]. CH_3O-PEG-NH_2 (MW 12,000 Da) and BLA-NCA were dissolved in distilled DCM-DMF (10:1), mixed, and allowed to react in Ar atmosphere for 72 h. After which, the polymer is precipitated, washed in 2:3 ethyl acetate-hexane three times, and collected by vacuum filtration. Complete drying was performed *in vacuo*.
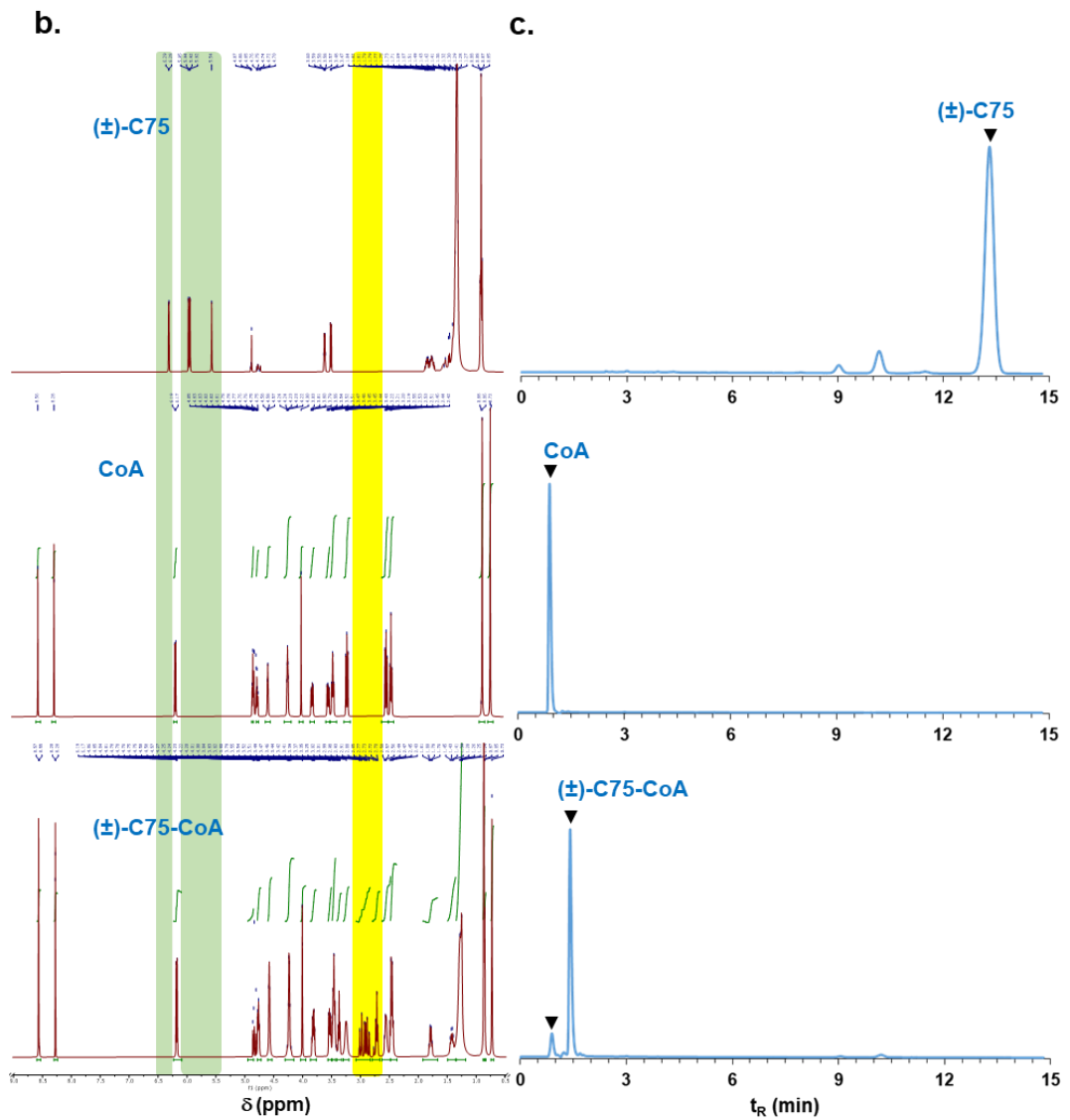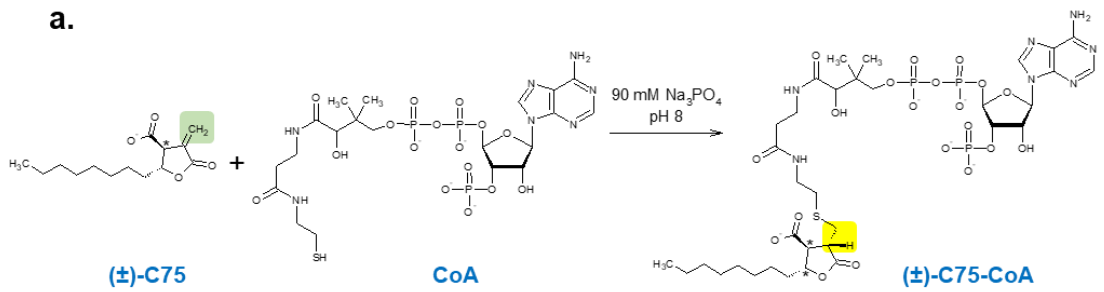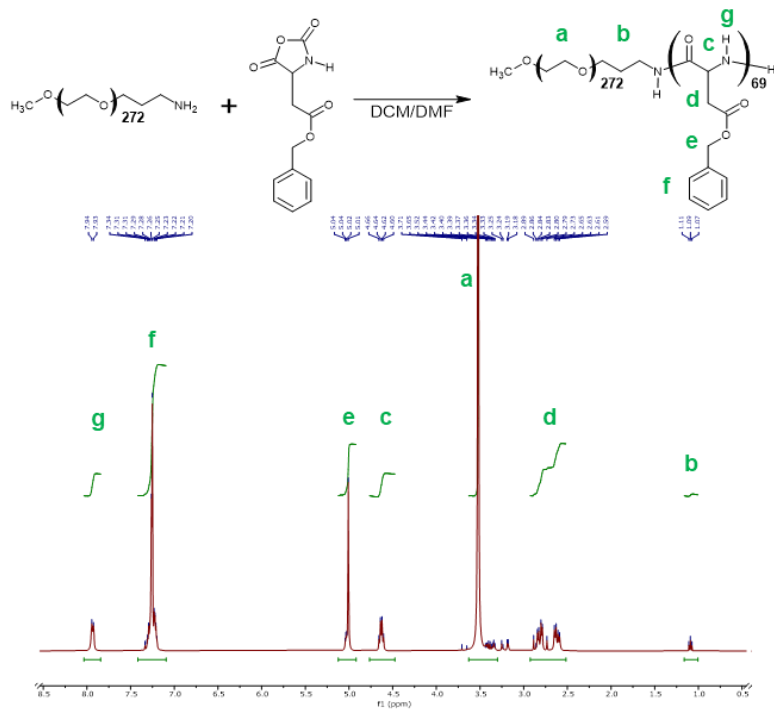
a.

(±)-C75   CoA   90 mM Na₃PO₄ pH 8   (±)-C75-CoA

b.

(±)-C75

CoA

(±)-C75-CoA

δ (ppm)

c.

(±)-C75

CoA

(±)-C75-CoA

t_R (min)

- 112 -

Figure S2 (previous page). Synthesis of (±)-C75-CoA (a), which involves the nucleophilic addition to the α,β-unsaturation of (±)-C75 by the thiol group of coenzyme A (CoA), to form (±)-C75-CoA. In the ^{1}H-NMR measurements (b), geminal alkene protons in (±)-C75 were highlighted in green while newly formed C-H bonds in (±)-C75-CoA were highlighted in yellow. HPLC profiles (c) of the starting materials were compared with that of the product.

Aminolysis of PEG-PBLA was carried out as previously reported[3,4]. Briefly, 150 mg freeze-dried PEG-PBLA was dissolved in 15 mL distilled NMP and cooled to 0 °C. In another reaction tube, distilled DET (4.7 mL, 100 times the molar equivalence of benzyl ester units) was mixed with NMP and cooled to 0 °C. PEG-PBLA in NMP solution was then added dropwise over 1 minute to the DET solution. The reaction was allowed to proceed in ice over 1 h reaction. After which, the polymer was added dropwise to 5 N aqueous HCl (34.1 mL, 1.3 × equivalent to the added 1° and 2° amine groups of DET) at <5 °C. The resulting acidified mixture was afterwards dialyzed (MWCO: 6,000–8,000) at 4 °C against a 0.01 N HCl 3-4 × and then against deionized water 2 ×. The final solution was freeze-dried to obtain PEG-PAsp(DET). Gel permeation chromatography (LC-2000 series, JASCO, Tokyo, Japan) was carried out using a Superdex™ 200 Increase 10/300GL (Cytiva, 28-9909-44, column L × I.D. 30 cm × 10 mm, 8.6 μm particle size) 10 mM CH_3COOH in 500 mM NaCl, 0.5 mL/min. ^{1}H NMR was recorded on a JEOL ECS 400 (400 MHz) spectrometer (JOEL Ltd., Tokyo Japan) and chemical shift was calculated as parts per million (ppm). Data was processed using MestReNova version 14.2.1-27684.

a.

b.

a.

b.

c.

A/C Ratio	% weight	
	Polymer	Drug
5 : 1	19.80%	80.20%
4 : 1	23.58%	76.42%
3 : 1	29.15%	70.85%
2 : 1	38.17%	61.83%
1 : 1	55.25%	44.75%
1 : 2	71.17%	28.83%
1 : 3	78.74%	21.26%
1 : 4	83.16%	16.84%
1 : 5	86.06%	13.94%

Figure S4. Physicochemical properties of (±)-C75-CoA micelles prepared in different anion/cation (A/C) ratios including size (a) and polydispersity (b). Experiments were performed in triplicate (values expressed in mean ± SD). Polydisperse size profiles are marked with Ψ. Table showing % by weight of micelle components at different A/C ratios (c).

a.

b.
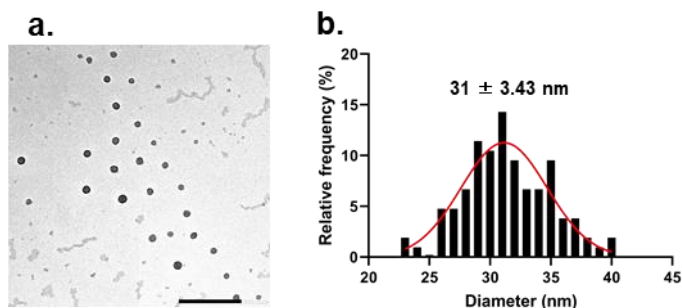
Figure S5. Transmission electron microscopy (TEM) image of (±)-C75-CoA micelle (a) and its size distribution profile (value expressed in mean ± SD, n = 105) (b). Scale bar = 100 µm, magnification 40×.
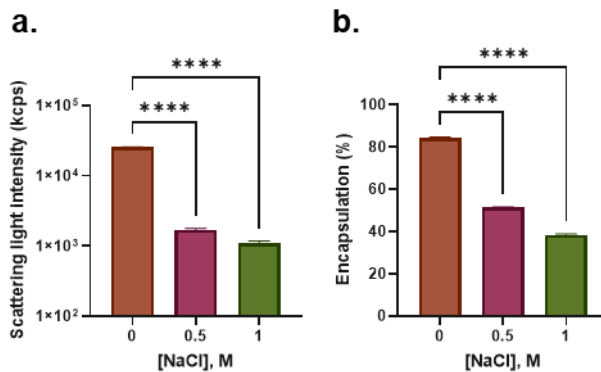
Figure S6. Changes in scattering light intensity (SLI) (a) and encapsulation (%) (b) of (±)-C75-CoA micelle (a) upon mixing with high NaCl concentration solutions. Experiments were performed in triplicate (values expressed in mean ± SD) and comparison of means among treatment groups were done using ANOVA (with Tukey's test as post-hoc analysis; **** $p < 0.0001$).

Figure S7. Microscopic images of U87MG and GT1-7 cells after treatment with FAO inhibitors. Scale bar = 100 μm, magnification 40×.

Figure S9. Microscopic images and analysis of cellular uptake of Fluor-CoA micelles in U87MG and GT1-7 spheroids. Representative U87MG and GT1-7 spheroid microscopic images (a) with scale bar = 100 μm, magnification 1.2×, nucleus (blue), Fluor-CoA (yellow) fluorescence signals are shown. Spheroid diameters in x and y dimensions (n = 10) were measured using Zen Zeiss software.

REFERENCES:

1   K. Makowski, P. Mera, D. Paredes, L. Herrero, X. Ariza, G. Asins, F. G. Hegardt, J. García and D. Serra, Chirality, 2013, 25, 281–287.

2   K. Kataoka, T. Matsumoto, M. Yokoyama, T. Okano, Y. Sakurai, S. Fukushima, K. Okamoto and

G. S. Kwon, J. Control. Release, 2000, 64, 143–153.

3   H. Uchida, K. Miyata, M. Oba, T. Ishii, T. Suma, K. Itaka, N. Nishiyama and K. Kataoka, J. Am. Chem. Soc., 2011, 133, 15524–15532.

4   H. Uchida, K. Itaka, T. Nomoto, T. Ishii, T. Suma, M. Ikegami, K. Miyata, M. Oba, N. Nishiyama and K. Kataoka, J. Am. Chem. Soc., 2014, 136, 12396–12405.

CHAPTER 2

Nanomedicine targeting brain lipid metabolism as a feasible approach for controlling energy balance

Objectives 2 and 4.

Article summary

This article is the continuation of the research presented in the previous article. In this manuscript, we focused in the application of C75-CoA loaded micelles for obesity, where the effects of C75-CoA micelles *in vitro* appear to be more adequate. Therefore, we focused on validating the effects of C75-CoA micelles in the hypothalamus, specifically on feeding, body weight and peripheral metabolism. The goal of this work is to develop C75-CoA-loaded PIC micelles that can be used for *in vivo* inhibition of hypothalamic CPT1A.

To achieve this goal, a new PIC micelle, with higher *in vivo* performance compared to the micelles used in the first article, was designed that could withstand the ionic strength of physiological fluids. A combination of a PEG-PAsp(Aldehyde)-Plys and PEG-PAsp(Hydrazide) polymers produces a C75-CoA micelle with a covalent bond between the polymers, allowing much more stability without major changes in size, morphology and surface properties.

Mice were injected via ICV with C75, C75-CoA or C75-CoA crosslinked micelle after a 3h fasting, and the effects of these treatments on food intake and body weight along 22h were evaluated. Subsequently, after treatment with the same conditions, another group of mice were sacrificed after 2.5h and brain and peripheral tissues were harvested. Hypothalamus, liver and BAT were processed for gene expression of hunger-related neuropeptides, peripheral energy metabolism and thermogenesis, respectively. Some brains were collected and sliced for c-FOS immunofluorescence to assess neuronal activity in relevant hypothalamic nuclei.

C75-CoA crosslinked micelles produced a stronger reduction in food intake and body weight than free C75 and C75-CoA. Furthermore, this reduction was paired to an increase in the anorexigenic POMC neuropeptide and a decrease in the orexigenic NPY. Peripherally, the micelle treatment produced and

increase in gluconeogenesis and FAO markers, consistent with a satiating effect, as well as an increase in BAT thermogenesis markers. The micelle treatment was also shown to produce an increase in PVN neuronal activity, but not ARC neuronal activity, compared to C75-CoA.

In summary, the developed C75-CoA-loaded micelle was suitable for *in vivo* experiments and was able to reduce body weight and food intake via modulation of hunger-related neuropeptides, and neuronal activation of the PVN. These effects were paired with a peripheral increase of gluconeogenesis, FAO and BAT thermogenesis markers.

Graphical abstract
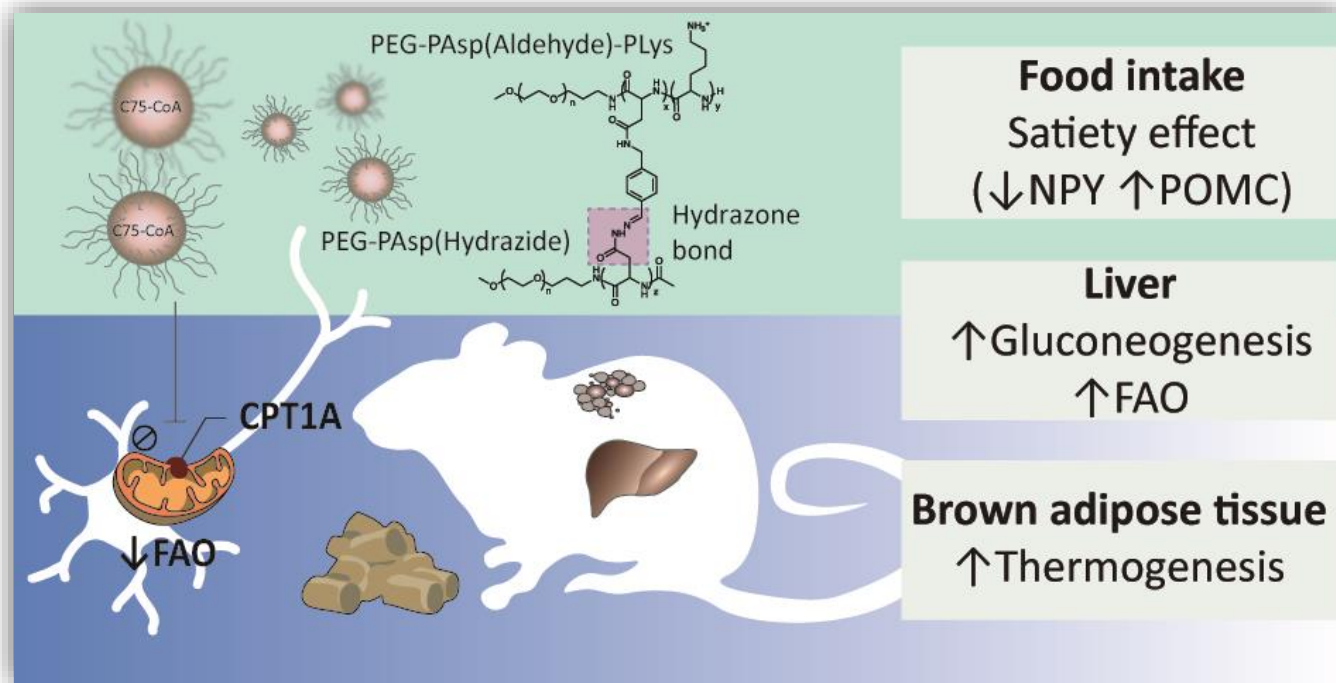
Figure 10. Graphical abstract for the second publication. New peptides with crosslinking ability were used to produce more stable, suitable for *in vivo* micelles. These micelles were used to treat mice and elicited a satiety effect through change in the expression of hunger neuropeptides, as well as increased FAO and gluconeogenesis in liver and increase thermogenesis in BAT.

Nanomedicine targeting brain lipid metabolism as a feasible approach for controlling energy balance

Jesús Garcia-Chica[a†], West Kristian Dizon Paraiso [b†‡], Sebastián Zagmutt[a], Anna Fosch[a], Ana Cristina Reguera[a], Sara Alzina[a], Laura Sánchez-García[a], Shigeto Fukushima[b], Kazuko Toh[b], Núria Casals[a] , Dolors Serra[cd], Laura Herrero[cd], Jordi Garcia[ce], Kazunori Kataoka[b], Xavier Ariza[ce], Sabina Quader[b]* and Rosalía Rodríguez-Rodríguez [ac]*

a.Basic Sciences Department, Faculty of Medicine and Health Sciences, Universitat Internacional de Catalunya (UIC), Sant Cugat del Vallès, E-08195 Spain.

b.Innovation Center of Nanomedicine, Kawasaki Institute of Industrial Promotion, Kawasaki, Kanagawa 210-0821 Japan

c.Centro de Investigación Biomédica en Red de Fisiopatología de la Obesidad y la Nutrición (CIBEROBN), Instituto de Salud Carlos III, Madrid, E-28029 Spain.

d.Department of Biochemistry and Physiology, School of Pharmacy and Food Sciences, Institut de Biomedicina de la Universitat de Barcelona (IBUB), Universitat de Barcelona, Barcelona, E-08028 Spain.

e.Department of Inorganic and Organic Chemistry, Faculty of Chemistry, Institut de Biomedicina de la Universitat de Barcelona (IBUB), Universitat de Barcelona (UB), Barcelona, E-08028 Spain.

ABSTRACT

Targeting brain lipid metabolism is a promising strategy to regulate energy balance and fight metabolic diseases such as obesity. The development of a stable platform for selective delivery of drugs, particularly to the hypothalamus is a challenge but a possible solution for these metabolic diseases. Attenuating fatty acid oxidation in the hypothalamus via CPT1A inhibition leads to satiety, but this target is difficult to reach *in vivo* with the current drugs. We propose using an advanced crosslinked polymeric micelle-type nanomedicine that can stably load the CPT1A inhibitor C75-CoA for *in vivo* control of energy balance. Central administration of the nanomedicine induced a rapid attenuation of food intake and body weight in mice via regulation of appetite-related neuropeptides and neuronal activation of specific hypothalamic regions driving chances in the liver and adipose tissue. This nanomedicine targeting the brain lipid metabolism was successful in the modulation of food intake and peripheral metabolism in mice.

New Concepts

Effective treatments to control feeding, body weight, and glucose homeostasis in metabolic diseases such as obesity or diabetes are insufficient, due to the difficulty of reaching specific brain targets that are in charge of energy balance. Here, we present the first nanomedicine acting on a brain target to drive a rapid modulation of food intake and peripheral metabolism, offering an innovative approach to managing metabolic diseases. The core-crosslinked polymeric micelle-based nanomedicine used in this investigation allows the encapsulation of a drug that modifies lipid metabolism in the brain, a target hard to reach

with conventional formulations. This investigation might contribute developing and validation a new generation of nanomedicine-based approaches targeting brain lipid metabolism to modulate feeding and body weight. Also, the nanomedicine highlights the significance of nanotechnology beyond the current biological applications, and facilitates understanding of the early stages of energy balance (i.e., acute satiating actions) that are crucial for developing complex diseases such as obesity and diabetes.

1. Introduction

Metabolic disorders such as obesity imply a disruption in energy homeostasis, leading to an imbalance between food intake and energy expenditure [1]. Despite major advances in understanding the pathogenesis and therapeutics of these metabolic disorders, the prevalence of obesity and type 2 diabetes continues to rise [2,3]. Against this backdrop, these metabolic diseases are still unmet medical needs and require the development of new therapeutic platforms.

The physiological control of energy balance is tightly modulated by the central nervous system (CNS), where the hypothalamus is the most critical area implicated [4,5]. Hypothalamic nuclei are sensitive to nutrients and hormones, and modify the expression, secretion, and activity of specific neurotransmitters and neuromodulators, resulting in changes in food intake, energy expenditure, and the function of key peripheral tissues such as the liver and adipose tissue [4,6,7]. Strong evidence suggests that lipid metabolism within the hypothalamus is a key signal of nutrient status further to modulate feeding behaviour and peripheral metabolism [8-10]. In particular, fatty acid (FA) sensing in hypothalamic neurons via accumulation of FAs or FA metabolites acts as a satiety signal and may decrease food intake and hepatic function [1,11].

A crucial target in brain lipid metabolism which controls energy balance is carnitine palmitoyl-transferase 1A (CPT1A) [12]. It is located in the mitochondria and promotes the entry of long-chain FAs for β-oxidation [13-16]. Since CPT1A is highly expressed in central and peripheral tissues, its regulatory potential in the energy balance is based on two different interventions: in peripheral tissues (i.e., liver and adipose tissue), overexpression of CPT1A and induction of fatty acid oxidation (FAO) ameliorates insulin resistance and prevents body weight gain [17,18], whereas in the CNS, CPT1A inhibition reduces food intake and body weight [19,20]. Particularly, in the arcuate (ARC) nucleus of the hypothalamus, genetic ablation of CPT1A prevents FAO, leading to a local accumulation of long-chain FAs which in turn mediates the action of several feeding-related hormones to inhibit food intake in lean rats [21]. Thus, selective inhibition of CPT1A in the hypothalamus, but not in the peripheral tissues, is a promising strategy for the management of metabolic disorders involving a disruption in energy balance. However, brain lipid metabolism is difficult to impact *in vivo* with the current formulations and drug.

(±)-C75 is a well-known CPT1A inhibitor that is converted to its active coenzyme A (CoA) form in the hypothalamus [22]. Although initially identified as a fatty acid synthase (FAS) inhibitor with a strong anorectic effect via malonyl-CoA accumulation [23-25], enantioselective synthesis of C75 revealed that the (+)-C75 and (±)-C75-CoA adducts were the active forms inhibiting CPT1A [22,26]. Therefore, to avoid the off-target effect on FAS and undesired actions in the periphery, it is crucial to deliver (±)-C75-CoA directly into the brain for CPT1A inhibition and energy balance regulation. A major challenge of (±)-C75-CoA as cargo is that it is a small, polar, and negatively-charged molecule, with low permeability across the cellular membrane. (±)-C75-CoA interacts with polycations through a combination of electrostatic and hydrophobic

interactions, as it possesses both phosphate and carboxylate groups, as well as an aliphatic side chain [27]. We used this particular property in designing a poly-ion complex (PIC) micelle, a polymeric formulation that allows for a direct and specific cellular transport of (±)-C75-CoA, demonstrating an efficient inhibition of CPT1A-dependent lipid metabolism in cellular models of neurons and glioma cells [28]. In the present study, we have developed a more robust core-crosslinked polymeric micelle (PM)-type nanomedicine, with a high entrapment efficiency of the specific CPT1A inhibitor (±)-C75-CoA (Fig.1). This crosslinked PM has proven to be useful for *in vivo* applications, showing an effective biological activity upon delivery of the CPT1A inhibitor in brain cells after intracerebroventricular (ICV) administration, particularly to neurons. In addition, central administration of this (±)-C75-CoA-loaded core-crosslinked PM induced a substantial reduction regulation of appetite-related neuropeptides, neuronal activation of specific regions and altered expression of metabolic biomarkers in peripheral tissues (**Fig.1**). This investigation led to the first nanomedicine targeting brain lipid metabolism which effectively modulated energy intake and peripheral tissue metabolism.

2. Results and discussion

2.1 Stability of crosslinked PM loading (±)-C75-CoA and uptake in neuronal cell lines

In this study we synthesized a triblock co-polymer using sequential *N*-carboxyanhydride (NCA) polymerization with polyethylene glycol (PEG) as a hydrophilic shell forming block, a poly(L-aspartamide) (PAsp) middle block functionalized via orthogonal side-chain modification with an aromatic aldehyde moiety (PAsp(Aldehyde)), and a poly(L-lysine) (PLys) cationic block
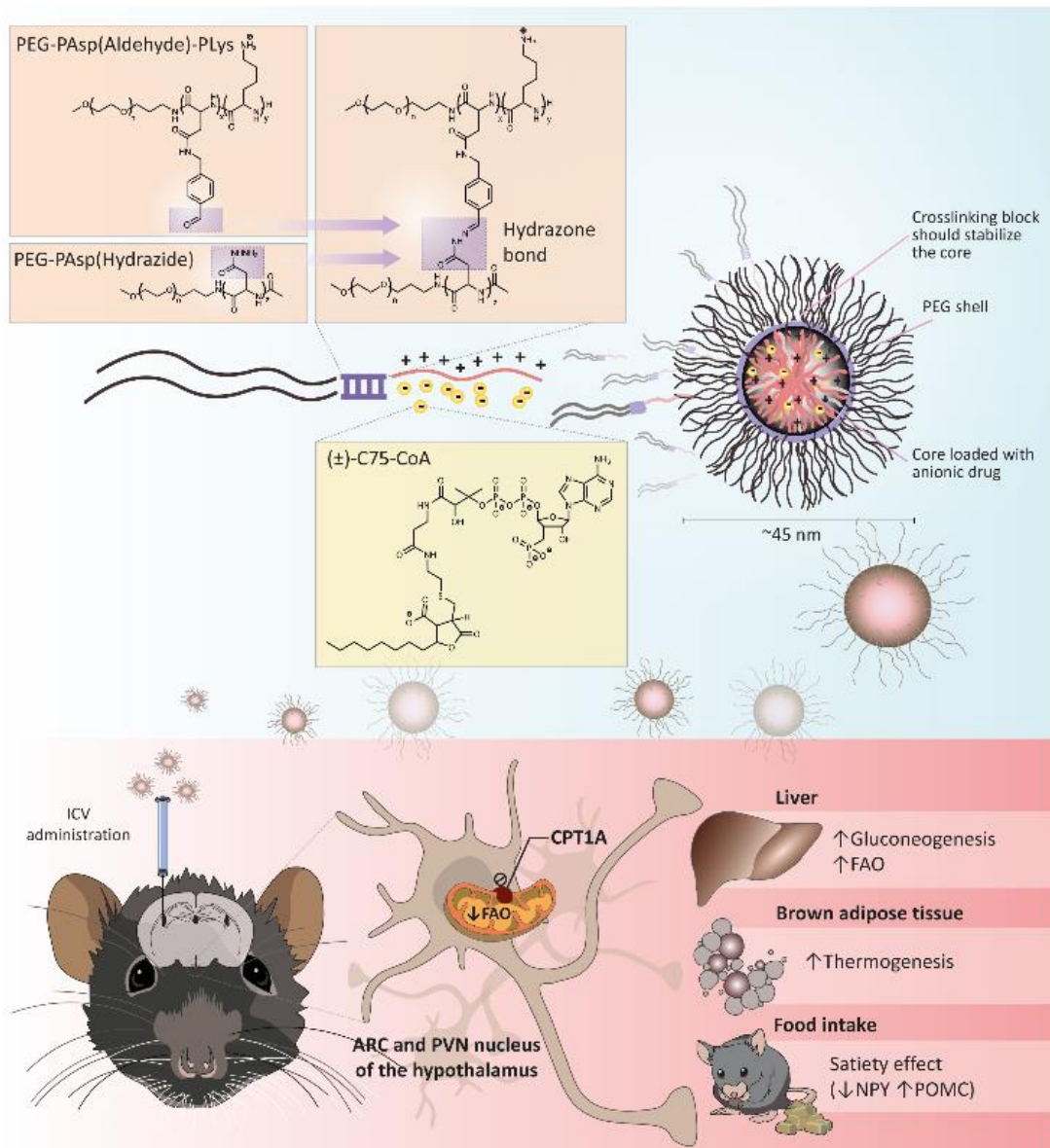
Figure 1. Schematic representation of the core-crosslinked polymeric micelle (PM)-type nanomedicine encapsulating the CPT1A inhibitor (±)-C75-CoA, and the effects of central administration of the nanomedicine in food intake, liver and brown fat metabolism via arcuate (ARC) and paraventricular (PVN) nucleus of the hypothalamus.

designed to form a PIC with (±)-C75-CoA (**Fig. 2**). Solutions of (±)-C75-CoA and

PEG-PAsp(Aldehyde)-PLys were combined in a 1:1 anion/cation ratio, defined
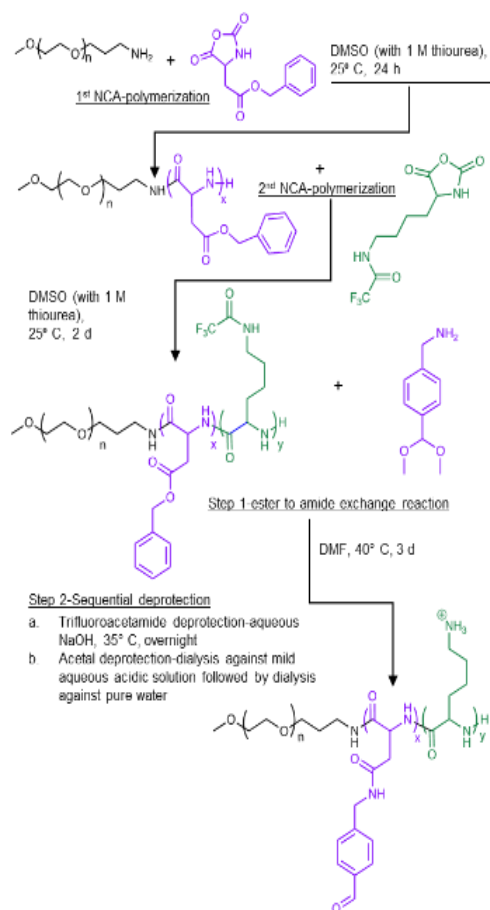
Figure 2. Preparation of the triblock polymer, PEG-PAsp(Aldehyde)-Plys.

as the ratio between the overall anionic charge imparted by the phosphate and carboxylate groups in (±)-C75-CoA and the overall cationic charge given by the protonated amines in the polymer. A PEG-PAsp diblock co-polymer functionalized with hydrazide groups (PEG-PAsp(Hydrazide)) was added to the micelle to crosslink the aldehyde-containing PEG-PAsp(Aldehyde)-PLys through hydrazone formation (**Fig. 1**). This aromatic aldehyde and hydrazide derived reversible hydrazone bonds [29,30] formed in the copolymer middle block provided increased protection and stability to the micelle by tightening the core and preventing premature release of the cargo (**Fig. 1**). (±)-C75-CoA and PEG-PAsp(Aldehyde)-PLys were mixed in pH 7.4 10 mM phosphate buffer that

spontaneously self-assembled to form core-shell structured PM. To crosslink the PM, PEG-PAsp(Hydrazide) was added in molar equivalence of hydrazide to the aldehyde functionality (**Fig. 1**). Upon filtration, both non-crosslinked and crosslinked PM gave monodisperse size profiles of around 40-45 nm hydrodynamic diameter by dynamic light scattering (DLS) measurement (**Fig. 3A; Supplementary Table S1, ESI§**). In comparison, the average core size of PMs was found to be c.a. 20 nm by transmission electron microscopy (TEM), which is smaller than the hydrodynamic diameter since the latter accounts for the PEG shell of the micelle (**Fig. S1, ESI§**). It is worth signifying that the middle block strengthens the micelle core even without crosslinking, possibly by providing hydrophobicity [31]. The polymer mixtures only (without (±)-C75-CoA) provided large aggregates, confirming that the cargo has a profound influence in producing well-defined PM-type structures that can be evident from the TEM images (**Fig. S1, ESI§**).

To confirm the advantages of the middle block, we prepared micelles from a PEG-PLys diblock copolymer (**Fig. S2A, ESI§**). We then added a polyanion (sodium dextran sulfate; DSS) to confirm the ionic interaction between the anionic cargo and the cationic PLys chain. Micelle dissociation with the increase of DSS concentration was observed for the diblock PM, evident by the drastic reduction of light scattering intensity, but for that of the triblock PM the impact of DSS addition was minimal (**Fig. S2B, ESI§**). A core-crosslinked PM prepared from PEG-PAsp(Aldehyde)-PLys triblock and PEG-PAsp(Hydrazide) diblock co-polymer incorporating crosslinking to hydrophobicity is expected to

Figure 3. Physicochemical characterization of the crosslinked polymeric micelles (PM) loading (±)-C75-CoA or Fluor-CoA and validation in neuronal cell lines. (A) Size profile of (±)-C75-CoA-PM. (B) Fluorescence emission spectra of FRET double-labelled (±)-C75-CoA-PM and mixed polymers. (C-E) Physicochemical properties of micelles in phosphate buffer (PB) and NaCl solution: (C) Hydrodynamic size, (D) Polydispersity, and (E) Scattered light intensity of non-crosslinked versus crosslinked PM.

give even higher stability. To confirm the participation of these two polymers in micellar assembly and subsequent interaction, we labelled the PEG-PAsp(Aldehyde)-PLys polymer with rhodamine and PEG-PAsp(Hydrazide) with fluorescein on their N-termini. When the labelled polymers are used to form PM with (±)-C75-CoA, we observed Förster resonance energy transfer (FRET) upon scanning the emitted light at 450-nm excitation (**Fig. 3B**), corroborating that they were associated in the PM core. The FRET profile of crosslinked PM was not altered with the addition of 1 M NaCl. However, upon adding DSS, signal intensity from the rhodamine-labelled polymer was reduced to 60%, which indicated that (±)-C75-CoA plays a significant role in the association of two polymers, as evidenced by FRET pairing. To further confirm whether (±)-C75-CoA was necessary for their increased interaction of the FRET-paired polymers, the FRET spectrum of a mixture of the two labelled polymers was measured. This led to similar FRET properties as that of the DSS-treated PM. However, when the FRET-paired polymers were mixed without (±)-C75-CoA and then treated with DSS, a residual FRET signal was observed. This suggests that there was still some form of interaction between the two polymers despite the release/absence of the (±)-C75-CoA cargo, possibly through covalent (hydrazone) bonds and other forces of attraction.

To check micellar stability in salt solution, we added 1 M NaCl to the PM solution. This led to a 15-nm increase in size for both type of micelles (**Fig. 3C**), however, the non-crosslinked PM gave an apparently more polydisperse size profile with a statistical decrease in scattered light intensity (**Fig. 3D-E**). The results attested to the PIC nature of the PM. PIC formation is mainly driven by the liberation of counterions [23] which is prompted when the PLys block and

anionic (±)-C75-CoA paired up, leading to a large entropic gain. The increased NaCl concentration apparently reduced this entropic gain, which resulted in PIC destabilization. This data provides additional evidence that the crosslinked PM is more stable than the non-crosslinked PM.

To test their differing effects on biological systems, we measured ATP synthesis of GT1-7 mouse hypothalamic neurons after short-term incubation with the PMs. This is an indirect approach to measure mitochondria fatty acid oxidation and CPT1A inhibition by the drug [28] (**Fig. 3F**). The crosslinked PM statistically reduced cellular ATP production to 41%, as compared to non-crosslinked PM (73%) and free (±)-C75-CoA (87%) (**Fig. 3F**). Moderation of ATP synthesis in *in vitro* neurons in response to PM treatment indicates inhibition of FAO, in agreement with previous data [28,33], and this attenuation was significantly higher compared to the non-crosslinked PM. Crosslinked PM exhibited higher apparent encapsulation of (±)-C75-CoA compared to non-crosslinked PM in both pH 7.4 phosphate buffer (PB) and artificial cerebrospinal fluid (aCSF) (**Fig. S3, ESI§**), with the latter mimicking conditions in the brain. Since more (±)-C75-CoA was entrapped in the crosslinked PM, it was expected to enter the cell more efficiently in contrast to the non-crosslinked PM.

To track its cellular uptake, we prepared PMs from a fluorescent derivative of CoA, Fluor-CoA [28], with a size profile similar to (±)-C75-CoA-PM (Fig. S4A, ESI§). Upon incubation with GT1-7 neuronal cells for 30 min, we observed that there was an evidently higher cellular uptake of Fluor-CoA-loaded crosslinked PM (4× that of free dye) as compared with the non-crosslinked PM (3× compared to free dye) (**Fig. 3G**). This points to another reason why the crosslinked PM has a greater ATP inhibitory effect compared to the non-crosslinked counterpart. Fluor-CoA was also released in cell culture medium or aCSF to a

lesser extent by the crosslinked PM (**Fig. S4C-D, ESI§**), despite both non-crosslinked and crosslinked PM having similar encapsulation rates (**Fig. S4B, ESI§**). In neuronal cells, the fluorescent tracer of the micelle showed endo-lysosomal entrapment, that was not appreciated in the mitochondria (**Fig. S5, ESI§**).

The increased stability of the crosslinked PM ensured a higher (±)-C75-CoA encapsulation rate, an enhanced ATP inhibitory capacity, and increased cellular uptake of fluorescein when using Fluor-CoA-loaded PM. This cellular uptake was also confirmed *in vivo*, since brain slices revealed fluorescent staining of the tracer of the crosslinked PM, particularly in the hypothalamic area, after ICV infusion of the nanomedicine (**Fig. S6, ESI§**).

Altogether, the formulation presented here, which is based on a specially designed triblock copolymer platform, allowed for remarkable stability better suited for *in vivo* applications when matched with the non-crosslinked PM. This could be explained by: i) increased hydrophobicity of the polymer, which enabled a better interaction with (±)-C75-CoA and ii) crosslinking of the two polymers through hydrazone formation. The polymer PEG chain (M_W 12 KDa) was important in imparting the measured physicochemical properties and decreasing aggregation tendency [32].

2.2 (±)-C75-CoA-loaded core crosslinked PMs induced a rapid attenuation of food intake and body weight and regulated the expression of hypothalamic neuropeptides

A major finding of this investigation is the remarkable acute effect of the central administration of the nanomedicine in feeding and body weight, with improvements in these actions compared to the free drug (±)-C75. In these

experiments, age-matched mice were administered ICV injections of vehicle, (±)-C75, (±)-C75-CoA, and (±)-C75-CoA-loaded core crosslinked PMs (from here on will be designated as (±)-C75-CoA-PM). Food intake and body weight were then monitored for 24 h (**Fig. 4A**). This timing is in agreement with previous studies monitoring the acute satiating effects of new therapeutics in lean rodent models [13,34,35]. Mice treated with (±)-C75-CoA-PM exhibited a substantial and rapid reduction of food intake in comparison to (±)-C75-CoA-, (±)-C75- and vehicle-treated mice (**Fig. 4B**). The satiating effect of (±)-C75-CoA-PM was appreciated after 1 h, being statistically different 4 h post-treatment versus the vehicle and free drugs. This action was maintained throughout the experiment (24 h) (**Fig. 4B**). In line with this result, body weight change measured at 24 h post-treatment was also significantly reduced in (±)-C75-CoA-PM-treated mice when evaluated against the control group (**Fig. 4C**). These acute effects on energy balance in lean mice are very promising and comparable to the satiating action of CPT1A inhibition after short timings (2 to 24h) in lean rodents using drug- or genetic-based approaches [21,23,36]. In agreement with the observed rapid effects on feeding, it has been reported that levels of malonyl-CoA, when elevated in the brain and particularly in the hypothalamus in response to energy surplus or glucose overload, induce a rapid inhibition of CPT1A leading to food intake reduction, and these changes appear very rapidly (from minutes to a few hours) [16,37].

Since alteration of brain CPT1A and malonyl-CoA levels is known to modify the expression of hunger-related neuropeptides in the hypothalamus [36], we measured the mRNA expression of these neuropeptides. Once released by different neuronal populations in the ARC nucleus of the hypothalamus, the following peptides exert opposing effects on feeding and metabolism: the neuropeptide Y (NPY) and agouti-gene related protein (AgRP) are orexigenic neuropeptides whereas the precursor protein, proopiomelanocortin (POMC),

is a signal to induce satiety and body weight attenuation [38,39]. For this analysis, hypothalamic extracts of mice were collected 2.5 h after treatment with vehicle, free drug or PM. These timings were based on previous studies altering malonyl-CoA levels and CPT1A activity in the hypothalamus, showing very rapid changes in the expression of these neuropeptides (2-3 hours post central inhibition of the target and lipid metabolism) [13,40]. While free (±)-C75-CoA was able to attenuate mRNA levels of the orexigenic neuropeptide NPY, (±)-C75-CoA-PM induced not only a significant reduction of NPY (**Fig. 4D**), but also upregulation of the anorexigenic neuropeptide POMC compared to vehicle (**Fig. 4E**). However, no changes were appreciated in the mRNA levels of AgRP in response to either free drug or PM (**Fig. 4F**).

Despite our results being too preliminary to discard important side effects in patients with metabolic diseases, the present results are promising in terms of toxicity. In particular, analysis of microglia activation by Iba1 immunofluorescence in different regions of the hypothalamus revealed no activation of microglia after ICV infusion of the nanomedicine, indicating the low toxic potential of the formulation in the inflammatory response at the timing and dose tested in mice (**Fig. S7, ESI§**). Subsequent investigations using more selective targeting-based approaches to a specific type of neurons and after longer periods of administration to analyse feeding behaviour, must be envisaged.

These data suggest that the nanomedicine (±)-C75-CoA-PM was more efficient in reducing body weight and food intake compared to the free drug and that the appetite-suppressing effect could be explained through the modulation of hunger-related neuropeptides in the hypothalamus, particularly the upregulation of POMC and the downregulation of NPY. The main satiety signal in the brain which led to changes in the expression of neuropeptides meant that there was a local accumulation of long-chain fatty acyl-CoAs in the

hypothalamus in response to FAO and CPT1A inhibition, indicating nutrient overload, as previously reported [9,21].

2.3 (±)-C75-CoA-PM modified liver and brown fat metabolism

The hunger-related hypothalamic neuropeptides released in the ARC nucleus connect to second order neurons located in other hypothalamic nuclei to control energy balance, not only in terms of satiety, but also in terms of liver and adipose tissue metabolism [41-43]. Therefore, the effect of central administration of the drug in the free form or PM form was also investigated in these primary metabolically active tissues. Particularly, markers of glycolysis, gluconeogenesis, and FAO were assayed in the liver (Fig. 5A), while markers of thermogenesis were measured in brown adipose tissue (BAT) (Fig. 5B) 2.5 h post-ICV injection of either vehicle, free drug, or PM.

In the liver, gluconeogenesis (PEPCK) and FAO (CPT1A) mRNA markers were significantly elevated by (±)-C75-CoA-PM in comparison to free drug or vehicle with no accompanying changes in the last stage of glucose production (G6Pase), which is consistent with a response to a satiating effect (Fig. 5A). In line with this, the expression of the pyruvate kinase liver isoform (PKL), a regulator of pyruvate production, remained unchanged by (±)-C75-CoA but was significantly reduced by (±)-C75-CoA-PM, supporting the idea that the nanomedicine is promoting FAO and initial stages of gluconeogenesis, but not pyruvate, to provide energy fuel to extrahepatic tissues in response to the satiating actions. Analysis of genes related to thermogenesis in BAT, which contributes to energy expenditure and body weight regulation [44], revealed a significant induction of the expression of several genes involved in BAT thermogenesis activation, probably contributing to energy expenditure and body weight loss after this treatment. In contrast, the free drug was not able to modify the expression of the genes under study (Fig. 5B).
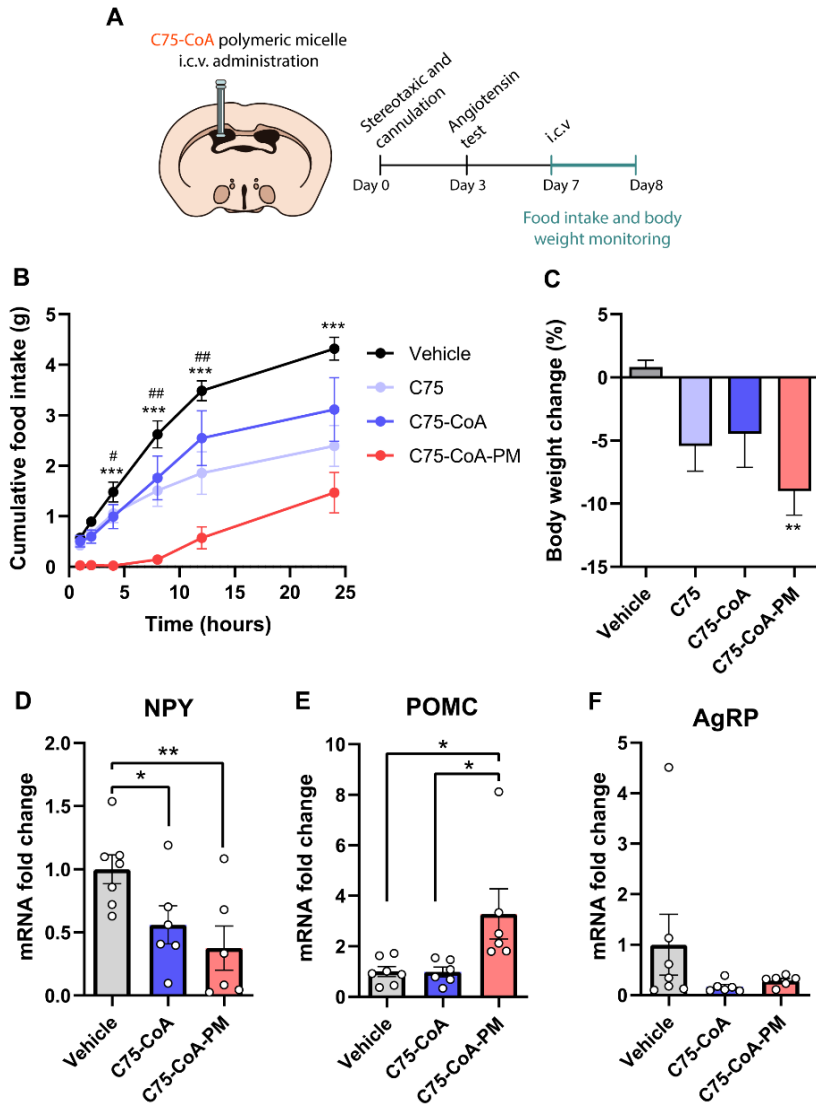
Figure 4. ICV administration of (±)-C75-CoA polymeric micelles (PM) rapidly reduced food intake and body weight in mice by regulating the expression of hypothalamic neuropeptides. (A) Diagram indicating the experimental protocol of surgery, administration and monitoring. (B) Cumulative food intake at different timings (***p<0.001 vs (±)-C75-CoA-PM; #p<0.05, ##p<0.01 vs (±)-C75-CoA) and (C) body weight change in mice after 24 h of central administration of vehicle, free drug or the nanomedicine ((±)-C75-CoA-PM) (**p<0.01 vs vehicle). (D-F) mRNA levels of the hypothalamic neuropeptides (D) NPY (orexigenic and energy expenditure inhibitor), (E) POMC (anorexigenic and energy expenditure activator) and (F) AgRP (orexigenic and energy expenditure inhibitor), 2.5 h post-injection (*p<0.05, **p<0.01). Data are expressed as mean ± SD (n=6-8), means were compared using one-way ANOVA with Tukey's post-hoc test.

Taken together, these results demonstrate that central administration of (±)-C75-CoA-PM led to transcriptional changes in metabolically active tissues in the periphery, such as the liver and BAT, whereas the expression of these markers remained unaffected in free (±)-C75-CoA-treated mice.

2.4 (±)-C75-CoA-PM activated neurons in specific hypothalamic nuclei

In order to assess the activation of neurons in different areas of the hypothalamus in response to free or nanomedicine (±)-C75-CoA, c-FOS immunostaining (a proto-oncogene expressed within neurons following depolarization, indicating neuronal activity) was explored in the hypothalamus. This analysis was performed in ARC and paraventricular nucleus (PVN), two major hypothalamic nuclei involved in feeding behavior, liver metabolism and thermogenesis [41,42]. The number of c-FOS positive cells was statistically increased in the PVN of (±)-C75-CoA-PM-injected mice as compared to those treated with vehicle, whereas no changes were appreciated in mice treated with (±)-C75-CoA (Fig. 6A and 6B). However, analysis in the ARC revealed a lower level of neuronal activation in mice treated with (±)-C75-CoA versus vehicle, whereas (±)-C75-CoA-PM-treated mice showed a partial restoration of this activation in parallel to the free drug (Fig. 6C and 6D).

The differential neuronal activation patterns in the hypothalamic nuclei PVN and ARC in response to the treatments can be explained by the remarkable satiating action and metabolic changes induced by (±)-C75-CoA-PM. Particularly, c-FOS measurements indicated that the nanomedicine could be initiating the following events: i) stimulation of anorexigenic POMC neurons in the ARC, which led to ii) activation of the PVN, which drove satiating effects, and iii) triggering changes in liver metabolism and BAT thermogenesis to regulate body weight (Fig. 6E). These observations are consistent with the
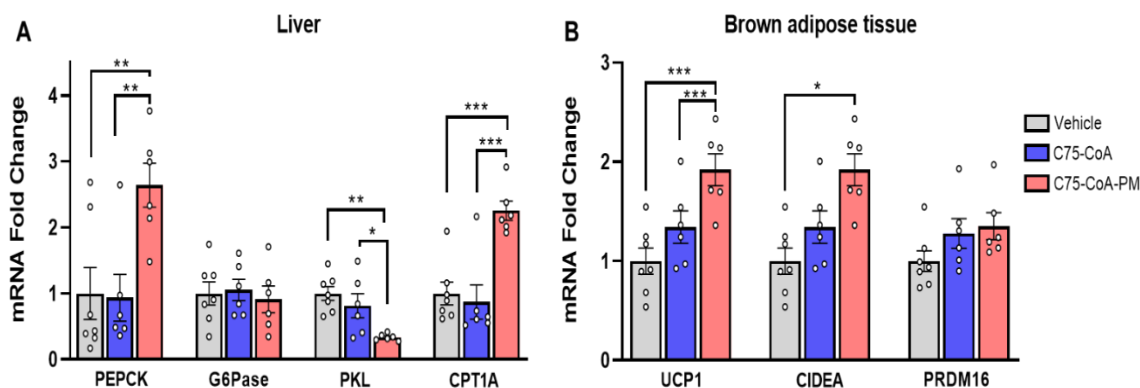
Figure 5. ICV administration of (±)-C75-CoA polymeric micelles (PM) modifies metabolic pathways in liver and brown adipose tissue (BAT). (A) Liver mRNA levels of genes involved in gluconeogenesis, glycolysis and fatty acid oxidation. (B) BAT mRNA levels of genes involved in thermogenesis activation. Tissues were collected 2.5 h post-injection of vehicle, free (±)-C75-CoA or (±)-C75-CoA-PM. Data are expressed as mean ± SD (n=6-8), means were compared using one-way ANOVA with Tukey's post-hoc test, *$p<0.05$, **$p<0.01$, ***$p<0.001$.

changes in the expression of neuropeptides POMC and NPY observed with the nanomedicine but not with the free drug. These in turn connect with the PVN neurons and regulate not only feeding, but also peripheral tissue metabolism. This ARC-PVN signal controlling the liver metabolism and BAT thermogenesis activation has been previously reported in response to other stimuli [45,47].

In contrast, the free (±)-C75-CoA did not induce neuronal activation in PVN but reduced c-FOS in the ARC (Fig. 6E), the latter being related to a reduction of NPY-expressing neurons contributing to the satiating effect of the free drug. The lack of neuronal activation in the PVN could explain the fact that the free drug did not reduce body weight nor alter the expression of genes related to liver metabolism and BAT thermogenesis. The differences observed between the nanomedicine and the free drug in the expression of hypothalamic neuropeptides, neuronal activation and in turn peripheral metabolism could also be related to the higher degree of uptake shown by the nanomedicine in neurons compared to the free cargo in cell cultures and the capacity of the

nanomedicine to reach hypothalamic areas regulating energy balance (Fig. S6, ESI§).

3. Conclusion

In this study, we have developed an inventive core crosslinked micelle-based approach to successfully encapsulate and centrally deliver a CPT1A inhibitor, to acutely regulate energy balance in mice. The effective delivery and higher neuronal uptake of the drug was evidenced in the potent and rapid satiating effect and significant body weight loss induced by central administration of (±)-C75-CoA-PM in mice, as well as in the substantial regulation of appetite-related hypothalamic neuropeptides and neuronal activation of PVN, which were not observed in response to free (±)-C75-CoA treatment. Altogether, the present study showcases the first nanomedicine targeting brain lipid metabolism, offering an innovative and selective therapeutic approach for treating diseases related to a dysregulation of energy balance such as obesity and diabetes. The findings of this study are expected to contribute to the corroboration and advancement of the novel prospect of nanomedicine-based approaches to modulate body weight and feeding by targeting brain lipid metabolism. Most significantly, the current study highlights the enormous potential of nanotechnology in healthcare, leading the way for a better understanding of energy balance in the early stages of obesity and diabetes that are crucial for understanding the developmental stages of these pathological conditions and thus finding an effective cure.
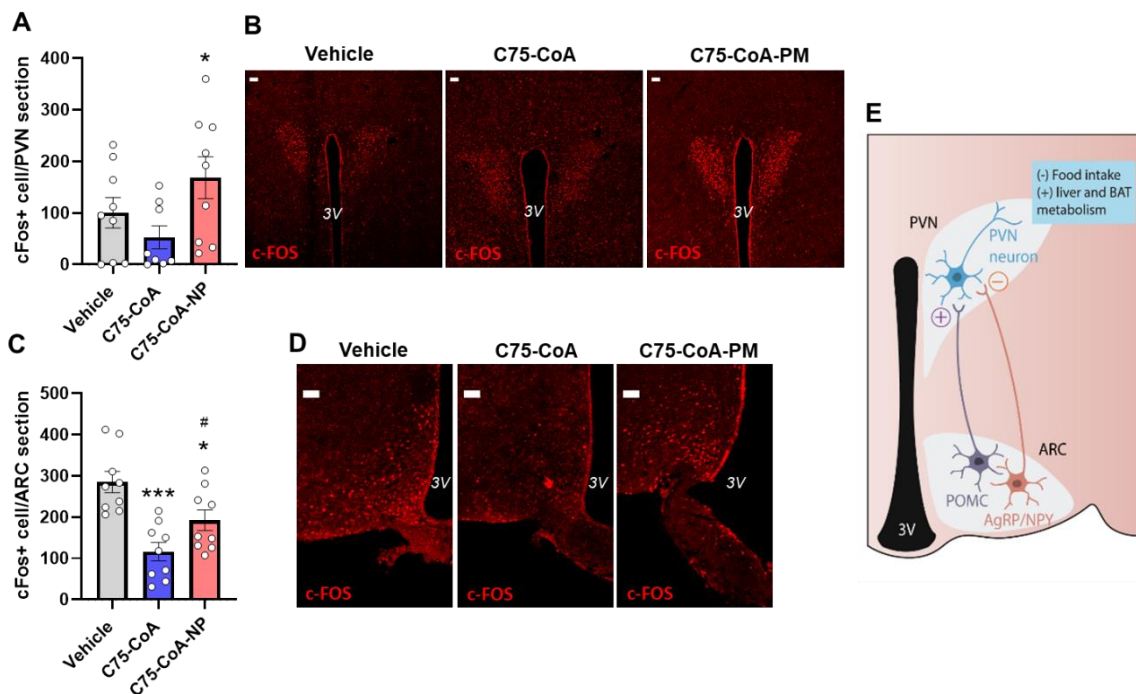
Figure 6. Neuronal activation in ARC and PVN hypothalamic nuclei by ICV administration of (±)-C75-CoA polymeric micelles (PM). (A) Quantification and (B) representative confocal images showing c-FOS positive cells in the PVN section. (C) Quantification and (D) representative confocal images showing c-FOS positive cells in the ARC section. (E) Schematic representation of ARC and PVN nuclei and the main type of neurons regulating energy balance. POMC activates PVN neurons leading to anti-obesity actions whereas NPY neurons lead to PVN inhibitory signal to promote feeding and body weight gain. Animals were perfused and brains collected 2 h post-injection of vehicle, free (±)-C75-CoA or (±)-C75-CoA-PM. Scale bars, 50 μm. Data are expressed as mean ± SD (3 animals, 3 slices/animal). Means

4. Experimental section

4.1 Preparation of the polymers and crosslinked micelles

4.1.1 Synthesis of triblock copolymer, PEG-PBLA-PLys(TFA). The synthesis of the triblock co-polymer, PEG–PBLA–PLys(TFA), was carried out by *N*-carboxyanhydride (NCA) ring-opening polymerization (ROP), as previously reported [56,57] but with modifications (Fig. 2). The initiator in the first ROP step was α-methoxy-ω-amino-poly(ethylene glycol) (M_w 12 KDa; PEG–NH$_2$, NOF,

Japan), to produce the PEG–poly(β-benzyl-L-aspartate) diblock copolymer (PEG–PBLA). PEG–NH$_2$ was dried overnight *in vacuo* and dissolved in distilled and dehydrated DMF (Wako Pure Chemical Industries, Japan). BLA–NCA (24 molar equivalence to PEG-NH$_2$) and thiourea (equivalent to 1M solution in DMF) added to the PEG–NH$_2$ solution as dry powder under inert atmosphere. The mixture was left to stir at 25 °C for 24 h. The resulting reaction mixture was dialyzed against water and the PEG-PBLA-NH$_2$ di-block polymer was recovered by freeze-drying. The freeze-dried di-block polymer was dissolved in dichloromethane and dropped in a mixture of *n*-hexane and ethyl acetate (6:4), followed by filtration of the precipitated polymer, and drying under vacuum. The degree of polymerization was found to be 22 BLA units by ^{1}H NMR. The obtained PEG-PBLA-NH$_2$ was subsequently used as initiator for the second ROP of Lys(TFA)–NCA to obtain PEG–PBLA–PLys(TFA). PEG-PBLA-NH$_2$ was) was dried overnight *in vacuo* and subsequently dissolved in distilled and dehydrated DMSO. Lys(TFA)–NCA (44 molar equivalence to PEG-PBLA-NH$_2$) along with thiourea (equivalent to 1 M solution in DMF) was introduced to the PEG-PBLA-NH$_2$ solution as a dry powder under Ar atmosphere, where the mixture was left to react at 25 °C for 48 h. The resulting reaction mixture was dialyzed against water and the PEG–PBLA–PLys(TFA) triblock polymer was recovered by freeze-drying. The freeze-dried triblock polymer was dissolved in methanol and subjected to diethyl ether precipitation and then finally drying *in vacuo*. For characterization purpose, an aliquot of the polymer was subjected to alkali-hydrolysis to remove the benzyl esters and TFA groups furnishing a water-soluble form of the triblock (PEG–PAsp–PLys) polymer. Upon ^{1}H NMR analysis of this PEG–PAsp–PLys polymer it was revealed that 40 units of lysine residues were added with 22 units of aspartate (Fig. S8A, ESI§). Gel Permeation Chromatography (GPC) analysis (Jasco HPLC system equipped with RI detector) confirmed (Fig. S8A, ESI§) that the polymer, PEG–PAsp–Plys,

has narrow and unimodal distribution of molecular weight (molecular weight distribution, M_w/M_n: 1.02).

4.1.2 Middle-block modification of PEG-PBLA-PLys(TFA) and subsequent sequential deprotection.

PEG–PBLA–PLys(TFA) was dissolved in anhydrous DMF (Sigma-Aldrich, cat. # 227056-100ML) to which an aromatic aminoacetal linker, 1-[4-(dimethoxymethyl)phenyl]methanamine (Enamine Ltd, (Kyiv, Ukraine) (30 eq) was added. The reaction mixture was stirred at 40 °C for 72 h. After which, deprotection of the PLys(TFA) chain was carried out by adding 3 mL of methanol and 100 µL of 5 N NaOH. The reaction was allowed to proceed overnight. The mixture was then dialyzed against 0.02 N HCl (3×) and water (2×) for 48 h using a 8 kDa molecular weight cut off (MWCO) dialysis bag (Spectra/Por, Spectrum Laboratories, cat. # 25223-650). The solution was freeze-dried under vacuum to obtain the modified triblock co-polymer (PEG-PAsp(Aldehyde)-PLys). ^{1}H NMR analysis confirmed the introduction of benzaldehyde groups onto the triblock polymer (Fig. S8B, ESI§).

4.1.3 Preparation of PEG-PAsp(Hydrazide) and PEG-PLys.

The synthesis of PEG-PBLA and its hydrazinolysis was carried out as previously reported [58]. While PEG-PLys was prepared similar to prior work [59]. Preparation of labelled polymers and FRET micelles is detailed in the supplementary information (ESI§).

4.1.4 Micelle preparation.

The crosslinked PM was formed by automatic self-assembly of polymers with the anionic drug cargo plus the hydrazone bond-formation between the polymers. Polymer solutions were each dispersed in 10 mM phosphate buffer (PB) pH 5.0 at 10 mg/mL concentration. The solutions were simply mixed with 36.87 mM (±)-(±)-C75-CoA or 7.88 mM Fluor-CoA (preparations of which were fully described in our previous work [28]) to attain a 1:1 anion/cation ratio, diluted with 10 mM PB pH 7.4 to desired

concentration, and then vortexed. The micelle was allowed to cross-link at 4 °C for 24 h before passing through a 0.22-µM syringe filter (Millex 13mm Durapore, Merck, cat. # SLGVJ13SL). The characterization of micelles is indicated in the supplementary information (ESI§).

4.2 Mice cannulation and administration of drugs and polymeric micelles

The protocols for animal care and use were approved by the Ethics and Research Committee at the University of Barcelona (Procedure ref. 10906 from the Generalitat de Catalunya). All experimental animal procedures were carried out in strict accordance with the European Communities directive 2010/63/EU legislation regulating animal research. All efforts were made to minimize animal suffering and to reduce the number of animals used.

Male (8-10 week old) C57BL/6J mice were used for the experiments. All animals were housed on a 12h/12h light/dark cycle (from 8am to 8pm) in a temperature- and humidity-controlled room, and allowed free access to water and standard laboratory chow. For fasting experiments, animals were randomly assigned to food-deprived (fasted group) or fed *ad libitum* groups (fed group). For tissue collection, animals were sacrificed by cervical dislocation under isoflurane anaesthesia during the light phase and hypothalamus, liver and adipose tissue were quickly removed and stored at - 80ºC.

For cannulation, cannulae were stereotaxically implanted into the lateral cerebral ventricle under anaesthesia, as previously described [60,61]. Cannulated mice were subjected to 16 h fasting before the beginning of the dark cycle. After that, mice were exposed to food and randomly assigned to the following treatments: 3 µl of vehicle (PBS), (±)-C75, (±)-C75-CoA, (±)-C75-CoA-PM (at 4.2 mM cargo concentration; injection dosage 126.5 µg/mouse), Fluor-CoA or Fluor-CoA-PM (at 2.95 mM cargo concentration; injection dosage 104 µg/mouse) by ICV injection 30 min before the beginning of the dark cycle. The

schedule of this protocol was based on previous publications analysing feeding pattern after ICV administration of drugs [13,14]. The dosage of (±)-C75 in the free form or PM form was also based on previous studies [13,22,24].

For feeding experiments, food intake was monitored at 1, 2, 4, 8, 12 and 24 hours after ICV administration, whereas body weight was measured before and 24 hours after treatment. For tissue collection and gene expression analysis, food intake and body weight were monitored 2 h after drug administration and mice were subsequently euthanized. Fresh tissues were then harvested and stored at -80ºC.

For brain immunofluorescence, mice were anesthetized under ketamine/xylazine and intracardially perfused with PBS and then 10% NBF at 2 hours after (±)-C75-CoA, (±)-C75-CoA-PM, Fluor-CoA or Fluor-CoA-PM. Brains were collected and post-fixated 24 h in 10% NBF at 4ºC, transferred to 30% sucrose at 4ºC for 2-3 days, frozen in isopentane, and sliced in 30 µm thick slices in the coronal plane throughout the entire rostral-caudal extent of the brain using a cryostat. The subsequent analysis for brain immunofluorescence or RT-PCR in tissues is detailed in the supplementary information (ESI§).

4.3 Statistical analysis

All results are expressed as mean ± SD. Statistical analysis was conducted using GraphPad Prism 9 Software (GraphPad Software, La Jolla, CA, USA). Statistical analysis was determined by ANOVA (more than 2 groups were compared) followed by Tukey's post-hoc test. $p < 0.05$ was considered statistically significant. The number of animals used in each experiment is specified in each figure legend.

Author Contributions

Conceptualization: S.Q. and R.R.-R.; Methodology: J.G.-C., W.K.D.P, S.Z., A.F., A.C.R., S.A., L.S., S.F. and K.T.; Investigation: J.G.-C., W.K.D.P, X.A., S.Q. and R.R.-R.; Visualization: J.G.-C., W.K.D.P, S.Q. and R.R.-R; Supervision: S.Q., R.R.-R., X.A. and K.K.; Writing-original draft: J.G.-C., W.K.D.P, S.Q. and R.R.-R.; Writing-review & editing: W.K.D.P, S.Q., R.R.-R., X.A., N.C., D.S., L.H., J.G., K.K.

Conflicts of interest

There are no conflicts to declare.

Acknowledgements

References

1   I. González-García, J. Fernø, C. Diéguez, R. Nogueiras and M. López, Neuroendocrinology, 2017, 104, 398–411.

2   World Health Organization., Obesity and overweight., https://www.who.int/news-room/fact-sheets/detail/obesity-and-overweight, (accessed 19 November 2019).

3   V. S. Malik, W. C. Willet and F. B. Hu, Nat. Rev. Endocrinol., 2020, 16, 615–616.

4   K. Timper and J. C. Brüning, Dis. Model. Mech., 2017, 10, 679–689.

5   T. Scherer, K. Sakamoto and C. Buettner, Nat. Rev. Endocrinol., 2021, 17, 468–483.

6   P. Dimitri, Front. Endocrinol. (Lausanne)., 2022, 13, e846880.

7   A. Fosch, S. Zagmutt, N. Casals and R. Rodríguez-Rodríguez, Int. J. Mol. Sci., 2021, 22, 6186.

8   M. López, C. J. Lelliott and A. Vidal-Puig, BioEssays, 2007, 29, 248–261.

9   S. Obici, Z. Feng, K. Morgan, D. Stein, G. Karkanias and L. Rossetti, Diabetes, 2002, 51, 271–5.

10   M. López, R. Nogueiras, M. Tena-Sempere and C. Diéguez, Nat. Rev. Endocrinol., 2016, 12, 421–32.

11   K. D. Bruce, A. Zsombok and R. H. Eckel, Front. Endocrinol. (Lausanne)., 2017, 8, 60.

12   I. R. Schlaepfer and M. Joshi, Endocrinology, 2020, 161, 1–14.

13   Z. Hu, S. H. Cha, S. Chohnan and M. D. Lane, Proc Natl Acad Sci U S A, 2003, 100, 12624–12629.

14   Z. Hu, Y. Dai, M. Prentki, S. Chohnan and M. D. Lane, J. Biol. Chem., 2005, 280, 39681–39683.

15   T. K. T. Lam, A. Pocai, R. Gutierrez-Juarez, S. Obici, J. Bryan, L. Aguilar-Bryan, G. J. Schwartz and L. Rossetti, Nat. Med., 2005, 11, 320–7.

16   R. Fadó, R. Rodríguez-Rodríguez and N. Casals, Prog. Lipid Res., 2021, 81, 101071.

17   J. M. Orellana-Gavaldà, L. Herrero, M. I. Malandrino, A. Pañeda, M. Sol Rodríguez-Peña, H. Petry, G. Asins, S. Van Deventer, F. G. Hegardt and D. Serra, Hepatology, 2011, 53, 821–32.

18   M. Weber, P. Mera, J. Casas, J. Salvador, A. Rodríguez, S. Alonso, D. Sebastián, M. C. Soler-Vázquez, C. Montironi, S. Recalde, R. Fucho, M. Calderón-Domínguez, J. F. Mir, R. Bartrons, J. C. Escola-Gil, D. Sánchez-Infantes, A. Zorzano, V. Llorente-Cortes, N. Casals, V. Valentí, G. Frühbeck, L. Herrero and D. Serra, FASEB J., 2020, 34, 11816–11837.

19   D. Serra, P. Mera, M. I. Malandrino, J. F. Mir and L. Herrero, Antioxid. Redox Signal., 2013, 19, 269–284.

20   J. Dai, K. Liang, S. Zhao, W. Jia, Y. Liu, H. Wu, J. Lv, C. Cao, T. Chen, S. Zhuang, X. Hou, S. Zhou, X. Zhang, X. W. Chen, Y. Huang, R. P. Xiao, Y. L. Wang, T. Luo, J. Xiao and C. Wang, Proc. Natl. Acad. Sci. U. S. A., 2018, 115, E5896–E5905.

21   S. Obici, Z. Feng, A. Arduini, R. Conti and L. Rossetti, Nat. Med., 2003, 9, 756–761.

22   P. Mera, A. Bentebibel, E. López-Viñas, A. G. Cordente, C. Gurunathan, D. Sebastián, I. Vázquez, L. Herrero, X. Ariza, P. Gómez-Puertas, G. Asins, D. Serra, J. García and F. G. Hegardt, Biochem. Pharmacol., 2009, 77, 1084–1095.

23   S. Gao and M. D. Lane, Proc. Natl. Acad. Sci. U. S. A., 2003, 100, 5628–33.

24   T. M. Loftus, D. E. Jaworsky, G. L. Frehywot, C. A. Townsend, G. V Ronnett, M. D. Lane and F. P. Kuhajda, Science, 2000, 288, 2379–81.

25   S. H. Cha, Z. Hu and M. D. Lane, Biochem. Biophys. Res. Commun., 2004, 317, 301–308.

26   K. Makowski, P. Mera, D. Paredes, L. Herrero, X. Ariza, G. Asins, F. G. Hegardt, J. García and D. Serra, Chirality, 2013, 25, 281–287.

27   M. C. Cheng, X. H. Qiang and C. M. Du, Chinese Sci. Bull., 2013, 58, 1256–1261.

28   W. K. D. Paraiso, J. Garcia-Chica, X. Ariza, S. Zagmutt, S. Fukushima, J. Garcia, Y. Mochida, D. Serra, L. Herrero, H. Kinoh, N. Casals, K. Kataoka, R. Rodríguez-Rodríguez and S. Quader, Biomater. Sci., 2021, 9, 7076–7091.

29   S. Quader, X. Liu, K. Toh, Y. L. Su, A. R. Maity, A. Tao, W. K. D. Paraiso, Y. Mochida, H. Kinoh, H. Cabral and K. Kataoka, Biomaterials, 2021, 267, e120463.

30   H. Shibasaki, H. Kinoh, H. Cabral, S. Quader, Y. Mochida, X. Liu, K. Toh, K. Miyano, Y. Matsumoto, T. Yamasoba and K. Kataoka, ACS Nano, 2021, 15, 5545–5559.

31   H. J. Kim, K. Miyata, T. Nomoto, M. Zheng, A. Kim, X. Liu, H. Cabral, R. J. Christie, N. Nishiyama and K. Kataoka, Biomaterials, 2014, 35, 4548–4556.

32   H. Cabral, K. Miyata, K. Osada and K. Kataoka, Chem. Rev., 2018, 118, 6844–6892.

33   J. W. McFadden, S. Aja, Q. Li, V. V. R. Bandaru, E. K. Kim, N. J. Haughey, F. P. Kuhajda and G. V. Ronnett, PLoS One, 2014, 9, e115642.

34   S. H. Cha, Z. Hu, S. Chohnan and M. D. Lane, Proc. Natl. Acad. Sci. U. S. A., 2005, 102, 14557–14562.

35   S. H. Cha, J. T. Rodgers, P. Puigserver, S. Chohnan and M. D. Lane, Proc. Natl. Acad. Sci. U. S. A., 2006, 103, 15410–15415.

36   Z. Hu, H. C. Seung, G. Van Haasteren, J. Wang and M. D. Lane, Proc. Natl. Acad. Sci. U. S. A., 2005, 102, 3972–3977.

37   H. C. Seung, M. Wolfgang, Y. Tokutake, S. Chohnan and M. D. Lane, Proc. Natl. Acad. Sci. U. S. A., 2008, 105, 16871–16875.

38   M. S. Vohra, K. Benchoula, C. J. Serpell and W. E. Hwa, Eur. J. Pharmacol., 2022, 915, 174611.

39   C. Quarta, M. Claret, L. M. Zeltser, K. W. Williams, G. S. H. Yeo, M. H. Tschöp, S. Diano, J. C. Brüning and D. Cota, Nat. Metab., 2021, 3, 299–308.

40   M. V. Kumar, T. Shimokawa, T. R. Nagy and M. D. Lane, Proc. Natl. Acad. Sci. U. S. A., 2002, 99, 1921–1925.

41   M. Schneeberger, R. Gomis and M. Claret, J. Endocrinol., 2014, 220, T25–T46.

42   E. Roh, D. K. Song and M. S. Kim, Exp. Mol. Med. 2016 483, 2016, 48, e216–e216.

43   C. Contreras, R. Nogueiras, C. Diéguez, K. Rahmouni and M. López, Redox Biol., 2017, 12, 854–863.

44   T. Yoneshiro, R. Rodríguez-Rodríguez, M. J. Betz and P. C. N. Rensen, Front. Endocrinol. (Lausanne)., 2020, 11, 845.

45   C. Contreras, I. González-García, P. Seoane-Collazo, N. Martínez-Sánchez, L. Liñares-Pose, E. Rial-Pensado, J. Fernø, M. Tena-Sempere, N. Casals, C. Diéguez, R. Nogueiras and M. López, Diabetes, 2017, 66, 87–99.

46   L. P. Klieverik, S. F. Janssen, A. Van Riel, E. Foppen, P. H. Bisschop, M. J. Serlie, A. Boelen, T. Ackermans, H. P. Sauerwein, E. Fliers and A. Kalsbeek, Proc Natl Acad Sci U S A, 2009, 106, 5966–5971.

47   M. T. Hackl, C. Fürnsinn, C. M. Schuh, M. Krssak, F. Carli, S. Guerra, A. Freudenthaler, S. Baumgartner-Parzer, T. H. Helbich, A. Luger, M. Zeyda, A. Gastaldelli, C. Buettner and T. Scherer, Nat. Commun., 2019, 10, 2717.

48   E. A. Nance, G. F. Woodworth, K. A. Sailor, T.-Y. Shih, Q. Xu, G. Swaminathan, D. Xiang, C. Eberhart and J. Hanes, Sci. Transl. Med., 2012, 4, 149ra119.

49   E. Nance, K. Timbie, G. W. Miller, J. Song, C. Louttit, A. L. Klibanov, T. Y. Shih, G. Swaminathan, R. J. Tamargo, G. F. Woodworth, J. Hanes and R. J. Price, J. Control. Release, 2014, 189, 123–132.

50   A. G. Godin, J. A. Varela, Z. Gao, N. Danné, J. P. Dupuis, B. Lounis, L. Groc and L. Cognet, Nat. Nanotechnol., 2017, 12, 238–243.

51   C. Paviolo, F. N. Soria, J. S. Ferreira, A. Lee, L. Groc, E. Bezard and L. Cognet, Methods, 2020, 174, 91–99.

52   R. G. Thorne and C. Nicholson, Proc. Natl. Acad. Sci. U. S. A., 2006, 103, 5567–5572.

53   A. Bonaccorso, T. Musumeci, M. F. Serapide, R. Pellitteri, I. F. Uchegbu and G. Puglisi, Colloids Surfaces B Biointerfaces, 2017, 154, 297–306.

54   S. Dante, A. Petrelli, E. M. Petrini, R. Marotta, A. Maccione, A. Alabastri, A. Quarta, F. De Donato, T. Ravasenga, A. Sathya, R. Cingolani, R.

Proietti Zaccaria, L. Berdondini, A. Barberis and T. Pellegrino, ACS Nano, 2017, 11, 6630–6640.

55   R. Rodriguez-Rodriguez and S. Quader, Nanomedicine (Lond)., 2022, 17, 495–498.

56   S. Fukushima, K. Miyata, N. Nishiyama, N. Kanayama, Y. Yamasaki and K. Kataoka, J. Am. Chem. Soc., 2005, 127, 2810–2811.

57   K. Miyata, M. Oba, M. Nakanishi, S. Fukushima, Y. Yamasaki, H. Koyama, N. Nishiyama and K. Kataoka, J. Am. Chem. Soc., 2008, 130, 16287–16294.

58   S. Quader, H. Cabral, Y. Mochida, T. Ishii, X. Liu, K. Toh, H. Kinoh, Y. Miura, N. Nishiyama and K. Kataoka, J. Control. Release, 2014, 188, 67–77.

59   K. Osada, T. Shiotani, T. A. Tockary, D. Kobayashi, H. Oshima, S. Ikeda, R. J. Christie, K. Itaka and K. Kataoka, Biomaterials, 2012, 33, 325–332.

60   R. Rodríguez-Rodríguez, C. Miralpeix, A. Fosch, M. Pozo, M. Calderón-Domínguez, X. Perpinyà, M. Vellvehí, M. López, L. Herrero, D. Serra   and N. Casals, Mol. Metab., 2019, 19, 75–85.

61   M. Pozo, R. Rodrguez-Rodrguez, S. Raḿrez, P. Seoane-Collazo, M. López, D. Serra, L. Herrero and N. Casals, Endocrinology, 2017, 158, 2226–2238.

SUPPLEMENTARY INFORMATION

EXPERIMENTAL SECTION

Characterization of micelles

For DLS measurements (Zetasizer Ultra, Malvern Panalytical, Spectris plc, UK), PM suspensions were diluted to 1 mg/mL and placed inside a ZEN2112 quartz cuvette. Light scattering data was measured using a 50-mW 532 nm DPSS laser incident beam at a detection angle of 173° with a He-Ne laser 633 nm (temperature = 25 °C). The autocorrelation function produced was analysed through the cumulant approach. Size is expressed as the hydrodynamic diameter, which was calculated with the Stokes–Einstein equation. Attenuator selection was automated. For zeta potential measurements, micelle suspensions were introduced in a ZEN1010 HC cell, using the Smoluchowski approach.

For quantification of cargo inside the micelles, PM solutions were pipetted into Amicon Ultra-0.5 mL centrifugal filters (MWCO 10,000, Merck Millipore, cat. # UFC501096) and spun (14,000 g, 15 min, 4 °C). The filtrate was then collected, weighed, and then transferred into UV-transparent 96-well plates. Its absorption at λ_{max} CoA = 259 nm was measured using a microplate reader (Infinite® M1000 Pro, Tecan Trading AG, Switzerland). Drug encapsulation was calculated by getting the ratio of the filtrate absorbance to that of the original (±)-C75-CoA solution added to form the PM.

Micelle and polymer morphology was observed on a Transmission Electron Microscope (JEM-2100, JEOL, Japan) operated with 120 kv acceleration voltages and approximately 60 µA beam current. The diluted micelle or polymer solution (0.1 mg/mL) was stained by mixing with uranyl acetate

solution (2%, w/v) and placed on 400-mesh copper grids before drying and observation.

Preparation of labelled polymers and FRET micelles

PEG–PBLA–PLys(TFA) (50 mg) was dissolved in anhydrous DMSO (Sigma-Aldrich, cat. # 276855-100ML) to which rhodamine-NHS ester (ThermoFisher Scientific, cat. # 46406:10 eq) was added. The reaction mixture was stirred at 40 °C for 72 h. After which, the labelled polymer was isolated by precipitation and washing in cold ether (3×). After drying *in vacuo*, aminolysis and deprotection were carried out as described in the main text.

PEG–PBLA (50 mg) was dissolved in anhydrous DMSO (Sigma-Aldrich, cat. # 276855-100ML) to which fluorescein-NHS ester (ThermoFisher Scientific, cat. # 46410:10 eq) was added. The reaction mixture was stirred at 40 °C for 72 h. After which, the labelled polymer was isolated by precipitation and washing in cold ether (3×). After drying *in vacuo*, hydrazinolysis was carried out as reported [1].

FRET micelles were prepared with buffered solutions of (±)-C75-CoA as above. FRET behaviour was confirmed by fluorescence spectroscopy (fluorescence spectrometer FP-8600DS, JASCO, Japan), where excitation wavelength 494 nm for fluorescein was used.

Cell culture, cellular uptake, fluorescent assays and ATP measurement

Murine hypothalamic neuronal cells GT1-7 (Merck Millipore, Sigma, Madrid, Spain) were cultured in DMEM (4.5 g/L glucose) as described [2]. For cellular uptake analysis, GT1-7 cells (5×10^4 cells / well) were seeded in 24-well plates 24 h prior to the assay. They were then incubated with PM suspension in medium (micelle amount equivalent to 0.1 mg/mL Fluor-CoA) for 30 min,

followed by washing of cell suspension then incubated with 50 µL Accutase® Cell Detachment Solution (Innovative Cell Technologies, San Diego, California) for 3 minutes at 37 °C, centrifuged and resuspended with DAPI, as described [2]. After final washing, the cells were resuspended. Mean fluorescence intensity and percentage of Fluor-CoA+ cells in FITC channel were measured by flow cytometry (BD LSRFortessa™ Flow Cytometer, BD Biosciences, San Jose, California) using FSC and SSC detection to gate out debris, and the UV (355 nm) and blue lasers (488 nm) for the detection of DAPI and Fluor-CoA, respectively. Data analysis was performed using FlowJo software (BD Biosciences, San Jose, California).

The protocol for ATP measurement was based on previous publication [2]. Briefly, produced ATP was quantified using a luminescence assay. The GT1-7 cells (2×10^5 cells/well) were seeded in a white, flat-bottom 96-well tissue culture plate 24 h prior to the assay. The cells were then incubated with control, free drug, or micelles (0.5 mM) in bicarbonate-free DMEM (Sigma-Aldrich, cat. # D5030-10L) supplemented with 2.5 mM glucose (Gibco, cat. # A2494001) and 275 nM oleate-BSA (Sigma-Aldrich, cat. # O3008-5ML) for 1 h in a separate incubator at 0% CO_2, 20% O_2, 37 °C. The assay was then performed according to manufacturer protocol (CellTiter-Glo® Luminescent Cell Viability Assay, Promega). Luminescence signal for 10 s was measured in each well using GloMax® Multi Detection System (Promega Corp, Madison, Wisconsin).

For colocalization analysis of the nanomedicine with acidic organelles, GT1-7 cells exposed to the polymeric micelle Fluorescein-CoA-PM for 1h at 37°C, were concomitantly incubated with LysoTracker® Red (Thermo Fisher Scientific, Waltham, MA, USA) for endolysosomes staining, and compared to MitoTracker® Red (Thermo Fisher Scientific, Waltham, MA, USA) for staining of mitochondria. Cells were then fixed with 4% paraformaldehyde and

counterstained with Hoechst for the nuclei visualization (blue). Images were taken using a Leica TCS SP8 confocal microscope.

Brain immunofluorescence

For neuronal activation analysis, hypothalamic slices containing PVN and ARC nuclei were extensively washed in 0.1% Triton X-100 KPBS buffer and blocked in 2% goat anti-serum in KPBS plus 0.1% Triton X-100. Sections were incubated with rabbit anti-c-FOS antibody (1:200, Cell Signaling) in blocking buffer for 1 h at room temperature. After washing with KPBS, slices were incubated with anti-rabbit Alexa Fluor 647 antibody (1:1000; Invitrogen) for 1 h at room temperature, followed by counterstaining with Hoechst 3328 for nuclear staining (1 mg/mL, Sigma-Aldrich). For the analysis of fluorescein in brain slices, immunostaining of brain cells was performed using antibodies against neurons (rabbit anti-NeuN, 1:500, Abcam; rabbit anti-NSE, 1:250, Abcam), astrocytes (rabbit anti-GFAP, 1:1000, Invitrogen) and microglia (rabbit anti-Iba1, 1:500, WAKO) in blocking buffer for 1h at room temperature, followed by incubation with the secondary antibody (Alexa Fluor 647) and Hoechst, as described above. After immunostaining, slices were mounted into Superfrost Plus Slides (Thermo Fisher) using antifade Fluoromount-G® (Southern Biotech) and coverslips. Images were taken using a Leica TCS SP8 confocal microscope equipped with a 20x and 40x objective. Fluorescence integrated density after image masking was calculated using ImageJ FIJI (NIH) software.

RNA extraction and RT-PCR

Total RNA was extracted from liver and BAT using Trizol Reagent (Fisher Scientific, Madrid, Spain). Retrotranscription and quantitative RT-PCR (qPCR) were performed as previously described [3]. SYBR Green or Taqman Gene

Expression assay primers used in the study (IDT DNA Technologies, Leuven, Belgium) are detailed in Table S2. Relative mRNA levels were measured using the CFX96 Real-time System, C1000 Thermal Cycler (BioRad). Relative gene expression was estimated using the comparative Ct ($2^{-\Delta\Delta ct}$) method and normalized to *Hprt/Gapdh*.

Table S1. Summary of size and polydispersity of the different micelles used. Preparation and size measurements were performed in triplicate (n = 3) and indicate mean ± s.d. except for [#], which was only prepared once (n = 1).

Cargo	Micelle type	Polymer/s used	Size (nm)	Polydispersity
(±)-C75-CoA	Non-crosslinked	PEG-PAsp(Aldehyde)-PLys	44.0 ± 0.28	0.13 ± 0.009
(±)-C75-CoA	Crosslinked	PEG-PAsp(Aldehyde)-PLys	43.1 ± 0.26	0.12 ± 0.013
(±)-C75-CoA	Non-crosslinked	PEG-PLys	41.4 ± 0.68	0.12 ± 0.019
(±)-C75-CoA	Crosslinked (FRET)	PEG-PAsp(Aldehyde)-PLys-Fluorescein	60.6 ± 3.58	0.14 ± 0.008
Fluor-CoA [#]	Non-crosslinked	PEG-PAsp(Aldehyde)-PLys	53.2	0.10
Fluor-CoA	Crosslinked	PEG-PAsp(Aldehyde)-PLys	43.9 ± 0.40	0.08 ± 0.006

Table S2. List of the primers used for the RT-PCR assays in hypothalamus, liver or adipose tissue.

SYBR Green primers		
Gene	**Direction**	**Sequence**
AgRP	For	5'-TTTGTCCTCTGAAGCTGTATGC
	Rev	5'- GCATGAGGTGCCTCCCTA
NPY	For	5'-TCCGCTCTGCGACACTACAT
	Rev	5'-TGCTTTCCTTCATTAAGAGGT
POMC	For	5'-TGAACATCTTTGTCCCCAGAG
	Rev	5'-TGCAGAGGCAAACAAGATTGG
PGC1-α	For	5'- GAAAGGGCCAAACAGAGAGA
	Rev	5'- GTAAATCACACGGCGCTCTT
CIDEA	For	5'-GCCTGCAGGAACTTATCAGC
	Rev	5'-AGAACTCCTCTGTGTCCACCA
PRDM16	For	5'-CCTAAGGTGTGCCCAGCA
	Rev	5'-CACCTTCCGCTTTTCTACCC
PEPCK	For	5'-CCACAGGCACTAGGGAAGGC
	Rev	5'-GGCGGAGCATATGCTGATCC
G6Pase	For	5'-TCAACCTCGTCTTCAAGTGGATT
	Rev	5'-CTGCTTTATTATAGGCACGGAGCT
PKLR	For	5'-AGATGCAACATGCGATTGCC
	Rev	5'-GCACAGCACTTGAAGGAAGC
CPT1A	For	5'-GACTCCGCTCGCTCATTC
	Rev	5'-AAGGCCACAGCTTGGTGA
HPRT	For	5'-GGACCTCTCGAAGTGTTGGATAC
	Rev	5'-GCTCATCTTAGGCTTTGTATTTGGCT
GAPDH	For	5'-TCCACTTTGCCACTGCA
	Rev	5'-GAGACGGCCGCATCTTCTT
TaqMan probes		
Gene	**Reference**	**Dye**
UCP-1	Mm.PT.58.7088262	Hex
GAPDH	Mm.PT.39a.1	Fam

Fig. S1. Transmission electron microscopy (TEM) images. (A) (±)-C75-CoA loaded Crosslinked micelle (B) (±)-C75-CoA loaded Non-crosslinked micelle (C) Mixture of PEG-PAsp(Aldehyde)-PLys and PEG-PAsp(Hydrazide) polymers in 10 mM phosphate buffer pH 7.4. Scale bar 50 nm.
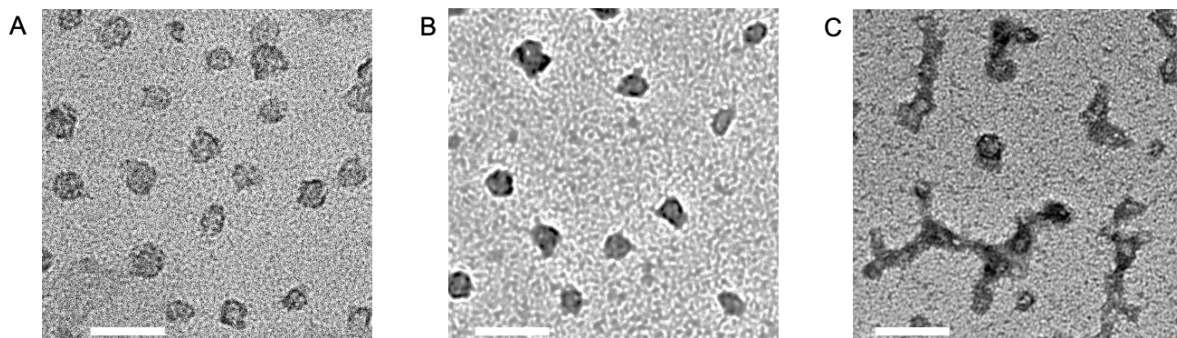
Fig. S2. Size profile and dissociation of non-crosslinked polymeric micelles (PM). (A) Size profile of non-crosslinked (±)-C75-CoA diblock PM. (B) Effect of dextran sulfate sodium (DSS) on scattered light intensity of diblock PM. Data are expressed as mean ± SEM (n=3-4).
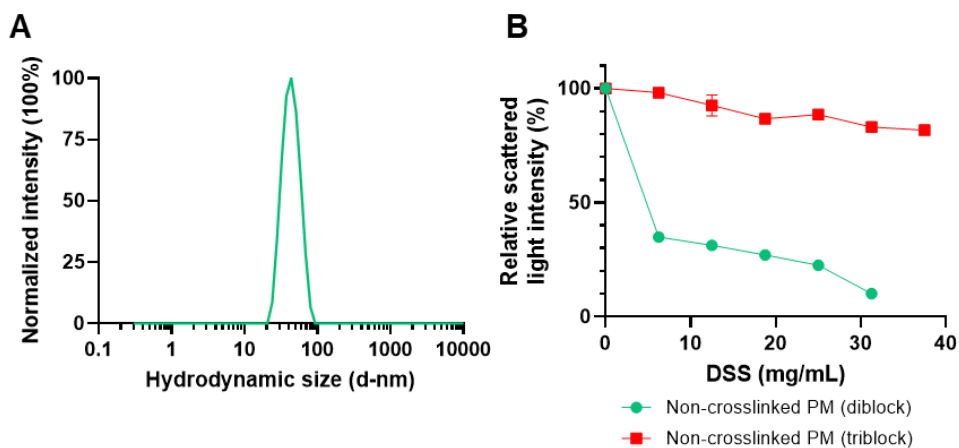
Fig. S3. Encapsulation efficiency of non-crosslinked and crosslinked micelles in response to phosphate buffer (PB) and artificial cerebrospinal fluid (aCSF). Data expressed as mean ± SEM (n=3-4) were compared using one-way ANOVA with Tukey's post-hoc test, ***p<0.001.
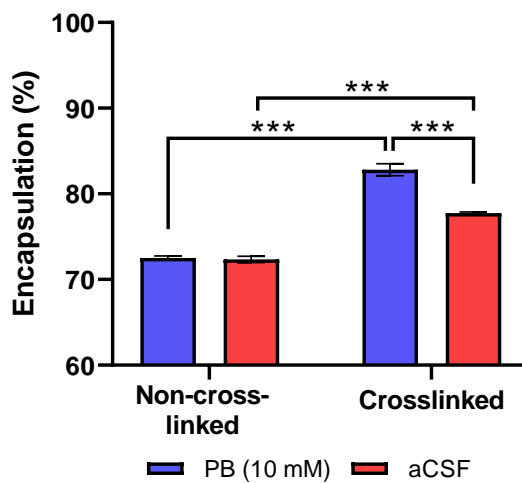
Fig. S4. Size profile, encapsulation and release of Fluor-CoA polymeric micelles (PM). (A) Size profile of Fluor-CoA PM. (B) Encapsulation of Fluor-CoA PM. (C) Release of Fluor-CoA PM in cell medium at 4ºC or 37ºC. (D) Release of the cargo in PBS or artificial cerebrospinal fluid (aCSF) at 37 ºC. Data are expressed as mean ± SEM (n=3-4), compared using one-way ANOVA with Tukey's post-hoc test, *p<0.05, **p<0.01, ***p<0.001.
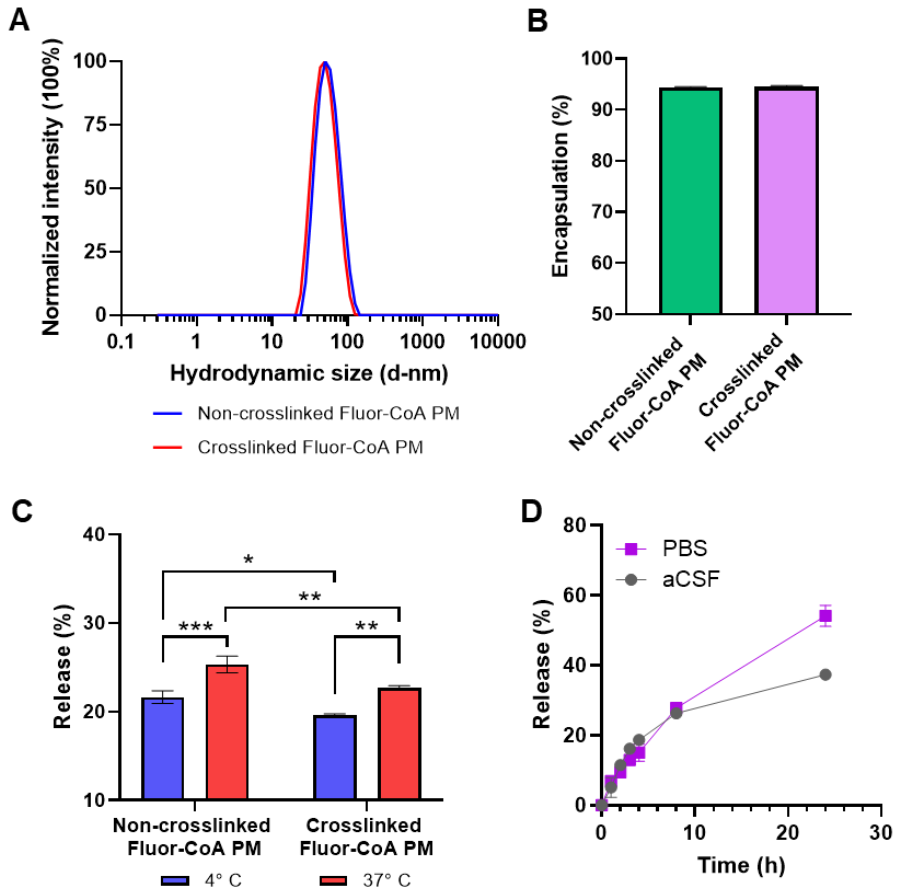
Fig. S5. Fluorescent localization of the fluorescent tracer of the micelle with endolysosomes and mitochondria. Representative images of GT1-7 neurons indicating endolysosomes (LysoTracker; red), mitochondria (MitoTracker; red), nuclei (blue) and the fluorescent cargo of the nanomedicine (Fluorescein, green) after 1 hour of treatment. Scale bar = 10μm.

| LysoTracker | FITC-fluorescein | Hoechst | Merged |

| MitoTracker | FITC-fluorescein | Hoechst | Merged |
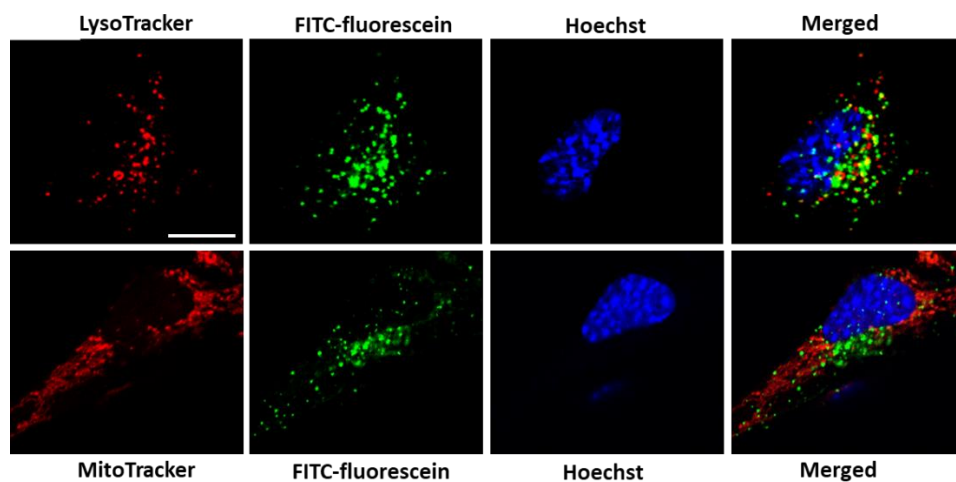
Fig. S6. Fluorescent tracer of the nanomedicine reaches the hypothalamus. Representative images of the main hypothalamic regions related to the regulation of food intake and energy expenditure, arcuate (ARC), ventromedial (VMH) and paraventricular hypothalamus (PVN), after 1 hour of ICV infusion of the nanomedicine. Scale bar = 50µm. The fluorescent tracer fluorescein is indicated in green (FITC).
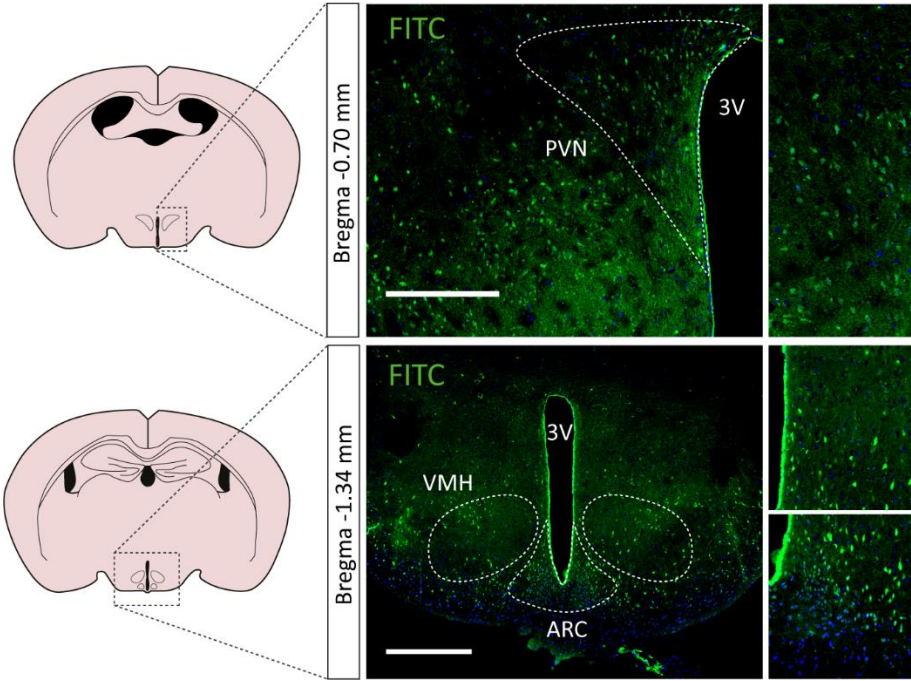
Fig. S7. Analysis of microglia activation in hypothalamus. Iba-1 expression at arcuate (ARC) and paraventricular (PVN) nucleus of the hypothalamus after 2 hours of treatment. (A) Vehicle, free cargo (fluorescein-CoA) and nanomedicine Iba-1 positive cells in ARC. (B) Quantification of the number of Iba-1 positive cells per ARC section. (C) Vehicle, free cargo (fluorescein-CoA) and nanomedicine Iba-1 positive cells in PVN. (D) Quantification of the number of Iba-1 positive cells per PVN section. All values are expressed in mean ± SD (n=3, 2 slice/animal). Scale bar = 50µm; magnification 40X. In (B, D) ns>0.05, using one-way ANOVA with Tukey's multiple comparison tests as post-hoc analysis. Iba-1 is indicated in red and nuclei in blue.
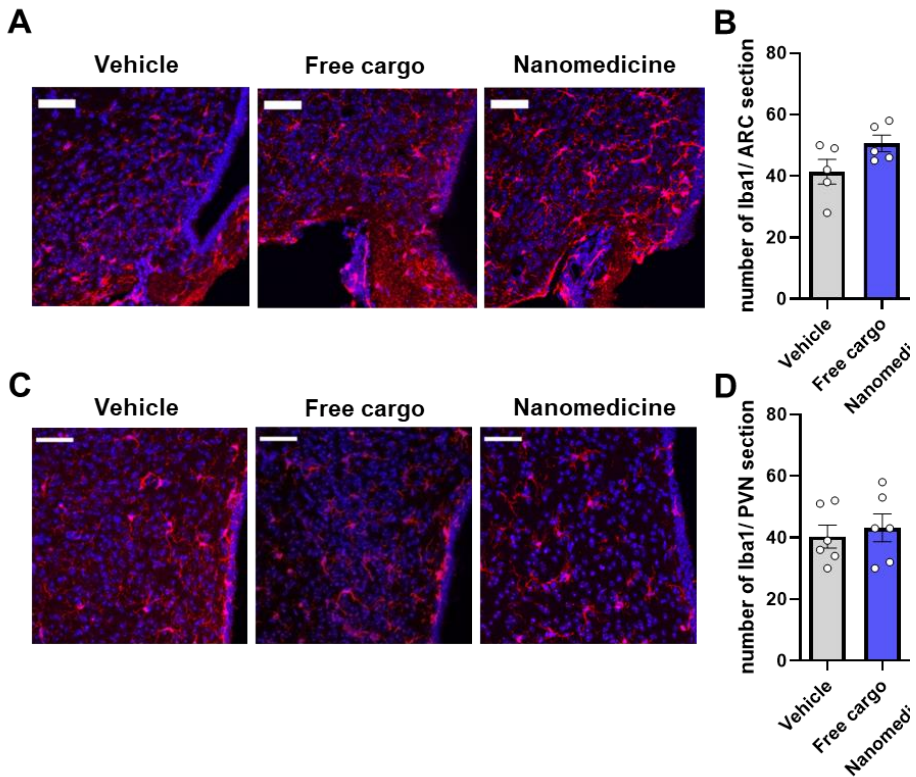
Fig. S8. Characterization of the triblock polymer. (A) ^{1}H NMR spectrum (400MHz, *D₂O*, 25°C) of the *PEG–PAsp–PLys* triblock polymer with gel chromatogram as an insert. (B) ^{1}H NMR spectrum (400MHz, DMSO-*d6*, 80° C) of the *PEG-PAsp(Aldehyde)-PLys-TFA* triblock polymer.
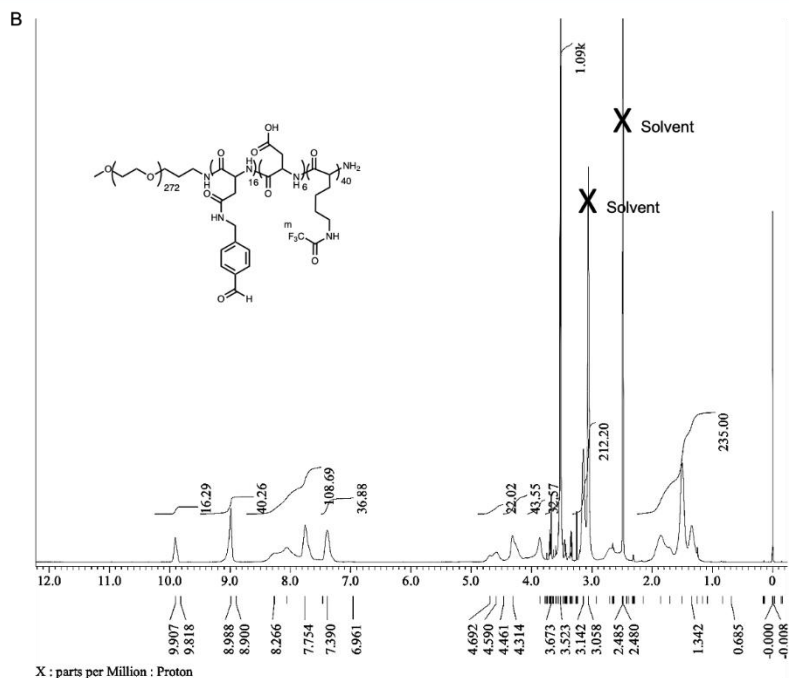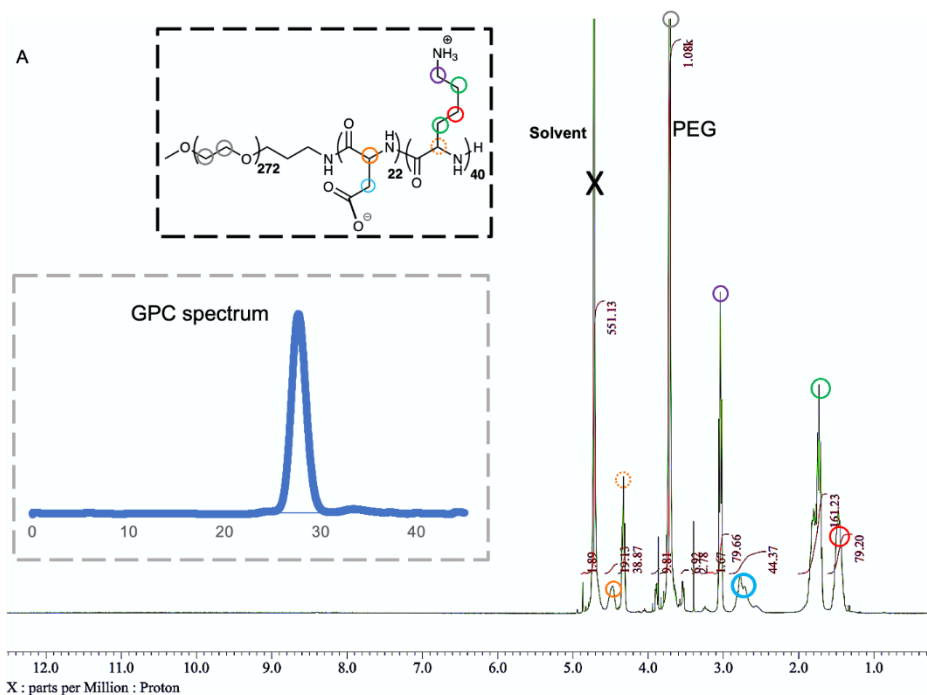
References:

1   S. Quader, H. Cabral, Y. Mochida, T. Ishii, X. Liu, K. Toh, H. Kinoh, Y. Miura, N. Nishiyama and K. Kataoka, J. Control. Release, 2014, 188, 67–77.

2   W. K. D. Paraiso, J. Garcia-Chica, X. Ariza, S. Zagmutt, S. Fukushima, J. Garcia, Y. Mochida, D. Serra, L. Herrero, H. Kinoh, N. Casals, K. Kataoka, R. Rodríguez-Rodríguez and S. Quader, Biomater. Sci., 2021, 9, 7076–7091.

3   R. Rodríguez-Rodríguez, C. Miralpeix, A. Fosch, M. Pozo, M. Calderón-Domínguez, X. Perpinyà, M. Vellvehí, M. López, L. Herrero, D. Serra and N. Casals, Mol. Metab., 2019, 19, 75–85.

ANNEX 1

C75-ketone derivative was not able to inhibit CPT1A but showed increased *in vitro* cytotoxicity.

MATERIALS AND METHODS

1. Synthesis of C75 derivatives

Two C75-derivatives were envisioned in order to covalently conjugate to PIC micelles, compounds **C75-Cl**, **(+)-C75=O** and **(+)-C75=O-CoA** (Fig A1).

C75-Cl synthesis was attempted by converting C75 carboxylic group into its carbonyl chloride. For this, C75 was dissolved in DCM with a catalytic amount of DMF, and $COCl_2$ was added in a molar proportion of 2:1 to C75. The mixture was agitated for 3h at RT, and then the volatiles were evaporated.

(+)-C75=O was synthesized by the substitution of the two terminal carbons of the alkyl chain of C75 by an acetyl group. The synthesis followed the pathway described for the stereoselective synthesis of (+)-C75, but starting substrates were changed (Makowski et al. 2012). Bromohexanol reacted with ethyl acetate to produce hydroxy-2-nonanone after decarboxylation. Protection of the carbonyl group as a cyclic ketal with ethylene glycol and oxidation afforded an aldehyde analogous to the nonanal used for the obtention of (+)-C75. With this substrate, synthesis of (+)-C75=O was carried out under similar conditions as to those previously described for (+)-C75.

Once (+)-C75=O was obtained, (+)-C75=O-CoA was synthesized incubating (+)-C75=O with CoA sodium salt in a pH8 sodium phosphate buffer, as described previously (Mera et al. 2009),
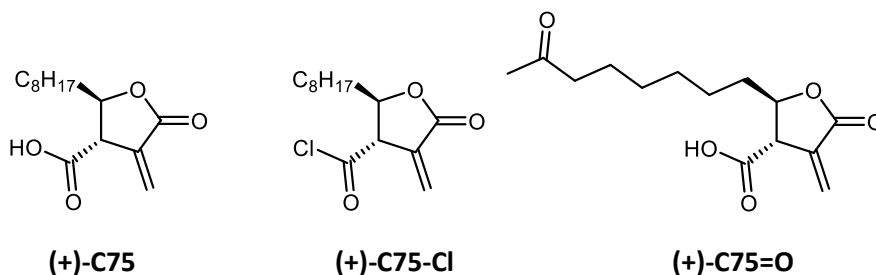
Figure A1. Chemical structure of reference compounds.

2. CPT1A inhibition of (+)-C75=O-CoA

A radiometric method was used for the assay of CPT1A activity, as described previously (Morillas et al. 2003). The activity was assayed in mitochondrial-enriched fractions obtained from yeast (4 mg protein). Enzyme activity was assayed for 5 min at 30°C in a total volume of 200 µl. The substrates were 400 µM H^3-L-carnitine and 50 µM palmitoyl-CoA. For the studies in vitro enzyme was pre-incubated with increasing concentration of drugs (0.1–100 mM) for 1 min.

3. Cytotoxicity of (+)-C75=O and (+)-C75=O-CoA

The *in vitro* cytotoxicity of (+)-C75=O and (+)-C75=O-CoA was evaluated against several cell lines using the colorimetric cell viability kit CCK-8 (Dojindo, Japan). The protocol used is described in Chapter 1. Roughly, $5 \times 10^3 - 2 \times 10^4$ cells were seeded in a 96-well plate 24 h prior to the assay, incubated with test solutions for 24 h and then viability was measured by addition of CCK-8 solution and measuring the absorbance of the product at 450 nm after 1-4 h using a microplate reader The cell lines used were GT1-7, U87MG, U373MG, a GBM cancer cell line, MCF-7, a breast cancer cell line, and sh-SY5Y, a neuroblastoma cell line.

RESULTS

C75=O-CoA does not show CPT1A inhibition but has an increased cytotoxic effect.

After several repetitions of the C75-Cl synthesis reaction, we could not obtain the expected product. However, the compound (+)-C75=O synthesis pathway

worked as was previously described, obtaining 25 mg of this compound. The synthesis of (+)-C75=O-CoA also worked as expected.

The first step after synthesis of (+)-C75=O-CoA was to assess its ability to inhibit CPT1A in comparison to C75-CoA. Unfortunately, while (+)-C75-CoA produce a 60% reduction of CPT1A activity, the new (+)-C75=O-CoA only produced a 15% inhibition, preventing its use as a CPT1A inhibitor (**Fig. Annex 2**).
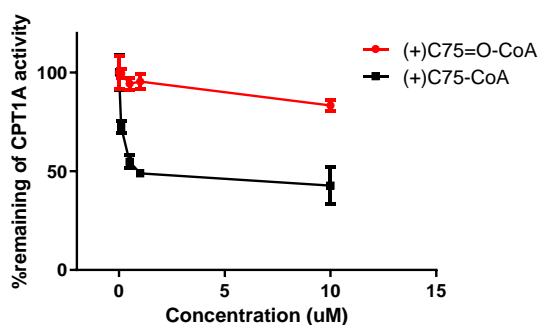
Figure A2. (+)-C75=O-CoA shows little CPT1A inhibitory capacity.

In parallel, we assessed the effects of (+)-C75=O and (+)-C75=O-CoA on cell viability in GT1-7 and U87MG. We discovered that (+)-C75=O and its CoA derivative induced an increased cytotoxicity compared to (+)-C75 and its CoA derivative. Furthermore, this increase is independent of the conjugated CoA, contrary to the case of (+)-C75. Seeing this increased effect, we tested its cytotoxicity in an ensemble of cell lines commonly used as cancer models. We used U373MG, MCF-7 and sh-SY5Y. Interestingly, (+)-C75=O and its CoA derivative held this increase cytotoxic effect in these cell lines compared to (+)-C75 and its CoA derivative (**Fig. Annex 3A and 3B**).

In conclusion, we attempted to synthesize two C75 derivates for chemical conjugation to polymeric micelles, by modifying parts of the molecule that

should not affect its CPT1A inhibition ability. However, we only achieved the synthesis of (+)-C75=O. which had lost most of its ability to inhibit CPT1A, but was surprisingly more cytotoxic than (+)-C75. This effect might be caused by interactions with a different protein or by the reactivity of the carbonyl group.

Future studies should be addressed at elucidating whether this drug interacts with CPT1A, FAS or any other protein, whether its effect is mediated by its specific interaction with one or few proteins or if it is mediated by non-specific interactions, and to investigate the mechanism by which this drug produces cytotoxicity. These experiments will help gauge the potential of this drug as an anti.cancer agent.
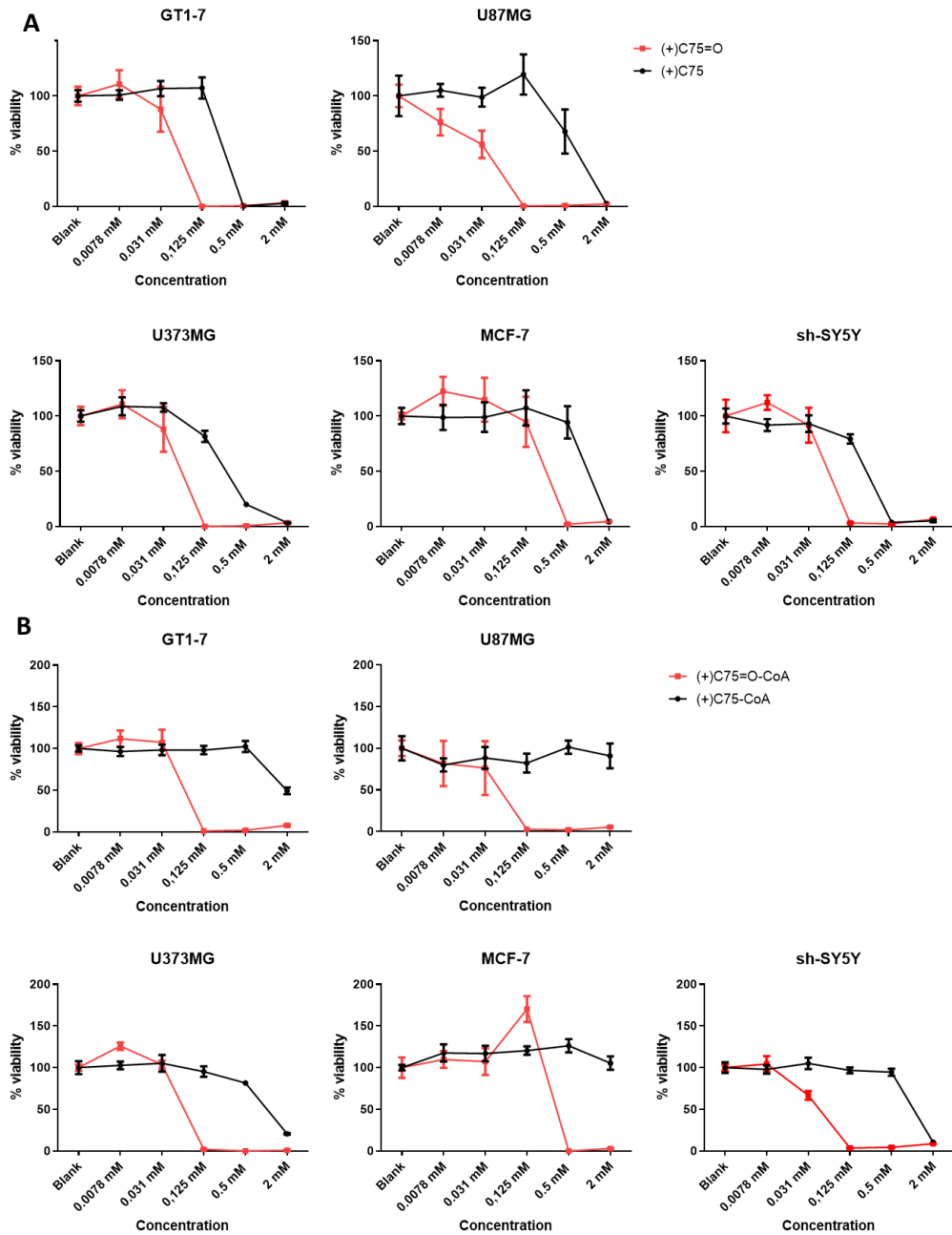
Figure A3. Comparison of the percentage of cell viability in different cell lines after treatment with a) (+)-C75=O and (+)-C75, and b) (+)-C75=O-CoA and (+)-C75-CoA.

DISCUSSION

The worldwide prevalence of obesity is steadily increasing, primarily due to excessive availability of energy in Western societies. The overconsumption of highly palatable foods coupled with an increasingly sedentary lifestyle are the main drivers for obesity development. Moreover, the increasing prevalence of obesity is accompanied by a surge in comorbidities, such as type II diabetes, hypertension or NAFLD. So far, anti-obesity drugs have not been able to produce the desired effect, as most drugs produce reductions of under 10% body weight. An exception is semaglutide, recently approved by the FDA and regulated in Europe as a type II diabetes drug, which has been shown to cause body weight reductions of drug capable of causing almost 15% body weight decrease (Wilding et al. 2021).

Since the hypothalamus integrates the central mechanism for the regulation of food intake, targeting specific cell populations in the hypothalamus could be a promising strategy to treat obesity. However, drugs aimed for hypothalamic neurons often face challenges in reaching their intended targets and can lead severe off-target effects. Currently, most prescribed drugs for obesity treatment focus on peripheral targets, but still present several side effects (Müller et al. 2022; Tak and Lee 2020).

In this thesis we have developed the first drug-loaded polymeric micelle aimed at the reduction of body weight by targeting hypothalamic CPT1A. There are very few examples of nanotechnological solutions targeting CPT1A, and all are focused on delivering either miRNA or siRNA to peripheral tumor tissue in prostate or colorectal cancer (Lin et al. 2021; Conte et al. 2020). There are also very few examples of nanoparticles targeting the hypothalamus, as most CNS-targeted nano-based therapies aim for a general brain neuron delivery (see our review by Garcia-Chica et al. 2020).

In the context of the bilateral Spain-Japan CONCORD project, in collaboration with Dr Sabina Quader and Prof. Kataoka from the Innovation Centre of

Nanomedicine, our research is also one of the first efforts to treat obesity through specific targeting of neuronal populations in the hypothalamus. A notable attempt to promote energy expenditure through the hypothalamus was recently described in Milbank et al. (Milbank et al. 2021), though the approach followed using exosomes loading gene therapy is radically different.

In the present investigation we developed polymeric nanomedicines loaded with C75-CoA, that are able to inhibit CPT1A in the brain, which is known to cause a reduction in body weight and food intake (Thomas M. Loftus et al. 2000; Makowski et al. 2013), and we have tested the ability of these nanomedicines to alter lipid metabolism *in vitro* and *in vivo*. The studies and drug administration route used in this work were initially designed aiming to target these nanomedicines to hypothalamic neurons through a dual-ligand surface decoration strategy enabling efficient crossing through the BBB and specific targeting to hypothalamic neurons or GBM tumor cells. The targeting ligands and receptors were chosen based off their differential expression in the target population. For hypothalamic neurons, a truncated derivative of NPY peptide was chosen (Ortiz et al. 2007), and for GBM cells, the cyclic RGD peptide, which has been shown to differentially bind GBM tumor cells (Anraku et al. 2017; Quader et al. 2021). However, the research began with non-surface-decorated micelles in order to validate the encapsulation process and their metabolic activity. Therefore, we synthesized in parallel (±)-C75-CoA, (+)-C75-CoA and (−)-C75-CoA for metabolic studies, and also Fluorescein-CoA, a fluorescent model particle used for uptake and micelle localization experiments.

In this thesis, two types of micelles were synthesized and tested, differing based on the polymers used. The first was formed by PEG-PAsp(DET) 12-69 (non-cross linked micelle), and the second by two polymers, PEG-PAsp(Aldehyde-PLys and PEG-PAsp(Hydrazide), which react between each

other forming a hydrazone bond (cross-linked micelle). The micelles are formed between oppositely charged block copolymers or other molecules by the release of counterions after the pairing of the oppositely charged segments (Cabral et al. 2018).

Non-cross-linked micelles were stable in water or phosphate buffer, but their stability was reduced when adding NaCl after micelle formation, in accordance with literature (Dautzenberg et al. 2004). This setback meant that non-crosslinked micelles could not be used for *in vivo* studies, which led to the necessity of developing a more stable formulation. The cross-linking of the polymers in the cross-linked micelle increases stability versus NaCl addition, which increases blood circulation time and therefore IV administration suitability. Even in cross-linked micelles, unwanted release of encapsulated drug ("leakage") usually occurs, influenced by factors such as temperature, salt concentration, pH and buffer choice. To reduce the unwanted leakage, a strategy to bind C75-CoA covalently to the polymer through a pH-sensitive bond was developed (Quader et al. 2017). Covalently bound drug should not be easily released from the polymer, even in a micelle destabilization event, and should have no activity until cleaved from the polymer in low pH environments, such as lysosomes or late endosomes. This strategy required C75 to be modified to add a reactive group for conjugation to the polymer (see Annex). We chose two possible modifications, the addition of a halogenated substituent near the lactone ring, or the addition of a ketone group (Fig 1-Annex). The former molecule was never obtained due to problems in the synthesis, but the latter was accomplished after a similar synthesis route to that of C75, but starting with different reactants. We expected this C75 derivative to preserve CPT1A inhibitory capacity, as the modification was performed far from the moiety needed for the docking in CPT1A active center. However, this C75-derived molecule had no CPT1A inhibitory activity (Fig 2-Annex). Therefore, this strategy was not followed through. However, we

observed that the (+)-C75=O molecule and its CoA derivative produced a stronger cytotoxic effect compared to (+)-C75. Notably, this effect, unlike that of (+)-C75 and its CoA conjugate, was independent of the conjugation of CoA (Fig 3-Annex). While many aspects of the (+)-C75=O molecule remain unknown, it is worth exploring whether this molecule can bind CPT1A, how it enters the cells and how it produces its cytotoxic effects.

An immediate consequence of the PIC micelles formation happening through interactions between oppositely charged blocks is the necessity for the drug to be negatively charged. For this reason, we were only able to encapsulate C75-CoA, as free C75 does not have sufficient negative charges. Encapsulation of C75 would have been useful as the encapsulation of a lower molecular weight drug would have increased the drug to polymer ratio, allowing the minimization of polymer concentration and thus possible side effects derived from the polymers, which in any case have been thoroughly shown to be innocuous (Maurya et al. 2019; Zielinska et al. 2020). Furthermore, it is known that C75-CoA is formed in the hypothalamus when C75 is administered (Mera et al. 2009). Encapsulation of C75 would also increase the concentration of the drug, therefore reducing the administration volume, which could be important for future applications via intranasal administration.

Regarding the cargo, several different nanomedicines were prepared. They could be classified in two groups: C75-CoA-loaded micelles and Fluorescein-CoA-loaded micelles. C75-CoA-loaded micelles were prepared encapsulating the racemic C75-CoA mixture and also separately encapsulating the (+)- and (−)-C75-CoA forms, with the purpose of elucidating the differential effects of encapsulated forms of C75 compared to the free forms of C75. On the other hand, the Fluorescein-CoA-loaded micelle was produced as a fluorescent model particle to better understand the *in vitro* characteristics of the micelle, as well as the *in vivo* biodistribution. Fluorescein does not conjugate to

Coenzyme A spontaneously under alkaline conditions, but is conjugated via a maleimide linker. Despite the different cargo, Fluorescein-CoA-loaded micelles present highly similar physicochemical characteristics compared to C75-CoA-loaded micelles.

After synthetizing and characterizing the different nanomedicines, we subsequently conducted *in vitro* assays using GT1-7, a hypothalamic neuronal cell line, and U87MG, a GBM cell line. In the first chapter, we investigated the ability of non-crosslinked micelles to enter these cells, modify lipid metabolism, and induce toxic effects. We also examined the effects of different forms of C75 and C75-CoA in cell survival and energy metabolism.

C75, etomoxir and fluorescein are small hydrophobic molecules that have been reported to readily enter cells and produce inhibitory and cytotoxic effects (Kuhajda 2000). However, there was no available literature data concerning C75-CoA uptake and its effects in cell culture. Using Fluorescein-CoA micelle, we observed that CoA conjugates were less internalized into GT1-7 and U87MG cell lines than the loaded micelles. Additionally, in 3D spheroids of the above cell lines, we found Fluorescein-CoA micelle to diffuse more easily through the spheroids than free Fluorescein-CoA conjugate. These results show that encapsulated CoA conjugates are more easily taken up by cells and that they also diffuse more easily through the extracellular matrix. Our hypothesis is that conjugation with CoA affects polarity and hydrophobicity of this moiety, severely reducing its ability to cross lipid membranes. Encapsulation in PIC micelles, extensively shown to be internalized by living cells, circumvents this issue.

We explored the effects of the different C75 and C75-CoA moieties in neuronal and GBM cell lines. In general, CoA forms produced less inhibition and cytotoxicity than their encapsulated counterparts. We also performed ATP

inhibition assays in order to elucidate whether encapsulation of C75-CoA moieties has an effect in their capacity to alter cell energy metabolism. We found that encapsulation increased ATP synthesis inhibition of all moieties.

We were also interested in unraveling the actions of the different enantiomeric mixtures of C75 and whether CoA conjugation and encapsulation had a specific role. In line with our hypothesis, each of the enantiomeric forms, (±)-C75-CoA, (+)-C75-CoA and (–)-C75-CoA, were more cytotoxic when encapsulated than their free counterparts. Moreover, there was no difference between the encapsulated enantiomeric forms in the total FAO inhibition assay, but there appear to be slight differences in the inhibition of the two fates of FAO, though the differences could be cell-line related. Interestingly, in the ATP synthesis inhibition assay, it is quite clear that encapsulated (–)-C75-CoA produces the strongest inhibition of ATP synthesis, even though (–)-C75-CoA has been proven not to inhibit CPT1A nor FAS (Makowski et al. 2013). One possible explanation might be that C75-CoA forms could be broken inside the cell, and that when (–)-C75-CoA is administered, it is broken down into (–)-C75, that inhibits FAS and indirectly CPT1A via malonyl-CoA accumulation. This possibility needs to be further explored, as it would also have strong implications for the mode of action of (±)-C75-CoA.

Taken together, these results suggest that in fact drug uptake, facilitated by encapsulation, increases cytotoxicity, as well as FAO and ATP inhibitory activity of C75-CoA.

After characterizing the behavior of C75-CoA micelles in cell culture, our interest turned toward exploring their *in vivo* effects. It is worth noting that, despite our initial interest in using C75-CoA micelles as a treatment for GBM, the relatively small cytotoxic effect of C75-CoA and C75-CoA micelles in

U87MG did not warrant their use for *in vivo* experiments. Hence, we redirected our focus to the use of C75-CoA micelles in obesity research.

For all *in vivo* experiments, we used (±)-C75-CoA crosslinked micelles. As mentioned earlier, these crosslinked micelles were developed to enhance stability of the micelles after administration. Additionally, they were found to improve ATP synthesis inhibition and cellular uptake in the GT1-7 cell line when compared to non-crosslinked micelles. On the other hand, *in vivo* experiments exploring the effect of C75-CoA micelles in food intake and body weight were primarily conduced with the micelle encapsulating the racemic mixture of C75. Previously, we tested both enantiopure forms and the racemic mixture of free C75, and no difference was observed between (+)-C75-CoA and (±)-C75-CoA (data not shown). This result was further supported by FAO inhibition assays.

A major finding of this research was that ICV administration of (±)-C75-CoA micelles was able to reduce food intake and body weight in lean mice compared to free (±)-C75-CoA and (±)-C75. The results are comparable to others obtained via drug-induced or genetic inhibition of CPT1A (Obici et al. 2003; Gao et al. 2003). These effects are suggested to occur due to a decrease in the expression of orexigenic neuropeptide NPY and increase of expression of anorexigenic neuropeptide POMC in neurons of the melanocortin system. Indeed, intraperitoneal administration of C75 has been shown to reduce expression of NPY and AgRP, and increase expression of POMC in lean mice, compared to fasted controls (Shimokawa et al. 2002). Similar findings have been described by ICV administration in lean rats (Aja et al. 2006). These results are in line with the aforementioned *in vitro* results, suggesting that C75-CoA is unable to reduce food intake and body weight similarly to free C75, and that encapsulation of C75-CoA enhances its cell uptake and its effects on food intake and body weight. Following experiments will address the ability of

(±)-C75-CoA micelles to reduce food intake and body weight in diet-induced obesity (DIO) mice models. (±)-C75 treatment, either orally or via ICV, has already been demonstrated to reduce food intake and body weight in DIO models (T M Loftus et al. 2000; Kim et al. 2004). We expect ICV (±)-C75-CoA micelles to behave similarly in lean and obese mice models regarding body weight loss and food intake reduction.

After showing the effect of C75-CoA micelle on hunger-related neuropeptides, we explored neuronal activation in the main hypothalamic neuronal circuits involved in feeding. The micelle treatment produced significant changes in neuronal activation of the ARC and PVN hypothalamic nuclei, specifically increasing c-FOS expression compared to the free drug. The results obtained are consistent with previous data (Gao et al. 2003). Although in this experiment we do not know precisely which specific neuronal subpopulation within the nucleus is activated, C75 would be expected to activate POMC neurons and inhibit NPY/AgRP neurons, according to previous literature using C75 or by gene deletion of CPT1A in the ARC (Shimokawa et al. 2002). However, there are other reports showing nonspecific neuronal activation by C75 (Takahashi et al. 2004). The observed inhibition of ARC neuronal activity despite the increase in PVN neuronal activity point to an activation of POMC but no NPY/AgRP. However, another interesting possibility is that PVN neuronal activation might occur due to C75-induced activation of the extrahypothalamic NTS and AP areas (Gao et al. 2003). Looking at c-FOS expression in these nuclei after treatment with C75-CoA micelle would help elucidate the actual mechanism for the activation of the PVN.

Additionally, (±)-C75-CoA micelle treatment, but not the free drug, affected the expression of energy metabolism markers in the liver. Specifically, CPT1A and PEPCK expression was elevated, whereas PKL was reduced. It has been previously described that genetic activation of CPT1A in the VMH causes

changes in peripheral energy metabolism markers, as well as hyperphagia and body weight increase (Mera et al. 2014). However, the described effects correspond to a long-term forced activation of CPT1A in the hypothalamus. We could not find any description on free C75 effects in peripheral energy metabolism markers. Nevertheless, increased expression of liver FAO (CPT1A) and gluconeogenesis (PEPCK) markers is consistent with a response to C75 treatment as well as fasting situation. Furthermore, elevated expression of thermogenesis markers in BAT suggests a sympathetic nervous system signaling through POMC neuronal activation (López et al. 2010).

Altogether, these results conclude that the observed effects are in fact caused by the C75-CoA micelle administration. Free C75-CoA was unable to induce most of these specific results, likely due to its inability to enter target cells as easily as C75-CoA micelle. To further confirm these findings, additional experiments such as neurocytometry to assess cell uptake *in* vivo, as well as *in vivo* CPT1A and FAO inhibition assays, should be conducted to rule out other possibilities.

We also examined hypothalamic microglia inflammation to ensure that the administration of C75-CoA-PM did not trigger any reactivity and also to verify that microglial inflammation was not the cause of the loss of appetite (Dantzer 2001; De Luca et al. 2020). Indeed, no significant differences were found in microglia activation by Iba1 staining across treatments and vehicle administration, confirming that none of the treatments triggered an inflammatory response that could lead to a loss of appetite.

We were interested in the cellular and subcellular localization of the C75-CoA-PM after ICV administration. Contrary to our initial hypothesis, ICV administered Fluorescein-CoA-PM are not internalized by astrocytes or microglia, but they appear to be internalized by neurons at the investigated

timepoints. There is a possibility that astrocytes internalize the micelles and then Fluorescein is passed to neurons. However, we have never observed stained astrocytes. Immunofluorescence colocalization between Fluorescein and neuronal markers yielded positive results but does not explain the totality of the fluorescein staining, which is both extensive throughout the brain, but very confined to specific cells. Taking into account that the internalization capacity of neurons in the micro and nano scale has been extensively documented (Rennick et al. 2021; Manzanares et al. 2020). Our current working hypothesis assumes that stained cells either belong to a neuronal population expressing a specific surface receptor we have not identified, or that they were in a specific electrophysiological state that allowed them to internalize the nanoparticles. The latter possibility, along with the importance of nanoparticle charge for brain distribution and neuronal uptake, have been already discussed (Dante et al. 2017; Bonaccorso et al. 2017). This will be evaluated in the near future.

In summary, the acute central administration of C75-CoA-PM shows promising results in reducing appetite, food intake, and body weight in lean mice by acting on hypothalamic neurons of the melanocortin system, while also producing positive peripheral effects. However, further research is needed on the precise mechanisms of cell uptake, localization, and neuronal activity inhibition. An immediate priority should involve decorating the micelles with specific ligands for hypothalamic neurons. Rigorously characterizing the cell uptake and distribution throughout the brain and body of these decorated micelles, and comparing this distribution to undecorated micelles, is crucial. Furthermore, it is imperative to assess the potential of this nanomedicine to produce similar effects in mouse models of obesity and establish a feasible and reliable administration pathway. If these challenges are addressed, the encapsulation of C75 could become a valuable strategy to achieve results with

lower doses and reduced side effects, opening the door to the repurposing and reevaluation of previously overlooked drugs.

CONCLUSIONS

The results obtained up to this point allows us to draw the following conclusions:

1. (±)-C75-CoA, its enantiomers, and Fluorescein-CoA can be effectively encapsulated in PIC micelles with various polymers.

2. The encapsulation of C75-CoA and Fluorescein-CoA produced micelles in the range of 60nm in size, with a neutral Z-potential, stability at 4°C, and ease of reproducibility. Fluorescein-CoA micelles serve as a suitable model for the behavior of C75-CoA micelles.

3. Fluorescein-CoA micelles exhibited higher internalization by GT1-7 neurons and U87MG glioblastoma cell lines than free Fluorescein-CoA *in vitro*, and they demonstrated deeper diffusion in 3D spheroids of these cell types.

4. All forms of encapsulated C75-CoA inhibited ATP synthesis and FAO more effectively in GT1-7 and U87MG cell lines compared to their non-encapsulated C75-CoA counterparts, without affecting cell viability. This suggests a notable effect on lipid metabolism.

5. Encapsulated C75-CoA forms showed higher cytotoxicity than free C75-CoA in GT1-7 and U87MG cell lines, comparable to the cytotoxic observed with free C75 forms and etomoxir.

6. ICV injection of (±)-C75-CoA crosslinked micelles led to a reduction in body weight and food intake in lean mice, compared to free drug and vehicle. This reduction is attributed to the modulation in hunger-related neuropeptides.

7. ICV Injection of (±)-C75-CoA crosslinked micelles induces a shift in liver energy metabolism markers consistent with a satiating effect in lean mice. Additionally, it stimulates an increase in BAT thermogenesis markers. These changes were not observed with free (±)-C75-CoA.

8. Injection of (±)-C75-CoA crosslinked micelles increased the activation of neurons in the PVN but not in the ARC, suggesting a specific mode of action for the micelle's inhibition.

9. In conclusion, our synthesis of C75-CoA-loaded PIC micelles demonstrates their ability to modulate *in vitro* lipid metabolism and reduce food intake and body weight in mice through the modulation of hunger-related hypothalamic neuropeptides.

As the next phase of our research, we have initiated the decoration of micelles with two different targeting ligands designed for hypothalamic neurons. The ligands chosen are PYY (25-36), a peptide derived from PYY, and salmon calcitonin. Both peptides exhibit strong tropism for hypothalamic neurons. With these modified micelles in hand, our goal is to validate their efficacy in obese mouse models. Additionally, we aim to characterize how the decoration alters micelle distribution in the brain and its impact on hunger and satiety. Furthermore, we are actively exploring alternative drug administration pathways, including intranasal administration, to enhance the versatility of our approaches.

ABBREVIATIONS

ACC	Acetyl-CoA Carboxylase
ACP	Acyl-carrier protein
AEI	Agencia Estatal de Investigación
AEMPS	Agencia Española de Medicamentos y Productos Sanitarios
AMED	Agency for Medical Research and Development (Japan)
AMPK	AMP-activated protein kinase
ANOVA	Analysis Of Variance
AP	Area Postrema
ARC	Arcuate nucleus
ASO	Anti-Sense Oligonucleotide
ASP	Acid Soluble Products
AT	Activity Thermogenesis
BAT	Brown Adipose Tissue
BBB	Blood-Brain Barrier
BLA-NCA	Benzyl-L-Aspartate *N*-Carboxyanhydride
BMI	Body Mass Index
BMR	Basal Metabolic Rate
BSA	Bovine Serum Albumin
CAC	Critical Association Concentration
CACT	Carnitine Acylcarnitine Transferase
CART	Cocaine and Amphetamine-Regulated Transcript
CCK	Cholecystokinin
CCK8	Cell Counting Kit-8
CIDEA	Cell Death Inducing DFFA Like Effector A
CLSM	Confocal Laser Scanning Microscopy
CNS	Central Nervous System
COI	Center Of Innovation (Japan)
CPT1	Carnitine Palmitoyl Transferase 1
CPT1A	Carnitine Palmitoyl Transferase 1 A

CPT1B	Carnitine Palmitoyl Transferase 1 B
CPT1C	Carnitine Palmitoyl Transferase 1 C
CPT2	Carnitine Palmitoyl Transferase 2
aCSF	Artificial Cerebrospinal Fluid
CVD	Cardiovascular Disease
DMF	Dimethyl Formamide
DCM	Dichloromethane
DET	Diethylene Triamine
DIO	Diet-Induced Obesity
DLS	Dynamic Light Scattering
DMH	Dorsomedial nucleus of the Hypothalamus
DMSO	Dimethyl Sulfoxide
DP	Degrees of Polymerization
DPSS	Diode-Pumped Solid State Laser
DS	Degrees of Substitution
DSS	Sodium Dextran Sulfate
ECM	Extracellular Matrix
ECS	Extracellular Space
EGFR	Epidermal Growth Factor Receptor
EPR	Enhanced Permeability and Retention
ETC	Electron Transport Chain
ETO	Etomoxir
FA	Fatty Acid
FACS	Fluorescence Activated Cell Sorter
FAO	Fatty Acid Oxidation
FAS	Fatty Acid Synthase
FBS	Fetal Bovine Serum
FDA	Food and Drug Administration
FITC	Fluorescein

FRET	Förster Resonance Energy Transfer
FSC	Forward Scatter
G6Pase	Glucose-6-Phosphatase
GABA	γ-Aminobutyric Acid
GAPDH	Glyceraldehyde-3-Phosphate Dehydrogenase
GBM	Glioblastoma Multiforme
GFAP	Glial Fibrillary Acidic Protein
GHS-R	Growth Hormone Secretagogue Receptor
GLP-1	Glucagon-like Peptide 1
GLP1R	Glucagon-like Peptide 1 Receptor
GLUT1	Glucose Transporter 1
GPC	Gel Permeation Chromatography
HPLC	High Performance Liquid Chromatography
HPRT	Hypoxanthine Phosphoribosyltransferase 1
IC_{50}	Inhibitory Concentration 50%
ICV	Intracerebroventricular
IDH	Isocitrate Dehydrogenase
IF	Immunofluorescence
JSPS	Japan Society for the Promotion of Science
JST	Japan Science and Technology Agency
LCFA	Long-Chain Fatty Acid
LEPR	Leptin Receptor
LH	Lateral Hypothalamus
LHA	Lateral Hypothalamic Area
MC3R	Melanocortin Receptor 3
MC4R	Melanocortin Receptor 4
MCD	Malonyl-CoA Decarboxylase
MCH	Melanin Concentration Hormone
MCIN	Ministerio de Ciencia e Innovación

ME	Median Eminence
MFI	Mean Fluorescence Intensity
α-MSH	α-melanocyte Stimulating Hormone
MW	Molecular Weight
NAFLD	Non-Alcoholic Fatty Liver Disease
NBF	Neutral-Buffered Formaline
NMP	*N*-methyl-2-pyrrolidone
NMR	Nuclear Magnetic Resonance
NP	Nanoparticle
NPY	Neuropeptide Y
NPY1R	Neuropeptide Y Receptor 1
NPY2R	Neuropeptide Y Receptor 2
NPY5R	Neuropeptide Y Receptor 5
NTS	Nucleus of the Solitary Tract
PAA	Poly Aminoacids
PB	Phosphate Buffer
PBLA	Poly(β-benzyl-L-Aspartate)
PBN	Parabrachial Nucleus
PBS	Saline Phosphate Buffer
PEG	Poly Ethylene Glycol
PEI	Poly Ethylene Imine
PEPCK	Phosphoenolpyruvate Carboxykinase
PGC1-α	Peroxisome Proliferator-activated Receptor γ Co-activator 1 α
PIC	Poly-Ion Complex
PKL	Piruvate Kinase Liver
PKLR	Piruvate Kinase Liver
PLGA	Poly(Lactic-co-Glycolic Acid)
PM	Polymeric Micelle
POMC	Proopiomelanocortin

PRDM16	PR Domain Containing 16
PVH	Paraventricular Hypothalamus
PVN	Paraventricular Nucleus
PYY	Peptide YY
ROP	Ring Opening Polymerization
RT	Room Temperature
SLI	Scattering Light Intensity
SLS	Static Light Scattering
SSC	Side Scatter
TCA	Tricarboxylic Acid
TDEE	Total Daily Energy Expenditure
TEF	Thermic Effect of Food
TEM	Transmission Electron Microscopy
TERT	Telomerase Reverse Transcriptase
THF	Tetrahydrofuran
UCP-1	Uncoupling Protein 1
UV	Ultra Violet
VMH	Ventromedial Hypothalamus
YY	Peptide YY
ZP	Zeta Potential

REFERENCES

Abbott, N.J., Rönnbäck, L., & Hansson, E. 2006. Astrocyte-endothelial interactions at the blood-brain barrier. *Nature Reviews Neuroscience* 7(1): p.41–53.

Aja, S. et al. 2006. Intracerebroventricular C75 decreases meal frequency and reduces AgRP gene expression in rats. *American Journal of Physiology - Regulatory Integrative and Comparative Physiology* 291(1): p.148–155.

Anand, B.K., & Brobeck, J.R. 1951. Hypothalamic control of food intake in rats and cats. *The Yale journal of biology and medicine* 24(2): p.123–140.

Anon. 2021. World Health Organization, Obesity and Overweight Fact Sheet. Available at: https://www.who.int/news-room/fact-sheets/detail/obesity-and-overweight.

Anraku, Y. et al. 2017. Glycaemic control boosts glucosylated nanocarrier crossing the BBB into the brain. *Nature Communications* 8(1).

Atasoy, D., Nicholas Betley, J., Su, H.H., & Sternson, S.M. 2012. Deconstruction of a neural circuit for hunger. *Nature* 488(7410): p.172–177.

Bae, Y., Fukushima, S., Harada, A., & Kataoka, K. 2003. Design of environment-sensitive supramolecular assemblies for intracellular drug delivery: Polymeric micelles that are responsive to intracellular pH change. *Angewandte Chemie - International Edition* 42(38): p.4640–4643.

Bae, Y., & Kataoka, K. 2009. Intelligent polymeric micelles from functional poly(ethylene glycol)-poly(amino acid) block copolymers. *Advanced Drug Delivery Reviews* 61(10): p.768–784.

Balaban, R.S. 1990. Regulation of oxidative phosphorylation in the mammalian cell. *American Journal of Physiology - Cell Physiology* 258(3

27-3).

Balaban, S., Lee, L.S., Schreuder, M., & Hoy, A.J. 2015. Obesity and cancer progression: is there a role of fatty acid metabolism? *BioMed research international* 2015(Table 1): p.274585.

Balke, H., & Nocito, A. 2013. Vom Schönheitsideal zur Krankheit - Eine Reise durch die Geschichte der Adipositas. *Praxis* 102(2): p.77–83.

Batterham, R.L. et al. 2002. Gut hormone PYY3-36 physiologically inhibits food intake. *Nature* 418(6898): p.650–654.

Bentebibel, A. et al. 2006. Novel effect of C75 on carnitine palmitoyltransferase I activity and palmitate oxidation. *Biochemistry* 45(14): p.4339–4350.

Beutler, L.R. et al. 2017. Dynamics of Gut-Brain Communication Underlying Hunger. *Neuron* 96(2): p.461-475.e5.

Bi, S., Kim, Y.J., & Zheng, F. 2012. Dorsomedial hypothalamic NPY and energy balance control. *Neuropeptides* 46(6): p.309–314.

De Bock, M. et al. 2016. Into rather unexplored terrain-transcellular transport across the blood-brain barrier. *Glia* 64(7): p.1097–1123.

Bonaccorso, A. et al. 2017. Nose to brain delivery in rats: Effect of surface charge of rhodamine B labeled nanocarriers on brain subregion localization. *Colloids and Surfaces B: Biointerfaces* 154: p.297–306.

Bouchard, C. et al. 1990. The Response to Long-Term Overfeeding in Identical Twins. *New England Journal of Medicine* 322(21): p.1477–1482.

Brady, P.S., & Brady, L.J. 1986. *Action in vivo and in vitro of 2-tetradecylglycidic acid, 2-tetradecylglycidyl-CoA and 2-tetradecylglycidylcarnitine on hepatic carnitine palmitoyltransferase.*

Brewis, A., Sturtzsreetharan, C., & Wutich, A. 2018. Obesity stigma as a globalizing health challenge. 14(1): p.1–6.

Brothers, S.P., & Wahlestedt, C. 2010. Therapeutic potential of neuropeptide y (NPY) receptor ligands. *EMBO Molecular Medicine* 2(11): p.429–439.

Brown, L.S. et al. 2019. Pericytes and neurovascular function in the healthy and diseased brain. *Frontiers in Cellular Neuroscience* 13(June): p.1–9.

Bruce, K.D., Zsombok, A., & Eckel, R.H. 2017. Lipid processing in the brain: A key regulator of systemic metabolism. *Frontiers in Endocrinology* 8(APR): p.1–11.

Cabral, H., Miyata, K., Osada, K., & Kataoka, K. 2018. Block Copolymer Micelles in Nanomedicine Applications. *Chemical Reviews* 118(14): p.6844–6892.

Careau, V. et al. 2021. Energy compensation and adiposity in humans. *Current Biology* 31(20): p.4659-4666.e2.

Casals, N. et al. 2016. Carnitine palmitoyltransferase 1C: From cognition to cancer. *Progress in Lipid Research* 61: p.134–148.

Cha, S.H., Hu, Z., Chohnan, S., & Daniel Lane, M. 2005. *Inhibition of hypothalamic fatty acid synthase triggers rapid activation of fatty acid oxidation in skeletal muscle*.

Cha, S.H., Hu, Z., Chohnan, S., & Lane, M.D. 2005. Inhibition of hypothalamic fatty acid synthase triggers rapid activation of fatty acid oxidation in skeletal muscle. *Proceedings of the National Academy of Sciences of the United States of America* 102(41): p.14557–14562.

Chamundeeswari, M., Jeslin, J., & Verma, M.L. 2019. Nanocarriers for drug delivery applications. *Environmental Chemistry Letters* 17(2): p.849–

865.

Cirillo, A. et al. 2014. High grade glioblastoma is associated with aberrant expression of ZFP57, a protein involved in gene imprinting, and of CPT1A and CPT1C that regulate fatty acid metabolism. *Cancer Biology and Therapy* 15(6): p.735–741.

Cole, N.B. et al. 2002. Lipid droplet binding and oligomerization properties of the Parkinson's disease protein α-synuclein. *Journal of Biological Chemistry* 277(8): p.6344–6352.

Conte, R. et al. 2020. Cationic polymer nanoparticles-mediated delivery of mir-124 impairs tumorigenicity of prostate cancer cells. *International Journal of Molecular Sciences* 21(3): p.7–10.

Cowley, M.A. et al. 2001. Leptin activates anorexigenic POMC neurons through a neural network in the arcuate nucleus. 411(May).

Cummings, D.E. et al. 2001. A Preprandial Rise in Plasma Ghrelin Levels Suggests a Role in Meal Initiation in Humans. *Diabetes* 50(8): p.1714–1719.

Currie, E., Schulze, A., Zechner, R., Walther, T.C., & Farese, R. V. 2013. Cellular fatty acid metabolism and cancer. *Cell Metabolism* 18(2): p.153–161.

D'agnony, G., Rosenfeld, I.S., Awaya, J., Ōmura, S., & Vagelos, P.R. 1973. Inhibition of fatty acid synthesis by the antibiotic cerulenin: Specific inactivation of β-ketoacyl-acyl carrier protein synthetase. *Biochimica et Biophysica Acta (BBA) - Lipids and Lipid Metabolism* 326(2): p.155–166.

D'Alessio, D.A. et al. 1988. Thermic effect of food in lean and obese men. *Journal of Clinical Investigation* 81(6): p.1781–1789.

Dante, S. et al. 2017. Selective Targeting of Neurons with Inorganic
Nanoparticles: Revealing the Crucial Role of Nanoparticle Surface
Charge. *ACS Nano* 11(7): p.6630–6640.

Dantzer, R. 2001. Cytokine-induced sickness behavior: Mechanisms and
implications. *Annals of the New York Academy of Sciences* 933(33):
p.222–234.

Dautzenberg, H., & Rother, G. 2004. Response of Polyelectrolyte Complexes
to Subsequent Addition of Sodium Chloride: Time-Dependent Static
Light Scattering Studies. *Macromolecular Chemistry and Physics* 205(1):
p.114–121.

Declercq, P.E. et al. 1987. Characterization of the mitochondrial carnitine
palmitoyltransferase enzyme system. I. Use of inhibitors. *Journal of
Biological Chemistry* 262(20): p.9812–9821.

Dériaz O, Fournier G, Tremblay A, Després JP, B.C. 1992. Lean-body-mass
before and after composition and resting energy. *Am J Clin Nutr* 56(5):
p.840–847.

Dietrich, M.O., & Horvath, T.L. 2012. Limitations in anti-obesity drug
development: The critical role of hunger-promoting neurons. *Nature
Reviews Drug Discovery* 11(9): p.675–691.

DiMicco, J.A., & Zaretsky, D. V. 2007. The dorsomedial hypothalamus: A new
player in thermoregulation. *American Journal of Physiology - Regulatory
Integrative and Comparative Physiology* 292(1).

Eknoyan, G. 2006. A History of Obesity, or How What Was Good Became
Ugly and Then Bad. *Advances in Chronic Kidney Disease* 13(4): p.421–
427.

Escartin, C. et al. 2007. Activation of astrocytes by CNTF induces metabolic

plasticity and increases resistance to metabolic insults. *Journal of Neuroscience* 27(27): p.7094–7104.

Fadó, R., Rodríguez-Rodríguez, R., & Casals, N. 2021. The return of malonyl-CoA to the brain: Cognition and other stories. *Progress in Lipid Research* 81.

Farias, M.M., Cuevas, A.M., & Rodriguez, F. 2011. Set-point theory and obesity. *Metabolic Syndrome and Related Disorders* 9(2): p.85–89.

Fosch, A. et al. 2023. Central Regulation of Brown Fat Thermogenesis in Response to Saturated or Unsaturated Long-Chain Fatty Acids. *International Journal of Molecular Sciences* 24(2).

Gao, S., & Lane, M.D. 2003. Effect of the anorectic fatty acid synthase inhibitor C75 on neuronal activity in the hypothalamus and brainstem. *Proceedings of the National Academy of Sciences of the United States of America* 100(10): p.5628–5633.

Gao, S., Serra, D., Keung, W., Hegardt, F.G., & Lopaschuk, G.D. 2013. Important role of ventromedial hypothalamic carnitine palmitoyltransferase-1a in the control of food intake. *Am J Physiol Endo-crinol Metab* 305: p.336–347.

Gao, Y., & Sun, T. 2016. Molecular regulation of hypothalamic development and physiological functions. *Molecular Neurobiology* 53(7): p.4275–4285.

Garcia-Chica, J. et al. 2020. An overview of nanomedicines for neuron targeting. *Nanomedicine* 15(16): p.1617–1636.

Garvey, W.T. 2022. Is Obesity or Adiposity-Based Chronic Disease Curable: The Set Point Theory, the Environment, and Second-Generation Medications. *Endocrine Practice* 28(2): p.214–222.

Guo, Q. et al. 2020. A dual-ligand fusion peptide improves the brain-neuron targeting of nanocarriers in Alzheimer's disease mice. *Journal of Controlled Release* 320: p.347–362.

Guo, R. et al. 2020. The function and mechanism of lipid molecules and their roles in the diagnosis and prognosis of breast cancer. *Molecules* 25(20).

Gupta, P., Furness, S.G.B., Bittencourt, L., Hare, D.L., & Wookey, P.J. 2020. Building the case for the calcitonin receptor as a viable target for the treatment of glioblastoma. *Therapeutic Advances in Medical Oncology* 12: p.1–15.

Guth, A. et al. 2020. Targeting fat oxidation in mouse prostate cancer decreases tumor growth and stimulates anti-cancer immunity. *International Journal of Molecular Sciences* 21(24): p.1–14.

Hainer, V. et al. 2000. *Intrapair resemblance in very low calorie diet-induced weight loss in female obese identical twins*.

Hamilton, J.A., Hillard, C.J., Spector, A.A., & Watkins, P.A. 2007. Brain uptake and utilization of fatty acids, lipids and lipoproteins: Application to neurological disorders. In *Journal of Molecular Neuroscience*, 2–11.

Harris, R.B.S., Kasser, T.R., & Martin, R.J. 1986. Dynamics of recovery of body composition after overeeding, food restriction or starvation of mature female rats. *Journal of Nutrition* 116(12): p.2536–2546.

Hetherington, A.W., & Ranson, S.W. 1940. Hypothalamic lesions and adiposity in the rat. *The Anatomical Record* 78(2): p.149–172.

Hill, J.O. 2009. Can a small-changes approach help address the obesity epidemic? a report of the joint task force of the american society for nutrition, institute of food technologists, and international food information council. *American Journal of Clinical Nutrition* 89(2): p.477–

484.

Hill, J.O., Wyatt, H.R., & Peters, J.C. 2012. Energy balance and obesity. *Circulation* 126(1): p.126–132.

Holubarsch, C.J.F. et al. 2007. A double-blind randomized multicentre clinical trial to evaluate the efficacy and safety of two doses of etomoxir in comparison with placebo in patients with moderate congestive heart failure: the ERGO (etomoxir for the recovery of glucose oxidation) study. *Clinical Science* 113(4): p.205–212.

Hu, K. et al. 2011. Lactoferrin conjugated PEG-PLGA nanoparticles for brain delivery: Preparation, characterization and efficacy in Parkinson's disease. *International Journal of Pharmaceutics* 415(1): p.273–283.

Hu, Z., Seung, H.C., Van Haasteren, G., Wang, J., & Lane, M.D. 2005. Effect of centrally administered C75, a fatty acid synthase inhibitor, on ghrelin secretion and its downstream effects. *Proceedings of the National Academy of Sciences of the United States of America* 102(11): p.3972–3977.

Institute, B.S. 2007. *Terminology for nanomaterials. Publicly available specification 136*.

Jais, A., & Brüning, J.C. 2022. Arcuate Nucleus-Dependent Regulation of Metabolism-Pathways to Obesity and Diabetes Mellitus. *Endocrine Reviews* 43(2): p.314–328.

Jariwala, N. et al. 2021. CPT1A and fatty acid β-oxidation are essential for tumor cell growth and survival in hormone receptor-positive breast cancer. *NAR Cancer* 3(3).

Jernberg, J.N., Bowman, C.E., Wolfgang, M.J., & Scafidi, S. 2017. Developmental regulation and localization of carnitine

palmitoyltransferases (CPTs) in rat brain. *Journal of Neurochemistry* 142(3): p.407–419.

Jiang, N. et al. 2022. Fatty acid oxidation fuels glioblastoma radioresistance with CD47-mediated immune evasion. *Nature Communications* 13(1): p.1–20.

Kahler, A., Zimmermann, M., & Langhans, W. 1999. Suppression of Hepatic Fatty Acid Oxidation and Food Intake in Men. 15(December): p.819–828.

Kaplan, L.M. et al. 2018. Perceptions of Barriers to Effective Obesity Care: Results from the National ACTION Study. *Obesity* 26(1): p.61–69.

Khodai, T., & Luckman, S.M. 2021. Ventromedial Nucleus of the Hypothalamus Neurons under the Magnifying Glass. *Endocrinology (United States)* 162(10): p.1–13.

Khosla, D. 2016. Concurrent therapy to enhance radiotherapeutic outcomes in glioblastoma. *Annals of Translational Medicine* 4(3): p.2–9.

Kim, E.K. et al. 2004. C75, a Fatty Acid Synthase Inhibitor, Reduces Food Intake via Hypothalamic AMP-activated Protein Kinase. *Journal of Biological Chemistry* 279(19): p.19970–19976.

Könner, A.C. et al. 2007. Insulin Action in AgRP-Expressing Neurons Is Required for Suppression of Hepatic Glucose Production. *Cell Metabolism* 5(6): p.438–449.

Kuhajda, F.P. 2000. Synthesis and antitumor activity of an inhibitor of fatty acid synthase. *Proceedings of the National Academy of Sciences* 97(7): p.3450–3454.

Lah Turnšek, T. et al. 2021. An update on glioblastoma biology, genetics, and

current therapies: Novel inhibitors of the G protein-coupled receptor CCR5. *International Journal of Molecular Sciences* 22(9).

Lam, T.K.T., Schwartz, G.J., & Rossetti, L. 2005. Hypothalamic sensing of fatty acids. *Nature Neuroscience* 8(5): p.579–584.

Lavasanifar, A., Samuel, J., & Kwon, G.S. 2002. Poly(ethylene oxide)-block-poly(L-amino acid) micelles for drug delivery. *Advanced Drug Delivery Reviews* 54(2): p.169–190.

Levine, J.A. 2002. Non-exercise activity thermogenesis (NEAT). *Best Practice and Research: Clinical Endocrinology and Metabolism* 16(4): p.679–702.

Levitsky, D.A., & Pacanowski, C.R. 2012. Free will and the obesity epidemic. *Public Health Nutrition* 15(1): p.126–141.

Liang, K. 2023. Mitochondrial CPT1A: Insights into structure, function, and basis for drug development. *Frontiers in Pharmacology* 14.

Lin, D. et al. 2021. iRGD-modified exosomes effectively deliver CPT1A siRNA to colon cancer cells, reversing oxaliplatin resistance by regulating fatty acid oxidation. *Molecular Oncology* 15(12): p.3430–3446.

Liu, H. et al. 2013. Fatty acid synthase causes drug resistance by inhibiting TNF-α and ceramide production. *Journal of Lipid Research* 54(3): p.776–785.

Liu, Q., & Zhang, J. 2014. Lipid metabolism in Alzheimer's disease. *Neuroscience Bulletin* 30(2): p.331–345.

Loftus, T M et al. 2000. Reduced food intake and body weight in mice treated with fatty acid synthase inhibitors. *Science (New York, N.Y.)* 288(5475): p.2379–81.

Loftus, Thomas M. et al. 2000. Reduced food intake and body weight in mice

treated with fatty acid synthase inhibitors. *Science* 288(5475): p.2379–2381.

Lopaschuk, G.D., Wall, S.R., Olley, P.M., & Davies, N.J. 1988. Etomoxir, a carnitine palmitoyltransferase I inhibitor, protects hearts from fatty acid-induced ischemic injury independent of changes in long chain acylcarnitine. *Circulation Research* 63(6): p.1036–1043.

López, M. et al. 2010. Hypothalamic AMPK and fatty acid metabolism mediate thyroid regulation of energy balance. *Nature Medicine* 16(9): p.1001–1008.

López, M., Nogueiras, R., Tena-Sempere, M., & Diéguez, C. 2016. Hypothalamic AMPK: a canonical regulator of whole-body energy balance. *Nature reviews. Endocrinology* 12(7): p.421–32.

De Luca, S.N., Miller, A.A., Sominsky, L., & Spencer, S.J. 2020. Microglial regulation of satiety and cognition. *Journal of Neuroendocrinology* 32(3): p.1–12.

Makowski, K. 2012. Síntesis de análogos de C75 y su evaluación como potenciales fármacos anoréxicos y antitumorales.

Makowski, K. et al. 2013. Differential pharmacologic properties of the two C75 enantiomers: (+)-C75 is a strong anorectic drug; (-)-C75 has antitumor activity. *Chirality* 25(5): p.281–287.

Manzanares, D., & Ceña, V. 2020. Endocytosis: The nanoparticle and submicron nanocompounds gateway into the cell. *Pharmaceutics* 12(4): p.1–22.

Maurya, A. et al. 2019. Strategic use of nanotechnology in drug targeting and its consequences on human health: A focused review. *Interventional Medicine and Applied Science* 11(1): p.38–54.

Mcgarry, J.D., & Brown, N.F. 1997. *The mitochondrial carnitine palmitoyltransferase system From concept to molecular analysis*.

Mera, P. et al. 2009. C75 is converted to C75-CoA in the hypothalamus, where it inhibits carnitine palmitoyltransferase 1 and decreases food intake and body weight. *Biochemical Pharmacology* 77(6): p.1084–1095.

Mera, P. et al. 2014. Long-term increased carnitine palmitoyltransferase 1A expression in ventromedial hypotalamus causes hyperphagia and alters the hypothalamic lipidomic profile. *PLoS ONE* 9(5): p.1–13.

Milbank, E. et al. 2021. Small extracellular vesicle-mediated targeting of hypothalamic AMPKα1 corrects obesity through BAT activation. *Nature Metabolism* 3(10): p.1415–1431.

Miyata, S. 2015. New aspects in fenestrated capillary and tissue dynamics in the sensory circumventricular organs of adult brains. *Frontiers in Neuroscience* 9(OCT).

Morillas, M. et al. 2003. Identification of conserved amino acid residues in rat liver carnitine palmitoyltransferase I critical for malonyl-CoA inhibition: Mutation of methionine 593 abolishes malonyl-CoA inhibition. *Journal of Biological Chemistry* 278(11): p.9058–9063.

Moullé, V.S., Picard, A., Le Foll, C., Levin, B.E., & Magnan, C. 2014. Lipid sensing in the brain and regulation of energy balance. *Diabetes and Metabolism* 40(1): p.29–33.

Mountjoy, K.G. 2015. Pro-Opiomelanocortin (POMC) Neurones, POMC-Derived Peptides, Melanocortin Receptors and Obesity: How Understanding of this System has Changed Over the Last Decade. *Journal of Neuroendocrinology* 27(6): p.406–418.

Müller, T.D. et al. 2015. Ghrelin. *Molecular Metabolism* 4(6): p.437–460.

Müller, T.D. et al. 2019. Glucagon-like peptide 1 (GLP-1). *Molecular Metabolism* 30: p.72–130.

Müller, T.D., Blüher, M., Tschöp, M.H., & DiMarchi, R.D. 2022. Anti-obesity drug discovery: advances and challenges. *Nature Reviews Drug Discovery* 21(3): p.201–223.

Murphy, M.P. 2009. How mitochondria produce reactive oxygen species. *Biochemical Journal* 417(1): p.1–13.

Musumeci, T. et al. 2018. Oxcarbazepine free or loaded PLGA nanoparticles as effective intranasal approach to control epileptic seizures in rodents. *European Journal of Pharmaceutics and Biopharmaceutics* 133: p.309–320.

New England Biolabs Inc. Reaction Conditions for Chemical Coupling with CoA-SH (S9352S).

Nicot, C. et al. 2004. C75 activates malonyl-CoA sensitive and insensitive components of the CPT system. *Biochemical and Biophysical Research Communications* 325(3): p.660–664.

Obici, S. et al. 2002. Central administration of oleic acid inhibits glucose production and food intake. *Diabetes* 51(2): p.271–275.

Obici, S., Feng, Z., Arduini, A., Conti, R., & Rossetti, L. 2003. Inhibition of hypothalamic carnitine palmitoyltransferase-1 decreases food intake and glucose production. *Nature Medicine* 9(6): p.756–761.

Orellana-Gavaldà, J.M. et al. 2011. Molecular therapy for obesity and diabetes based on a long-term increase in hepatic fatty-acid oxidation. *Hepatology* 53(3): p.821–832.

Ortiz, A.A. et al. 2007. A novel long-acting selective neuropeptide Y2 receptor polyethylene glycol-conjugated peptide agonist reduces food intake and body weight and improves glucose metabolism in rodents. *Journal of Pharmacology and Experimental Therapeutics* 323(2): p.692–700.

Pahuja, R. et al. 2015. Trans-blood brain barrier delivery of dopamine-loaded nanoparticles reverses functional deficits in parkinsonian rats. *ACS Nano* 9(5): p.4850–4871.

Pandey, P.R., Liu, W., Xing, F., Fukuda, K., & Watabe, K. 2012. *Anti-Cancer Drugs Targeting Fatty Acid Synthase (FAS)*.

Pandit, R., Chen, L., & Götz, J. 2020. The blood-brain barrier: Physiology and strategies for drug delivery. *Advanced Drug Delivery Reviews* 165–166: p.1–14.

Perevoshchikova, I. V, Quinlan, C.L., Orr, A.L., Gerencser, A.A., & Brand, M.D. 2013. Sites of superoxide and hydrogen peroxide production during fatty acid oxidation in rat skeletal muscle mitochondria. *Free Radical Biology and Medicine* 61: p.298–309.

Petővári, G. et al. 2020. Inhibition of Metabolic Shift can Decrease Therapy Resistance in Human High-Grade Glioma Cells. *Pathology and Oncology Research* 26(1): p.23–33.

Picard, A. et al. 2014. Physiological and pathophysiological implications of lipid sensing in the brain. *Diabetes, Obesity and Metabolism* 16: p.49–55.

Pizer, E.S. et al. 2000. Malonyl-coenzyme-A is a potential mediator of cytotoxicity induced by fatty-acid synthase inhibition in human breast cancer cells and xenografts. *Cancer Research* 60(2): p.213–218.

Quader, S. et al. 2017. cRGD peptide-installed epirubicin-loaded polymeric

micelles for effective targeted therapy against brain tumors. *Journal of Controlled Release* 258: p.56–66.

Quader, S. et al. 2021. Supramolecularly enabled pH- triggered drug action at tumor microenvironment potentiates nanomedicine efficacy against glioblastoma. *Biomaterials* 267(April 2020): p.120463.

Quarta, C. et al. 2021. POMC neuronal heterogeneity in energy balance and beyond: an integrated view. *Nature Metabolism* 3(3): p.299–308.

Rapoport, S.I. 2001. In vivo fatty acid incorporation into brain phospholipids in relation to plasma availability, signal transduction and membrane remodeling. *Journal of Molecular Neuroscience* 16(2–3): p.243–261.

Ren, Z.L. et al. 2022. Linking Nonalcoholic Fatty Liver Disease and Brain Disease: Focusing on Bile Acid Signaling. *International Journal of Molecular Sciences* 23(21).

Rennick, J.J., Johnston, A.P.R., & Parton, R.G. 2021. Key principles and methods for studying the endocytosis of biological and nanoparticle therapeutics. *Nature Nanotechnology* 16(3): p.266–276.

Rodríguez, E.M., Blázquez, J.L., & Guerra, M. 2010. The design of barriers in the hypothalamus allows the median eminence and the arcuate nucleus to enjoy private milieus: The former opens to the portal blood and the latter to the cerebrospinal fluid. *Peptides* 31(4): p.757–776.

Ronnett, G. V., Kleman, A.M., Kim, E.K., Landree, L.E., & Tu, Y. 2006. Fatty acid metabolism, the central nervous system, and feeding. *Obesity (Silver Spring, Md.)* 14 Suppl 5.

Ross, R.A., Rossetti, L., Lam, T.K.T., & Schwartz, G.J. 2010. Differential effects of hypothalamic long-chain fatty acid infusions on suppression of hepatic glucose production. *American Journal of Physiology -*

Endocrinology and Metabolism 299(4).

Rubino, F. et al. 2020. Joint international consensus statement for ending stigma of obesity. *Nature Medicine* 26(4): p.485–497.

Sarma, S., Sockalingam, S., & Dash, S. 2021. Obesity as a multisystem disease: Trends in obesity rates and obesity-related complications. *Diabetes, Obesity and Metabolism* 23(S1): p.3–16.

Schlaepfer, I.R., & Joshi, M. 2020. CPT1A-mediated Fat Oxidation, Mechanisms, and Therapeutic Potential. *Endocrinology (United States)* 161(2).

Schröder, R., Bien, K., Kott, R., Meyers, I., & Vössing, R. 1991. The relationship between Ki-67 labeling and mitotic index in gliomas and meningiomas: demonstration of the variability of the intermitotic cycle time. *Acta Neuropathologica* 82(5): p.389–394.

Schwartz, M.W., Woods, S.C., Porte, D., Seeley, R.J., & Baskin, D.G. 2000. Central nervous system control of food intake. *Nature* 404(6778): p.661–671.

Scott, M.M. et al. 2009. Leptin targets in the mouse brain. *Journal of Comparative Neurology* 514(5): p.518–532.

Shi, J., Kantoff, P.W., Wooster, R., & Farokhzad, O.C. 2017. Cancer nanomedicine: Progress, challenges and opportunities. *Nature Reviews Cancer* 17(1): p.20–37.

Shimokawa, T., Kumar, M. V., & Lane, M.D. 2002. Effect of a fatty acid synthase inhibitor on food intake and expression of hypothalamic neuropeptides. *Proceedings of the National Academy of Sciences of the United States of America* 99(1): p.66–71.

Sierra, A.Y. et al. 2008. CPT1c is localized in endoplasmic reticulum of neurons and has carnitine palmitoyltransferase activity. *Journal of Biological Chemistry* 283(11): p.6878–6885.

Speakman, J.R. et al. 2011. Set points, settling points and some alternative models: Theoretical options to understand how genes and environments combine to regulate body adiposity. *DMM Disease Models and Mechanisms* 4(6): p.733–745.

Sperry, J. et al. 2020. Glioblastoma Utilizes Fatty Acids and Ketone Bodies for Growth Allowing Progression during Ketogenic Diet Therapy. *iScience* 23(9).

Spiegelman, B.M., & Flier, J.S. 2001. Obesity and the Regulation Review of Energy Balance total fast of approximately 150 days! This impressive energy reserve is due both to the high energy content of triglycerides versus polysaccharides, and the fact. *Cell* 104: p.531–543.

Stark, R., Reichenbach, A., & Andrews, Z.B. 2015. Hypothalamic carnitine metabolism integrates nutrient and hormonal feedback to regulate energy homeostasis. *Molecular and Cellular Endocrinology* 418: p.9–16.

Sun, Y., Wang, P., Zheng, H., & Smith, R.G. 2004. Ghrelin stimulation of growth hormone release and appetite is mediated through the growth hormone secretagogue receptor. *Proceedings of the National Academy of Sciences of the United States of America* 101(13): p.4679–4684.

Sutton, A.K., Myers, M.G., & Olson, D.P. 2016. The Role of PVH Circuits in Leptin Action and Energy Balance. *Annual Review of Physiology* 78: p.207–221.

Sweeney, M.D., Zhao, Z., Montagne, A., Nelson, A.R., & Zlokovic, B. V. 2019. Blood-brain barrier: From physiology to disease and back. *Physiological*

Reviews 99(1): p.21–78.

Tak, Y.J., & Lee, S.Y. 2020. Anti-obesity drugs: Long-term efficacy and safety: An updated review. *World Journal of Men's Health* 38.

Takahashi, K.A., Smart, J.L., Liu, H., & Cone, R.D. 2004. The Anorexigenic Fatty Acid Synthase Inhibitor, C75, Is a Nonspecific Neuronal Activator. *Endocrinology* 145(1): p.184–193.

Van Tellingen, O. et al. 2015. Overcoming the blood-brain tumor barrier for effective glioblastoma treatment. *Drug Resistance Updates* 19: p.1–12.

Thomsen, M.S., Routhe, L.J., & Moos, T. 2017. The vascular basement membrane in the healthy and pathological brain. *Journal of Cerebral Blood Flow and Metabolism* 37(10): p.3300–3317.

Thon, M., Hosoi, T., & Ozawa, K. 2016. Possible integrative actions of leptin and insulin signaling in the hypothalamus targeting energy homeostasis. *Frontiers in Endocrinology* 7(OCT).

Tracey, T.J., Steyn, F.J., Wolvetang, E.J., & Ngo, S.T. 2018. Neuronal lipid metabolism: Multiple pathways driving functional outcomes in health and disease. *Frontiers in Molecular Neuroscience* 11(January): p.1–25.

Urbanska, K., Sokolowska, J., Szmidt, M., & Sysa, P. 2014. Glioblastoma multiforme - An overview. *Wspolczesna Onkologia* 18(5): p.307–312.

Wakil, S.J., Stoops, J.K., & Joshi, V.C. 1983. Fatty acid synthesis and its regulation. *Ann. Rev. Biochem.* (52): p.537–79.

Wang, D. et al. 2015. Whole-brain mapping of the direct inputs and axonal projections of POMC and AgRP neurons. *Frontiers in Neuroanatomy* 9(MAR).

Wang, P. et al. 2018. Systemic delivery of BACE1 siRNA through neuron-

targeted nanocomplexes for treatment of Alzheimer's disease. *Journal of Controlled Release* 279: p.220–233.

Waterson, M.J., & Horvath, T.L. 2015. Neuronal Regulation of Energy Homeostasis: Beyond the Hypothalamus and Feeding. *Cell Metabolism* 22(6): p.962–970.

Weber, M. et al. 2020. Liver CPT1A gene therapy reduces diet-induced hepatic steatosis in mice and highlights potential lipid biomarkers for human NAFLD. *FASEB Journal* 34(9): p.11816–11837.

Weller, M. et al. 2021. EANO guidelines on the diagnosis and treatment of diffuse gliomas of adulthood. *Nature Reviews Clinical Oncology* 18(3): p.170–186.

Wilczewska, A.Z., Niemirowicz, K., Markiewicz, K.H., & Car, H. 2012. Nanoparticles as drug delivery systems. *Pharmacological Reports* 64(5): p.1020–1037.

Wilding, J.P.H. et al. 2021. Once-Weekly Semaglutide in Adults with Overweight or Obesity. *New England Journal of Medicine* 384(11): p.989–1002.

Wing, R.R. et al. 2011. Benefits of modest weight loss in improving cardiovascular risk factors in overweight and obese individuals with type 2 diabetes. *Diabetes Care* 34(7): p.1481–1486.

Wolfgang, M.J., & Lane, M.D. 2006. Control of energy homeostasis: role of enzymes and intermediates of fatty acid metabolism in the central nervous system. *Annual review of nutrition* 26: p.23–44.

Woods, S.C., Lotter, E.C., McKay, L.D., & Porte, D. 1979. Chronic intracerebroventricular infusion of insulin reduces food intake and body weight of baboons. *Nature* 282(5738): p.503–505.

Wu, J. 2021. The enhanced permeability and retention (Epr) effect: The significance of the concept and methods to enhance its application. *Journal of Personalized Medicine* 11(8).

Yang, D. et al. 2022. Lipid metabolism and storage in neuroglia: role in brain development and neurodegenerative diseases. *Cell and Bioscience* 12(1): p.1–16.

Yu, Y.H. et al. 2015. Metabolic vs. hedonic obesity: A conceptual distinction and its clinical implications. *Obesity Reviews* 16(3): p.234–247.

Yue, J.T.Y., & Lam, T.K.T. 2012. Lipid sensing and insulin resistance in the brain. *Cell Metabolism* 15(5): p.646–655.

Zagmutt, S. et al. 2023. CPT1A in AgRP neurons is required for sex-dependent regulation of feeding and thirst. *Biology of Sex Differences* 14(1): p.1–26.

Zagmutt, S., Mera, P., Soler-Vázquez, M.C., Herrero, L., & Serra, D. 2018. Targeting AgRP neurons to maintain energy balance: Lessons from animal models. *Biochemical Pharmacology* 155(July): p.224–232.

Zhang, F., Lin, Y.A., Kannan, S., & Kannan, R.M. 2016. Targeting specific cells in the brain with nanomedicines for CNS therapies. *Journal of Controlled Release* 240: p.212–226.

Zhu, H. et al. 1997. *Functional Studies of Yeast-Expressed Human Heart Muscle Carnitine Palmitoyltransferase I 1*.

Zielinska, A. et al. 2020. Polymeric Nanoparticles: Production, Characterization, Toxicology and Ecotoxicology. *Molecules* 25: p.3731.
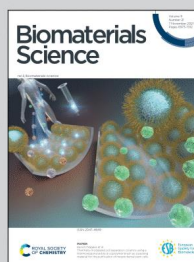
APPENDIX

Publications in PDF format
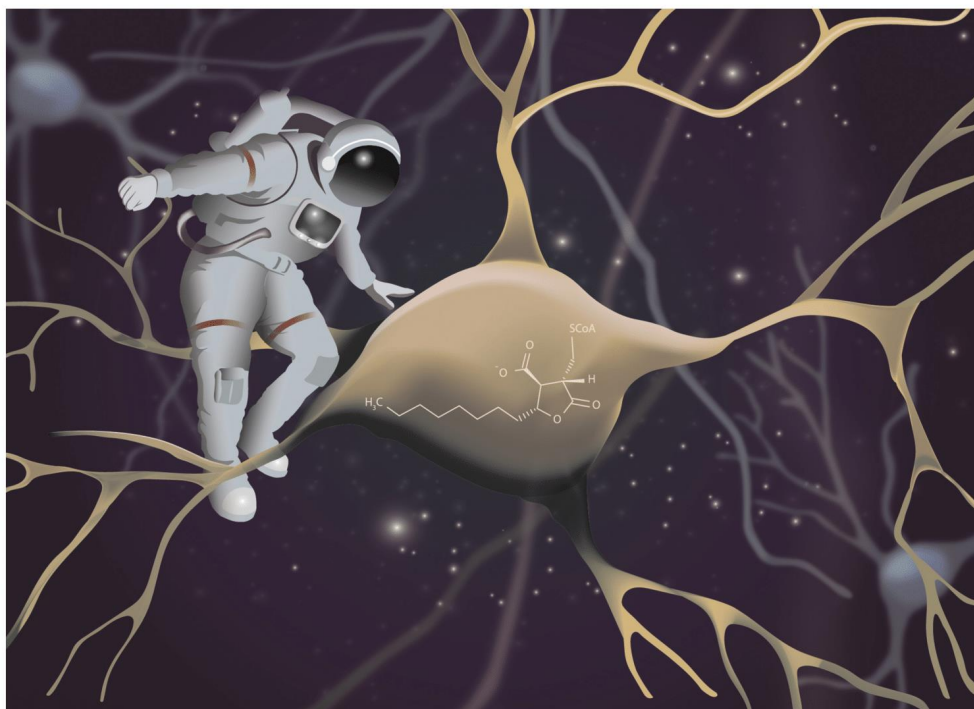
Reporting the findings from CPT Obesity Cancer Drug Delivery (COnCorD), a collaborative project led by Dr. Sabina Quader (Innovation Center of NanoMedicine, Japan) and Dr. Rosalía Rodríguez (Department of Basic Sciences, Faculty of Medicine and Health Sciences, International University of Catalunya, Spain).

Poly-ion complex micelles effectively deliver CoA-conjugated CPT1A inhibitors to modulate lipid metabolism in brain cells

This paper describes the development of poly-ion complex (PIC) micelles to deliver the specific Carnitine palmitoyltransferase 1A (CPT1A) inhibitors, (±)-C75-CoA into glioma cells and neurons, a novel strategy to manipulate fatty acid metabolism in particular brain cells as a treatment strategy for obesity and brain cancers.

Image Credit: Sebastián Zagmutt Caroca

ROYAL SOCIETY
OF **CHEMISTRY**

rsc.li/biomaterials-science

Check for updates

Poly-ion complex micelles effectively deliver CoA-conjugated CPT1A inhibitors to modulate lipid metabolism in brain cells†

West Kristian D. Paraiso, [a] Jesús Garcia-Chica,[b,c] Xavier Ariza, [c,e]
Sebastián Zagmutt,[b] Shigeto Fukushima,[a] Jordi Garcia, [c,e] Yuki Mochida,[a]
Dolors Serra,[d,e] Laura Herrero,[d,e] Hiroaki Kinoh,[a] Núria Casals,[b,e] Kazunori Kataoka,[a]
Rosalía Rodríguez-Rodríguez *[b] and Sabina Quader *[a]

Carnitine palmitoyltransferase 1A (CPT1A) is a central player in lipid metabolism, catalyzing the first step to fatty acid oxidation (FAO). Inhibiting CPT1A, especially in the brain, can have several pharmacological benefits, such as in treating obesity and brain cancer. C75-CoA is a strong competitive inhibitor of CPT1A. However, due to its negatively charged nature, it has low cellular permeability. Herein, we report the use of poly-ion complex (PIC) micelles to deliver the specific CPT1A inhibitors ($\pm$)-, (+)-, and (−)-C75-CoA into U87MG glioma cells and GT1-7 neurons. PIC micelles were formed through charge-neutralization of the cargo with the cationic side chain of PEG-poly{N-[N'-(2-aminoethyl)-2-aminoethyl]aspartamide} (PEG-PAsp(DET)), forming particles with 55 to 65 nm diameter. Upon short-term incubation with cells, the micelle-encapsulated CPT1A inhibitors resulted in up to 5-fold reduction of ATP synthesis compared to the free drug, without an apparent decline in cell viability. Micelle treatment showed a discernible decrease in ^{14}C-palmitate oxidation into CO_2 and acid-soluble metabolites, confirming that the substantial lowering of ATP production has resulted from FAO inhibition. Micelle treatment also diminished IC_{50} by 2 to 4-fold over the free drug-treated U87MG after long-term incubation. To measure the cellular uptake of these CoA-adduct loaded PIC micelles, we synthesized a fluorescent CoA derivative and prepared Fluor-CoA micelles which showed efficient internalization in the cell lines, both in 2D and 3D culture models, especially in neurons where uptake reached up to 3-fold over the free dye. Our results starkly demonstrate that the PIC micelles are a promising delivery platform for anionic inhibitors of CPT1A in glioma cells and neurons, laying the groundwork for future research or clinical applications.

1. Introduction

Lipids, which include triglycerides, phospholipids, steroids, and other fat-soluble biological molecules, are important elements of the brain's structure and function, where they constitute 50% of its dry weight.[1,2] Among these, fatty acids (FAs) function as an energy source, lipid membrane component, and starting material for signaling molecules.[3] Carnitine palmitoyltransferase 1 (CPT1) is an enzyme that catalyzes the rate-limiting step in fatty acid oxidation (FAO) – transesterification of LCFA-CoA (long-chain fatty acid-coenzyme A) and carnitine to form CoA and LCFA-carnitine esters. The resulting LCFA-carnitine can then be transported across membranes for further metabolism.[4] In mammals, there are three different CPT1 isoforms: CPT1A, which is the most ubiquitous isoform and highly expressed in the liver, kidneys, and pancreas, and also in astrocytes and neurons; CPT1B, which is expressed mainly in muscle and brown adipose tissue; and CPT1C,

*a*Innovation Center of Nanomedicine, Kawasaki Institute of Industrial Promotion, Kawasaki, Kanagawa 210-0821, Japan. E-mail: sabina-q@kawasaki-net.ne.jp; Tel: +81-44-589-5920

*b*Basic Sciences Department, Faculty of Medicine and Health Sciences, Universitat Internacional de Catalunya, Sant Cugat del Vallès, E-08195 Spain.
E-mail: rrodriguez@uic.es; Tel: +34-935-042-002

*c*Department of Inorganic and Organic Chemistry, Faculty of Chemistry, Institut de Biomedicina de la Universitat de Barcelona (IBUB), Universitat de Barcelona, Barcelona, E-08028 Spain

*d*Department of Biochemistry and Physiology, School of Pharmacy and Food Sciences, Institut de Biomedicina de la Universitat de Barcelona (IBUB), Universitat de Barcelona, Barcelona, E-08028 Spain

*e*Centro de Investigación Biomédica en Red de Fisiopatología de la Obesidad y la Nutrición (CIBEROBN), Instituto de Salud Carlos III, Madrid, E-28029 Spain

†Electronic supplementary information (ESI) available. See DOI: 10.1039/d1bm00689d

Biomater. Sci.

which is found exclusively in neurons and has residual CPT1 activity.[5]

The CPT1 system is pivotal for the regulation of FA metabolism in most of the tissues. In the brain, particularly in hypothalamic neurons, CPT1A has been revealed as a potential target against obesity.[4,6] Accordingly, the knockdown and pharmacological inhibition of CPT1A in the hypothalamus contribute to reduced food intake in rodents because of the accumulation of LCFA-CoA in the neurons.[7,8] This is thought to be a satiety signal as it precedes the reduced expression of orexigenic (feeding-promoting) proteins, leading to reduced food intake,[9,10] making it an appealing target for obesity treatment. In addition to hypothalamic neurons for the regulation of energy homeostasis, CPT1A is crucial to the survival of certain cancer types, including brain cancer. Glioblastoma (GBM) in particular has been linked with increased CPT1A expression and FA metabolism alterations. Importantly, this elevated expression of CPT1A is a very common event (90–95% cases) among human diffuse gliomas.[11–13] CPT1A-expressing tumor cells show increased FAO, promoting survival in conditions of metabolic stress like glucose deprivation and hypoxia.[14] While tumor molecular heterogeneity is an emerging critical concern in oncology, the homogeneous elevated expression of CPT1A in GBM is indeed an attractive molecular target for its therapy.

Several pharmacological inhibitors of CPT1A, which act by competing with the natural inhibitor malonyl-CoA, have been investigated.[15] Examples include etomoxir (ETO) and (±)-C75, which are converted to their CoA derivatives and act on CPT1A,[16,17] leading to decreased body weight and food intake in rodents.[16,17] However, ETO was deemed too toxic for clinical use, exemplified by causing severe hepatotoxicity as a side effect.[18,19]

The more promising compound is (±)-C75 (4-methylene-2-octyl-5-oxotetrahydrofuran-3-carboxylic acid). It is converted intracellularly by endogenous acyl-CoA synthetase to its CoA adduct, (±)-C75-CoA, a strong competitive inhibitor to CPT1A.[16] Its systemic administration in rats led to food intake decline and body weight decrease, as the drug was shown to cross the BBB and get converted to (±)-C75-CoA in the ARC hypothalamic nucleus.[17,20] Makowski et al.[8] performed the stereoselective synthesis of (+)-C75 [(2R,3S) isomer] and (−)-C75 [(2S,3R) isomer] to explain their differential pharmacological activities. (+)-C75 was found to be an anorectic by inhibiting CPT1 activity after conversion to (+)-C75-CoA. On the other hand, the effect of (−)-C75 on CPT1A activity is indirect, acting via FAS inhibition causing an increase in malonyl-CoA levels, which is the physiological inhibitor of CPT1. In addition, the effects of (−)-C75 without the CoA adduct on food intake were negligible, but it shows antitumor effects in several cell lines.[8] The presence of the CoA adduct in C75 is therefore crucial in exerting a selective inhibitory effect on CPT1 while limiting the off-target effect on FAS, but it considerably reduces the uptake of the drug into the target cell. Therefore, strategies to deliver C75 derivatives with an intact CoA adduct into the target cells are needed. Additionally, since brain CPT1 is implicated in

both cancer and obesity, the administration of (±)-C75-CoA and its pure enantiomer CoA forms into specific brain cells presents a novel therapeutic strategy to treat both diseases.

The chemical structure of (±)-C75-CoA presents challenges to cellular entry. It is a small, polar, and charged metabolite, having low permeability across the cell membrane,[21] consequently needing a delivery system for intracellular transport. With its phosphate groups ionized at physiological pH, its anionic state, together with its long aliphatic side-chain, enables CoA to interact with cation-conjugated polymers through a combination of electrostatic and hydrophobic interactions.[22] Therefore, forming a poly-ion complex (PIC) micelle with (±)-C75-CoA is a sound approach in designing a delivery system since this neutralizes the overall negative charge that would hinder its cellular entry. Although PIC micelles are well used for various nucleic acid-based macromolecular cargoes such as plasmid DNA, mRNA, siRNA, and anti-sense oligonucleotides (ASOs),[23–25] applications for small, ionic molecule delivery[26] are relatively scarce.

The cationic polymer used is PEG-poly{N-[N′-(2-aminoethyl)-2-aminoethyl]aspartamide} (PEG-PAsp(DET)), which has a monoprotonated side chain at pH 7.4, at which point it only causes minimal membrane destabilization. At pH 5.5, the side chain becomes diprotonated, selectively destabilizing the endosomal membrane once inside the cell, enabling less toxic gene transfer into cells.[27,28] This system has been used for mRNA transfection into neurons[29] as well as astrocytes and oligodendrocytes,[30] making it an excellent candidate for (±)-C75-CoA delivery. We have successfully prepared PIC micelles from PEG-PAsp(DET) which encapsulated (±)-C75-CoA and its pure enantiomer forms, potentiating the opportunity to study their biological activity on LCFA metabolism defying the cellular entry limitation. Accordingly, the micelles were tested on two brain-derived cell lines, U87MG human glioma cells and GT1-7 murine hypothalamic neurons, which revealed that FAO and ATP syntheses were successfully inhibited in both. Using a model particle encapsulating a fluorescent CoA derivative, we were also able to demonstrate that the PIC micelle is efficiently taken up by the cells and both in 2D and 3D culture models. This paper is the first report to describe the delivery of CoA-conjugated CPT1A inhibitors using PIC micelles to target CPT1A and modulate the lipid metabolism in glioma cells and neurons.

2. Results and discussion

2.1 Preparation of C75-CoA micelles

The preparation of (±)-C75-CoA was carried out as previously described[17] (see detailed information in the ESI†). Enantioselective syntheses of (+)-C75 [(2R,3S) isomer] and (−)-C75 [(2S,3R) isomer] were performed by using enantiomeric chiral auxiliaries also as previously reported[8] (Fig. S1, ESI†). (±)-C75-CoA was formed by nucleophilic addition to the α,β-unsaturated (±)-C75 by the –SH group of CoA. We confirmed the synthesis by comparing the ^{1}H NMR and HPLC profiles of

Biomaterials Science

the starting materials and product (Fig. S2, ESI†). PEG-PAsp (DET) was prepared by the anionic ring-opening polymerization of benzyl-L-aspartate N-carboxyanhydride (BLA-NCA) initiated from the terminal –NH$_2$ group of CH$_3$O-PEG-NH$_2$ (MW 12 000) to form CH$_3$O-PEG-b-poly(β-benzyl-L-aspartate) (PEG-PBLA), and then subsequent aminolysis with diethylenetriamine (DET) (Fig. S3, ESI†). The degrees of polymerization (DP) and substitution (DS) were measured from the ^{1}H NMR spectra. Using the proton peak intensity ratio of the PEG methylene protons (δ = 3.4–3.6 ppm) to the aromatic ring protons (δ = 7.1–7.5 ppm) in the polypeptide side chain of PBLA, DP was calculated to be 69. After aminolysis, the same PEG methylene protons were then compared with all the methylene protons in the DET side chains (δ = 2.7–3.6 ppm), and the DS was found to be 63.

The aqueous solutions of ($\pm$)-C75-CoA and PEG-PAsp(DET) were mixed in a 1:1 anion/cation (A/C) ratio, defined as the ratio between the overall anionic charge imparted by the phosphate and carboxylate groups in ($\pm$)-C75-CoA and the overall cationic charge given by the protonated secondary amines in PEG-PAsp(DET). We diluted the solutions using 10 mM phosphate buffer (PB) at pH 7.4 to give 57 nm PIC micelles with a unimodal size profile and narrow polydispersity (PdI). The 1:1 A/C ratio was selected based on the optimal physicochemical properties obtained with this micelle, mainly the smallest

micellar size and lowest PdI value (Fig. S4, ESI†). The zeta potential (ZP) was also close to neutral (Fig. 1, Table 1). At pH 7.4, around 51% of the aminoethylene units in the PEG-PAsp (DET) side chain are protonated,[27] and this imparts a cationic charge to the block co-polymer for neutralizing the negative charge of the anionic cargo, forming PIC micelles. The PEG chain of the polymer (MW 12 000) was also crucial in imparting these measured physicochemical properties, decreasing aggregation tendency and maintaining a neutral surface charge.[23] Transmission electron microscopy (TEM) revealed that ($\pm$)-C75-CoA micelles are spherical in shape and possess a core size of 31 nm with a unimodal size distribution (Fig. S5, ESI†). The core size of the micelle does not include the PEG outer shell; hence it is smaller than the hydrodynamic diameter obtained using DLS. Size and PEGylation are important considerations for brain-targeted nanoparticles (NPs). NP diffusion in the brain is affected by the finite width of the brain extracellular space (ECS) and pores in the extracellular matrix (ECM).[31] When surface PEG density is sufficiently high, 114 nm NPs can diffuse effectively in human and rodent brains.[32] This was corroborated in subsequent literature, and now ECS widths are estimated to be 80–220 nm in diameter while pores are around 100 nm.[33–35] Increased PEG surface density is also shown to restrain the non-specific cellular uptake of NPs,[36] which removes another impediment for
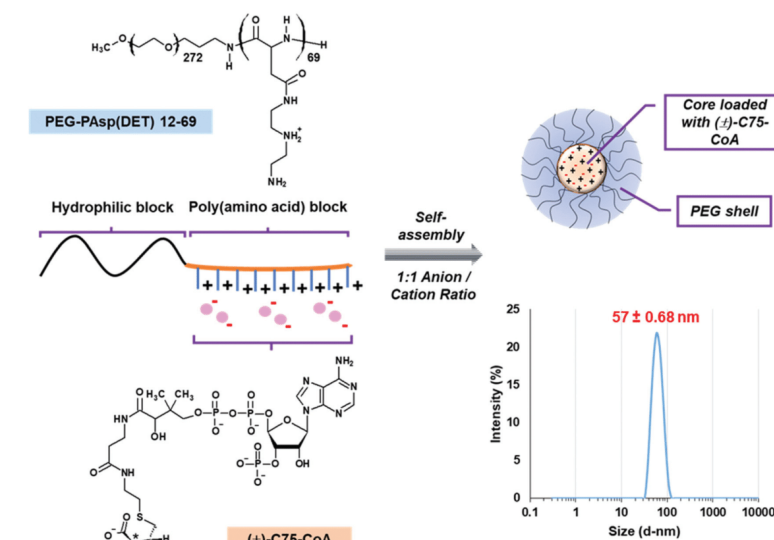

Fig. 1 Schematic of the poly-ion complex (PIC) micelle formation of ($\pm$)-C75-CoA with PEG-PAsp(DET), including its size distribution profile (hydrodynamic size *versus* intensity %).

with time (R^2 = 0.7432) (Fig. 2d). However, there was no significant change between the initial and final values. Overall, despite the tendency to gradually change over time, it is reasonable to conclude that micelle integrity was maintained for 28 days in storage at 4 °C.

PIC micelles from charged block copolymers exhibit critical association behavior,[24] which predicts the stability of a drug delivery system in an environment where it is highly diluted. Using static light scattering (SLS), we measured the scattered light intensity of diluted PIC micelle solutions as expressed by the following equation:

$$\frac{Kc}{\Delta R(\theta)} = \frac{1}{M_{w,app}} + 2A_2 c$$

where $M_{w,app}$ is the apparent molecular weight of the micelle, A_2 is the second virial coefficient, c is the concentration of the micelle solution, $\Delta R(\theta)$ is the difference between the Rayleigh ratio of the micelle solution and the solvent (10 mM phosphate buffer), and K, the Debye constant, is calculated using

$$4\pi^2 n^2 \left(\frac{dn}{dc}\right)^2 / \lambda^4 N_A$$

where N_A is Avogadro's number.

Abrupt changes in the $Kc/\Delta R(\theta)$ values in the Debye plot reveal changes in the molecular weight of micelles. When these measurements are near-constant at a certain concentration range, micelle integrity is maintained. At lower (±)-C75-CoA micelle concentrations (0.005 to 0.1 mg mL^{-1}), a sharp decrease in $Kc/\Delta R(\theta)$ was apparent (Fig. 3). However, at higher concentrations (0.15 to 1.0 mg mL^{-1}), $Kc/\Delta R(\theta)$ values became nearly constant. The point of intersection of two straight lines drawn from the lower and higher concentration range gives the critical association concentration (CAC) of the micelle, which is 0.09 mg mL^{-1}. Thus, given its low CAC value, the micelle formed from PEG-PAsp(DET) is expected to have excellent stability in dilute systems. The equivalent drug concentration at CAC is 0.03 mM (±)-C75-CoA. Concentrations much higher

Fig. 3 Critical association behavior of (±)-C75-CoA micelle. Purple squares indicate lower micelle concentrations while blue squares indicate higher micelle concentrations. The known Rayleigh ratio of toluene was used as the calibration standard and the detection angle θ = 90° was used. Measurements were carried out at 25 °C.

than this were employed in subsequent biological experiments.

2.2 Inhibition of fatty acid metabolism

2.2.1 ATP synthesis. LCFAs need to enter the mitochondria to undergo β-oxidation. They are first esterified into the LCFA-CoA form and subsequently shuttled into the mitochondria by CPT1A (Fig. 4a). Upon entry, the LCFA-CoA undergoes β-oxidation to form several acetyl-CoA molecules, which then enter the Krebs cycle. Acetyl-CoA is eventually degraded into CO_2, and in the process produces NADH, which enters the electron transport chain (ETC) to finally yield ATP.[37,38] By this pathway, FAO inhibition is known to impair ATP production. We examined whether C75-CoA will show this effect by measuring ATP concentration in cells after incubation with free and micellar C75-CoA (Fig. 4b and c) for 45 minutes. In general, the micelle effect is well-pronounced as the ATP concentrations from micelle-treated cells are significantly lower than those from free drug-treated groups. This suggests that the effective delivery of C75-CoA inside the cells leads to a higher concentration of the compound reaching the mitochondria, further steering into a substantial inhibition of FAO by the nano-encapsulated drugs.

U87MG is the most widely used cell line for human glioma research.[39] It was also reported to express CPT1A,[12] making it an appropriate model for our subsequent experiments. For U87MG, neither ETO nor the free drugs with the CoA adduct were able to effectively reduce ATP levels (Fig. 4b). Nevertheless, cells treated with (±)-, (−)- and (+)-C75-CoA micelles showed significant reduction in ATP levels compared to their corresponding non-encapsulated drugs. This ATP lowering effect is particularly appreciated with the (−)-C75-CoA micelle, which was the most effective compared to all other groups. Although the lack of effect of ETO in ATP levels did not correlate with previous publications,[40,41] we observed a reduction in FAO assay with ETO in U87MG (Fig. 5c), confirming the inhibitory effect of this drug on the mitochondrial metabolism, although the dosage-dependent off-target effects attributed to ETO could explain the result in ATP levels.[42]

GT1-7 is an immortalized murine hypothalamic neuronal cell line which is used in endocrinology and metabolism studies.[43] It was also reported to express CPT1A[44] and since it is in our interest to measure its inhibition in the hypothalamus, this cell line is an appropriate in vitro model. ATP levels in GT1-7 were discernibly reduced in response to ETO and by the free (±)- and (−)-C75-CoA derivatives, but no changes were observed in the (+)-C75-CoA-treated group (Fig. 4c). Drug encapsulation led to a statistical enhancement in ATP reduction induced by both (+)- and (−)-C75-CoA forms. As shown in U87MG, the (−)-C75-CoA micelle is still most effective in reducing ATP among all treatment groups including ETO.

A concurrent cell viability assay confirmed that the treatments in both U87MG and GT1-7 cells did not cause any apparent cell death, compared with the non-treated group (Fig. 4d and e). This highlights one of the advantages of the delivery system that we used, since PEG-PAsp(DET) causes only
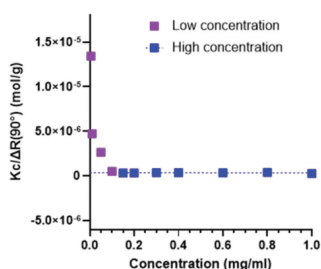
- 239 -

Table 1 Physicochemical characteristics of (±)-C75-CoA, palmitoyl-CoA and fluorescein-CoA micelles. Experiments were performed in triplicate, with values expressed as mean ± SD

Cargo		Micelle			
Molecule	MW (g mol^{-1})	Size (d-nm)	Polydispersity	Zeta potential (mV)	Encapsulation (%)
(±)-C75-CoA	1004	56.7 ± 0.68	0.055 ± 0.0037	−0.29 ± 1.98	84.2 ± 0.52
(+)-C75-CoA	1004	63.5 ± 1.45	0.054 ± 0.0082	−0.68 ± 2.25	82.2 ± 0.01
(−)-C75-CoA	1004	55.0 ± 0.38	0.024 ± 0.0232	0.17 ± 2.62	87.3 ± 0.03
Palmitoyl-CoA	1005.9	59.5 ± 0.69	0.022 ± 0.0017	2.37 ± 0.85	66.8 ± 0.05
Fluorescein-CoA	1175.8	56.9 ± 0.16	0.037 ± 0.0070	0.38 ± 1.46	94.3 ± 0.18

diffusion. The size of the (±)-C75-CoA micelle is therefore ideal for moving through the brain parenchyma.

(+)- and (−)-C75-CoA were synthesized from the same procedure as (±)-C75-CoA and their corresponding micelles were also successfully prepared, with near-similar physicochemical properties (Table 1). Additionally, micelles loaded with other CoA derivatives were prepared in order to confirm the applicability of the delivery system to molecules with similar structures. First, we used commercially available palmitoyl-CoA since its hydrophobic tail resembled that of (±)-C75 and their molecular weights were also numerically close. Micelle formation with palmitoyl-CoA was indeed observed based on DLS measurements. However, when we used CoA (767.5 g mol^{-1}) or malonyl-CoA (853.6 g mol^{-1}), micelle formation was not detected. The probable reasons are that their MWs were much smaller from (±)-C75-CoA and that they did not possess the characteristic hydrophobic moieties, despite having the phosphate groups necessary for PIC formation. This indicates that hydrophobicity was to some degree a part of the driving force for micelle formation. To determine the percentage of (±)-C75-CoA loaded inside the micelle, ultracentrifugation was used to remove the unencapsulated free drug. The ratio of the drug concentration in the upper fraction of the filter and the total drug added in the micelle preparation was calculated. From this, we ascertained that (±)-, (+)-, and (−)-C75-CoA micelles all have high drug encapsulation rates (above 80%). The ionic interaction between the drug and polymer was further con-

firmed by the statistically significant decrease in scattering light intensity and % encapsulation when the (±)-C75-CoA micelle was mixed with concentrated salt solutions (0.5 or 1 M NaCl) (Fig. S6, ESI†). The formation of PIC is driven primarily by the liberation of counterions[23] which is prompted when the cationic DET side chain and anionic drug paired up, leading to a large entropic gain. The increased NaCl concentration apparently reduced this entropic gain, which resulted in the destabilization of the PIC structure.

Next, to evaluate its long-term stability in cold storage, the change in micelle characteristics was monitored every 7 days for a total of 28 days during storage at 4 °C (Fig. 2). The purpose of this experiment was to ensure that micelles prepared in advance can still be used in biological assays after a few days of storage enabling easy and efficient reproducibility of experimental results. One-way analysis of variance (ANOVA) revealed apparent linear relationships between each physicochemical parameter and incubation time. We observed the micelle size to increase slightly with time ($R^2 = 0.9609$) (Fig. 2a). This increase in size was accompanied by a steady increase in scattering light intensity ($R^2 = 0.9984$) (Fig. 2b) as expected, indicating that no apparent decrease in particle concentration occurred. There was also no apparent change in PdI throughout the observation period (Fig. 2c). The size profile remained monodisperse, as the PdI remained well below 0.1, which was narrow. ZP stayed close to neutral all throughout the observation period, despite a weak increase associated
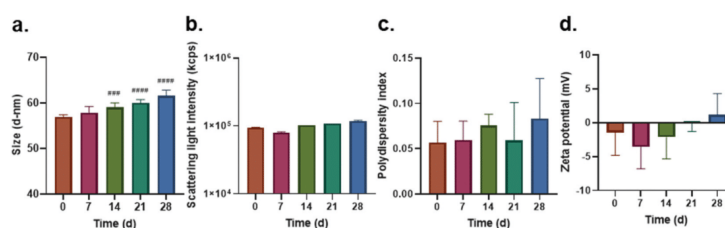

Fig. 2 Long term stability studies of the (±)-C75-CoA micelle, including measuring changes in physicochemical properties over 28 days in storage at 4 °C: size (a), scattering light intensity (b), polydispersity (c), and zeta potential (d). Experiments were performed in triplicate (values expressed in mean ± SD) and linear relationships were established using ANOVA. Comparison of means among treatment groups was done using ANOVA (with Tukey's test as *post-hoc* analysis; [###]$P < 0.001$, [####]$P < 0.0001$ *versus* day 0 of measurement).

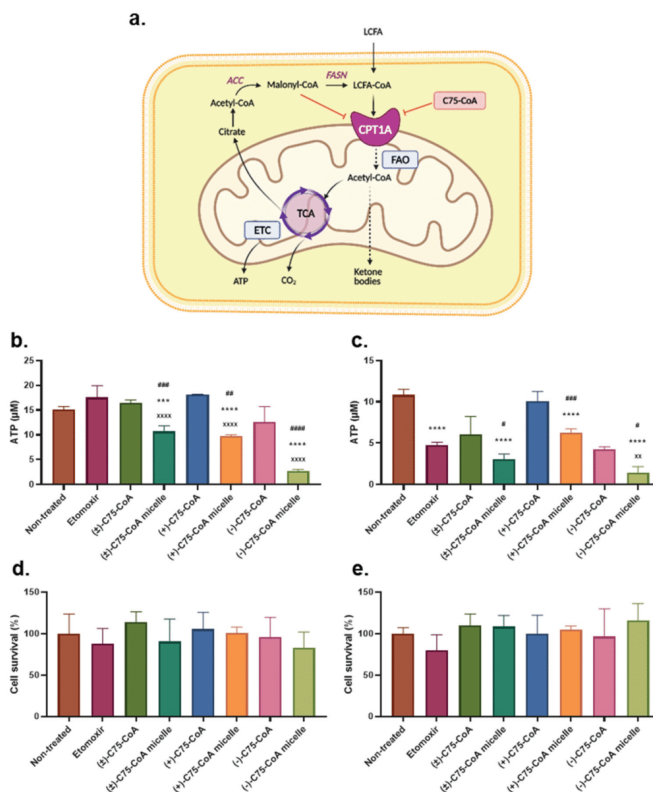**Paper**

Biomaterials Science

Fig. 4 Illustration of ATP generation from LCFA metabolism (a). Levels of ATP produced by U87MG (b) and GT1-7 (c) after treatment with FAO inhibitors. Simultaneous Calcein AM cell viability assay for U87MG (d) and GT1-7 (e) using the same conditions and treatments as ATP assay. Experiments were performed in quadruplicate (values expressed in mean $\pm$ SD) and comparison of means among treatment groups was done using ANOVA (with Tukey's test as *post-hoc* analysis; ***$P < 0.001$, ****$P < 0.0001$ *versus* non-treated cells; [xx]$P < 0.01$, [xxxx]$P < 0.0001$ *versus* ETO; [#]$P < 0.05$, [##]$P < 0.01$, [###]$P < 0.001$, [####]$P < 0.0001$ *versus* the corresponding free form of C75-CoA). Concentrations of all inhibitors used = 0.5 mM.

minimal toxicity.[27] Although other cationic polymers like poly-(L-lysine) and poly(ethylenimine) (PEI) are well-used to deliver anionic molecules, their toxicity upon micellar disassembly limits their biological applications.[45] Overall, our results verify that for both cell types, the micelles were more successful in reducing ATP synthesis as compared to the free drugs, without causing excessive cell death.

2.2.2 FAO assay. Palmitate oxidation in both U87MG and GT1-7 cells was evaluated in terms of: oxidation to CO_2 (Fig. 5a and d), conversion to acid-soluble products (ASPs) (Fig. 5b and e) and total FAO rate calculated as the sum of ASP plus CO_2 oxidation (Fig. 5c and f). The final fate of palmitate oxidation in both cell types was significantly different. In particular,

most of the palmitate oxidation levels measured in U87MG cells come from ASPs (ranging 7.5 nmol mg^{-1} prot h^{-1}), with minimal contribution of oxidation to CO_2 (ranging 0.1 nmol mg^{-1} prot h^{-1}), whereas GT1-7 cell lines showed more equal contribution of palmitate oxidation to ASPs and CO_2 total FAO. The differences in palmitate oxidation fate between GBM and neuronal cell lines agree with previous publications indicating the different metabolic profile of both cell types.[12,40,46,47]

In U87MG cells, ETO effectively reduced FAO in terms of both CO_2 and ASP (Fig. 5a–c), since ASP oxidation was the main pathway contributing to the total reduction of FAO. In contrast, the free forms of C75-CoA were unable to modify these oxidation parameters compared to non-treated cells.
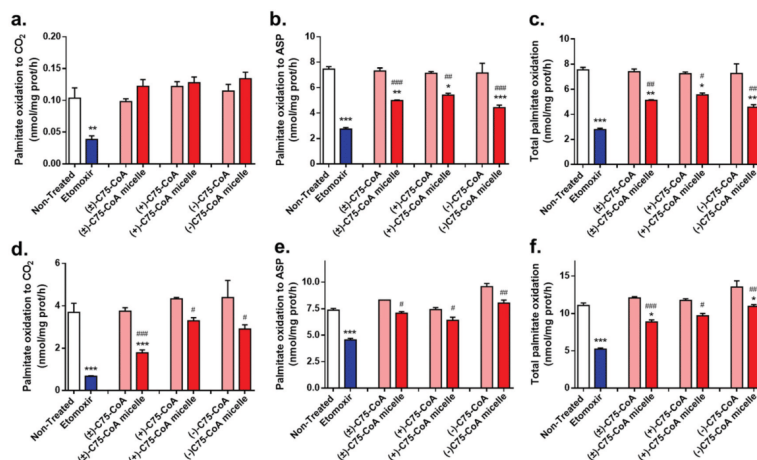
Fig. 5 FAO oxidation in U87MG (a−c) and GT1-7 (d−f) cells after treatment with C75-CoA derivatives in free form or nano-encapsulated in micelles. ETO was used as the positive control of FAO inhibition. FAO is represented as palmitate oxidation to CO_2 (a and d), ASP (b and e), and total palmitate oxidation (CO_2 + ASP; c and f). The results are the mean ± SD of two independent experiments performed as biological triplicates (n = 5−6 samples per condition). Comparison of means were done using ANOVA followed by Tukey's comparison test; *P < 0.05, **P < 0.01, ***P < 0.001 *versus* non-treated cells; #P < 0.05, ##P < 0.01, ###P < 0.001 *versus* the corresponding form of C75-CoA. Concentrations of all inhibitors used = 1 mM.

Micelles of the three forms of C75-CoA led to a substantial attenuation of total FA oxidation (Fig. 5c), reaching similar levels to ETO-treated cells. These changes were due to palmitate oxidation to ASP (Fig. 5b), probably reducing the generation of TCA intermediary metabolites and ketone bodies crucial for GBM cell proliferation.[12,40] Similar levels of FAO attenuation were reached in (±)-, (+)- and (−)-C75-CoA micelle-treated U87MG cells (Fig. 5c).

In GT1-7, ETO was also able to reduce FAO, whereas it remained unchanged after treatment with the free C75-CoA forms, in line with previous results (Fig. 5d−f). The micelle forms of C75-CoA derivatives induced a statistically significant attenuation in total FAO, with the contribution of both palmitate fates, to CO_2 and ASP, being similar to the total oxidation of FA (Fig. 5d−f). Cells treated with the (±)-C75-CoA micelle showed the highest reduction in FAO compared to non-treated conditions, reaching similar levels to those induced by ETO (Fig. 5c).

Altogether, our results indicate that the delivery of C75-CoA derivatives using a PIC micelle resulted in a substantial improvement in FAO inhibition by these drugs in both U87MG and GT1-7 cell lines. We have also evidenced the differential contribution of either CO_2 or ASPs to FA oxidation in both cell lines, in agreement with the literature. Considering the recently identified role of FAO as a metabolic node in the aggressive phenotype of glioma cell lines,[40,41] and the significant role of FA oxidation and CPT1 in neuronal metabolism and survival,[44,47] the improved FAO inhibition showed by these micelles indicates

the potential of these nanoparticles to modify brain metabolism in associated diseases such as cancer.

2.3 Cytotoxicity of C75-CoA micelles

Since GBM cells overexpress CPT1A[11] to increase their chances of survival, inhibiting this enzyme would negatively affect their proliferation. We incubated free and micellar C75-CoA with U87MG for 72 h, with ETO as a comparison drug. The drug and micelle-produced responses generally followed a sigmoidal shape (Fig. 6a−d). C75-CoA (racemic and pure enantiomer forms) is overall significantly more cytotoxic to the respective free drug (Fig. 6e). Notably, the mean IC_{50} of free (±)-C75-CoA was decreased 4-fold when delivered in micelle form. After 72 h, the difference between the mean IC_{50} of (±)- and (−)-C75-CoA micelles is not statistically significant; however, the (+)-C75-CoA micelle is discernibly less cytotoxic than the (±)-C75-CoA micelle. Free (+)-C75-CoA is less cytotoxic than ETO. On the other hand, ETO shows comparable toxicity to (±)- and (−)-C75-CoA micelles despite being a free drug, owing to other mechanisms outside of CPT1 inhibition such as the production of reactive oxygen species.[38,48]

Two-way ANOVA revealed that the mean IC_{50} values of all FAO inhibitors were all found to decrease with time in a linear fashion (R^2 > 0.9). The cytotoxicity of the (±)-C75-CoA micelle was demonstrated to be more pronounced at longer incubation periods, approaching comparable values to ETO after 72 h (Fig. 6f). Note that the decrease in cell viability is achieved only upon lengthier exposure, since the 45 min incubation in
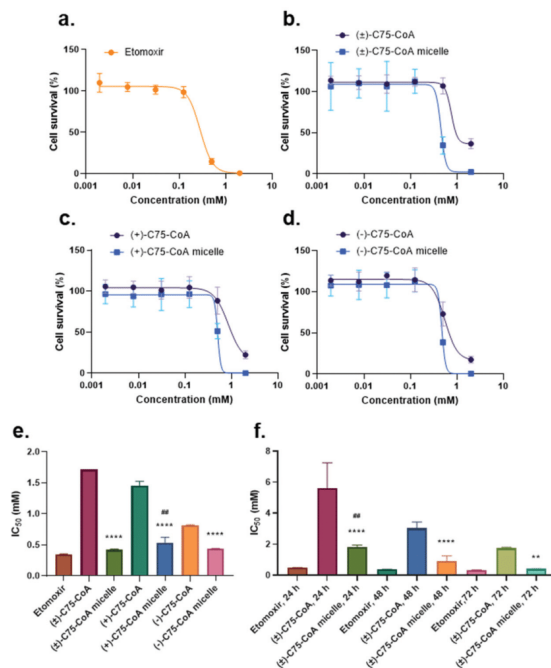
Fig. 6 Cytotoxicity of FAO inhibitors on U87MG at 72 h incubation, including the dose–response curves of ETO (a) and the free *versus* micelle forms of ($\pm$)-C75-CoA (b), (+)-C75-CoA (c), and (−)-C75-CoA (d). IC_{50} of ETO, free and micelle forms of ($\pm$)-, (+)-, and (−)-C75-CoA at 72 h incubation (e) and only for ($\pm$)-C75-CoA at 24-, 48-, and 72 h incubation periods (f). Experiments were performed in triplicate (n = 4 samples per condition; values expressed in mean $\pm$ SD) and comparison of means among treatment groups was done using one-way ANOVA (with Tukey's test as *post-hoc* analysis; **P < 0.01, ****P < 0.001 *versus* the corresponding form of C75-CoA; ##P < 0.01 *versus* ETO).

the ATP assay (Fig. 4c) was not enough to kill the cells. Cellular morphologies were also retained after short-term incubation with both free and micellar ($\pm$)-C75-CoA in the FAO assay (Fig. S7, ESI†), including the neuronal and astrocytic processes for GT1-7 and U87MG, respectively. These results provide the initial evidence to support the further development of these PIC micelles as a therapeutic platform against GBM. It also shows that the delivery of ($\pm$)-C75-CoA inside the cells is important in amplifying its growth inhibitory properties. Given its anionic state, it is assumed to have limited permeability across the cell membrane,[21] with the micelle state neutralizing this negative charge and promoting its transport into the cell through endocytosis.

2.4 Quantification of cellular uptake using fluorescein-CoA encapsulated PIC micelle in 2D and 3D culture models

To confirm that the PIC micelle type system facilitated the cellular uptake of CoA-conjugated ($\pm$)-C75 by neutralizing the
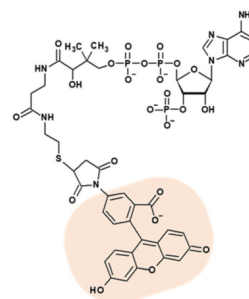

Fig. 7 Structure of Fluor-CoA. The fluorescein moiety (highlighted) enables uptake evaluation using flow cytometry or confocal microscopy.
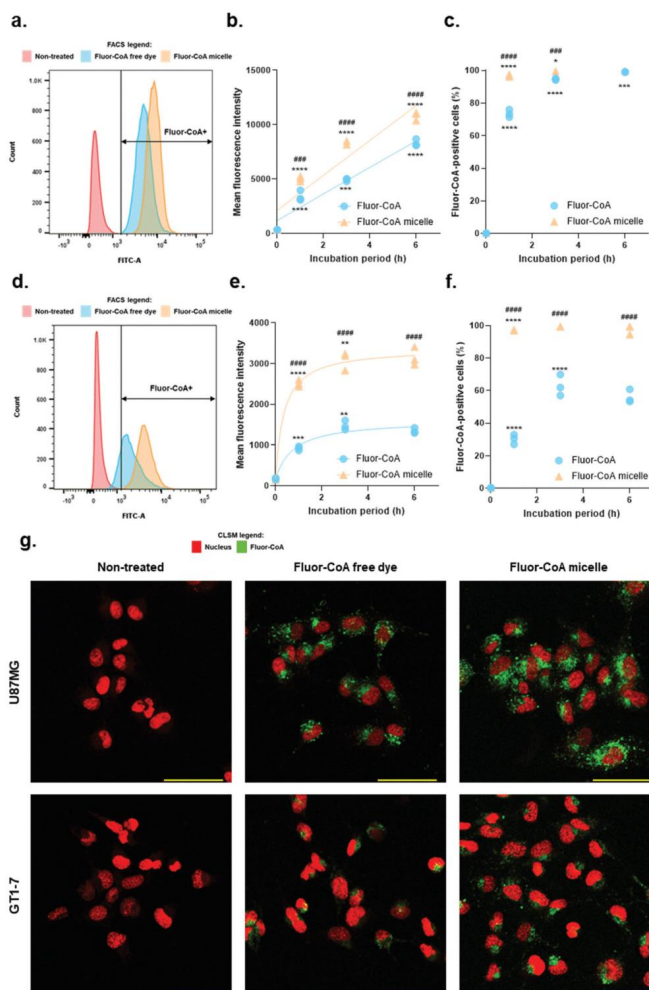
Fig. 8 Analysis of cellular uptake of Fluor-CoA micelles *versus* free dye in 2D cultures using flow cytometry and confocal microscopy. U87MG data (a–c) are presented as sample histogram (a), mean fluorescence intensity (b), and percentage of Fluor-CoA-positive cells (c). GT1-7 data (d–f) are presented as sample histogram (d), mean fluorescence intensity (e), and percentage of Fluor-CoA-positive cells (f). Experiments were performed in triplicate (values expressed in mean $\pm$ SD) and comparison of means among treatment groups was done using ANOVA (with Tukey's test as *post-hoc* analysis; *$P < 0.05$, **$P < 0.01$, ***$P < 0.001$, ****$P < 0.0001$ *versus* measurement at a preceding time point; ###$P < 0.001$, ####$P < 0.0001$ *versus* corresponding free Fluor-CoA). Representative confocal microscopy images (g) of U87MG and GT1-7 after 1 h incubation with Fluor-CoA free dye and micelles. Scale bar = 50 μm, magnification 5×.

negative charges, we synthesized a fluorescein analogue of CoA (Fig. 7; Fluorescein-CoA; herein Fluor-CoA) and encapsulated it inside the PIC micelle. Fluor-CoA was prepared by simple maleimide chemistry starting from fluorescein-5-maleimide (FAM). The resulting compound had a MW (1175.8 g mol^{-1}) close to ($\pm$)-C75-CoA (1004 g mol^{-1}), including the same number of carboxylate and phosphate groups, which therefore imparted analogous physicochemical properties. The fluorescein moiety also imparted sufficient hydrophobic character to CoA, which is necessary for PIC micelle formation. The

addition of fluorescence emission ($\lambda_{excitation}$ = 475–490 nm, $\lambda_{emission}$ = 510–520 nm) made cellular uptake studies using confocal microscopy or flow cytometry possible. The –SH group of CoA added to the maleimide ring of FAM to give the desired product (Fig. S8a, ESI†), which we confirmed by comparing the ^{1}H NMR and HPLC profiles of the starting materials and product (Fig. S8b and c, ESI†). In the chromatogram, the Fluor-CoA peak is revealed by both the fluorescence and UV absorbance (λ_{max} of CoA) detectors. In a similar fashion to ($\pm$)-C75-CoA, the aqueous solution of Fluor-CoA was combined
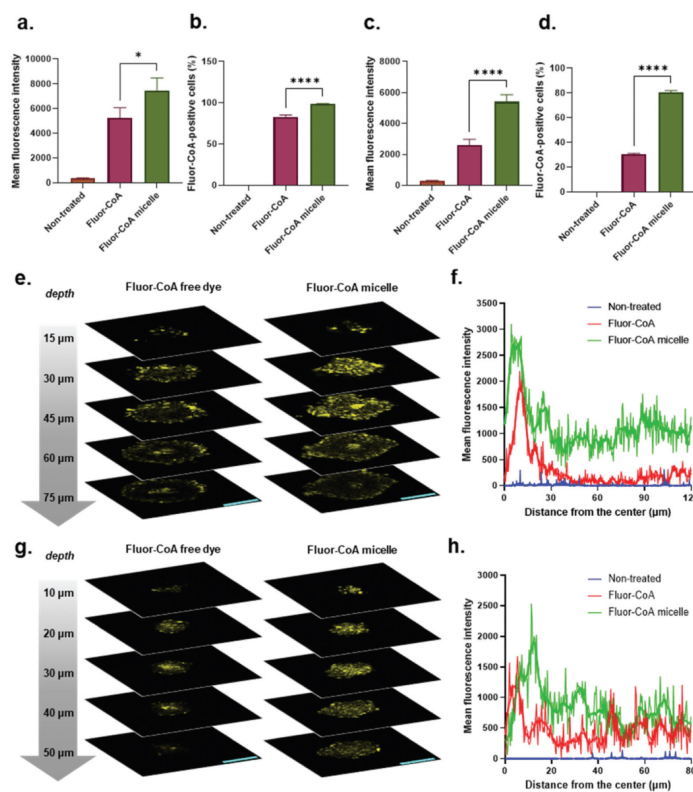

Fig. 9 Analysis of cellular uptake of Fluor-CoA micelles *versus* free dye in 3D cultures using flow cytometry and confocal microscopy. FACS analysis for U87MG presented as mean fluorescence intensity (a), and percentage of Fluor-CoA + cells (b) and for GT1-7 presented as mean fluorescence intensity (c), and percentage of Fluor-CoA + cells (d). Experiments were performed in triplicate (values expressed in mean $\pm$ SD) and comparison of means among treatment groups was done using ANOVA (with Tukey's test as *post-hoc* analysis) (*$p < 0.05$, ****$p < 0.0001$). Representative confocal microscopy images of U87MG (e) and GT1-7 (g) spheroids taken at Z-positions. Yellow signals represent fluorescence from the FITC channel. Scale bar = 100 μm, magnification 1.2×. Radial profile of fluorescence from Fluor-CoA micelles *versus* free dye in U87MG (f) and GT1-7 (h) spheroids. Actual fluorescence intensity as well as 10-point moving average as represented by a smoothing curve is shown. All data were taken after 3 h incubation with Fluor-CoA micelle or free dye.

with PEG-PAsp(DET) in a 1 : 1 anion/cation ratio in 10 mM phosphate buffer (PB) pH 7.4 to give 57 nm micelles with a narrow polydispersity (Table 1).

Cellular uptake in both U87MG and GT1-7 was visualized using confocal laser scanning microscopy (CLSM) and quantified using flow cytometry (Fig. 8). We incubated the micelles with the cells at different time points (1, 3, or 6 h) and at a fixed concentration of Fluor-CoA micelles (0.25 mg mL^{-1}), which contained 0.1 mg mL^{-1} free dye. The equivalent Fluor-CoA concentration was therefore used in the free dye-treated groups. In flow cytometry, DAPI-stained dead cells were excluded in order to measure only live cells. The data we obtained included mean fluorescence intensity (MFI), to indicate the extent of micelle internalization, and percentage of Fluor-CoA + cells after gating, to quantify the % of cell population in which the free or micellar Fluor-CoA has entered.

Internalization of both free dye and micelles increased with time in both cells (Fig. 8). Mutually, micellar uptake in terms of MFI was statistically higher than free dye uptake, at all measured time points (Fig. 8b and e). In addition, the values for %Fluor-CoA + cells were discernibly greater for the micelle compared to the free dye, for both cell lines (Fig. 8c and f). Even after 1 h of incubation, the micelles entered more than 95% of the cells. For U87MG specifically, MFI corresponding to micelle uptake was 1.5-fold elevated, on average, compared to that of the free dye (Fig. 8b). We found that cellular uptake displayed a strong linear trend that increased over time for both the micelle ($R^2 = 0.8708$) and free dye ($R^2 = 0.9394$). This meant that the cells were expected to continue internalization beyond the 6 h observation period. In terms of %Fluor-CoA + cells, free dye uptake started at only 70% (1 h) but gradually increased and eventually matched the corresponding value for the micelle at 6 h (Fig. 8c). However, the micelle-treated cells still produced a higher fluorescence signal, signifying that the overall amount of Fluor-CoA delivered to the cells was higher. Mo et al.[49] previously described the tendency of U87MG to internalize polymeric NPs at a steady linear rate up to 6 h, which supports our findings.

The difference between micellar and free Fluor-CoA uptake was more amplified in GT1-7. The MFI of micelle uptake was around 2 to 3 times higher than free dye uptake through all the time points that we measured, which clearly indicated the penetration-enhancing effects of the micelle (Fig. 8e). In terms of %Fluor-CoA + cells, the uptake started from 30% at 1 h, doubled at 3 h, and then plateaued (Fig. 8f). Unlike in U87MG, the rates of internalization did not increase in a linear fashion but fit a non-linear model called the Padé (1,1) approximant (Fluor-CoA $R^2 = 0.9493$; Fluor-CoA micelle $R^2 = 0.9870$). In addition, the free drug entered only around 60% of the cell population even at a 6 h incubation period, never quite reaching the 98% uptake that the micelle attained after only 1 h of incubation. The saturable uptake of PEGylated polymeric micelles has previously been demonstrated for neurons by Rabanel et al.[50] who attributed it to their limited capacity to accommodate NPs.

Multi-cellular spheroids were generated by seeding cells in low-adhesion plates and allowing them to form clusters by

secreting their own ECM,[51] which provides additional penetration barriers for the NPs,[52] therefore more accurately modeling the in vivo environment as compared to the monolayer culture. We found that micellar internalization was also 1.4- and 2-fold higher compared to the free dye in U87MG and GT1-7 spheroids, respectively (Fig. 9a and c). In GT1-7 spheroids, 30% of the cells internalized the free dye, compared to the 80% which internalized the micelles (Fig. 9d). For U87MG, the difference of %Fluor-CoA + cells between the free dye- and micelle-treated groups remained small but still statistically significant, similar to the 2D culture model (Fig. 9b).

Confocal images from the periphery to the core of the spheroids show the contrasting penetration abilities between Fluor-CoA free dye and micelles (Fig. 9e–h, Fig. S9, ESI†). For both cell lines, the peak of Fluor-CoA is found between 0 and 20 μm from the periphery. The signal steadily decreased towards the core. Generally, the fluorescence intensity coming from micelle-treated spheroids is consistently higher in micelle-treated spheroids, confirming what was already shown in flow cytometry measurements: that internalization of Fluor-CoA micelles is higher than that of the free dye. Through the confocal images, we also demonstrated that Fluor-CoA micelles have higher penetrating ability than the free Flour-CoA. The results suggest that even in a 3D model with additional barriers, our above findings in the monolayer hold true. Additionally, this implies that the PIC micelles that we prepared are equipped to navigate through the pores of the ECM.

3. Conclusion

We have successfully prepared PIC micelles loaded with the CPT1A inhibitors (±)-, (+)-, and (−)-C75-CoA. The cationic block-copolymer PEG-PAsp(DET) provided a platform by neutralizing the negative charge of the cargo molecules, generating micelles with optimal physicochemical properties (55–65 nm size range and neutral surface charge) that are stable in long term storage. Through targeting CPT1A, FAO was effectively impeded, which led to overall decreased metabolism of ^{14}C-palmitate into CO_2 and acid-soluble products. We found that these results were consistent with the ATP inhibition experiments, where ATP production in both U87MG and GT1-7 was diminished up to 5-fold by the micelles, in comparison with the free drug counterparts. During these short-term incubation experiments, no apparent decrease in viability was induced by the micelles. When we assayed the cytotoxicity in glioma cells after longer incubation periods, C75-CoA micelles inhibited cell growth more discernibly compared to the free drug forms, where IC_{50} was reduced 2 to 4-fold. (±)- and (−)-C75-CoA micelles even showed comparable efficacy to the known FAO inhibitor ETO. The fluorescent dye-loaded model particle, Fluor-CoA micelle, showed a statistically increased internalization in both cell lines as well, in comparison with the free dye, reaching a 2 to 3-fold increase especially in GT1-7 neurons. Higher cellular internalization corroborated the cyto-

toxicity and FAO inhibition results, that delivery through the PIC micelle resulted in increased cellular concentration of the cargo, which further led to increased biological activity. Although internalization was generally time-dependent, we showed that the micellar uptake kinetics differed between the cell lines. Effective cellular entry of the Fluor-CoA micelle was further confirmed in 3D spheroids derived from both cell lines, inferring the superior activity of CoA-adducts when loaded in micelles in a biological model that is transitional in complexity between standard 2D *in vitro* and diseased tissue *in vivo*. The size range and neutral surface charge of these PIC micelles, combined with their efficient penetration in 3D spheroids, imply that this platform is ideal in navigating through the brain parenchyma. This justifies further exploration of its *in vivo* properties in subsequent studies. This PIC micelle has previously been reported to be effective in gene delivery to the brain including in glial cells like astrocytes and oligodendrocytes[30] as well as neurons.[29] From our data, we can compellingly conclude that uptake in neuronal and glioma cells of small anionic cargoes like Fluor-CoA and by extension, C75-CoA, is thoroughly improved by using PIC micelles. Additionally, the advantage of using a micelle-type delivery system was more pronounced for the neurons. Drug delivery into neurons is generally more challenging compared to other cells and this is reflected in the fact that there is a lack of neuron-targeted delivery systems present in the clinic.[53] Our results contribute to the growing pool of knowledge on glioma- and neuron-targeted delivery, therefore warranting further development into effective brain therapeutics, especially those that involve the delivery of CPT1A inhibitors and other negatively charged molecules for the management of diseases where modulating the lipid metabolism is a key emerging strategy.

4. Materials and methods

4.1 Synthesis of (±)-C75-CoA, (+)-C75-CoA and (−)-C75-CoA

The preparation of (±)-C75-CoA was carried out as previously described[17] (see detailed information in the ESI†). The enantioselective synthesis of (+)-C75 and (-)-C75 was performed by using enantiomeric chiral auxiliaries (Fig. S1, ESI†).

4.2 Synthesis of PEG-PAsp(DET)

The preparation of PEG-PBLA through the NCA ring-opening polymerization of BLA-NCA (Chuo Kaseihin Co., Inc.) using CH_3O-PEG-NH$_2$ (MW 12 000; NOF Corp.) was carried out as previously reported.[54] The subsequent aminolysis of the polymer with freshly distilled DET (TCI, cat. # D0493) was carried out also as described earlier.[27,28] See detailed information in the ESI†.

4.3 Preparation and characterization of PIC micelles

PEG-PAsp(DET) was dissolved in 10 mM phosphate buffer pH 7.4 at 10 mg mL^{-1} concentration by overnight stirring at 4 °C, after which the solution was passed through a 0.22 µM filter.

The polymer and (±)-C75-CoA solutions were mixed in a 1 : 1 anion-to-cation ratio, vortexed, and then again filtered (0.22 µM) under sterile conditions prior to succeeding experiments. For DLS measurements (Zetasizer Ultra, Malvern Panalytical, Spectris plc, UK), micelle suspensions were diluted to 1 mg mL^{-1} and placed inside a ZEN2112 quartz cuvette. Light scattering data were measured using a 50 mW 532 nm DPSS laser incident beam at a detection angle of 173° with a He–Ne laser 633 nm (temperature = 25 °C). The autocorrelation function produced was analyzed through the cumulant approach. Size is expressed as the hydrodynamic diameter, which was calculated with the Stokes−Einstein equation. Attenuator selection was automated. For zeta potential measurements, micelle suspensions were introduced in a ZEN1010 HC cell, using the Smoluchowski approach. During stability studies, micelles were kept at 4 °C and measurements were repeated every 7 d for 28 d in total.

For static light scattering (SLS) measurements, a dynamic light scattering photometer DLS-8000 (Otsuka Electronics, Osaka, Japan) was used. Measurements were performed using a detection angle of 90° with a He–Ne laser 633 nm at 25 °C on micelle solutions with a concentration range of 0.005 to 1 mg mL^{-1}. To measure background light scattering, the solvent phosphate buffer pH 7.4 (10 mM) was used. Calibration was performed using toluene.

Micelle morphology was observed on a transmission electron microscope (JEM-2100, JEOL, Japan) operated with 120 kV acceleration voltages and approximately 60 µA beam current. The diluted micelle (1 mg mL^{-1}) was stained by mixing with uranyl acetate solution (2%, w/v) and placed on 400-mesh copper grids before drying and observation. The micelle diameter (n = 105) was measured using IC Measure version 2.0.0.245.

4.4 Quantification of drug inside PIC micelles

Micelle solutions were pipetted into Amicon Ultra-0.5 mL centrifugal filters (MWCO 10 000, Merck Millipore, cat. # UFC501096) and spun (14 000 g, 15 min, 4 °C). The filtrate was then collected, weighed, and then transferred into UV-transparent 96-well plates. Its absorption at λ_{max} CoA = 259 nm was measured using a microplate reader (Infinite® M1000 Pro, Tecan Trading AG, Switzerland). Drug encapsulation was calculated by obtaining the ratio of the filtrate absorbance to that of the original (±)-C75-CoA solution added to form the micelle.

4.5 Cell cultures and treatments

The glioblastoma U87MG cell line (Merck Millipore, Sigma, Madrid, Spain) was cultured in DMEM (4.5 g L^{-1} glucose) supplemented with 10% FBS while murine hypothalamic neuronal cells GT1-7 (Merck Millipore, Sigma, Madrid, Spain) were cultured in DMEM (4.5 g L^{-1} glucose) supplemented with 10% FBS, 4 mM L-glutamine, 1% penicillin–streptomycin, and 1 mM sodium pyruvate at 37 °C in a humidified atmosphere of 95% air and 5% CO_2.

4.6 Cytotoxicity assays

The *in vitro* cytotoxicity of etomoxir (ETO, Cayman, cat. # 11969) and free and micellar C75-CoA derivatives (racemic and pure enantiomers) was evaluated against U87MG. The cells (3×10^4 cells per well) were seeded in a 96-well plate 24 h prior to the assay. The cells were incubated with the test solutions, and then viability was measured after 24, 48, and 72 h of exposure, by adding cell-counting kit-8 (CCK8) (Dojindo, cat. # CK04) and measuring the product absorbance at $\lambda_{max} = 450$ nm after 2 h using a microplate reader (Infinite® M1000 Pro, Tecan Trading AG, Switzerland).

4.7 Synthesis of Fluor-CoA and preparation of Fluor-CoA micelles

The synthetic procedure of Fluor-CoA was adopted from a previous protocol.[55] Briefly, 11.1 mg of CoA sodium salt hydrate was dissolved in 100 μL of 10 mM phosphate buffer pH 7.4. To this, 4.8 mg of fluorescein-5-maleimide (TCI, cat. # F0810) in 900 μL of DMF was added. The reaction mixture was stirred overnight at 30 °C, after which benzene was added the resulting mixture, flash-frozen using liquid N_2 and then dried *in vacuo*. To confirm product formation, HPLC was performed [LC-2000 series, JASCO, Tokyo, Japan; C-18 RP-column (TSKgel ODS-100 V 5 μm particle size, 4.6 mm I.D. × 15 cm, TOSOH Bioscience, cat. # 21455), mobile phase 7 : 3 100 mM phosphate buffer pH 3/acetonitrile, flow rate 1.2 mL/minute, detection: UV absorption at λ_{max} CoA = 259 nm and λ_{max} fluorescein = 460 nm, fluorescence detection ($\lambda_{excitation} = 494$ nm, $\lambda_{emission} = 521$ nm)]. The HPLC peak passing all the detection criteria corresponds to the compound with both CoA and fluorescein moieties. ^{1}H NMR was recorded on a JEOL ECS 400 (400 MHz) spectrometer (JOEL Ltd, Tokyo Japan) and the chemical shift was calculated as parts per million (ppm). Data were processed using MestReNova version 14.2.1-27684.

PEG-PAsp(DET) and Fluor-CoA solutions in 10 mM phosphate buffer pH 7.4 were then mixed in a 1 : 1 anion-to-cation ratio, vortexed, and then again filtered (0.22 μM) under sterile conditions.

4.8 Measurement of ATP levels

The measurement of ATP levels in parallel to cell viability assays was performed according to a previously reported procedure.[38] Produced ATP was quantified using a luminescence assay. Cells (2×10^5 cells per well) were seeded in a white, flat-bottom 96-well tissue culture plate 24 h prior to the assay. The cells were then incubated with ETO, C75-CoA, and C75-CoA micelles (0.5 mM) in bicarbonate-free DMEM (Sigma-Aldrich, cat. # D5030) supplemented with 2.5 mM glucose (Gibco, cat. # A2494001) and 275 nM oleate-BSA (Sigma-Aldrich, cat. # O3008) for 45 minutes in a separate incubator with 0% CO_2. The assay was done according to the manufacturer's protocol (CellTiter-Glo® Luminescent Cell Viability Assay, Promega, cat. # G9241). ATP was quantified using a calibration curve. The luminescence signal for 10s was measured in each well using a

GloMax® Multi Detection System (Promega Corp, Madison, Wisconsin).

The relative viability was determined using the Calcein AM assay. In parallel to the ATP measurements, cells (2×10^4 cells per well) were seeded in a white 96-well tissue culture plate 24 h prior to the assay. The cells were then incubated with ETO, C75-CoA, and C75-CoA micelles (1 mM) in bicarbonate-free DMEM (with 25 mM glucose and 6 mM glutamine) for 45 minutes in a separate incubator with 0% CO_2. The assay was then performed according to manufacturer's protocol (Calcein AM; Invitrogen). Calcein AM was added to each well 30 min before measuring fluorescence intensity ($\lambda_{excitation} = 495$ nm, $\lambda_{emission} = 515$ nm) using a microplate reader (Infinite® M1000 Pro, Tecan Trading AG, Switzerland). Viability was normalized against non-treated cells.

4.9 Measurement of FAO

Palmitate oxidation to CO_2 and acid-soluble products (ASPs), essentially acyl-carnitine, Krebs cycle intermediates, and acetyl-CoA, were measured in U87 and GT1-7 cell lines grown in 12-well plates. Cells were treated with ETO, C75-CoA (racemic and enantiomers), and C75-CoA micelles (racemic and enantiomers) (1 mM) in DMEM (4.5 g L^{-1} glucose) for 45 minutes. On the day of the assay, cells were washed in KRBH-0.1% BSA, preincubated for 30 min at 37 °C in KRBH-1% BSA. Cells were then incubated for 3 h at 37 °C with fresh KRBH containing 2.5 mM glucose and 80 nM of labeled palmitate per well. Oxidation was measured as described.[56] The scintillation values were normalized to the protein content of each well and the results for CO_2 and ASPs are expressed as previously described.[56]

4.10 Confocal laser scanning microscopy (CLSM)

Confocal images were taken using an LSM880 confocal microscope (Carl Zeiss, Oberkochen, Germany) at a magnification of 5× using white light, 488- and 633 nm lasers for $\lambda_{excitation}$ of Fluor-CoA and NucSpot® 650, respectively. U87MG and GT1-7 cells (6×10^4 cells per well) were seeded in a μ-slide 8-well chambered coverslip (ibidi, cat. # 80826) 24 h prior to observation. Cells were then incubated with 100.0 μL of nanoparticle suspension in medium (0.25 mg Fluor-CoA micelle per mL containing 0.1 mg Fluor-CoA per mL) with NucSpot® 650 (Biotium, cat. # 40082) as the nuclear stain (1 μL mL^{-1} suspension) and Verapamil HCl as the efflux pump inhibitor (1 μL mL^{-1} suspension) for 1 h. Cells were then washed 2 × with PBS (−) before replacing medium with DMEM containing trypan blue (0.5 μL mL^{-1}) to quench fluorescent dyes attached on the cell surface.

4.11 Quantification of cellular uptake using FACS

U87MG and GT1-7 cells (3×10^5 cells per well) were seeded in 6-well plates 24 h prior to the assay. Cells were then incubated with the nanoparticle suspension in medium (0.25 mg of Fluor-CoA micelle per mL containing 0.1 mg of Fluor-CoA per mL) with varying incubation times (1, 3, and 6 h). The cell suspension was washed twice with 1 mL PBS (−) and then incu-

- 248 -

bated with 300 μL of Accutase® Cell Detachment Solution (Innovative Cell Technologies, San Diego, California) for 3 minutes at 37 °C. The cells were collected by adding 1 mL of PBS (−), transferring to a 25 mL plastic tube, and then spinning at 300 g for 5 min at 4 °C. They were further washed twice with PBS (−) and twice with 2% FBS in PBS (−). After the final washing, they were resuspended in 500 μL of 1 μg mL^{-1} DAPI in 2% FBS in PBS (−) to stain live cells, then passed through a cell strainer and kept on ice. The mean fluorescence intensity and percentage of Fluor-CoA + cells in the FITC channel were measured by flow cytometry (BD LSRFortessa™ Flow Cytometer, BD Biosciences, San Jose, California) using FSC and SSC detection to gate out debris, and the UV (355 nm) and blue lasers (488 nm) for the detection of DAPI and Fluor-CoA, respectively. Data analysis was performed using FlowJo software (BD Biosciences, San Jose, California).

4.12 Spheroid culture and uptake measurement

For spheroid culture, cell suspensions (50 μL) were seeded into each well (1 × 10^3 cells per well) of a low-adhesion Prime Surface™ 96-well U-bottom plate (Sumitomo Bakelite Co., Japan) and incubated for 3 d. The spheroids were then incubated with Fluor-CoA free dye or micelle suspension (50 μL) in medium (final concentration: 0.25 mg of Fluor-CoA micelle per mL containing 0.1 mg of Fluor-CoA per mL) for 3 h, after which they were harvested using a pipette and collected into a 25 mL plastic tube. Washing and analysis were performed as mentioned above.

For confocal imaging, the spheroids were also incubated with NucSpot® 650 (Biotium, cat. # 40082) as the nuclear stain (1 μL mL^{-1} suspension) and Verapamil HCl as the efflux pump inhibitor (1 μL mL^{-1} suspension) in addition to Fluor-CoA free dye or micelle suspension. After 3 h, they were then harvested using a pipette and collected in a 25 mL plastic tube. The spheroids were collected by centrifugation at 700 rpm for 3 min at 4 °C and washed twice with PBS (−) before fixing with 4% paraformaldehyde for 30 min. After fixing, the spheroids were further washed with PBS (−) before mounting with 90% glycerol in a μ-slide 8-well chambered coverslip (ibidi, cat. # 80826). Images were taken with a LSM880 confocal microscope (Carl Zeiss, Oberkochen, Germany) at a magnification of 1.2× using white light, 488- and 633 nm lasers for $\lambda_{\text{excitation}}$ of Fluor-CoA and NucSpot® 650, respectively. Z-stack images were taken at 15 μm intervals for U87MG and at 10 μm intervals for GT1-7. Image analysis was done using Zeiss Zen software, including the measurement of spheroid diameters and radial fluorescence profile.

4.13 Statistical analysis

Data are expressed as means ± SD of assays performed at least in triplicate. Several statistical analyses were performed using GraphPad version 9: (1) statistical significances were determined Student's t-test (column analysis), one-way ANOVA with Tukey's post-hoc (grouped analysis), or two-way ANOVA and (2) relationships between variables were analyzed using linear and non-linear regression using the same software.

Author contributions

Conflicts of interest

The authors have no other relevant affiliations or financial involvement with any organization or entity with a financial interest in or financial conflict with the subject matter or materials discussed in the manuscript apart from those disclosed.

Acknowledgements

References

1 K. D. Bruce, A. Zsombok and R. H. Eckel, *Front. Endocrinol.*, 2017, **8**, 1–11.
2 J. A. Hamilton, C. J. Hillard, A. A. Spector and P. A. Watkins, in *Journal of Molecular Neuroscience*, Springer, 2007, vol. 33, pp. 2–11.

3 E. Currie, A. Schulze, R. Zechner, T. C. Walther and R. V. Farese, *Cell Metab.*, 2013, **18**, 153–161.

4 N. Casals, V. Zammit, L. Herrero, R. Fadó, R. Rodríguez-Rodríguez and D. Serra, *Prog. Lipid Res.*, 2016, **61**, 134–148.

5 R. Fadó, R. Rodríguez-Rodríguez and N. Casals, *Prog. Lipid Res.*, 2021, 81.

6 I. R. Schlaepfer and M. Joshi, *Endocrinol.*, 2020, 161.

7 A. Pocai, T. K. T. Lam, S. Obici, R. Gutierrez-Juarez, E. D. Muse, A. Arduini and L. Rossetti, *J. Clin. Invest.*, 2006, **116**, 1081–1091.

8 K. Makowski, P. Mera, D. Paredes, L. Herrero, X. Ariza, G. Asins, F. G. Hegardt, J. García and D. Serra, *Chirality*, 2013, **25**, 281–287.

9 S. Obici, Z. Feng, A. Arduini, R. Conti and L. Rossetti, *Nat. Med.*, 2003, **9**, 756–761.

10 R. Lage, M. J. Vázquez, L. Varela, A. K. Saha, A. Vidal-Puig, R. Nogueiras, C. Diéguez and M. López, *FASEB J.*, 2010, **24**, 2670–2679.

11 A. Cirillo, A. Di Salle, O. Petillo, M. A. B. Melone, G. Grimaldi, A. Bellotti, G. Torelli, M. S. De' Santi, G. Cantatore, A. Marinelli, U. Galderisi and G. Peluso, *Cancer Biol. Ther.*, 2014, **15**, 735–741.

12 J. Sperry, M. C. Condro, L. Guo, D. Braas, N. Vanderveer-Harris, K. K. O. Kim, W. B. Pope, A. S. Divakaruni, A. Lai, H. Christofk, M. G. Castro, P. R. Lowenstein, J. E. Le Belle and H. I. Kornblum, *iScience*, 2020, **23**, 101453.

13 G. Petővári, T. Dankó, I. Krencz, Z. Hujber, H. Rajnai, E. Vetlényi, R. Raffay, J. Pápay, A. Jeney and A. Sebestyén, *Pathol. Oncol. Res.*, 2020, **26**, 23–33.

14 K. Zaugg, Y. Yao, P. T. Reilly, K. Kannan, R. Kiarash, J. Mason, P. Huang, S. K. Sawyer, B. Fuerth, B. Faubert, T. Kalliomäki, A. Elia, X. Luo, V. Nadeem, D. Bungard, S. Yalavarthi, J. D. Growney, A. Wakeham, Y. Moolani, J. Silvester, A. Y. Ten, W. Bakker, K. Tsuchihara, S. L. Berger, R. P. Hill, R. G. Jones, M. Tsao, M. O. Robinson, C. B. Thompson, G. Pan and T. W. Mak, *Genes Dev.*, 2011, **25**, 1041–1051.

15 S. M. Ceccarelli, O. Chomienne, M. Gubler and A. Arduini, *J. Med. Chem.*, 2011, **54**, 3109–3152.

16 A. Bentebibel, D. Sebastián, L. Herrero, E. López-Viñas, D. Serra, G. Asins, P. Gómez-Puertas, F. G. Hegardt, P. Gómez-Puertas and F. G. Hegardt, *Biochemistry*, 2006, **45**, 4339–4350.

17 P. Mera, A. Bentebibel, E. López-Viñas, A. G. Cordente, C. Gurunathan, D. Sebastián, I. Vázquez, L. Herrero, X. Ariza, P. Gómez-Puertas, G. Asins, D. Serra, J. García and F. G. Hegardt, *Biochem. Pharmacol.*, 2009, **77**, 1084–1095.

18 R. Conti, E. Mannucci, P. Pessotto, E. Tassoni, P. Carminati, F. Giannessi and A. Arduini, *Diabetes*, 2011, **60**, 644–651.

19 R. S. O'Connor, L. Guo, S. Ghassemi, N. W. Snyder, A. J. Worth, L. Weng, Y. Kam, B. Philipson, S. Trefely, S. Nunez-Cruz, I. A. Blair, C. H. June and M. C. Milone, *Sci. Rep.*, 2018, **8**, 1–9.

20 K. Makowski, P. Mera, J. Ariza, D. Serra, J. Garcia, L. Herrero, M. López and A. Venegas, *Rev. Bionatura*, 2019, **4**, 1–5.

21 A. Gautier and M. J. Hinner, *Site-Specific Protein Labeling Methods Protoc*, 2015, pp. 1–267.

22 M. C. Cheng, X. H. Qiang and C. M. Du, *Chin. Sci. Bull.*, 2013, **58**, 1256–1261.

23 H. Cabral, K. Miyata, K. Osada and K. Kataoka, *Chem. Rev.*, 2018, **118**, 6844–6892.

24 A. Harada and K. Kataoka, *Polym. J.*, 2018, **50**, 95–100.

25 S. Quader and K. Kataoka, *Mol. Ther.*, 2017, **25**, 1501–1513.

26 C. Wang, Q. Chen, Z. Wang and X. Zhang, *Angew. Chem., Int. Ed.*, 2010, **49**, 8612–8615.

27 H. Uchida, K. Miyata, M. Oba, T. Ishii, T. Suma, K. Itaka, N. Nishiyama and K. Kataoka, *J. Am. Chem. Soc.*, 2011, **133**, 15524–15532.

28 H. Uchida, K. Itaka, T. Nomoto, T. Ishii, T. Suma, M. Ikegami, K. Miyata, M. Oba, N. Nishiyama and K. Kataoka, *J. Am. Chem. Soc.*, 2014, **136**, 12396–12405.

29 C. Y. Lin, F. Perche, M. Ikegami, S. Uchida, K. Kataoka and K. Itaka, *J. Controlled Release*, 2016, **235**, 268–275.

30 S. T. Crowley, Y. Fukushima, S. Uchida, K. Kataoka and K. Itaka, *Mol. Ther. – Nucleic Acids*, 2019, **17**, 465–476.

31 H. Helmbrecht, A. Joseph, M. McKenna, M. Zhang and E. Nance, *Curr. Opin. Chem. Eng.*, 2020, **30**, 112–119.

32 E. A. Nance, G. F. Woodworth, K. A. Sailor, T.-Y. Shih, Q. Xu, G. Swaminathan, D. Xiang, C. Eberhart and J. Hanes, *Sci. Transl. Med.*, 2012, **4**, 149ra119–149ra119.

33 E. Nance, K. Timbie, G. W. Miller, J. Song, C. Louttit, A. L. Klibanov, T. Y. Shih, G. Swaminathan, R. J. Tamargo, G. F. Woodworth, J. Hanes and R. J. Price, *J. Controlled Release*, 2014, **189**, 123–132.

34 A. G. Godin, J. A. Varela, Z. Gao, N. Danné, J. P. Dupuis, B. Lounis, L. Groc and L. Cognet, *Nat. Nanotechnol.*, 2017, **12**, 238–243.

35 C. Paviolo, F. N. Soria, J. S. Ferreira, A. Lee, L. Groc, E. Bezard and L. Cognet, *Methods*, 2020, **174**, 91–99.

36 C. Curtis, M. McKenna, H. Pontes, D. Toghani, A. Choe and E. Nance, *Nanoscale*, 2019, **11**, 22515–22530.

37 Y. Ma, S. M. Temkin, A. M. Hawkridge, C. Guo, W. Wang, X. Y. Wang and X. Fang, *Fatty acid oxidation: An emerging facet of metabolic transformation in cancer*, Elsevier B.V., 2018, vol. 435.

38 L. S. Pike, A. L. Smift, N. J. Croteau, D. A. Ferrick and M. Wu, *Biochim. Biophys. Acta., Bioenerg.*, 2011, **1807**, 726–734.

39 M. Allen, M. Bjerke, H. Edlund, S. Nelander and B. Westermark, *Sci. Transl. Med.*, 2016, **8**, 354re3–354re3.

40 S. Kant, P. Kesarwani, A. Prabhu, S. F. Graham, K. L. Buelow, I. Nakano and P. Chinnaiyan, *Cell Death Dis.*, 2020, **11**, 1–13.

41 B. Juraszek, J. Czarnecka–Herok and K. A. Nałęcz, *J. Neurochem.*, 2021, **156**, 642–657.

42 A. S. Divakaruni, W. Y. Hsieh, L. Minarrieta, T. N. Duong, K. K. O. Kim, B. R. Desousa, A. Y. Andreyev, C. E. Bowman, K. Caradonna, B. P. Dranka, D. A. Ferrick, M. Liesa, L. Stiles, G. W. Rogers, D. Braas, T. P. Ciaraldi, M. J. Wolfgang, T. Sparwasser, L. Berod, S. J. Bensinger and A. N. Murphy, *Cell Metab.*, 2018, **28**, 490–503e7.

43 Y. Arai, H. Ishii, M. Kobayashi and H. Ozawa, *J. Physiol. Sci.*, 2017, **67**, 313–323.

44 B. Taïb, K. Bouyakdan, C. Hryhorczuk, D. Rodaros, S. Fulton and T. Alquier, *J. Biol. Chem.*, 2013, **288**, 37216–37229.

45 A. C. Hunter, *Adv. Drug Delivery Rev.*, 2006, **58**, 1523–1531.

46 S. J. Choi, F. Kim, M. W. Schwartz and B. E. Wisse, *Am. J. Physiol. Metab.*, 2010, **298**, E1122–E1130.

47 J. F. Mir, S. Zagmutt, M. P. Lichtenstein, J. García-Villoria, M. Weber, A. Gracia, G. Fabriàs, J. Casas, M. López, N. Casals, A. Ribes, C. Suñol, L. Herrero and D. Serra, *Mol. Neurobiol.*, 2018, **55**, 7216–7228.

48 H. Lin, S. Patel, V. S. Affeck, I. Wilson, D. M. Turnbull, A. R. Joshi, R. Maxwell, E. A. Stoll, V. S. Affleck, I. Wilson, D. M. Turnbull, A. R. Joshi, R. Maxwell and E. A. Stoll, *Neuro. Oncol.*, 2017, **19**, 43–54.

49 L. Mo, L. Hou, D. Guo, X. Xiao, P. Mao and X. Yang, *Int. J. Pharm.*, 2012, **436**, 815–824.

50 J. M. Rabanel, P. A. Piec, S. Landri, S. A. Patten and C. Ramassamy, *J. Controlled Release*, 2020, **328**, 679–695.

51 R. Vadivelu, H. Kamble, M. Shiddiky and N.-T. Nguyen, *Micromachines*, 2017, **8**, 94.

52 A. Tchoryk, V. Taresco, R. H. Argent, M. Ashford, P. R. Gellert, S. Stolnik, A. Grabowska and M. C. Garnett, *Bioconjugate Chem.*, 2019, **30**, 1371–1384.

53 J. Garcia-Chica, W. K. D. Paraiso, S. Tanabe, D. Serra, L. Herrero, N. Casals, J. Garcia, X. Ariza, S. Quader and R. Rodriguez-Rodriguez, *Nanomedicine*, 2020, **15**, 1617–1636.

54 S. Quader, H. Cabral, Y. Mochida, T. Ishii, X. Liu, K. Toh, H. Kinoh, Y. Miura, N. Nishiyama and K. Kataoka, *J. Controlled Release*, 2014, **188**, 67–77.

55 New England Biolabs Inc., Reaction Conditions for Chemical Coupling with CoA-SH (S9352S), https://international.neb.com/protocols/2012/08/09/reaction-conditions-for-chemical-coupling-with-coa-sh-s9352s, (accessed 11 May 2020).

56 M. I. Malandrino, R. Fucho, M. Weber, M. Calderon-Dominguez, J. F. Mir, L. Valcarcel, X. Escoté, M. Gómez-Serrano, B. Peral, L. Salvadó, S. Fernández-Veledo, N. Casals, M. Vázquez-Carrera, F. Villarroya, J. J. Vendrell, D. Serra and L. Herrero, *Am. J. Physiol.– Endocriol. Metab.*, 2015, **308**, E756–E769.

Biomaterials Science

rsc.li/biomaterials-science

ROYAL SOCIETY
OF CHEMISTRY

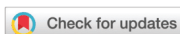**PAPER**
Sabina Quader,
Rosalía Rodríguez-Rodríguez *et al.*
Nanomedicine targeting brain lipid
metabolism as a feasible approach for
controlling the energy balance

10 YEARS ANNIVERSARY

ESB European
Society for
Biomaterials

Check for updates

Nanomedicine targeting brain lipid metabolism as a feasible approach for controlling the energy balance†

Jesús Garcia-Chica,‡[a] West Kristian Dizon Paraiso, [ID] ‡§[b] Sebastián Zagmutt,[a] Anna Fosch,[a] Ana Cristina Reguera,[a] Sara Alzina,[a] Laura Sánchez-García,[a] Shigeto Fukushima,[b] Kazuko Toh,[b] Núria Casals,[a,c] Dolors Serra, [ID] [c,d] Laura Herrero,[c,d] Jordi Garcia, [ID] [c,e] Kazunori Kataoka,[b] Xavier Ariza, [ID] [c,e] Sabina Quader [ID] *[b] and Rosalía Rodríguez-Rodríguez [ID] *[a,c]

Targeting brain lipid metabolism is a promising strategy to regulate the energy balance and fight metabolic diseases such as obesity. The development of stable platforms for selective delivery of drugs, particularly to the hypothalamus, is a challenge but a possible solution for these metabolic diseases. Attenuating fatty acid oxidation in the hypothalamus *via* CPT1A inhibition leads to satiety, but this target is difficult to reach *in vivo* with the current drugs. We propose using an advanced crosslinked polymeric micelle-type nanomedicine that can stably load the CPT1A inhibitor C75-CoA for *in vivo* control of the energy balance. Central administration of the nanomedicine induced a rapid attenuation of food intake and body weight in mice *via* regulation of appetite-related neuropeptides and neuronal activation of specific hypothalamic regions driving changes in the liver and adipose tissue. This nanomedicine targeting brain lipid metabolism was successful in the modulation of food intake and peripheral metabolism in mice.

New concepts

Effective treatments to control feeding, body weight, and glucose homeostasis in metabolic diseases such as obesity or diabetes are insufficient, due to the difficulty of reaching specific brain targets that are in charge of energy balance. Here, we present the first nanomedicine acting on a brain target to drive a rapid modulation of food intake and peripheral metabolism, offering an innovative approach to managing metabolic diseases. The core-crosslinked polymeric micelle-based nanomedicine used in this investigation allows the encapsulation of a drug that modifies lipid metabolism in the brain, a target hard to reach with conventional formulations. This investigation might contribute to developing and validating a new generation of nanomedicine-based approaches targeting brain lipid metabolism to modulate feeding and body weight. Also, this nanomedicine highlights the significance of nanotechnology beyond the current biological applications and facilitates the understanding of the early stages of energy balance (*i.e.*, acute satiating actions) that are crucial for developing complex diseases such as obesity and diabetes.

[a]*Basic Sciences Department, Faculty of Medicine and Health Sciences, Universitat Internacional de Catalunya (UIC), Sant Cugat del Vallès, E-08195, Spain. E-mail: rrodriguez@uic.es; Tel: +34-935-042-002*

[b]*Innovation Center of Nanomedicine, Kawasaki Institute of Industrial Promotion, Kawasaki, Kanagawa 210-0821, Japan. E-mail: sabina-q@kawasaki-net.ne.jp; Tel: +81-44-589-5920*

[c]*Centro de Investigación Biomédica en Red de Fisiopatología de la Obesidad y la Nutrición (CIBEROBN), Instituto de Salud Carlos III, Madrid, E-28029, Spain*

[d]*Department of Biochemistry and Physiology, School of Pharmacy and Food Sciences, Institut de Biomedicina de la Universitat de Barcelona (IBUB), Universitat de Barcelona, Barcelona, E-08028, Spain*

[e]*Department of Inorganic and Organic Chemistry, Faculty of Chemistry, Institut de Biomedicina de la Universitat de Barcelona (IBUB), Universitat de Barcelona (UB), Barcelona, E-08028, Spain*

†Electronic supplementary information (ESI) available. See DOI: https://doi.org/10.1039/d2bm01751b

‡These authors contributed equally to this work.

§Present address: Red Arrow Therapeutics Co., Ltd, Tokyo 113-0033, Japan.

1. Introduction

Metabolic disorders such as obesity imply a disruption in energy homeostasis, leading to an imbalance between food intake and energy expenditure.[1] Despite the major advances in understanding the pathogenesis and therapeutics of these metabolic disorders, the prevalence of obesity and type 2 diabetes continues to rise.[2,3] Against this backdrop, these metabolic diseases have still unmet medical needs and require the development of new therapeutic platforms.

The physiological control of energy balance is tightly modulated by the central nervous system (CNS), where the hypothalamus is the most critical area implicated.[4,5] Hypothalamic nuclei are sensitive to nutrients and hormones and modify the expression, secretion, and activity of specific neurotransmitters and neuromodulators, resulting in changes in food intake, energy expenditure, and the function of key peripheral tissues such as the liver and adipose tissue.[4,6,7] Strong evidence suggests that lipid metabolism within the hypothalamus is a key signal of nutrient status further to modulate feeding behaviour and peripheral metabolism.[8–10] In particular, fatty acid (FA) sensing in hypothalamic neurons via accumulation of FAs or FA metabolites acts as a satiety signal and may decrease food intake and hepatic function.[1,11]

A crucial target in brain lipid metabolism which controls the energy balance is carnitine palmitoyl-transferase 1A (CPT1A).[12] It is located in the mitochondria and promotes the entry of long-chain FAs for β-oxidation.[13–16] Since CPT1A is highly expressed in central and peripheral tissues, its regulatory potential in the energy balance is based on two different interventions: in peripheral tissues (i.e., liver and adipose tissue), overexpression of CPT1A and induction of fatty acid oxidation (FAO) ameliorate insulin resistance and prevent body weight gain,[17,18] whereas in the CNS, CPT1A inhibition reduces food intake and body weight.[19,20] Particularly, in the arcuate (ARC) nucleus of the hypothalamus, genetic ablation of CPT1A prevents FAO, leading to a local accumulation of long-chain FAs which in turn mediates the action of several feeding-related hormones to inhibit food intake in lean rats.[21] Thus, selective inhibition of CPT1A in the hypothalamus, but not in the peripheral tissues, is a promising strategy for the management of metabolic disorders involving a disruption in energy balance. However, brain lipid metabolism is difficult to reach in vivo with the current formulations and drugs.

(±)-C75 is a well-known CPT1A inhibitor that is converted to its active coenzyme A (CoA) form in the hypothalamus.[22] Although initially identified as a fatty acid synthase (FAS) inhibitor with a strong anorectic effect via malonyl-CoA accumulation,[23–25] enantioselective synthesis of C75 revealed that the (+)-C75 and (±)-C75-CoA adducts were the active forms inhibiting CPT1A.[22,26] Therefore, to avoid the off-target effect on FAS and undesired actions in the periphery, it is crucial to deliver (±)-C75-CoA directly into the brain for CPT1A inhibition and energy balance regulation. A major challenge of (±)-C75-CoA as cargo is that it is a small, polar, and negatively charged molecule, with low permeability across the cellular membrane. (±)-C75-CoA interacts with polycations through a combination of electrostatic and hydrophobic interactions, as it possesses both phosphate and carboxylate groups, as well as an aliphatic side chain.[27] We used this particular property in designing a poly-ion complex (PIC) micelle, a polymeric formulation that allows for a direct and specific cellular transport of (±)-C75-CoA, demonstrating an efficient inhibition of CPT1A-dependent lipid metabolism in cellular models of neurons and glioma cells.[28] In the present study, we have developed a more robust core-crosslinked polymeric micelle (PM)-type nano-

medicine, with a high entrapment efficiency of the specific CPT1A inhibitor (±)-C75-CoA (Fig. 1). This crosslinked PM has proven to be useful for in vivo applications, showing an effective biological activity upon delivery of the CPT1A inhibitor in brain cells after intracerebroventricular (ICV) administration, particularly to neurons. In addition, central administration of this (±)-C75-CoA-loaded core-crosslinked PM induced a substantial reduction in food intake and body weight in mice as compared to the free drug, as well as significant regulation of appetite-related neuropeptides, neuronal activation of specific hypothalamic regions and altered expression of metabolic biomarkers in peripheral tissues (Fig. 1). This investigation led to the first nanomedicine targeting brain lipid metabolism, which effectively modulated energy intake and peripheral tissue metabolism.

2. Results and discussion

2.1 Stability of crosslinked polymeric micelles (PM) loading (±)-C75-CoA and uptake in neuronal cell lines

In this study, we synthesized a triblock co-polymer using sequential N-carboxyanhydride (NCA) polymerization with polyethylene glycol (PEG) as a hydrophilic shell forming block, a poly(L-aspartamide) (PAsp) middle block functionalized via an orthogonal side-chain modification with an aromatic aldehyde moiety (PAsp(Aldehyde)), and a poly(L-lysine) (PLys) cationic block designed to form a PIC with (±)-C75-CoA (Fig. 2). Solutions of (±)-C75-CoA and PEG-PAsp(Aldehyde)-PLys were combined in a 1 : 1 anion/cation ratio, defined as the ratio between the overall anionic charge imparted by the phosphate and carboxylate groups in (±)-C75-CoA and the overall cationic charge given by the protonated amines in the polymer. A PEG-PAsp diblock co-polymer functionalized with hydrazide groups (PEG-PAsp(Hydrazide)) was added to the micelle to crosslink the aldehyde-containing PEG-PAsp(Aldehyde)-PLys through hydrazone formation (Fig. 1). This aromatic aldehyde and hydrazide-derived reversible hydrazone bonds[29,30] formed in the copolymer middle block provided increased protection and stability to the micelle by tightening the core and preventing premature release of the cargo (Fig. 1). (±)-C75-CoA and PEG-PAsp(Aldehyde)-PLys were mixed in 10 mM phosphate buffer (pH 7.4) that spontaneously self-assembled to form a core–shell structured PM. To crosslink the PM, PEG-PAsp (Hydrazide) was added in molar equivalence of hydrazide to the aldehyde functionality (Fig. 1). Upon filtration, both non-crosslinked and crosslinked PMs gave monodisperse size profiles of around 40–45 nm hydrodynamic diameter, determined by dynamic light scattering (DLS) measurements (Fig. 3A; ESI Table S1†). In comparison, the average core size of PMs was found to be ca. 20 nm by transmission electron microscopy (TEM), which is smaller than the hydrodynamic diameter, since the latter accounts for the PEG shell of the micelle (Fig. S1, ESI†). It is worth highlighting that the middle block strengthens the micelle core even without crosslinking, possibly by providing hydrophobicity.[31] The polymer mixtures only
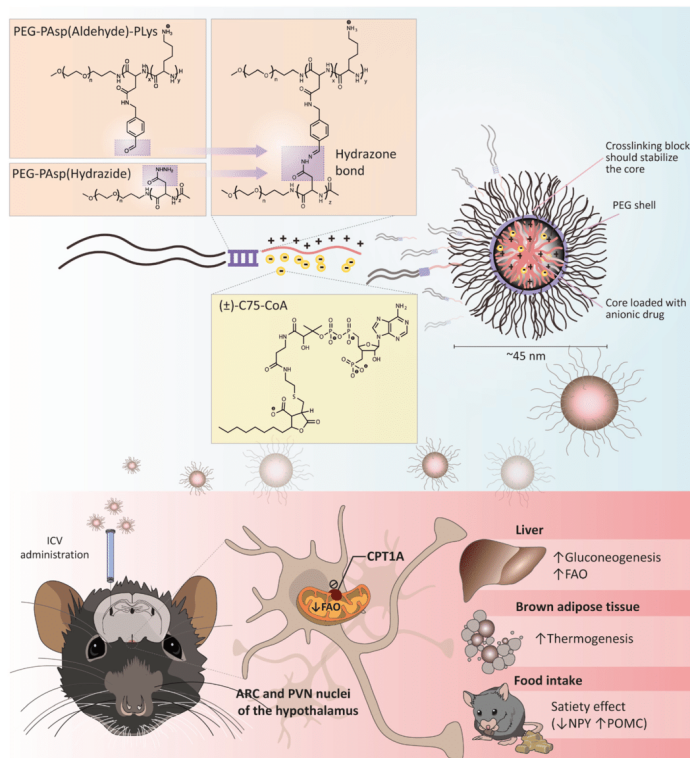
- 255 -

Fig. 1 Schematic representation of the core-crosslinked polymeric micelle (PM)-type nanomedicine encapsulating the CPT1A inhibitor (±)-C75-CoA, and the effects of central administration (ICV) of the nanomedicine on food intake and liver and brown fat metabolism *via* the arcuate (ARC) and paraventricular (PVN) nuclei of the hypothalamus.

(without (±)-C75-CoA) provided large aggregates, confirming that the cargo has a profound influence in producing well-defined PM-type structures, which was evident from the TEM images (Fig. S1, ESI†).

To confirm the advantages of the middle block, we prepared micelles from a PEG-PLys diblock copolymer (Fig. S2A, ESI†). We then added a polyanion (sodium dextran sulfate; DSS) to confirm the ionic interaction between the anionic cargo and the cationic PLys chain. Micelle dissociation with the increase of DSS concentration was observed for the diblock PM, evident by the drastic reduction of light scattering intensity, but for that of the triblock PM the impact of DSS addition was minimal (Fig. S2B, ESI†). A core-crosslinked PM prepared from the PEG-PAsp(Aldehyde)-PLys triblock and PEG-PAsp (Hydrazide) diblock co-polymer incorporating crosslinking to provide hydrophobicity is expected to give even higher stabi-

lity. To confirm the participation of these two polymers in the micellar assembly and subsequent interaction, we labelled the PEG-PAsp(Aldehyde)-PLys polymer with rhodamine and PEG-PAsp(Hydrazide) with fluorescein on their N-termini. When the labelled polymers were used to form PMs with (±)-C75-CoA, we observed Förster resonance energy transfer (FRET) upon scanning the emitted light at 450 nm excitation (Fig. 3B), corroborating that they were associated with the PM core. The FRET profile of crosslinked PMs was not altered with the addition of 1 M NaCl. However, upon adding DSS, the signal intensity from the rhodamine-labelled polymer was reduced to 60%, which indicated that (±)-C75-CoA plays a significant role in the association of two polymers, as evidenced by FRET pairing. To further confirm whether (±)-C75-CoA was necessary for the increased interaction of the FRET-paired polymers, the FRET spectrum of a mixture of the two labelled
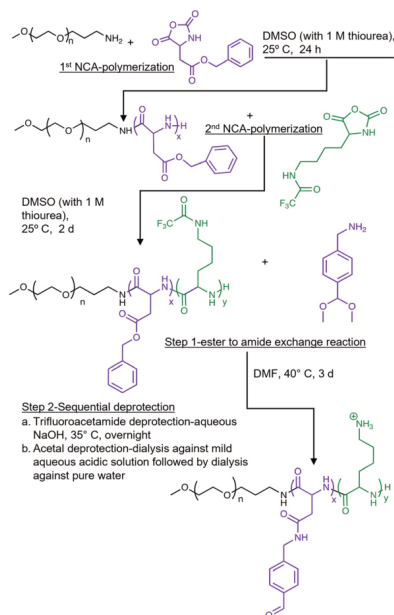
Fig. 2 Preparation of the triblock polymer, PEG-PAsp(Aldehyde)-PLys.

polymers was measured. This revealed similar FRET properties to those of the DSS-treated PM. However, when the FRET-paired polymers were mixed without (±)-C75-CoA and then treated with DSS, a residual FRET signal was observed. This suggests that there was still some form of interaction between the two polymers despite the release/absence of the (±)-C75-CoA cargo, possibly through covalent (hydrazone) bonds and other forces of attraction.

To check micellar stability in salt solution, we added 1 M NaCl to the PM solution. This led to a 15 nm increase in size for both types of micelles (Fig. 3C); however, the non-cross-linked PM gave an apparently more polydisperse size profile with a statistical decrease in scattered light intensity (Fig. 3D and E). The results attested to the PIC nature of the PM. PIC formation is mainly driven by the liberation of counterions,[32] which is prompted when the PLys block and anionic (±)-C75-CoA paired up, leading to a large entropic gain. The increased NaCl concentration apparently reduced this entropic gain, which resulted in PIC destabilization. These data provide additional evidence that the crosslinked PM is more stable than the non-crosslinked PM.

To test their differing effects on biological systems, we measured the ATP synthesis of GT1-7 mouse hypothalamic neurons after short-term incubation with the PMs. This is an indirect approach to measure mitochondria FAO and CPT1A inhibition by the drug[28] (Fig. 3F). The crosslinked PM statistically reduced cellular ATP production to 41%, as compared to the non-crosslinked PM (73%) and free (±)-C75-CoA (87%) (Fig. 3F). Moderation of the ATP synthesis in *in vitro* neurons in response to PM treatment indicates inhibition of FAO, in agreement with the previous data,[28,33] and this attenuation was significantly higher compared to the non-crosslinked PM. The crosslinked PM exhibited higher apparent encapsulation of (±)-C75-CoA compared to the non-crosslinked PM in both pH 7.4 phosphate buffer (PB) and artificial cerebrospinal fluid (aCSF) (Fig. S3, ESI†), with the latter mimicking conditions in the brain. Since more (±)-C75-CoA was entrapped in the cross-linked PM, it was expected to enter the cell more efficiently in contrast to the non-crosslinked PM.

To track its cellular uptake, we prepared PMs from a fluorescent derivative of CoA, Fluor-CoA,[28] with a size profile similar to (±)-C75-CoA-PM (Fig. S4A, ESI†). Upon incubation with GT1-7 neuronal cells for 30 min, we observed that there was an evidently higher cellular uptake of Fluor-CoA-loaded crosslinked PM (4× that of the free dye) as compared with the non-cross-linked PM (3× compared to the free dye) (Fig. 3G). This points to another reason why the crosslinked PM has a greater ATP inhibitory effect compared to the non-crosslinked counterpart. Fluor-CoA was also released in the cell culture medium or aCSF to a lesser extent by the crosslinked PM (Fig. S4C and D, ESI†), despite both non-crosslinked and crosslinked PM having similar encapsulation rates (Fig. S4B, ESI†). In neuronal cells, the fluorescent tracer of the micelle showed *endo*-lysosomal entrapment, which was not appreciated in the mitochondria (Fig. S5, ESI†).

The increased stability of the crosslinked PM ensured a higher (±)-C75-CoA encapsulation rate, an enhanced ATP inhibitory capacity, and increased cellular uptake of fluorescein when using the Fluor-CoA-loaded PM. This cellular uptake was also confirmed *in vivo*, since the brain slices revealed fluorescent staining of the tracer of the crosslinked PM, particularly in the hypothalamic area, after ICV infusion of the nanomedicine (Fig. S6, ESI†), as previously indicated with other types of polymeric nanomedicines.[48–50]

Altogether, the formulation presented here, which is based on a specially designed triblock copolymer platform, allowed for remarkable stability better suited for *in vivo* applications when matched with the non-crosslinked PM. This could be explained by: (i) increased hydrophobicity of the polymer, which enabled a better interaction with (±)-C75-CoA and (ii) crosslinking of the two polymers through hydrazone formation. The polymer PEG chain (M_W 12 kDa) was important in imparting the measured physicochemical properties and decreasing aggregation tendency.[32]

2.2 (±)-C75-CoA-loaded core crosslinked PMs induced rapid attenuation of food intake and body weight and regulated the expression of hypothalamic neuropeptides

A major finding of this investigation is the remarkable acute effect of the central administration of the nanomedicine on feeding and body weight, with improvements in these actions
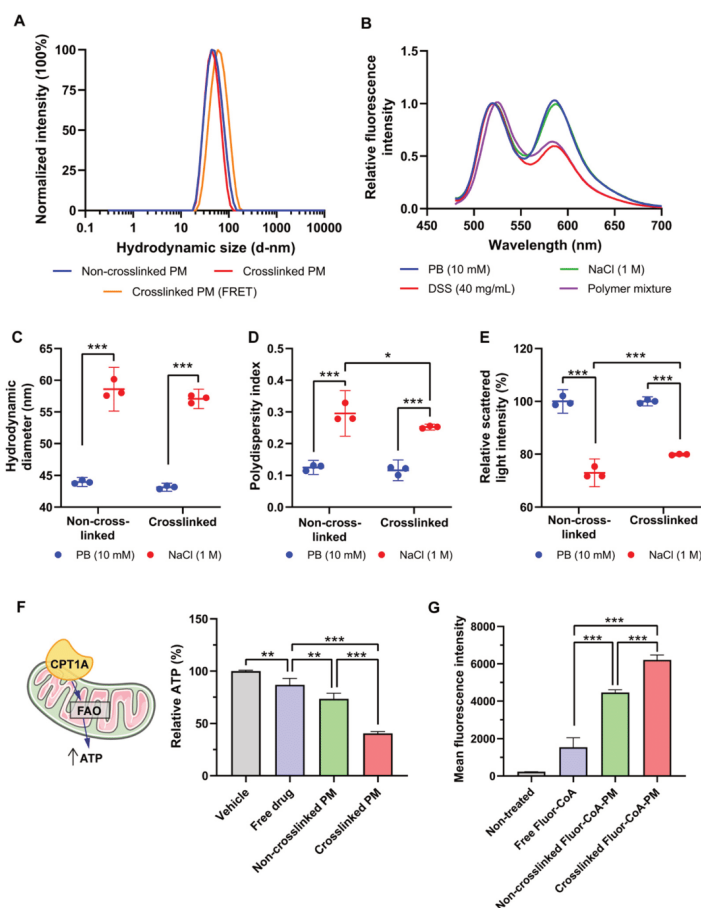
- 257 -

Fig. 3 Physicochemical characterization of the crosslinked polymeric micelles (PMs) loading (±)-C75-CoA or Fluor-CoA and validation in the neuronal cell lines. (A) Size profile of (±)-C75-CoA-PM. (B) Fluorescence emission spectra of the FRET double-labelled (±)-C75-CoA-PM and mixed polymers. (C–E) Physicochemical properties of the micelles in phosphate buffer (PB) and NaCl solution: (C) hydrodynamic size, (D) polydispersity, and (E) scattered light intensity of non-crosslinked *versus* crosslinked PM. (F) Measurement of ATP levels as an indirect indicator of fatty acid oxidation (FAO) and CPT1A activity in neuronal cells treated with the vehicle, free drug, non-crosslinked and crosslinked-PM. (G) Cellular uptake of Fluor-CoA non-crosslinked or crosslinked micelles. Data are expressed as mean ± SD (n = 3–4). Means were compared using one-way ANOVA along with Tukey's *post hoc* test. *p < 0.05, **p < 0.01 and ***p < 0.001.

compared to the free drug (±)-C75 administration. In these experiments, age-matched mice were administered ICV injections of the vehicle: (±)-C75, (±)-C75-CoA, and (±)-C75-CoA-loaded core crosslinked PMs (from here on will be designated as (±)-C75-CoA-PM). Food intake and body weight were then monitored for 24 h (Fig. 4A). This timing was in agreement

with the previous studies monitoring the acute satiating effects of new therapeutics in lean rodent models.[13,34,35] Mice treated with (±)-C75-CoA-PM exhibited a substantial and rapid reduction of food intake in comparison with (±)-C75-CoA-, (±)-C75- and vehicle-treated mice (Fig. 4B). The satiating effect of (±)-C75-CoA-PM was appreciated after 1 h, being statistically
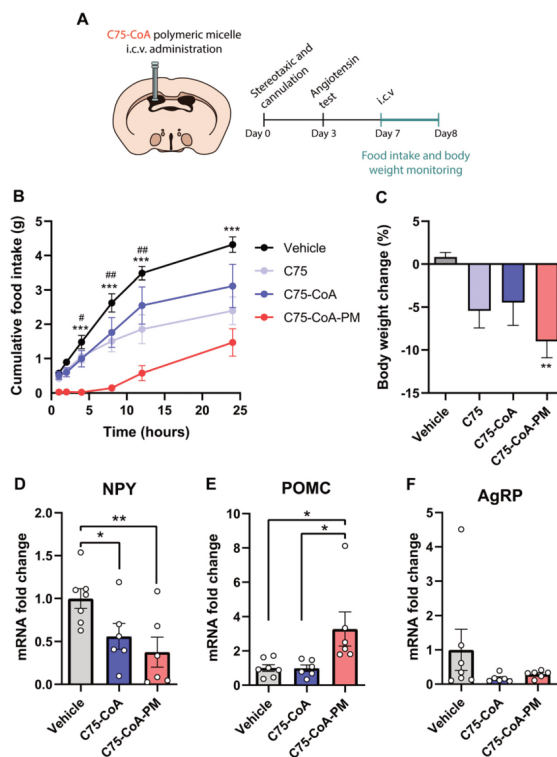
Fig. 4 ICV administration of (±)-C75-CoA polymeric micelles (PM) rapidly reduced food intake and body weight in mice by regulating the expression of hypothalamic neuropeptides. (A) Diagram indicating the experimental protocol of surgery, administration and monitoring. (B) Cumulative food intake at different timings (***$p < 0.001$ *vs.* (±)-C75-CoA-PM; #$p < 0.05$ and ##$p < 0.01$ *vs.* (±)-C75-CoA) and (C) body weight change in mice after 24 h of central administration of the vehicle, free drug or the nanomedicine ((±)-C75-CoA-PM) (**$p < 0.01$ *vs.* vehicle)). (D–F) mRNA levels of the hypothalamic neuropeptides (D) NPY (orexigenic and energy expenditure activator), (E) POMC (anorexigenic and energy expenditure activator) and (F) AgRP (orexigenic and energy expenditure inhibitor), 2.5 h post-injection (*$p < 0.05$ and **$p < 0.01$). Data are expressed as mean ± SD ($n = 6$–8). Means were compared using one-way ANOVA along with Tukey's *post hoc* test.

different 4 h post-treatment *versus* the vehicle and free drugs. This action was maintained throughout the experiment (24 h) (Fig. 4B). In line with this result, body weight change measured at 24 h post-treatment was also significantly reduced in (±)-C75-CoA-PM-treated mice when evaluated against the control group (Fig. 4C). These acute effects on energy balance in lean mice are very promising and comparable to the satiating action of CPT1A inhibition after short timings (2 to 24 h) in lean rodents using drug- or genetic-based approaches.[21,23,36] In agreement with the observed rapid effects on feeding, it has been reported that the levels of malonyl-CoA, when elevated in the brain and particularly in the hypothalamus in response to energy surplus or glucose overload, induces rapid inhibition of

CPT1A, leading to food intake reduction, and these changes appear very rapidly (from minutes to a few hours).[16,37]

Since alteration of brain CPT1A and malonyl-CoA levels is known to modify the expression of hunger-related neuropeptides in the hypothalamus,[36] we measured the mRNA expression of these neuropeptides. Once released by different neuronal populations in the ARC nucleus of the hypothalamus, the following peptides exert opposing effects on feeding and metabolism: the neuropeptide Y (NPY) and agouti-gene related protein (AgRP) are orexigenic neuropeptides, whereas the precursor protein, proopiomelanocortin (POMC), is a signal that induces satiety and body weight attenuation.[38,39] For this analysis, hypothalamic extracts of mice were collected

2.5 h after the treatment with the vehicle, free drug or PM. These timings were based on previous studies with altering malonyl-CoA levels and CPT1A activity in the hypothalamus, showing very rapid changes in the expression of these neuropeptides (2–3 hours post central inhibition of the target and lipid metabolism).[13,40] While free (±)-C75-CoA was able to attenuate the mRNA levels of the orexigenic neuropeptide NPY, (±)-C75-CoA-PM induced not only a significant reduction of NPY (Fig. 4D), but also upregulation of the anorexigenic neuropeptide POMC compared to the vehicle (Fig. 4E). However, no changes were appreciated in the mRNA levels of AgRP in response to either free drug or PM (Fig. 4F).

Despite our results being too preliminary to discard important side effects in patients with metabolic diseases, the present results are promising in terms of toxicity. In particular, analysis of microglial activation by Iba1 immunofluorescence in different regions of the hypothalamus revealed no activation of microglia after ICV infusion of the nanomedicine, indicating the low toxic potential of the formulation in the inflammatory response at the timing and dose tested in mice (Fig. S7, ESI†). Subsequent investigations using more selective targeting-based approaches to a specific type of neurons and after longer periods of administration to analyse feeding behaviour must be envisaged.

These data suggest that the nanomedicine (±)-C75-CoA-PM was more efficient in reducing body weight and food intake compared to the free drug, and that the appetite-suppressing effect could be explained through the modulation of hunger-related neuropeptides in the hypothalamus, particularly the upregulation of POMC and the downregulation of NPY. The main satiety signal in the brain which led to changes in the expression of neuropeptides meant that there was a local accumulation of long-chain fatty acyl-CoAs in the hypothalamus in response to FAO and CPT1A inhibition, indicating nutrient overload, as previously reported.[9,21]

2.3   (±)-C75-CoA-PM modified liver and brown fat metabolism

The hunger-related hypothalamic neuropeptides released in the ARC nucleus connect to second order neurons located in other hypothalamic nuclei to control energy balance, not only in terms of satiety, but also in terms of liver and adipose tissue metabolism.[41–43] Therefore, the effect of central administration of the drug in the free form or PM form was also investigated in these primary metabolically active tissues. Particularly, markers of glycolysis, gluconeogenesis, and FAO were assayed in the liver (Fig. 5A), while markers of thermogenesis were measured in the brown adipose tissue (BAT) (Fig. 5B) 2.5 h post-ICV injection of either vehicle, free drug, or PM.

In the liver, gluconeogenesis (PEPCK) and FAO (CPT1A) mRNA markers were significantly increased by (±)-C75-CoA-PM in comparison with the free drug or vehicle with no accompanying changes in the last stage of glucose production (G6Pase), which is consistent with a response to a satiating effect (Fig. 5A). In line with this, the expression of the pyruvate kinase liver isoform (PKL), a regulator of pyruvate production, remained unchanged when using (±)-C75-CoA, but was significantly reduced by (±)-C75-CoA-PM, supporting the idea that the nanomedicine can promote FAO and the initial stages of gluconeogenesis, but not pyruvate, to provide energy fuel to extrahepatic tissues in response to the satiating actions.

The analysis of genes related to thermogenesis in the BAT, which contributes to energy expenditure and body weight regulation,[44] revealed significant induction of the expression of several genes involved in BAT thermogenesis activation, probably contributing to energy expenditure and body weight loss after this treatment. In contrast, the free drug was not able to modify the expression of the genes under study (Fig. 5B).

Taken together, these results show that central administration of (±)-C75-CoA-PM led to transcriptional changes in metabolically active tissues in the periphery, such as the liver and BAT, whereas the expression of these markers remained unaffected in free (±)-C75-CoA-treated mice.

2.4   (±)-C75-CA-PM activated neurons in specific hypothalamic nuclei

In order to assess the activation of neurons in different areas of the hypothalamus in response to the free drug or nanomedicine (±)-C75-CoA, c-FOS immunostaining (a proto-onco-
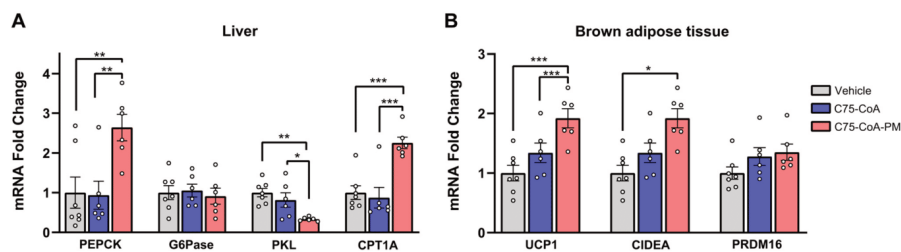

Fig. 5 ICV administration of (±)-C75-CoA polymeric micelles (PM) modifies metabolic pathways in the liver and brown adipose tissue (BAT). (A) Liver mRNA levels of genes involved in gluconeogenesis, glycolysis and fatty acid oxidation. (B) BAT mRNA levels of genes involved in thermogenesis activation. Tissues were collected 2.5 h post-injection of vehicle, free (±)-C75-CoA or (±)-C75-CoA-PM. Data are expressed as mean ± SD (*n* = 6–8). Means were compared using one-way ANOVA along with Tukey's *post hoc* test; *$p < 0.05$, **$p < 0.01$ and ***$p < 0.001$.

gene expressed within neurons following depolarization, indicating neuronal activity) was explored in the hypothalamus. This analysis was performed in ARC nucleus and paraventricular nucleus (PVN), two major hypothalamic nuclei involved in feeding behavior, liver metabolism and thermogenesis.[41,42] The number of c-FOS positive cells statistically increased in the PVN of (±)-C75-CoA-PM-injected mice as compared to those treated with the vehicle, whereas no changes were seen in mice treated with (±)-C75-CoA (Fig. 6A and B). However, analysis in the ARC revealed a lower level of neuronal activation in mice treated with (±)-C75-CoA *versus* vehicle, whereas (±)-C75-CoA-PM-treated mice showed partial restoration of this activation in parallel to the free drug (Fig. 6C and D).

The differential neuronal activation patterns in the hypothalamic nuclei PVN and ARC in response to the treatments can be explained by the remarkable satiating action and metabolic changes induced by (±)-C75-CoA-PM. Particularly, c-FOS measurements indicated that the nanomedicine could be initiating the following events: (i) stimulation of anorexigenic POMC neurons in the ARC, which led to (ii) activation of the PVN, which drove satiating effects, and (iii) triggering of changes in liver metabolism and BAT thermogenesis to regulate body weight (Fig. 6E). These observations are consistent with the changes in the expression of the neuropeptides POMC and NPY observed with the nanomedicine but not with the free drug. These in turn connect with the PVN neurons and regulate not only feeding, but also peripheral tissue metabolism. This ARC–PVN signal controlling the liver metabolism and BAT thermogenesis activation has been previously reported in response to other stimuli.[45–47]

In contrast, the free (±)-C75-CoA did not induce neuronal activation in the PVN but reduced c-FOS in the ARC (Fig. 6E), the latter being related to a reduction of NPY-expressing neurons, contributing to the satiating effect of the free drug. The lack of neuronal activation in the PVN could explain the fact that the free drug did not reduce body weight nor alter the expression of genes related to liver metabolism and BAT thermogenesis. The differences observed between the nanomedicine and the free drug in the expression of hypothalamic neuropeptides, neuronal activation and in turn peripheral metabolism could also be related to the higher degree of uptake shown by the nanomedicine in the neurons compared to the free cargo in the cell cultures and the capacity of the nanomedicine to reach hypothalamic areas regulating energy balance (Fig. S6, ESI†).
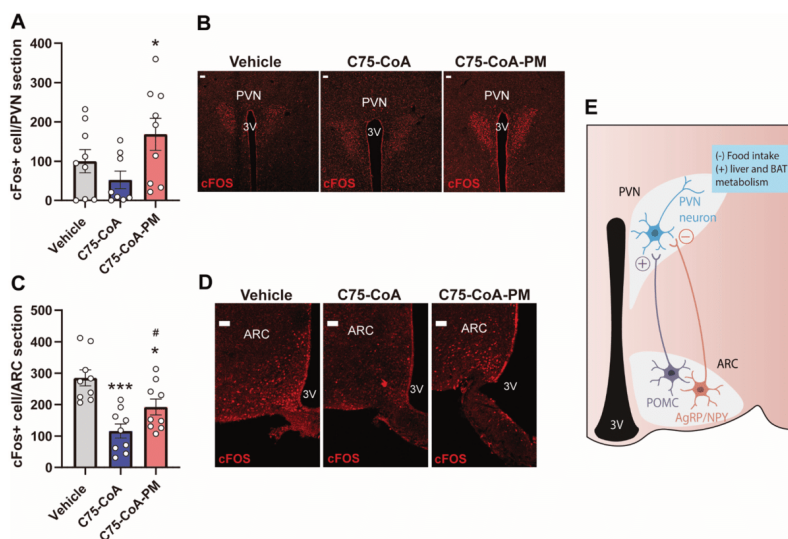

Fig. 6 Neuronal activation in the arcuate (ARC) and paraventricular (PVN) hypothalamic nuclei by ICV administration of (±)-C75-CoA polymeric micelles (PM). (A) Quantification and (B) representative confocal images showing c-FOS positive cells in the PVN section. (C) Quantification and (D) representative confocal images showing cFOS positive cells in the ARC section. (E) Schematic representation of ARC and PVN nuclei and the main types of neurons regulating energy balance. POMC activates PVN neurons leading to anti-obesity actions, whereas NPY neurons lead to a PVN inhibitory signal to promote feeding and body weight gain. Animals were perfused and the brains were collected 2 h post-injection of vehicle, free (±)-C75-CoA or (±)-C75-CoA-PM. Scale bars, 50 μm. Data are expressed as mean ± SD (3 animals, 3 slices per animal). Means were compared using one-way ANOVA along with Tukey's *post hoc* test. *$p < 0.05$ and ***$p < 0.001$ *vs.* vehicle. #$p < 0.05$ *vs.* free (±)-C75-CoA.

3. Conclusion

In this study, we have developed an inventive core crosslinked micelle-based approach to successfully encapsulate and centrally deliver a CPT1A inhibitor, to acutely regulate energy balance in mice. The effective delivery and higher neuronal uptake of the drug was evidenced by the potent and rapid satiating effect and significant body weight loss induced by the central administration of (±)-C75-CoA-PM in mice, as well as by the substantial regulation of appetite-related hypothalamic neuropeptides and neuronal activation of the PVN, which were not observed in response to the free (±)-C75-CoA treatment. Altogether, the present study showcases the first nanomedicine targeting brain lipid metabolism, offering an innovative and selective therapeutic approach for treating diseases related to dysregulation of energy balance such as obesity and diabetes. The findings of this study are expected to contribute to the corroboration and advancement of the novel prospects of nanomedicine-based approaches to modulate body weight and feeding by targeting brain lipid metabolism. Most significantly, the current study highlights the enormous potential of nanotechnology in healthcare, leading the way for a better understanding of energy balance in the early stages of obesity and diabetes that are crucial for understanding the developmental stages of these pathological conditions and thus finding an effective cure.

4. Experimental section

4.1 Preparation of the polymers and crosslinked micelles

4.1.1 Synthesis of the triblock copolymer, PEG-PBLA-PLys
(TFA). The synthesis of the triblock co-polymer, PEG-PBLA-PLys(TFA), was carried out by N-carboxyanhydride (NCA) ring-opening polymerization (ROP), as previously reported[51,52] but with modifications (Fig. 2). The initiator used in the first ROP step was α-methoxy-ω-amino-poly(ethylene glycol) (M_w: 12 kDa; PEG-NH$_2$, NOF, Japan), to produce the PEG-poly(β-benzyl-L-aspartate) diblock copolymer (PEG-PBLA). PEG-NH$_2$ was dried overnight in $vacuo$ and dissolved in distilled and dehydrated DMF (Wako Pure Chemical Industries, Japan). BLA-NCA (24 molar equivalence to PEG-NH$_2$) and thiourea (equivalent to 1 M solution in DMF) were added to the PEG-NH$_2$ solution as a dry powder under an inert atmosphere. The mixture was left to stir at 25 °C for 24 h. The resulting reaction mixture was dialyzed against water and the PEG-PBLA-NH$_2$ di-block polymer was recovered by freeze-drying. The freeze-dried di-block polymer was dissolved in dichloromethane and dropped in a mixture of n-hexane and ethyl acetate (6 : 4), followed by filtration of the precipitated polymer, and drying under vacuum. The degree of polymerization was found to be 22 BLA units by ^{1}H NMR.

The obtained PEG-PBLA-NH$_2$ was subsequently used as an initiator for the second ROP of Lys(TFA)-NCA to obtain PEG-PBLA-PLys(TFA). PEG-PBLA-NH$_2$ was dried overnight in $vacuo$ and subsequently dissolved in distilled and dehydrated DMSO. Lys(TFA)-NCA (44 molar equivalence to PEG-PBLA-NH$_2$) along with thiourea (equivalent to 1 M solution in DMF) was introduced to the PEG-PBLA-NH$_2$ solution as a dry powder under an Ar atmosphere, where the mixture was left to react at 25 °C for 48 h. The resulting reaction mixture was dialyzed against water and the PEG-PBLA-PLys(TFA) triblock polymer was recovered by freeze-drying. The freeze-dried triblock polymer was dissolved in methanol and subjected to diethyl ether precipitation and was finally dried in $vacuo$. For characterization purposes, an aliquot of the polymer was subjected to alkali hydrolysis to remove the benzyl esters and TFA groups, furnishing a water-soluble form of the triblock (PEG-PAsp-PLys) polymer. Upon ^{1}H NMR analysis of this PEG-PAsp-PLys polymer, it was revealed that 40 units of lysine residues were added with 22 units of aspartate (Fig. S8A, ESI†). Gel Permeation Chromatography (GPC) analysis (Jasco HPLC system equipped with an RI detector) confirmed (Fig. S8A, ESI†) that the polymer, PEG-PAsp-Plys, has a narrow and unimodal distribution of molecular weight (molecular weight distribution, M_w/M_n: 1.02).

4.1.2 Middle-block modification of PEG-PBLA-PLys(TFA) and the subsequent sequential deprotection. PEG-PBLA-PLys (TFA) was dissolved in anhydrous DMF (Sigma-Aldrich, cat. # 227056-100ML), to which an aromatic aminoacetal linker, 1-[4-(dimethoxymethyl)phenyl]methanamine (Enamine Ltd (Kyiv, Ukraine) (30 eq.)) was added. The reaction mixture was stirred at 40 °C for 72 h. Then, deprotection of the PLys(TFA) chain was carried out by adding 3 mL of methanol and 100 μL of 5 N NaOH. The reaction was allowed to proceed overnight. The mixture was then dialyzed against 0.02 N HCl (3×) and water (2×) for 48 h using a 8 kDa molecular weight cutoff (MWCO) dialysis bag (Spectra/Por, Spectrum Laboratories, cat. # 25223-650). The solution was freeze-dried under vacuum to obtain the modified triblock co-polymer (PEG-PAsp(Aldehyde)-PLys). ^{1}H NMR analysis confirmed the introduction of benzaldehyde groups onto the triblock polymer (Fig. S8B, ESI†).

4.1.3 Preparation of the PEG-PAsp(hydrazide) and PEG-PLys.
The synthesis of PEG-PBLA and its hydrazinolysis were carried out as previously reported,[53] while PEG-PLys was prepared similar to a previous study.[54] The preparation of labelled polymers and FRET micelles is detailed in the ESI.†

4.1.4 Micelle preparation. The crosslinked PM was formed by automatic self-assembly of polymers with the anionic drug cargo plus the hydrazone bond formation between the polymers. Polymer solutions were each dispersed in 10 mM phosphate buffer (PB) (pH 5.0) at 10 mg mL^{-1} concentration. The solutions were simply mixed with 36.87 mM (±)-C75-CoA or 7.88 mM Fluor-CoA (preparations of which are fully described in our previous work[28]) to attain a 1 : 1 anion/cation ratio, diluted with 10 mM PB (pH 7.4) to the desired concentration, and then vortexed. The micelle was allowed to cross-link at 4 °C for 24 h before passing through a 0.22 μM syringe filter (Millex 13 mm Durapore, Merck, cat. # SLGVJ13SL). The characterization of micelles is indicated in the ESI.†

4.2 Mouse cannulation and administration of drugs and polymeric micelles

The protocols for animal care and use were approved by the Ethics and Research Committee at the University of Barcelona (procedure ref. 10906 from the Generalitat de Catalunya). All experimental animal procedures were carried out in strict accordance with the European Communities directive 2010/63/EU legislation regulating animal research. All efforts were devoted to minimize animal suffering and to reduce the number of animals used.

Male (8–10 weeks old) C57BL/6J mice were used for the experiments. All animals were housed under conditions of a 12 h/12 h light/dark cycle (from 8 am to 8 pm) in a temperature- and humidity-controlled room, and allowed free access to water and standard laboratory chow. For fasting experiments, animals were randomly assigned to food-deprived (fasted group) or fed *ad libitum* groups (fed group). For tissue collection, animals were sacrificed by cervical dislocation under isoflurane anaesthesia during the light phase and the hypothalamus, liver and adipose tissue were quickly removed and stored at −80 °C.

For cannulation, cannulae were stereotaxically implanted into the lateral cerebral ventricle under anaesthesia, as previously described.[55,56] Cannulated mice were subjected to 16 h fasting before the beginning of the dark cycle. After that, mice were exposed to food and randomly assigned to the following treatments: 3 µl of vehicle (PBS), (±)-C75, (±)-C75-CoA, (±)-C75-CoA-PM (at 4.2 mM cargo concentration; injection dosage: 126.5 µg per mouse), Fluor-CoA or Fluor-CoA-PM (at 2.95 mM cargo concentration; injection dosage: 104 µg per mouse) by ICV injection 30 min before the beginning of the dark cycle. The schedule of this protocol was based on previous publications analysing feeding pattern after ICV administration of drugs.[13,14] The dosage of (±)-C75 in the free form or PM form was also based on previous studies.[13,22,24]

For feeding experiments, food intake was monitored at 1, 2, 4, 8, 12 and 24 hours after ICV administration, whereas body weight was measured before and 24 hours after the treatment. For tissue collection and gene expression analysis, food intake and body weight were monitored 2 h after drug administration and the mice were subsequently euthanized. Fresh tissues were then harvested and stored at −80 °C.

For brain immunofluorescence, mice were anesthetized using ketamine/xylazine and intracardially perfused with PBS and then with 10% NBF at 2 hours after (±)-C75-CoA, (±)-C75-CoA-PM, Fluor-CoA or Fluor-CoA-PM treatment. Brains were collected and post-fixated 24 h in 10% NBF at 4 °C, transferred to 30% sucrose at 4 °C for 2–3 days, frozen in isopentane, and sliced into 30 µm thick slices in the coronal plane throughout the entire rostral–caudal extent of the brain using a cryostat. The subsequent analysis for brain immunofluorescence or RT-PCR in the tissues is detailed in the ESI.†

4.3 Statistical analysis

All results are expressed as mean ± SD. Statistical analysis was conducted using GraphPad Prism 9 Software (GraphPad Software, La Jolla, CA, USA). Statistical analysis was performed by ANOVA (more than 2 groups were compared) followed by Tukey's *post-hoc* test. $p < 0.05$ was considered statistically significant. The number of animals used in each experiment is specified in each figure legend.

Author contributions

Conceptualization: S. Q. and R. R.-R.; methodology: J. G.-C., W. K. D. P., S. Z., A. F., A. C. R., S. A., L. S.-G., S. F. and K. T.; investigation: J. G.-C., W. K. D. P., X. A., S. Q. and R. R.-R.; visualization: J. G.-C., W. K. D. P., S. Q. and R. R.-R; supervision: S. Q., R. R.-R., X. A. and K. K.; writing – original draft: J. G.-C., W. K. D. P., S. Q. and R. R.-R.; writing – review and editing: W. K. D. P., S. Q., R. R.-R., X. A., N. C., D. S., L. H., J. G., K. K.

Conflicts of interest

There are no conflicts to declare.

Acknowledgements

References

1 I. González-García, J. Fernø, C. Diéguez, R. Nogueiras and M. López, *Neuroendocrinology*, 2017, **104**, 398–411.
2 World Health Organization, Obesity and overweight, https://www.who.int/news-room/fact-sheets/detail/obesity-and-overweight, (accessed 19 November 2019).
3 V. S. Malik, W. C. Willet and F. B. Hu, *Nat. Rev. Endocrinol.*, 2020, **16**, 615–616.
4 K. Timper and J. C. Brüning, *Dis. Models Mech.*, 2017, **10**, 679–689.

5 T. Scherer, K. Sakamoto and C. Buettner, *Nat. Rev. Endocrinol.*, 2021, **17**, 468–483.

6 P. Dimitri, *Front. Endocrinol.*, 2022, **13**, e846880.

7 A. Fosch, S. Zagmutt, N. Casals and R. Rodríguez-Rodríguez, *Int. J. Mol. Sci.*, 2021, **22**, 6186.

8 M. López, C. J. Lelliott and A. Vidal-Puig, *BioEssays*, 2007, **29**, 248–261.

9 S. Obici, Z. Feng, K. Morgan, D. Stein, G. Karkanias and L. Rossetti, *Diabetes*, 2002, **51**, 271–275.

10 M. López, R. Nogueiras, M. Tena-Sempere and C. Diéguez, *Nat. Rev. Endocrinol.*, 2016, **12**, 421–432.

11 K. D. Bruce, A. Zsombok and R. H. Eckel, *Front. Endocrinol.*, 2017, **8**, 60.

12 I. R. Schlaepfer and M. Joshi, *Endocrinology*, 2020, **161**, 1–14.

13 Z. Hu, S. H. Cha, S. Chohnan and M. D. Lane, *Proc. Natl. Acad. Sci. U. S. A.*, 2003, **100**, 12624–12629.

14 Z. Hu, Y. Dai, M. Prentki, S. Chohnan and M. D. Lane, *J. Biol. Chem.*, 2005, **280**, 39681–39683.

15 T. K. T. Lam, A. Pocai, R. Gutierrez-Juarez, S. Obici, J. Bryan, L. Aguilar-Bryan, G. J. Schwartz and L. Rossetti, *Nat. Med.*, 2005, **11**, 320–327.

16 R. Fadó, R. Rodríguez-Rodríguez and N. Casals, *Prog. Lipid Res.*, 2021, **81**, 101071.

17 J. M. Orellana-Gavaldà, L. Herrero, M. I. Malandrino, A. Pañeda, M. Sol Rodríguez-Peña, H. Petry, G. Asins, S. Van Deventer, F. G. Hegardt and D. Serra, *Hepatology*, 2011, **53**, 821–832.

18 M. Weber, P. Mera, J. Casas, J. Salvador, A. Rodríguez, S. Alonso, D. Sebastián, M. C. Soler-Vázquez, C. Montironi, S. Recalde, R. Fucho, M. Calderón-Domínguez, J. F. Mir, R. Bartrons, J. C. Escola-Gil, D. Sánchez-Infantes, A. Zorzano, V. Llorente-Cortes, N. Casals, V. Valentí, G. Frühbeck, L. Herrero and D. Serra, *FASEB J.*, 2020, **34**, 11816–11837.

19 R. Rodríguez-Rodríguez, A. Fosch, J. Garcia-Chica, S. Zagmutt and N. Casals, *J. Neuroendocrinol.*, 2023, DOI: **https://doi.org/10.1111/jne.13234**.

20 J. Dai, K. Liang, S. Zhao, W. Jia, Y. Liu, H. Wu, J. Lv, C. Cao, T. Chen, S. Zhuang, X. Hou, S. Zhou, X. Zhang, X. W. Chen, Y. Huang, R. P. Xiao, Y. L. Wang, T. Luo, J. Xiao and C. Wang, *Proc. Natl. Acad. Sci. U. S. A.*, 2018, **115**, E5896–E5905.

21 S. Obici, Z. Feng, A. Arduini, R. Conti and L. Rossetti, *Nat. Med.*, 2003, **9**, 756–761.

22 P. Mera, A. Bentebibel, E. López-Viñas, A. G. Cordente, C. Gurunathan, D. Sebastián, I. Vázquez, L. Herrero, X. Ariza, P. Gómez-Puertas, G. Asins, D. Serra, J. García and F. G. Hegardt, *Biochem. Pharmacol.*, 2009, **77**, 1084–1095.

23 S. Gao and M. D. Lane, *Proc. Natl. Acad. Sci. U. S. A.*, 2003, **100**, 5628–5633.

24 T. M. Loftus, D. E. Jaworsky, G. L. Frehywot, C. A. Townsend, G. V. Ronnett, M. D. Lane and F. P. Kuhajda, *Science*, 2000, **288**, 2379–2381.

25 S. H. Cha, Z. Hu and M. D. Lane, *Biochem. Biophys. Res. Commun.*, 2004, **317**, 301–308.

26 K. Makowski, P. Mera, D. Paredes, L. Herrero, X. Ariza, G. Asins, F. G. Hegardt, J. García and D. Serra, *Chirality*, 2013, **25**, 281–287.

27 M. C. Cheng, X. H. Qiang and C. M. Du, *Chin. Sci. Bull.*, 2013, **58**, 1256–1261.

28 W. K. D. Paraiso, J. Garcia-Chica, X. Ariza, S. Zagmutt, S. Fukushima, J. Garcia, Y. Mochida, D. Serra, L. Herrero, H. Kinoh, N. Casals, K. Kataoka, R. Rodríguez-Rodríguez and S. Quader, *Biomater. Sci.*, 2021, **9**, 7076–7091.

29 S. Quader, X. Liu, K. Toh, Y. L. Su, A. R. Maity, A. Tao, W. K. D. Paraiso, Y. Mochida, H. Kinoh, H. Cabral and K. Kataoka, *Biomaterials*, 2021, **267**, e120463.

30 H. Shibasaki, H. Kinoh, H. Cabral, S. Quader, Y. Mochida, X. Liu, K. Toh, K. Miyano, Y. Matsumoto, T. Yamasoba and K. Kataoka, *ACS Nano*, 2021, **15**, 5545–5559.

31 H. J. Kim, K. Miyata, T. Nomoto, M. Zheng, A. Kim, X. Liu, H. Cabral, R. J. Christie, N. Nishiyama and K. Kataoka, *Biomaterials*, 2014, **35**, 4548–4556.

32 H. Cabral, K. Miyata, K. Osada and K. Kataoka, *Chem. Rev.*, 2018, **118**, 6844–6892.

33 J. W. McFadden, S. Aja, Q. Li, V. V. R. Bandaru, E. K. Kim, N. J. Haughey, F. P. Kuhajda and G. V. Ronnett, *PLoS One*, 2014, **9**, e115642.

34 S. H. Cha, Z. Hu, S. Chohnan and M. D. Lane, *Proc. Natl. Acad. Sci. U. S. A.*, 2005, **102**, 14557–14562.

35 S. H. Cha, J. T. Rodgers, P. Puigserver, S. Chohnan and M. D. Lane, *Proc. Natl. Acad. Sci. U. S. A.*, 2006, **103**, 15410–15415.

36 Z. Hu, H. C. Seung, G. Van Haasteren, J. Wang and M. D. Lane, *Proc. Natl. Acad. Sci. U. S. A.*, 2005, **102**, 3972–3977.

37 H. C. Seung, M. Wolfgang, Y. Tokutake, S. Chohnan and M. D. Lane, *Proc. Natl. Acad. Sci. U. S. A.*, 2008, **105**, 16871–16875.

38 M. S. Vohra, K. Benchoula, C. J. Serpell and W. E. Hwa, *Eur. J. Pharmacol.*, 2022, **915**, 174611.

39 C. Quarta, M. Claret, L. M. Zeltser, K. W. Williams, G. S. H. Yeo, M. H. Tschöp, S. Diano, J. C. Brüning and D. Cota, *Nat. Metab.*, 2021, **3**, 299–308.

40 M. V. Kumar, T. Shimokawa, T. R. Nagy and M. D. Lane, *Proc. Natl. Acad. Sci. U. S. A.*, 2002, **99**, 1921–1925.

41 M. Schneeberger, R. Gomis and M. Claret, *J. Endocrinol.*, 2014, **220**, T25–T46.

42 E. Roh, D. K. Song and M. S. Kim, *Exp. Mol. Med.*, 2016, **48**, e216–e216.

43 C. Contreras, R. Nogueiras, C. Diéguez, K. Rahmouni and M. López, *Redox Biol.*, 2017, **12**, 854–863.

44 T. Yoneshiro, R. Rodríguez-Rodríguez, M. J. Betz and P. C. N. Rensen, *Front. Endocrinol.*, 2020, **11**, 845.

45 C. Contreras, I. González-García, P. Seoane-Collazo, N. Martínez-Sánchez, L. Liñares-Pose, E. Rial-Pensado, J. Fernø, M. Tena-Sempere, N. Casals, C. Diéguez, R. Nogueiras and M. López, *Diabetes*, 2017, **66**, 87–99.

46 L. P. Klieverik, S. F. Janssen, A. Van Riel, E. Foppen, P. H. Bisschop, M. J. Serlie, A. Boelen, T. Ackermans, H. P. Sauerwein, E. Fliers and A. Kalsbeek, *Proc. Natl. Acad. Sci. U. S. A.*, 2009, **106**, 5966–5971.

47 M. T. Hackl, C. Fürnsinn, C. M. Schuh, M. Krssak, F. Carli, S. Guerra, A. Freudenthaler, S. Baumgartner-Parzer, T. H. Helbich, A. Luger, M. Zeyda, A. Gastaldelli, C. Buettner and T. Scherer, *Nat. Commun.*, 2019, **10**, 2717.

48 A. Bonaccorso, T. Musumeci, M. F. Serapide, R. Pellitteri, I. F. Uchegbu and G. Puglisi, *Colloids Surf., B*, 2017, **154**, 297–306.

49 S. Dante, A. Petrelli, E. M. Petrini, R. Marotta, A. Maccione, A. Alabastri, A. Quarta, F. De Donato, T. Ravasenga, A. Sathya, R. Cingolani, R. Proietti Zaccaria, L. Berdondini, A. Barberis and T. Pellegrino, *ACS Nano*, 2017, **11**, 6630–6640.

50 R. Rodriguez-Rodriguez and S. Quader, *Nanomedicine*, 2022, **17**, 495–498.

51 S. Fukushima, K. Miyata, N. Nishiyama, N. Kanayama, Y. Yamasaki and K. Kataoka, *J. Am. Chem. Soc.*, 2005, **127**, 2810–2811.

52 K. Miyata, M. Oba, M. Nakanishi, S. Fukushima, Y. Yamasaki, H. Koyama, N. Nishiyama and K. Kataoka, *J. Am. Chem. Soc.*, 2008, **130**, 16287–16294.

53 S. Quader, H. Cabral, Y. Mochida, T. Ishii, X. Liu, K. Toh, H. Kinoh, Y. Miura, N. Nishiyama and K. Kataoka, *J. Controlled Release*, 2014, **188**, 67–77.

54 K. Osada, T. Shiotani, T. A. Tockary, D. Kobayashi, H. Oshima, S. Ikeda, R. J. Christie, K. Itaka and K. Kataoka, *Biomaterials*, 2012, **33**, 325–332.

55 R. Rodríguez-Rodríguez, C. Miralpeix, A. Fosch, M. Pozo, M. Calderón-Domínguez, X. Perpinyà, M. Vellvehí, M. López, L. Herrero, D. Serra and N. Casals, *Mol. Metab.*, 2019, **19**, 75–85.

56 M. Pozo, R. Rodrguez-Rodrguez, S. Raḿrez, P. Seoane-Collazo, M. López, D. Serra, L. Herrero and N. Casals, *Endocrinology*, 2017, **158**, 2226–2238.

- 265 -